Optische gepulste neuronen geïntegreerd op een fotonische chip

All-Optical Spiking Neurons Integrated on a Photonic Chip

Thomas Van Vaerenbergh

Promotoren: prof. dr. ir. P. Bienstman, prof. dr. ir. J. Dambre
Proefschrift ingediend tot het behalen van de graad van
Doctor in de Ingenieurswetenschappen: Fotonica

Vakgroep Informatietechnologie
Voorzitter: prof. dr. ir. D. De Zutter
Faculteit Ingenieurswetenschappen en Architectuur
Academiejaar 2013 - 2014

UNIVERSITEIT
GENT

ISBN 978-90-8578-694-8
NUR 965, 959
Wettelijk depot: D/2014/10.500/40

Promotoren:

Prof. Dr. Ir. Peter Bienstman
Prof. Dr. Ir. Joni Dambre

Examencommissie:

Prof. Dr. Ir. Luc Taerwe (voorzitter)	Universiteit Gent, Bouwkundige Constructies
Prof. Dr. Ir. Peter Bienstman (promotor)	Universiteit Gent, INTEC
Prof. Dr. Ir. Joni Dambre (promotor)	Universiteit Gent, ELIS
Dr. Ir. Michiel Hermans (secretaris)	Universiteit Gent, ELIS
Prof. Dr. Ir. Dirk Aeyels	Universiteit Gent, SYSTeMS
Prof. Dr. Ir. Guy Verschaffelt	Vrije Universiteit Brussel, Aphy
Dr. Alejandro M. Yacomotti	CNRS, LPN

Universiteit Gent
Faculteit Ingenieurswetenschappen en Architectuur

Vakgroep Informatietechnologie
Sint-Pietersnieuwstraat 41, B-9000 Gent, België

Tel.: +32-9-264.89.33
Fax.: +32-9-331.35.93

Dit werk kwam tot stand in het kader van een
aspirantenbeurs van het Fonds voor Wetenschappelijk
Onderzoek - Vlaanderen (FWO-Vlaanderen).

Dankwoord

Wanneer je de kaft van dit werk bekijkt staat mijn naam daar nogal eenzaam te blinken onder die titel. Deze pagina's bieden me gelukkig de gelegenheid om één en ander recht te zetten. In tegenstelling tot wat je uit die visuele lapsus zou kunnen concluderen heb ik me de afgelopen vier jaar niet als een kluizenaar teruggetrokken, in de hoop door voldoende contemplatie, ergens vlak voor mijn beurs op was, na de zoveelste meditatiesessie, uiteindelijk een ultieme staat van verlichting te bereiken, om daarna snel-snel mijn geniale bevindingen neer te pennen en alsnog enkele wetenschappelijk publicaties binnen te halen. Integendeel, een doctoraat, of eerder een wetenschapper in het algemeen, mag vandaag de dag wel degelijk interageren met zijn medemens, en laat duidelijk zijn dat ik die mogelijkheid ten volle benut heb. Dit boekje is er niet alleen dankzij mijn eigen bloed, zweet en tranen[1]. Ik heb zowaar hulp gekregen, véél hulp en daarom dien ik - voor ik in het wetenschapsjargon duik - eerst een aantal mensen te bedanken!

Wie op de kaft verder kijkt dan zijn of haar neus lang is, ziet al snel twee andere namen opduiken: Peter Bienstman en Joni Dambre, mijn twee promotoren[2]. Mijn beide pollekes mag ik kussen dat zij mij de afgelopen jaren begeleid hebben. Ik kreeg veel vrijheid, af en toe een schouderklopje, en op de juiste momenten werd ik er ook aan herinnerd dat ik al eens een artikel mocht schrijven over wat ik aan het doen was. Zonder die artikels had ik dit boekje niet mogen schrijven, dus die kleine duwtjes in de juiste richting waren zeker nuttig.

Twee namen die op de kaft ontbreken zijn echter Martin Fiers en Koen Alexander, respectievelijk mijn voormalige thesisbegeleider en één van mijn twee thesisstudenten (over de andere vertel ik straks nog even). Wie al eens verder durft bladeren doorheen deze papierbundel zal al snel op werk stuiten dat enkel door een intense samenwerking met hen tot stand is kunnen komen. Bedankt daarvoor!

---

[1] Goed, goed, we overdrijven hier een beetje, er was gelukkig enkel sprake van een beetje zweet doordat ik quasi elke dag de Plateau-berg moest opfietsen.

[2] Beiden prof. dr. ir., maar uit notationale eenvoud laat ik dit soort extra titels in de loop van dit dankwoord even achterwege. Geïnteresseerde lezers kunnen de correcte aansprekingen gemakkelijk consulteren op de voorgaande pagina's.

Graag bedank ik ook de juryleden van mijn examencommissie, Michiel Hermans, Peter, Joni, Guy Verschaffelt, Alejandro Giacomotti, Dirk Aeyels, Luc Taerwe, zonder wie ik niet had mogen overgaan tot mijn publieke verdediging. Jullie feedback was zeer welkom en ik hoop dat ik jullie opmerkingen intussen goed heb verwerkt.

Mijn geldschieters, het FWO, dien ik zeker ook te vermelden want onderzoek doen is tof, maar zonder jullie financiële bijdrage op het eind van de maand was dat niet mogelijk geweest.

Als ik de vorige paragrafen herlees valt me op dat ik nog veel bedankingswerk voor de boeg heb, maar laat ik eerst enkele jaren teruggaan in de tijd. Ik zat toen in de derde bachelor en volgde het vak Fotonica, gegeven door Roel Baets, stichtend lid van de onderzoeksgroep waar ik enkele jaren later in zou belanden. Een zeer enthousiasmerende lesgever was me dat, die me zin deed krijgen in meer. De oplossing was snel gevonden, diezelfde zomer deed ik onder auspiciën van stagebegeleider Ronny Bockstaele een maand lang fotonica-gelieerd werk in zijn spin-off. Toen wist ik het zeker, dit was iets voor mij! Daarna volgden nog een keuzevak Microfotonica, alwaar ik Martin leerde kennen als een gemotiveerde practicum-assistent. Niet veel later volgden de thesisvoorstellen voor het jaar daarop. Bleek dat Martin een thesis begeleidde die over neurale netwerken (een onderwerp dat me door een stage bij Lunahra bvba ook nauw aan het hart lag) èn fotonica ging. Hij verwees me door naar de promotor die bij die thesis hoorde. Zo leerde ik Peter kennen, en iets later ook Joni. Thesissen bood me voldoende uitdaging om te willen tekenen voor vier onderzoeksjaren extra.

En zo begon die (toch voor mij) legendarische periode, ik belandde ergens in september op mijn bureau, en beetje bij beetje leerde ik mijn bureaugenoten kennen. Dat ging met vallen en opstaan, basketfanaat Diedrik miste al eens een shot in onze mini-basketbalring of wou mijn reactievermogen testen tijdens momenten van opperste concentratie, waardoor ik meermaals zo'n balletje in mijn oog kreeg. Maar later bleek gelukkig dat daar geen verborgen agenda achter zat. Samen met Peter, mijn 'eiland'-genoot toonde hij me de weg naar de meetkamer, een nieuwe wereld die voor het voormalige programmerend thesisstudentje dat ik toen nog was openging. Toeval wou namelijk dat Peter voor zijn doctoraat dezelfde component onderzocht als mij, de microring, maar dan voor een totaal andere toepassing. Een nieuwe samenwerking was geboren, uren of zelfs dagenlang hebben we over die ringen gediscussieerd. Peter overtuigde me ook om voor mijn eerste niet-Europese conferentie te submitten, en hielp me zelfs aan een slaapplaats tijdens mijn daar aan gekoppelde city-trip Hong Kong. Dat zal nog lang in mijn hersenpan gegrift staan. Aan mijn andere kant zat Thijs, een zowaar sympathieke Hollander die ik stiekem altijd een beetje beschouwd heb als de vaderfiguur van onze bureau. Blijkt nu recent dat hij zijn roeping ook zelf heeft ingezien, wat een geluk moet zijn voor de toekomstige boreling. Hij hielp me regelmatig ook al eens bij mijn experimenteel werk of als ik vragen had over microdisk lasers (en daar had ik er veel van in de tijd dat ik Koen begeleidde). Had ik al gezegd dat mijn bureau groot is? En internationaal? Verder bleken er nog Sukumar en Rajesh, twee jolige Indiërs die me introduceerden in het Diwali festival (festival van het licht, een grootschalig Indisch festival dat verklaart waarom er zoveel Indiërs in de fotonica komen werken in onze groep). Ook China was vertegenwoordigd door Honghui, en - topologisch gezien het verst van mijn bureaustoel - zat Eva, die met haar aanstekelijke vrolijkheid voor de nodige motivatie zorgt/zorgde onder de bureaugenoten. Stond ook altijd klaar voor advies als ik daar behoefte aan had.

Noot aan de lezer: intussen zijn er al wat individuën uit de originele bureauschikking vervangen. We zijn tegenwoordig met negen, en daardoor had ik ook het plezier om nieuwe beloftevolle PhD-studenten te leren kennen zoals Raphaël, een wel-opgevoede Brasschatenaar[3] die met twee woorden spreekt, een passie voor wetenschap heeft en toch nog boeiende andere gesprekken kan aanknopen. Er was ook een passage van Martijn in onze bureau, de voormalige beschermheilige van de clean room. There is as well Amin, proving that Perzians are really nice people with their heart on the right spot. Pijush also entered the office, and the newest newbies are Andreas and Haolan. Thanks all for being there, and giving me an 'almost at home'-feeling in my office.

Men zou bijna denken dat onze groep slechts één bureau telt, niets is minder waar. Eva kan de bureau aan de overkant van de gang zien en keek lang uit op pokerface-Karel, eilandgenoot van Martin - jawel, diezelfde van daarnet. Vermits Martin in het begin van mijn doctoraat de nobele taak had aangevat om me te leren wat ècht programmeren was stond ik nogal veel in die andere bureau. Goed, de gehele waarheid is natuurlijk ook dat Martin me overtuigde om in Linux te werken en hij toendertijd de enige was die mijn geknoei op dat besturingssysteem terug recht kon trekken. Aldaar zaten ook twee onverlaten, Yannick en Bart genaamd, die mijn bureaudecoratie al eens overhoop kwamen gooien. Ik had in die dagen een mooie medaille van Aditya gekregen (thanks for that New Dehli tourist gadget you once gave me, and the nice collaboration during microphotonics!), en daar moeten die twee kastaars van over de gang jaloers op geweest zijn. Chance dat ik daar pas zeer laat achtergekomen ben, zodat ik hen tegen dat ik het eindelijk wist toch al sympathiek vond.

Laat ik even duidelijk maken dat de boog niet altijd even strak gesponnen stond bij ons, met alle voornoemde namen (en bijhorende liefjes) gingen we al eens regelmatig een pintje pakken in de Vooruit, de Ploeg en dies meer. Daarbij waren meestal de leden van de cadeau-maffia aanwezig, tortelduifjes Elewout (ondanks alles denk ik dat je mijn aanwezigheid stiekem best wel verdraagt) en Cristina (vrouwelijke dansgoeroe van de groep), Wout en Marie en ook mijn persoonlijke postdoc, Kristof (mannelijke dansgoeroe van de groep, ook wel genaamd : 'Hij die zijn collega's leerde dansen'). Andere 'anciens' die al vaak eens hun hoofd vertoonden op die evenementen waren Tom en Joris R., mensen die ons in contact brachten met de buitenwereld, en toonden dat het meestal wel goed kwam na dat doctoraat.

---

[3] Volgens de overleveringen zou hij stiekem geëmigreerd zijn uit Wilrijk, maar voorlopig heb ik nog geen zwart-op-wit bewijzen van deze verdachtmakingen onder ogen gehad.

Tijd voor nog meer collega's! Over de vakgroepen heen had ik ook het genoegen om naast co-promotor Joni, met Benjamin Schrauwen (merci voor de tip om Izhikevich te lezen!), Ken (zotte programmeur die de begindagen van mijn doctoraat best aangenaam heeft gemaakt) en Michiel H. (tof dat je elke keer weer afkomt met van die coole concepten tijdens de PRC meetings).

Nu ik dan toch over de PRC meetings bezig ben, naast Kristof, Martin, Michiel en beide promotoren was daar ook de polyglot Bendix terug te vinden. Recent maakte ook Andrew zijn intrede. Hun aanwezigheid in het PRC-groepje maakt duidelijk dat er ook in de toekomst nog belangrijke nieuwe reservoir computing concepten zullen ontstaan in onze fotonica-groep!

Ook het Caphe-Ipkiss verhaal moet ik ten berde brengen. Martin verliet zo'n jaar geleden ons PRC-groepje om zijn eigen software spin-off rond Caphe en Ipkiss, twee nu al wereldbefaamde softwaretools die in onze groep zijn ontwikkeld, te starten samen met Wim, Pieter D., Erwin, Pierre, Joris G. (bedankt trouwens voor die keren dat ik per ongeluk een map simulatieresultaten per ongeluk had gewist en je me uit de nood probeerde te helpen!).

And I'm still not there yet, the list is almost endless, I also have to mention Herbert (waardige opvolger voor het matrix-practicum bij microfotonica!), Sarvagya (once we will write a paper about this effective index story), Nannisha (it's a pity you're gone, who else is going to teach me how to cook decent Thai food?), Gunay (gewoon beginnen schrijven aan je boek, dat is het beste advies dat ik kan geven), Pauline (Bedankt om me de trucjes van al je meetopstellingen te willen uitleggen...) and Sam, Michael (die automatische meetsetup van jou heeft mij veel tijd bespaard), Kristien (redster in nood in gevallen van extreem geknoei met mijn laptop), Ang Li, Daan, Jan-Willem, Chen, Paul, Ananth, Sarah, Frédéric, Geert (altijd paraat voor advies bij problemen in de meetkamer), Dries, Alfonso, Muhammed, Pieter, François, Ananth, Shahram and Leili (another two friendly Perzians, Leili being the girlfriend of office-mate Amin), Jeroen, Utsav, Jesper, ... A lot of people with whom I had interesting discussions about work and non-work-related topics.

I should also mention my stay in LPN, CNRS. Thanks to Alejandro, Philippe, Samir, Kamel and Ariel for letting me join your group during those few months. Working on these photonic crystal cavities gave me a lot valuable new insights. Thanks to all my room mates in the Cité U, I really had a pleasant time there. Bedankt ook aan beide Ilses om me daar in die toen volledig door sneeuw bedekte straten te komen opzoeken.

Recent werd ik ook goed onthaald door de beide Guys, Mulham en Romain in de VUB. Hopelijk komt er nog iets uit die experimenten die we zijn gestart!

Ik had overigens ook enorm veel geluk met mijn thesisstudenten, ik heb er in totaal twee gehad. Koen vermelde ik eerder al, maar er was ook nog Michiel C., die zich heeft bezig gehouden om beurskoersen te proberen voorspellen met (photonic) reservoir computing. Het ga je goed daar bij de collega's van ELIS.

Met zoveel collega's is het achteraf gezien bizar dat ik ook nog met andere mensen contact had, maar er waren wel degelijk Jense, Brenda (van een mogelijkheid tot ondervoeding is in jouw aanwezigheid geen sprake), Sophie, Michel, Erik en Sarah (ik plan nog steeds jullie te komen opzoeken!), die me de vinger aan de pols deden houden in het modale burgie-huishouden. Gelukkig waren daarbij meestal Kathleen (die plant leeft nog, ik zweer het!) en Seba (ik hoop dat ik je voor je naar Princeton vertrekt nog eens meekrijg op Boomtown) aanwezig, zodat ik daar niet als enige doctoraatstudent tussen al dat 'belastingbetalend werkmens'-geweld stond!

Buiten die burgie-huiskamergroep was er ook een heel team dat klaar voor me stond om me te voeden, te luisteren naar mijn verzuchtingen, met mij naar toneel, thé dansants, film, jazzfestivals te gaan, mij te kleden. Ellen (rots in de branding, en vat vol goede ideeën, door jou tel ik nu elk jaar af tot het vriest zodat ik nog eens in Hulst kan gaan schaatsen en zo draag ik veel mooie herinneringen aan mijn weekends in het Waasland en omstreken mee - goed dat jij eindelijk in Gent bent komen wonen), Marijke (zonder mensen als jij was het concept rookthee me volledig ontgaan, wat zonde zou zijn, bedankt trouwens voor het naleeswerk van mijn premature doctoraatshoofdstukken) en Sonny (jaja, ooit kook ik nog eens terug voor jullie), Dominique (bij jou heb ik het gevoel dat ik nog eens zal mogen opscheppen dat ik je al kende toen je nog jong en onbekend was, blijven schrijven De Meyst! Om je wat entertainment te bieden verstopte ik alvast zeven taalfouten in dit dankwoord, benieuwd of je ze vindt. Ik hoop stiekem ook op de verderzetting van onze leesclub.), Freek (het Gentse horeca-leven had er zonder jouw introductie stukken anders uitgezien voor mij, speciaal voor jou deze quizvraag: 'Hoe heet het Europese project dat momenteel loopt waarin het einddoel is het volledige menselijke brein te simuleren?'), Ruth (wanneer gaan we nog eens naar de Roma?), Ingrid (chance dat er toch iemand op mijn mentale gezondheid let! Er zijn ook maar weinig mensen met wie naar de film gaan zo tof is als met jou...), Jean-Luc, Anja, Laura en Eline (met jullie gaan lunchen geeft me altijd een beetje een vakantiegevoel), Lode, lindy-hoppende Rein (altijd aangenaam om je tegen het lijf te lopen in de verste uithoeken ter wereld, zoals in Peking), Joksie, Tineke, Ramses, Inge (ongeneerd chique gaan eten, blij dat jij er was om dat met me te doen), Elke en Matthias (altijd een beetje thuiskomen in jullie bungalow) en pas in mijn laatste doctoraatsjaar er bij gekomen: Dorien (ben ik even blij dat je op Jazz Middelheim op me toestapte, zonder jouw creatieve chaos had ik mijn vrije tijd de laatste maanden heel wat saaier doorgebracht) en Sofie (zonder jou was er van Fig. 1.1 geen sprake, ik ben ontzettend blij dat ik via Eva zo'n gepersonaliseerde reisbegeleidster heb ontmoet, bedankt ook voor de goede zorgen in tijden van schrijfmoeheid en om me tijdens het badmintonnen toch nog de indruk te willen geven dat ik alvast een beetje vooruitgang maak). Of ik nu in Gent, Antwerpen of Sint-Niklaas vertoefde, altijd stonden jullie voor me klaar. Of toch verdacht veel. Ik ga er al lang niet meer van uit dat ik ooit iets equivalents zal kunnen terugdoen van wat jullie voor mij beteken(d)en.

Buiten mijn vriendenkring kreeg ik ook nog steun uit familiale hoek (tante, nonkel, nicht, bedankt om me te komen opzoeken in Parijs en neef en Irene, ik hoop dat we elkaar nog tijdens veel Gentse Feesten edities tegen het lijf lopen). Speciale vermelding verdienen hier alvast oma en opa, jammer dat jullie er niet meer bij zijn. Mijn bezoekjes aan Molenberg hadden vaak een therapeutische uitwerking. Aan de andere zijde van de familie motiveerde pepe, vanop zijn wolkje daarboven, me ook om dit doctoraat tot een goed einde te brengen, door mij vijftig jaar geleden het goede voorbeeld te geven. Speciale dank ook voor Jo en Suzy om me in de periode dat ik mijn bureau beu gezien was bij jullie in de living te laten verderschrijven.

Tot slot dienen ook nog de leden van het geslacht Van Vaerenbergh-Van Den Meersschaut aan bod te komen: moeder, vader (bedankt voor het nalezen van mijn Nederlandstalige samenvatting!) en zus. Zij boden me de afgelopen vier jaar telkens weer een plaats waar ik me kon terugtrekken van al dat Gents geweld. Fris gewassen, gestreken en gevoed kon ik dankzij jullie zorgen na één van de vele weekendjes thuis weer monter het strijdperk tegemoet treden. Bedankt beste ouders en zusje (het spijt me overigens zeer dat ik niet gewoon postbode ben geworden dierbare zus, maar dat is een ander verhaal) voor het onuitputtelijke begrip, de goede zorgen en de steun die jullie me boden. Niet iedereen heeft even veel geluk met zijn thuisfront!

Ter conclusie zou ik graag iedere thesisstudent die erover twijfelt om al dan niet een doctoraat aan te vatten willen aanraden om het gewoon te doen! Van dit soort jobs zijn er niet veel.

Gent, 21 mei 2014
Thomas Van Vaerenbergh

Table of Contents

Dankwoord **i**

Nederlandse samenvatting **xxxix**
- 1 Neuromorf rekenen xl
- 2 Fotonica xl
- 3 Neuromorf rekenen op basis van fotonica xli
- 4 Optische gepulste neuronen geïntegreerd op een fotonische chip xlii

English summary **xlv**
- 1 Neuromorphic computing xlvi
- 2 Photonics xlvi
- 3 Neuromorphic computing using photonics xlvii
- 4 All-optical spiking neurons integrated on a photonic chip xlvii

1 Introduction **1**
- 1.1 Neuromorphic computing 2
- 1.2 Photonics and the link with optical computation 4
- 1.3 Neuromorphic computing using photonics 6
- 1.4 All-optical spiking neurons integrated on a photonic chip 7
- 1.5 Thesis outline 9
- 1.6 Publications 10
- References 13

2 Optical Spiking Neural Networks **17**
- 2.1 Neural networks 17
  - 2.1.1 Training 18
  - 2.1.2 Neuron type 19
  - 2.1.3 Network topology 23
    - 2.1.3.1 Feedforward versus recurrent neural networks . . 23
    - 2.1.3.2 The combination of feedforward and recurrent neural network properties using reservoir computing 24

2.2 Optical implementations of neural networks 25
    2.2.1 Photonic reservoir computing 26
    2.2.2 Optical Spiking Neural Networks 28
2.3 Excitability in nonlinear dynamical systems 30
    2.3.1 Nonlinear dynamical systems theory 31
        2.3.1.1 Saddle-node or fold bifurcation 32
        2.3.1.2 Andronov-Hopf bifurcation 33
        2.3.1.3 Saddle-node on an invariant circle bifurcation . . 35
    2.3.2 The origin of excitability and its classification 35
2.4 Excitability in optics 38
    2.4.1 Adler model 40
    2.4.2 Slow-fast dynamics 41
2.5 Conclusion 44
References 45

3 Phenomenological modeling of photonic integrated circuits 53
3.1 Towards phenomenological models 54
3.2 Implementation details 57
    3.2.1 The need for a new software package 57
    3.2.2 Choice of programming language 58
3.3 Signal representation 59
    3.3.1 Travelling waves 59
    3.3.2 Envelope approximation 60
3.4 Scatter matrices 61
    3.4.1 Passive component 62
    3.4.2 Reciprocal component 63
    3.4.3 Example scatter matrices 63
        3.4.3.1 Scatter matrix of a waveguide 64
        3.4.3.2 Scatter matrix of a directional coupler 64
3.5 Beyond the scatter-matrix: the node description 64
3.6 Generalized source term 66
3.7 Generalized connection matrix of a circuit 67
    3.7.1 Derivation of the generalized connection matrix 67
    3.7.2 Application of the framework to a microring resonator . . . 69
        3.7.2.1 Frequency-domain simulations 71
        3.7.2.2 Time-domain simulations 74
    3.7.3 Speeding up the matrix calculations 74
3.8 Integration of the state variables 76
    3.8.1 Node elimination during time-domain simulations 77
        3.8.1.1 Efficient evaluation of the time derivative of the system 77

3.8.1.2 Node elimination in a nanophotonic reservoir . . 78
3.8.2 Choice of integration algorithm 79
3.8.2.1 Stability, accuracy and speed 79
3.8.2.2 Numeric integration of coupled nonlinear cavity dynamics 80
3.9 Temporal Coupled Mode Theory 82
3.9.1 Derivation of CMT equations for a microring resonator . . 84
3.10 Extending the framework to CMT-models 86
3.10.1 Reshaping the system equation towards CMT 87
3.10.2 Calculation of the linear transmission 88
3.10.3 Increasing sparseness 89
3.10.4 Applicability of the extended framework 91
3.11 Example: frequency simulation of a Coupled Resonator Optical Waveguide circuit 92
3.12 Future work 94
3.12.1 Multiwavelength simulations 94
3.12.2 Time-domain model of dispersion 94
3.12.3 Co-simulation of electronic and photonic circuits 95
3.12.4 Noise modeling 95
3.12.5 Variability and yield analysis 96
3.13 Conclusion 96
References 97

4 Cascadable excitability in microrings 105
4.1 Excitability in thermo-electrical nonlinear photonic components 106
4.2 Silicon-on-insulator microring resonator 108
4.2.1 CMT-equations of a nonlinear microring 109
4.2.2 Numerical details of the simulations 110
4.3 Nonlinear dynamical analysis of bistability and self-pulsation . . 111
4.3.1 Physical origin of bistability in a ring 112
4.3.2 Physical origin of self-pulsation in a ring 113
4.3.3 Power sweep for fixed wavelength 114
4.3.3.A Calculation of the steady state equations 115
4.3.4 Phase-plane analysis 116
4.3.4.A Calculation of the nullclines 117
4.3.4.B Proof of the bijection between $(\Delta T, N)$-plane and $da/dt = 0$-surface 117
4.3.5 2D approximation 118
4.3.5.A Calculation details of the 2D approximation . . . 119
4.3.6 Bifurcation analysis of the onset of bistability and the onset of self-pulsation 119

- 4.4 Excitability: single and double ring configuration 122
  - 4.4.1 Threshold behaviour 123
  - 4.4.2 Refractory period 125
  - 4.4.3 Cascadability 127
  - 4.4.4 Energy consumption and speed 128
- 4.5 Measurement of the microring neurons 128
  - 4.5.1 Fabrication, design and measurement setup 129
  - 4.5.2 Single microring self-pulsation 130
  - 4.5.3 Single microring excitability 131
  - 4.5.4 Cascadable microring excitability 133
- 4.6 Derivation and analysis of the scaling laws of the cavity dynamics 135
  - 4.6.1 Context of the calculation method 136
  - 4.6.2 Dimensionless version of simplified rate equations 136
  - 4.6.3 Influence of cavity design on nonlinearity enhancement . . 140
    - 4.6.3.1 Influence of Q_i and k on p, ep and qp 140
    - 4.6.3.2 Influence of V on p, ep and qp 141
    - 4.6.3.3 Influence of Q_i and k on q and e 142
  - 4.6.4 Linear stability analysis 142
  - 4.6.5 Influence of model parameters on bistability, self-pulsation and excitability 146
    - 4.6.5.1 Influence of q: FCD versus SSA 146
    - 4.6.5.2 Influence of timescale ratio ϵ 146
    - 4.6.5.3 Influence of free carrier lifetime τ_{fc} 150
    - 4.6.5.4 Influence of f: FCA versus FCD 150
  - 4.6.6 Summary of the derivation: towards design guidelines . . . 152
- 4.7 Future work 153
- 4.8 Conclusion 154
- References 155

5 Cascadable excitability in microdisk lasers **159**
- 5.1 Excitability in integrated semiconductor lasers 160
  - 5.1.1 Excitability due to optical injection in single-mode semiconductors 161
  - 5.1.2 Excitability near the onset of passive Q-switching 161
  - 5.1.3 Excitability in asymmetric Semiconductor Ring Lasers . . . 162
  - 5.1.4 Excitability due to optical injection in microdisk lasers . . . 163
- 5.2 The microdisk laser 163
  - 5.2.1 Rate equation model of a single microdisk laser 164
  - 5.2.2 Bifurcation diagram for increasing current 165
- 5.3 Optical injection 166
- 5.4 Excitability 168

5.4.1 Neuron circuit 169
5.4.2 Reaction of the system to a typical trigger pulse 170
5.4.3 Threshold behaviour as a function of input pulse power . . 172
5.4.4 Threshold behaviour as a function of input pulse phase . . 174
5.4.5 Integrating behaviour 176
5.4.6 Refractory period 177
5.4.7 Complex addition of two input pulse streams 179
5.5 Towards cascadability 180
5.5.1 Connection of the disk neurons 181
5.5.2 Rate equation model of two coupled microdisk lasers . . . 183
5.6 Transfer of the excitation 184
5.6.1 Symmetrical coupling - Oscillations 185
5.6.2 Asymmetrical coupling - Unidirectional excitation transfer 186
5.7 Sensitivity to parameter variations 188
5.7.1 Influence of current variations 188
5.7.2 Influence of detuning variations 190
5.7.3 Compensating for variations in detuning 191
5.8 Future work 192
5.9 Conclusion 194
References 195

6 Conclusions and Perspectives 201
6.1 High-level simulations of nonlinear photonic integrated circuits . 202
6.2 Cascadable excitability 202
6.2.1 A microring as a spiking neuron 203
6.2.2 A microdisk as a spiking neuron 203
6.2.3 Towards large-scale optical Spiking Neural Networks 205
References 206

List of Figures

1 (a) Als de trigger puls voldoende sterk is, exciteert het de ring, met een vaste pulsvorm. Lagere triggersterktes resulteren in subthreshold oscillaties. (b) Als de resonanties van twee identieke all-pass ringen voldoende dicht bij elkaar liggen, zullen ze exciteerbaar zijn bij hetzelfde pompsignaal, wat te zien is aan de uitgang van het circuit als twee afzonderlijke pulsen. xlii

2 (links) De gebruikte topologie om twee microdisklasers te cascaderen. De connecties tussen beide lasers komt overeen met een faseverschil $\Delta\phi$. (rechts, boven) Als een externe perturbatie de eerste disk triggert, exciteert die op zijn beurt de tweede disk. Als beide disks hetzelfde locking signaal ontvangen exciteert de tweede disk op zijn beurt terug de eerste disk door de symmetrie van het systeem. Dit proces herhaalt zichzelf en resulteert in alternerende excitaties tussen de twee disks. (rechts, onder) Symmetriebreking door het creëren van een faseverschil tussen de twee locking signalen van de disks kan de pulstransfer unidirectioneel maken: de tweede disk herexciteert de eerste disk niet. xliv

1 (a) If the trigger pulse is sufficiently strong it excites the ring with a fixed pulse shape, while for lower trigger powers subthreshold oscillations are visible. (b) If the resonances of two identical All-Pass (AP) rings with common bus waveguide are sufficiently close to each other, they will show excitability for the same pump wavelength and power, which is visible in the output of the circuit as two seperate pulses. xlviii

2 (left) Topology used to cascade two microdisk lasers. The connection between both lasers corresponds to a phase difference $\Delta\phi$. (right,top) If an external perturbation triggers the first disk, it excites in its turn the second disk. If both disks receive the same locking signal, due to the symmetry, the second disk excites again the first disk, and as this process repeats itself this results in alternating excitations between the two disks. (right,bottom) Symmetry breaking by inducing a difference in phase between the two locking signals of the disks can make the pulse transfer unidirectional: the second disk does not re-excite the first disk. xlix

1.1 The human brain outperforms state-of-the-art computer hardware with respect to parallelization and power consumption. It processes massive amounts of time-dependent data in parallel, while its power consumption is comparable to a simple light bulb. Furthermore, by learning from previous experiences it is able to solve tasks, even without having a fixed algorithm for them. . . . 2

1.2 Just like its biological example, Spiking Neural Networks (SNNs) consist of interconnected neurons, that communicate with each other by sending spikes. 3

1.3 Prototype of a CMOS chip with an on-chip optical interconnect overlay (reproduced from [12]). Optical interconnects would allow to increase the information transfer rate and this transfer of large amounts of information would happen at higher speeds and using less power than using current electronic interconnects 5

1.4 An integrated optical neuron should be excitable and this excitability should be cascadable. 8

2.1 Different neuron models have different types of output signals. Due to the increase in temporal detail, there is an increase in information content from the binary output of the perceptron, over the analog output of an analog neuron, to the spike-trains produced by a spiking neuron. 20

2.2 The input of a neuron is a linearly combination of the output signals of the other neurons. A connection from neuron j to i has a weight w_{ij}. If the Neural Network (NN) is time-dependent, then the connection also has a delay τ_{ij}. 21

2.3 (left) A feedforward Neural Network (FNN) has no feedback loops, which makes it relatively easy to train (right) A Recurrent Neural Network has feedback, providing memory, but is more difficult to train. 23

2.4 (left) The Reservoir Computing paradigm combines the easy trainability of a Feedforward Neural Network (FNN) in the readout layer with the dynamic richness of a Recurrent Neural Network (RNN) in the reservoir. (right) the RNN in the reservoir can be replaced by another nonlinear dynamic system, paving the way towards hardware implementations. 24

2.5 The details of the local connection topology of a fully connected optical neuron (grey circle) embedded in a 2D-mesh implementation of a Photonic Reservoir Computing (PRC) network. The power division over the different output branches of the splitter is determined by the splitting ratio S. Adopted from [37, 44]. 27

2.6 In a saddle-node bifurcation a stable Fixed Point (FP) (black circle) and unstable FP (white circle) collide and disappear. Arrows indicate the direction of the flow on the x-axis. 32

2.7 Two different types of Andronov-Hopf bifurcations: in a supercritical Andronov-Hopf bifurcation a stable Limit Cycle (LC) originates from a stable FP, while in a subcritical Andronov-Hopf bifurcation an unstable LC collides with a stable FP, resulting in an unstable FP. In most physical systems with subcritical Andronov-Hopf bifurcation the unstable FP is surrounded by another stable LC. 34

2.8 A saddle-node on a invariant circle bifurcation gives rise to a LC. . 35

2.9 Neural excitability can be subdivided in three classes based on the frequency-current relation at the onset of spiking [18]. 37

2.10 The three optical excitability types have a different characteristic pulse shape [75]. The smooth pulse shape of type 1 excitability is linked with the Adler model discussed in Sec. 2.4.1, while the block-shape of type 2 excitability is linked to slow-fast dynamics discussed in Sec. 2.4.2. Type 3 excitability will not be discussed in-depth in this dissertation, but an important feature here is that, in between the excitations, at the rest state there is no output light. 39

2.11 The Adler model describes how a sufficiently strong perturbation can let the system cross the stable manifold of the unstable FP (a saddle, hollow circle in the figure), and initiates as such a perturbation, as the system has the make a full round trip before it can return to the stable rest state (full circle). 40

2.12 (left) If in a slow-fast system the slow (vertical) nullcline intersects the middle branch (from A to C) of the S-shaped fast nullcline, the intersection is an unstable FP and the system oscillates with a typical blockwaved pulse shape. (right) If the slow nullcline intersects the fast nullcline in one of the stable branches, near the oscillation onset, excitability appears. 42

3.1 A microring can be investigated using different simulation algorithms. A full vectorial Finite Difference Time Domain (FDTD), by discretizing the Maxwell's equations both in space and time will return a detailed distribution of the electromagnetic fields. However, to reduce simulation time, one can also use an eigenmode solver to calculate the mode profile of the waveguides. One can then calculate effective refractive indices based on this mode profile, and use this information in black box models that do not incorporate any spatial information of the field distribution. For instance, the ring can be considered to be a combination of a directional coupler and a waveguide, which can be modelled using a scatter-matrix. 55

3.2 In scatter-matrix theory a linear N-port optical component is treated as a black box. Its input-output relationship is fully determined by the scatter-matrix **S**. 62

3.3 Properties of a node with N ports in Caphe. A linear and instantaneous node is described by its scatter-matrix **S**. State variables (e.g., temperature and free carriers), accompanied by the corresponding (nonlinear) Ordinary Differential Equations (ODEs), can be added to this description. This makes the node non-instantaneous. 65

3.4 A microring resonator consists of two parts: a directional coupler and a bent waveguide. In Caphe, we would probe this component with two memory-containing components, a source (the laser) and a detector (the Optical Spectrum Analyzer (OSA)) each having only one port. If the memoryless nodes are eliminated from the circuit, the transmission of the ring is summarized in a small (2×2) generalized connection matrix $\mathbf{C}_{in,ex}$, being equal to the scatter-matrix S of this microring. 70

3.5 The power transmission of a critical coupled ring as a function of wavelength, calculated by Caphe. The ring properties are $A = \tau = 0.85$, $L = 50\,\mu\text{m}$, $n_{eff}\,(1550\,\text{nm}) = 2.43$ and $n_g = 4.3$. We also show the Lorentzian approximation of the spectrum of one of the resonance peaks, calculated using Eq. (3.28). 72

3.6 A Coupled Ring Optical Waveguide (CROW) circuit can be subdivided in multiple sections that consist of a directional coupler and two waveguides. Port numbers in such a section are shown in the left. A N ring CROW circuit contains $N+1$ coupling sections. . . . 75

3.7 Calculating the frequency response of a passive circuit. Using KLU, a sparse matrix solver suited for circuit-like matrices, we can easily calculate scatter matrices of very large circuits. 76

3.8 At every time step Eq. (3.34) needs to be evaluated. For this purpose we first calculate $\mathbf{s}_{ext,MC}$. Next we calculate $\mathbf{s}_{in,MC}$. And finally $\mathbf{s}_{in,MC}$ is used $\mathbf{s}_{in,MC}$ in the evaluation of $\mathbf{f}(\mathbf{a}, \mathbf{s}_{in}, t)$. 77

3.9 (left) Topology of a nanophotonic reservoir, containing both memoryless (ML) and memory-containing (MC) nodes. Each circle represents a Semiconductor Optical Amplifier (SOA) (MC), which are connected via waveguides (ML) and splitters (ML, not shown) to other SOAs, detectors and sources (MC) (right) Due to the nearest neighbour connection topology of the network and sparse implementation of the matrix products, both the simulation time and memory use increase linearly with the number of SOAs, but this increase is less steep if the ML nodes are eliminated. The offset in the memory consumption graph is related to initialization overhead in Python. 79

3.10 (left) When using forward Euler integration, larger timesteps decrease the accuracy. (right) An adaptive stepsize integration algorithm automatically uses the optimal dt when targeting a given accuracy level. Indeed, during the sudden jump in the input the integration step is clearly decreased. Parameters are identical as in [50]. 81

3.11 Structure of a Coupled Mode Theory (CMT) resonator with p ports and m modes. The matrix S couples light directly from input to output ports, the matrix K^T couples light from the input to the modes, the matrix M contains information about the resonance frequencies, losses and intermodal coupling and the matrix D couples light from the states to the output. 82

3.12 (left) In a long chain of inline Photonic Crystal (PhC) cavities, incorporation of the CMT formalism improves the simulation speed. In this simulation we used an equally long input signal as in Fig. 3.10(a). (right) A similar improvement can be seen in a simulation of a nanophotonic reservoir of inline PhC cavities in the topology of Fig. 3.9(a). In the latter simulation we used the same input signals as in Fig. 3.9(b), and this time the signals travel in two directions through the connections. 91

3.13 (left) The the κ_i of a Coupled Ring Optical Waveguide (CROW) can be optimized to match a desired filter characteristic. (right) If realistic process variations are added to the original design specifications, performance deteriorates. 93

4.1 The transmission of an all-pass ring is minimal at the resonance wavelength, while the energy in the cavity is maximal. For high input powers, this implies that nonlinear interactions will be enhanced in the ring for wavelengths near the resonance wavelength. 108

4.2 The transmission of an all-pass ring with $(\lambda_{r,eff}-\lambda_r) \propto \Delta T \propto |a|^2$ gets skewed to the right for higher input powers. This results in bistability (blue points are stable FPs, while red points are unstable).112

4.3 Changes in temperature or free carrier concentration change the effective resonance wavelength, resulting in different detuning scenarios with respect to an input signal at a fixed wavelength. This can result in self-pulsation. 113

4.4 For a detuning $\lambda - \lambda_r = 62\,\text{pm}$, $P_{out}(P_{in})$ is bistable (left figure), for $P_{in} > 191\,\mu\text{W}$ the lower P_{out}-branch becomes unstable, which is an indication of self-pulsation. For $P_{in} = 0.6\,\text{mW}$ and $(a, \Delta T, N)(t{=}0){=}(0, 0.7, 0)$ this gives the self-pulsation time-traces on the right. 115

4.5 On the phase portrait for $P_{in} = 0.6\,\text{mW}$ and a 62 pm detuning, the $d(N,a)/dt = 0$, $d(\Delta T,a)/dt = 0$ nullclines only intersect at the three FPs (orange circles). In correspondence with Fig. 4.4 two of those FPs are unstable (open circle), while one is stable (filled circle). The example time-trace from Fig. 4.4 (black line) clearly follows both the $d(\Delta T,N)/dt$ directions on the $da/dt = 0$-surface (grey arrows) and the corresponding direction changes indicated by the nullclines. Moreover, (grey) contour lines of $da/dt = 0$ for $|a|^2 = 1\,\text{fJ} - 31\,\text{fJ}$ are elliptic and do not overlap (Sec. 4.3.4.B). 116

4.6 The phase portrait obtained by neglecting the Two Photon Absorption (TPA)-contribution in γ_{loss} in Eq. (4.6), looks similar to Fig. 4.5 and still explains (approximately) the dynamic behaviour of the time-trace of the 4D-system from Fig. 4.4 (black line). Furthermore, the time-trace with a corresponding initial condition in the 2D-approximation (dashed magenta lines) follows qualitative the 4D-behaviour, both in phase-plane and in time-domain, although the shape of the limit cycle (LC) is slightly different. The yellow line is the separatrix of the simplified system. 118

4.7 At the red side of the resonance (e.g., left: $\delta\lambda = 62\,\mathrm{pm}$) the Andronov-Hopf (Andronov-Hopf (AH)) bifurcation (blue dot) tends to be supercritical, while it can be subcritical at the blue side of the resonance (e.g., right: $\delta\lambda = -16\,\mathrm{pm}$). FPs (black) and both maximum and minimum values of the LCs (magenta) in a $\Delta T(P_{in})$-bifurcation diagram, calculated using PyDSTool [1], illustrate this. Moreover, at $\delta\lambda = 62\,\mathrm{pm}$ the ring is bistable in-between two Saddle-Node (SN) bifurcations (red dots), while at $\delta\lambda = -16\,\mathrm{pm}$ a stable and unstable LC annihilate in a LC Fold bifurcation at $P_{in} = 2.836\,\mathrm{mW}$ (black dots indicate the maximum and minimum of the LC at this bifurcation). Relevant P_{in}-values used in the other figures are indicated. 120

4.8 For some input powers and wavelength settings the LC encloses a stable FP (filled circle) in the $(\Delta T, N)$ phase-plane. This indicates a subcritical AH bifurcation. We illustrate this here for $P_{in} = 2.85\,\mathrm{mW}$ and $\delta\lambda = -16\,\mathrm{pm}$. Depending on the initial conditions, the trajectory will converge to the LC (black curve $(\Delta T, N)(t{=}0) = (1.5\,\mathrm{K}, 8\mathrm{e}16\,\mathrm{cm}^{-3})$) or to the FP (magenta curve $(\Delta T, N)(t{=}0) = (1.2\,\mathrm{K}, 8\mathrm{e}16\,\mathrm{cm}^{-3})$). 121

4.9 A temporary increase from $P_{in} = 1.8\,\mathrm{mW}$ to $2.9\,\mathrm{mW}$ at $\delta\lambda = -16\,\mathrm{pm}$, during 2 ns, triggers an excitation. Although for this input power no LC is present, the excitation can be seen as a reminiscent of the nearby LC from Fig. 4.8. 122

4.10 The excitability-threshold power $P_{threshold}$ is more λ than P_{in}-dependent. Trigger pulses are $T_{tr} = 10\,\mathrm{ns}$ long and have been sent in the opposite direction as the pump light. 123

4.11 The refractory period T_{rf} is the time after a pulse during which the ring is insensitive to a second perturbation (a). It is on the order of magnitude of τ_{th}, and is not much power dependent for $\delta\lambda = -35\,\mathrm{pm}$ (b), while there is a clear wavelength dependency for $P_{in} = 1.8\,\mathrm{mW}$ (c). $P_{tr} = 1.65\,\mathrm{mW}$ for (b) and $P_{tr} = 3.42\,\mathrm{mW}$ for (c) (the need for the high P_{tr}-value of the latter is necessary to be above threshold for all wavelengths in the sweep range, as can be inferred from Fig. 4.10(b)). The refractory period can be predicted by looking at the time needed for $\Delta T(t)$ to relax to the rest state ($T_{rf,predict.}$). Moreover, the width of the pulse T_{width} is proportional to the rise time of the temperature, i.e., the time needed to reach the maximum temperature after a pulse. In the phase portrait we indicate the trajectory the ring makes during the external perturbations with cyan, while we use black for the rest of the response. 125

4.12 If a ring is excited by a trigger signal, this excitation can excite another ring. To demonstrate this we send a Continuous Wave (CW) pump signal with $P_{in} = 1.8\,\text{mW}$ and $\delta\lambda = -16\,\text{pm}$ through the common bus of a series of two Add-Drop (AD) filters. By exciting the first ring via the drop port (with a 10 ns trigger with $P_{tr} = 250\,\mu\text{W}$, $\lambda_{tr} = \lambda$) we guarantee that the external trigger pulse never reaches the second ring. The second pulse in the circuit's output, which corresponds to the second ring's excitation, is thus triggered by the first pulse, originating from the first ring. In contrast to the perturbation of the first ring (caused by the trigger), the second ring is initially perturbed (by the first ring) towards lower ΔT and N (right phase portrait). This causes the delay between the two excitations to be bigger than the delay between the trigger and the first pulse (time-trace bottom left). 127

4.13 Schematic of the setup for a single-ring measurement. Light of a tunable laser (TL), polarized with polarization controllers (PC) is coupled in and out the chip via grating couplers (GC). The ring output is measured with a 10 GHz photodiode and visualized with a 1 GHz real-time scope. In the excitability experiment a second TL is used, mostly coupled in the opposite direction via a circulator. The pulses are created using a signal generator (SG) and a pulse pattern generator (PPG) and an electro-optical modulator (EOM). At the bottom, spectral details of both the single-ring (left figure) and double-ring resonances (right figure), used in this chapter, are included. 129

4.14 Both the input power and wavelength clearly change the pulse shape and period of the self-pulsation in an AP ring with a 550 nm × 220 nm cross section, a 4.5 μm radius, near the resonance wavelength at 1530.708 nm. (a) Input power sweep with pump wavelength detuning $\delta\lambda = \lambda - \lambda_r = 40\,\text{pm}$. Power values are those at the output of the laser. Due to the grating coupler the on-chip input power of the ring is expected to be $\sim 6\,\text{dB}$ lower. (b) Detuning sweep of the same ring with 5.0 dBm output power at the TL laser. The self-pulsation period is on the order of $\sim 50\,\text{ns}$. 131

4.15 (a) If the trigger power is sufficiently high (≥ 7 dBm@TL) the ring excites with a fixed pulse shape, while for lower trigger powers subthreshold oscillations are visible. The 4 dBm pump light is detuned at $\delta\lambda = -4$ pm from the $\lambda_r = 1530.708$ nm resonance. The trigger light is tuned $\delta\lambda_{tr} = 9$ pm near another ring resonance at $\lambda_{r'} = 1550.671$ nm. (b) The refractory period is on the order of magnitude of the self-pulsation period. The pump settings are similar to (a), while the trigger pulse settings are $\delta\lambda_{tr} = 9$ pm and $P_{tr} = 5$ dBm. Mentioned power values are those at the output of the lasers, due to GCs and EOM the on-chip input power of the ring is expected to be ∼ 6 dB lower for the pump light and ∼ 14 dB lower for the trigger signal. 132

4.16 If the resonances of two identical AP rings with common bus waveguide are sufficiently close to each other, they will show self-pulsation (a) and excitability (b) for the same pump wavelength and power. Both rings have a 5.0 μm radius. The self-pulsation is measured at 10.5 dBm@TL (this starts at ∼ 1529.120 nm and ends around 1529.260 nm in hysteresis with single-ring self-pulsation), the excitability with the pump at $\lambda = 1529.007$ nm and $P_{in} = 13.60$ dBm, while $P_{tr} = 12.00$ dBm. Trigger pulse and pump light are now co-directional. On-chip powers are therefore expected to be resp. 10.00 dB and 18.00 dB lower, as ∼ 4 dB is lost in a splitter used to combine pump and trigger signals. 133

4.17 In simulations, triggering two cascaded AP rings through the common bus with a 5 ns power increase from 1.8 mW to 2.59 mW at $\delta\lambda = -16$ pm results in a similar time-lapse between two pulses in the time-trace (left) as in Fig 4.12. The phase-plane (right) clearly illustrates how the excitation of the first ring delays the excitation of the second ring, by kicking its trajectory towards lower N. . . . 135

4.18 At $\delta = -3$ and $p = 18.676$ the microring self-pulsates, while at $\delta = 0.5$ and $p = 23.345$ the ring is excitable: a sufficiently strong perturbation can trigger a pulse. Ring parameters are $q = 0.397$, $\epsilon = 0.0815$, $f = 0.0714$ and $e = 5$. Simulations are done with Caphe. . . 140

4.19 In phase plane, the signal makes, both for the self-pulsation time-trace ($\delta = -3$ and $p = 18.676$, top) and the excitability time-trace ($\delta = 0.5$ and $p = 23.345$, bottom) from Fig 4.18, a fast transition between the upper and lower branch of the $dn/d\tau$=0 nullcline, while in between these transitions it slowly follows those branches. 141

4.20 The steady state response at $\delta = -3$ is, in between two saddle-node (SN) bifurcations, bistable and has also a supercritical Hopf-bifurcation. At $\delta = 0.5$ no bistability is present, but an unstable limit cycle branch (LC) originates from a subcritical Hopf-bifurcation and annihilates with a stable limit cycle branch in a limit cycle fold (LC Fold). To visualize the limit cycles, both the minimum and maximum values of the cycles are plotted. Stable and unstable Fixed Points (FP) or limit cycles are indicated with resp. solid or dashed lines. 144

4.21 By tracking both the saddle-node bifurcations (BI onset) and Hopf bifurcation (SP onset) in the (δ,p)-plane we can determine resp. the bistability (BI) and self-pulsation (SP) region, which partly overlap (BI&SP). A limit cycle fold (LC Fold) originates from a Generalized Hopf bifurcation on the self-pulsation onset, for higher δ excitability is present, if p is below, but sufficiently close, to this limit cycle fold. In between the self-pulsation onset and limit cycle fold a stable fixed point coexists with an unstable limit cycle, surrounded by a stable one (Stable FP&LC). 145

4.22 While the bistability region is only slightly dependent on the exact q-value, the self-pulsation region and the corresponding excitability region shifts clearly to higher δ for increasing q. Calculation done for $q = 0.5q_0$ (dotted line), $q = q_0$ (solid line) and $q = 1.5q_0$ (dashed line), with $q_0 = 0.397$, i.e., the value from Fig. 4.18. For reference we also included the bistability curve for $q = 0$ (dash-dotted line), i.e., without any free carrier effects. 147

4.23 While the bistability region is independent of ϵ (with $q = 0.397$ fixed), the self-pulsation region becomes larger for smaller ϵ. For $\delta = -3$ a Generalized Hopf bifurcation is present, while this is not the case for $\delta = 0.5$, as the Hopf bifurcation is then always subcritical. Self-pulsation appears in between $n_{H,-/+}$ (SP onset, blue (or dark gray) lines), while bistability appears in between $n_{b,-/+}$ (BI onset, red (or middle gray) lines). For a given δ, self-pulsation is only possible below a critical value ϵ_{sp}. As before, a limit cycle fold curve (LC Fold, black line) reveals the excitability regions. 148

4.24 Summary of the regions with self-pulsation (SP) and bistability (BI) in the (ϵ,δ)-plane. The color levels represent the 'on' free carrier detuning $n_{H,-}$ and the 'off' free carrier detuning $n_{H,+}$ (with $q = 0.397$ fixed, definitions illustrated in Fig. 4.23). $(\epsilon_{sp},\delta_{sp})$ encloses the region where some input powers result in self-pulsation (solid line), similarly (ϵ_b,δ_b) encloses the region with bistability (dotted line). Furthermore, the curve $p(n_{H,-}) = p(n_{b,-})$ (dashed line) divides the region with bistability into a domain where $BI \cap SP = \emptyset$ where self-pulsation sets in only for powers above the bistable knee for up-switching, and a domain where $BI \cap SP \neq \emptyset$, where self-pulsation is present at the upper branch of the bistability curve. Finally, the Generalized Hopf bifurcation location $(\epsilon_{GH},\delta_{GH})$ on the $n_{H,-/+}$-surfaces is tracked (orange (or light gray) line), indicating excitability is mainly present at the blue side of the resonance. 149

4.25 If $\epsilon = \frac{\tau_{fc}}{\tau_{th}}$ is changed by tweaking τ_{fc}, $q \propto \sqrt{\epsilon}$ due to $q \propto \sqrt{\tau_{fc}}$. Consequently, the decreasing q for $\epsilon \to 0$ causes the self-pulsation region to disappear (e.g., $\delta = -3$ and $\delta = 0.5$). 151

4.26 If $q = q_0\sqrt{\frac{\epsilon}{\epsilon_0}}$ (q_0, ϵ_0 are the values used in Fig. 4.18), this changes the color levels of the 'on' free carrier detuning $n_{H,-}$ and the 'off' free carrier detuning $n_{H,+}$ with respect to Fig. 4.24, such that the self-pulsation region now disappears for $\epsilon \to 0$. For lower δ the self-pulsation region comes closer towards $\epsilon = 0$, e.g., at $\delta = -15$ the self-pulsation region disappears at $\epsilon \approx 1.5 \times 10^{-3}$. Moreover, δ_b is now slightly ϵ-dependent (dotted line). Additionally, a second bistability region appears for $\epsilon > 1.4$ near $\delta \approx 2.4$, which results in Bogdanov-Takens (BT) bifurcations (red (or middle gray) line) when $n_{b,+}$ intersects with $n_{H,-}$. 152

5.1 The bifurcation diagram of the microdisk laser for increasing current reveals three lasing regimes. Just above the laser threshold the output is bidirectional (II), at high injection currents it is unidirectional (IV), while in between those two regimes an oscillatory regime appears (III). For both output powers $P_{out,i} = |E_{out,i}|^2$, the extrema are plotted. If the output is constant, maximum and minimum power are equal and the markers overlap. If the output power oscillates, two markers are plotted per current, per mode. Inset: geometry of the microdisk laser. 165

5.2 (left) The bifurcation lines form the boundaries of the different locking regions. Here, $I = 2.3$ mA, red lines represent Hopf-bifurcations, while blue lines correspond to Saddle-Node on an Invariant Circle (SNIC) bifurcations. We will use the SNIC bifurcation to induce excitability. (right) When crossing the SN_1 bifurcation at $\Delta\omega = -15$ ns^{-1}, $|E_{in}| = 2.77$ $\sqrt{\mu\text{W}}$ the oscillatory unlocked behaviour becomes steady-state. At $t = 10$ ns the locking amplitude is raised from 2.65 to 2.76 $\sqrt{\mu\text{W}}$, at $t = 20$ ns, the bifurcation is crossed by again increasing $|E_{in}|$ to 2.78 $\sqrt{\mu\text{W}}$. . . . 167

5.3 (left) When increasing the injection strength $|E_{in}|$ from zero to the locking strength, the self-pulsation frequency decreases to zero. This is a consequence of the SNIC bifurcation. (right) In addition, the amplitude of the of the self-pulsation in the mode energy grows from zero to a finite size for increasing $|E_{in}|$. Both simulations are done at $\Delta\omega = -15$ ns^{-1}. 168

5.4 In the proposed ‘neuron’ topology a constant locking signal (CW) locks the microdisk just above the SN_1-bifurcation. Sufficiently strong pulses at the other input of the splitter, perturb the microdisk, and can cause an excitation. The excitation results in a power peak in the E^- mode that can be collected as the actual output of the system. 169

5.5 The response of the microdisk to a 0.2 ns pulse of 1.0 μW, with a π phase shift with the locking signal, shows that the backward output pulse corresponding to the suppressed mode has the cleanest pulse shape. 171

5.6 The optically-injected microdisk shows clear threshold behaviour as a function of the amplitude and phase of the input pulse. a)-c) Response to pulses of fixed length (0.2 ns), for different pulse powers, out of phase with the locking signal. a: Time traces. b: Output peak power as a function of input peak power. c: Pulse latency as a function of input peak power. d)-f) Response to pulses of fixed peak power and length (1.4 μW, 0.24 ns), but varying phase. d: Time traces. e: Output peak power as a function of phase. f: Pulse latency as a function of input pulse phase. 173

5.7 The Adler model can help to understand why stronger supertreshold pulses result in less latency of the output pulse: a stronger pulse reduces the roundtrip distance in phase-space the system has to make before it can return to the rest state, and this will in the amplitude domain correspond to a reduced latency of the output pulse of the disk. 174

5.8 The microdisk laser reacts as well to a phase-modulated locking signal, in which the phase of the locking signal experiences a block pulse of fixed length (0.2 ns) and size $n\frac{\pi}{4}$ ($n \in \{0,...,7\}$) at 10 ns. . . 175

5.9 If two subthreshold input pulses (in this case, 0.6 μW, 0.2 ns, out of phase with the locking signal) arrive sufficiently close to each other to the microdisk, they can excite the microdisk. 176

5.10 The output pulse rate of a microdisk excited with subthreshold pulse-trains is sublinearly dependent on the input-pulse rate and therefore shows similarities with the typical sigmoidal input power versus output power characteristics of classical artificial neurons. a) Input rate-output rate characteristic of the neuron, when the input-pulse train consists of subthreshold pulses ($|E_{in}|^2$ = 1 μW peak power, 1 ns length). b)-c) time-traces, for input rates 1 GHz (a), and 4 GHz (b). 177

5.11 The microdisk has a refractory period: after a perturbation, the disk is temporarily less sensitive to new input perturbations. (left) Response to a sequence of two equally high superthreshold pulses (1 μW, 0.2 ns, out of phase with the locking signal). (right) The second pulse has a slightly higher power (1.5 μW). 177

5.12 The relative refractory period of the microdisk is clearly dependent on the power of the second trigger pulse. For high powers of this second pulse it converges to the absolute refractory time, which corresponds with the moment the disk is having its first excitation. Input pulses are 0.2 ns wide, out of phase with the locking signal and the power of the first input pulse is 1 μW. 178

5.13 The output pulse rate as response to the superposition of two input pulse streams depends on the optical phase difference between the two input pulse trains. One stream is constant (6 GHz, 1 μW peak power and 0.1 ns duration) and purely excitatory (relative phase with respect to the CW is π), while the other pulse stream has a varying rate r_2, the horizontal axis represents its phase. Peak power and duration are the same as for the first stream. The error bars give the 80% certainty interval for the inverse interpulse delays. 179

5.14 (a) The output of a microdisk neuron can be connected by a waveguide to the input of another microdisk neuron. The connection between both lasers corresponds to a phase difference $\Delta\phi$. (b) Input and output power of the first disk when the second disk is 'turned off' (current as well as locking signal are absent). The bottom graph shows the phase difference between the output pulse and the locking signal. This phase can be used to choose an optimal $\Delta\phi$ to allow the first disk to excite the second one. 181

5.15 If the first disk is excited it will in turn excite the second disk, which will re-excite the first disk, resulting in a continuous excitation transfer between the two disks. Both disks are pumped with a 2.3 mA current and $\Delta\phi = 2.8$ rad. The locking signals for both disks are 3.8 $\sqrt{\mu\text{W}}$. The input pulse is 1 $\sqrt{\mu\text{W}}$ strong and 0.1 ns long. . . 185

5.16 The excitation transfer between the two disks in Fig. 5.15 can be made unidirectional by breaking the symmetry of the system. (a) Symmetry breaking by difference in locking amplitude. The locking signal for the first disk has an amplitude of 4 $\sqrt{\mu\text{W}}$. For the second disk, the locking amplitude is 3.9 $\sqrt{\mu\text{W}}$. Both disks are pumped with a 2.3 mA current, $\Delta\phi = 2.8$ rad. The input pulse is 3 μW strong and 0.2 ns long. (b) Symmetry breaking by difference in locking phase. The locking signals for both disks have an amplitude of 3.55 $\sqrt{\mu\text{W}}$, while $\phi_{CW_2} = \phi_{CW_1} + \frac{\pi}{2}$. Both disks are pumped with a 2.3 mA current, $\Delta\phi = 4.2$ rad. The input pulse is 1 μW strong and 0.1 ns long. 187

5.17 Influence of variations of the current through disks 1 and 2, ΔI_1 and ΔI_2, respectively. Unperturbed, both currents are 2.3 mA, $\Delta\phi = 4.2$ rad. The locking signals for both disks are 3.55 $\sqrt{\mu\text{W}}$ and the input pulse is 1 μW strong and 0.15 ns long. As we are interested in an unidirectional excitation transfer, the optimal current setting appears when both disks only excite once. We represent a single excitation of the respective disk using black pixels, so the cross section of the black regions in both plots defines the domain with a unidirectional excitation transfer. In the light grey regions, the disk output is oscillating, independent of the perturbation. In the white regions, there is neither oscillation, nor excitation. In the dark grey regions, the disk shows more complex multipulse excitability (two pulses or more, after which the system decays again). The white cross represents the unperturbed system ($\Delta I_1 = 0$ and $\Delta I_2 = 0$). 189

5.18 Influence of variations of the frequency detunings of both disks, $\Delta\omega_1$ and $\Delta\omega_2$, respectively. Unperturbed, the detuning is $-20\ \text{ns}^{-1}$. The locking amplitude for both disks is $3.55\ \sqrt{\mu\text{W}}$. The input pulse is $1\ \mu$W strong and 0.15 ns long. The colors represent the same behaviours as in Fig. 5.17. 190

5.19 (a) If the detuning of the second laser is $-40\ \text{ns}^{-1}$ (e.g., due to process variations), the dynamics of Fig. 5.16(b) can not be obtained, even though the other parameters are identical. (b) However, for this $-40\ \text{ns}^{-1}$ detuning of the second laser the desired unidirectional pulse transfer can be obtained by increasing I_2 to 1.7 mA and using $3.55\ \sqrt{\mu\text{W}}$ and $\sqrt{3}\cdot 3.55\ \sqrt{\mu\text{W}}$, as locking signal amplitudes for disk 1 and 2, respectively. 191

List of Tables

4.1 Parameter values used in the simulations. 111
4.2 Description and formula of the model parameters and, if appropriate, their default value. 139

5.1 Model parameters used in this chapter are based on the values and definitions proposed in [31] and [22]. Comparable values can be found in [24]. 166

List of Acronyms

A

AD	Add-Drop
AH	Andronov-Hopf
AP	All-Pass

C

CMOS	Complementary Metal Oxide Semiconductor
CMT	Coupled Mode Theory
CW	Continuous Wave
CROW	Coupled Ring Optical Waveguide
CMA-ES	Covariance Matrix Adaptation Evolution Strategy

E

ER	Extinction Ratio
EAM	Electro-Absorption Modulator
EOM	Electro-Optic Modulator

F

FEM	Finite Element Methods
FCA	Free Carrier Absorption
FCD	Free Carrier Dispersion
FDTD	Finite Difference Time Domain
FNN	Feedforward Neural Network
FP	Fixed Point
FSR	Free Spectral Range

G

GUI	Graphical User Interface

I

InP	Indium Phosphide

K

KLU	Clark Kent sparse LU factorization

L

LC	Limit Cycle
LIF	Leaky-Integrate and Fire

M

MC	memory-containing
ML	memoryless
MNA	Modified Nodal Analysis
MOSFET	Metal-Oxide-Semiconductor Field-Effect Transistor

N

NN	Neural Network

O

ODE	Ordinary Differential Equation
OSA	Optical Spectrum Analyzer

P

PhC	Photonic Crystal
PRC	Photonic Reservoir Computing

R

RC	Reservoir Computing
RNN	Recurrent Neural Network

S

SA	Saturable Absorber
SOA	Semiconductor Optical Amplifier
SOI	Silicon-On-Insulator
SNN	Spiking Neural Network
SNIC	Saddle-Node on Invariant Circle
SRL	Semiconductor Ring Laser
SPA	Single Photon Absorption
SSA	Surface State Absorption
SSM	Split-Step Method

T

TE	Transverse-electric
TM	Transverse-magnetic
TPA	Two Photon Absorption
TDTW	Time-Domain Travelling Wave

V

VCSEL	Vertical Cavity Surface-Emitting Laser

W

WDM	Wavelength Division Multiplexing

Nederlandse samenvatting –Summary in Dutch–

Vanaf de geboorte worden onze hersenen continu geconfronteerd met steeds nieuwe uitdagingen. Vaak moeten die hersenen taken leren oplossen waarmee ze nog nooit eerder in aanraking kwamen. Soms kunnen ze bij het oplossen van zo een nieuwe taak gebruik maken van een stappenplan. Wanneer bijvoorbeeld je ouders je stapsgewijs uitlegden hoe je een fles melk moet openen, dan duurde het wellicht niet lang eer je daar zelf toe in staat was. Maar in andere gevallen zijn onze hersenen in staat om taken op te lossen zonder dat een gedetailleerd stappenplan voorhanden is. Als een kind begint met lopen doet het dat door het voorbeeld van volwassenen na te bootsen. Gelukkig hoeven ouders hun kinderen tijdens deze leerfase niet te voorzien van een gebruikshandleiding van de eigen benen.

Om onze levenskwaliteit te verbeteren voelen we de drang om sommige taken naar machines over te hevelen, taken die we vroeger oplosten met onze eigen hersencapaciteit. Als we een algoritme hebben voor dergelijke taken, hebben we genoeg aan de combinatie van een computer en een software-ingenieur. In andere gevallen, waarin er geen algoritme voorhanden is, zijn de algoritme-gebaseerde traditionele computers hulpeloos en moeten we van aanpak veranderen. In dergelijke gevallen bestaat de oplossing erin om onze hersenen na te bootsen. Onze hersenen bestaan uit neuronen, die onderling verbonden zijn en met elkaar communiceren door het uitzenden van pulsen. Wanneer zo een neuron een voldoende groot aantal pulsen van andere neuronen ontvangt, zal het - afhankelijk van de interne dynamica van dit neuron - zelf een puls uitzenden. Het neuron 'pulseert' dan. Door het aanpassen van de sterktes van de neuronverbindingen kunnen we delen van onze hersenen trainen om nieuwe taken op te lossen.

Het doel van dit doctoraatsonderzoek is om een optische chip te bouwen die het biologische raamwerk van onze hersenen voldoende dicht benadert en daardoor taken kan oplossen waarvoor geen algoritmes bestaan. Door de geparalelliseerde manier van rekenen zal dit ons toelaten om eenzelfde vermogen-efficiëntie als van het biologische voorbeeld te verkrijgen. Daardoor heeft deze technologie het potentieel om de meer traditionele manieren waarin serieel gerekend wordt te overtreffen. Die laatste zijn gebaseerd op een Von Neumann architectuur, zoals in de huidige computerhardware gebruikelijk is. Een neuromorfische hardware implementatie in fotonica heeft het potentieel om een elektronische implementatie te overstijgen door de intrinsiek rijkere dynamica en hogere snelheden in fotonische systemen.

Dit interdisciplinair project combineert technieken uit machinaal leren, zoals neuromorf rekenen, met fotonica.

1 Neuromorf rekenen

Neuromorphic computing, in het Nederlands letterlijk vertaald als neuromorf rekenenen, bootst het grote neurale netwerk in onze hersenen na in hardware. Er zijn ontzettend veel redenen om dit te doen. Inderdaad, in het dagelijkse leven functioneren onze hersenen net als de CPU's in onze computers als de centrale verwerkingseenheid van ons lichaam. Wegens hun grote flexibiliteit zijn ze in staat om een enorm aantal taken uit te voeren, in een continu veranderende omgeving. Hierbij verbruiken ze slechts het vermogen-equivalent van een gloeilamp. Onze hersenen kunnen dit omdat ze bestaan uit een gigantisch netwerk van neuronen die grote hoeveelheden tijdsafhankelijke informatie in parallel kunnen verwerken. Daarenboven kunnen onze hersenen leren van voorbeelden wanneer ze bepaalde taken oplossen. Dit in tegenstelling tot traditionele computerchips die oorspronkelijk serieel werken en enkel een vooropgesteld algoritme kunnen volgen. Gebruik makend van fundamenteel verschillende computationele principes overtreffen artificiële neurale netwerken conventionele seriële computeralgoritmes in een variëteit van taken, zoals autonome signaalgeneratie, controlefuncties in robotica, voorspelling van chaotische tijdreeksen en spraakherkenning. Hoewel de huidige neurale netwerktechnieken uitzonderlijk goed presteren in een verscheidenheid aan taken, worden ze gesimuleerd op traditionele computers. Hierdoor genieten ze niet van het volledige potentieel van het biologische geïnspireerde ontwerp. Dit vraagt om de ontwikkeling van een specifieke chip.

2 Fotonica

Fotonica is een breed onderzoeksdomein waarin, in het algemeen, toepassingen van elektromagnetische straling met een golflengte dicht tegen die van het zichtbaar licht onderzocht worden (zowel infrarood, zichtbaar licht en UV-straling zijn daarbij inbegrepen). Het onderzoeksgebied is ontstaan door de verschijning van de eerste laser, en de naam verwijst zowel naar het concept van een foton als naar elektronica. De naam benadrukt daardoor dat in veel van de toepassingen de deeltje-golf dualiteit van licht een belangrijke rol speelt, terwijl het onderzoeksgebied eveneens dezelfde weg kiest richting grootschalige, kostenefficiënte miniaturizatie als in de elektronica-industrie gebruikelijk is. Naast de laser hebben veel van de successen van dit onderzoeksgebied een fundamentele rol in ons dagdagelijks technologiegebruik: fotonica is onmisbaar geweest voor de ontwikkelijk van zeer verschillende toepassingen, zoals state-of-the-art schermtechnologie, DVD's, laser pointers, efficiënte oogchirurgietechnieken en hogesnelheidsdatatransfer.

3 Neuromorf rekenen op basis van fotonica

Het idee om een neuromorfische chip te implementeren in fotonica is eerder nieuw, en was bij de start van dit onderzoek nog niet experimenteel gedemonstreerd. Hoewel de technologie nog niet zo matuur is als elektronica is het een beloftevol platform. Inderdaad, de transfer van grote hoeveelheden informatie kan in het optische domein gebeuren tegen hogere snelheden en met een lager vermogenverbruik dan in eender welke elektronische implementatie.

Biologische neuronen communiceren door middel van pulsen. Artificiële neuronen die eveneens informatie overbrengen via pulstreinen worden gepulste neuronen genoemd. Om te kunnen reageren op inputpulsen van andere neuronen moeten ze exciteerbaar zijn. Hiermee wordt bedoeld dat een voldoende sterke perturbatie van het ingangsignaal één of meerdere pulsen met een vast pulsformaat moet initiëren. Gelukkig zijn een behoorlijk aantal geïntegreerde optische componenten exciteerbaar. Hieronder bevinden zich zowel lasers als andere componenten. Daardoor lijken deze componenten geschikt om gebruikt te worden als een basisbouwsteen van een geïntegreerde versie van een gepulst neuraal netwerk in optica. In zo een implementatie worden de neuronen verbonden met elkaar door golfgeleiders en vermogensplitters. Deze vorm van implementatie laat een dense integratie toe van optische gepulste neurale netwerken, wat niet kan bereikt worden met een vezelgebaseerde opstelling met individuele componenten. Bovendien zijn in een elektronische chip, in tegenstelling tot in een fotonische neuromorfische chip, meerdere componenten nodig om één enkel neuron te kunnen representeren. Zoals eerder aangetoond in onze onderzoeksgroep is een bijkomstig voordeel van een coherente fotonische implementatie dat de fase die overeenkomt met de interconnectielengte een nuttige computationele rol kan spelen. Dat laatste is onmogelijk in een meer traditionele elektronische implementatie. Daarenboven herbergt fotonica een hele zoo van dynamisch rijke effecten, waarvan sommige extreem snel kunnen zijn (zoals bvb. het optische Kerr-effect). Bijgevolg is het een zeer interessant platform voor snel en energie-efficiënt neuromorf rekenen.

4 Optische gepulste neuronen geïntegreerd op een fotonische chip

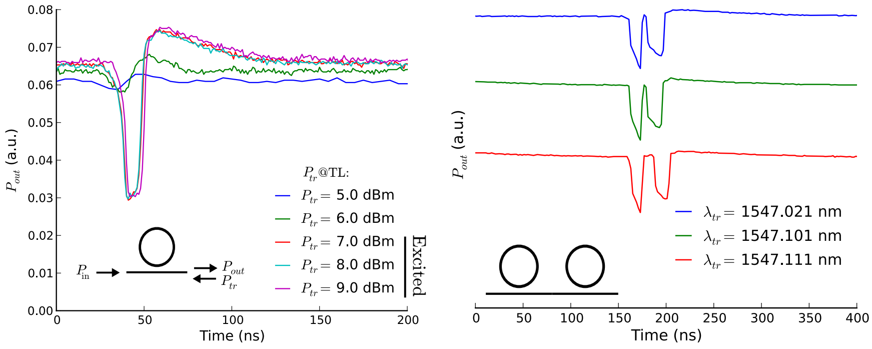

(a) (b)

Figuur 1: (a) Als de trigger puls voldoende sterk is, exciteert het de ring, met een vaste pulsvorm. Lagere triggersterktes resulteren in subthreshold oscillaties. (b) Als de resonanties van twee identieke all-pass ringen voldoende dicht bij elkaar liggen, zullen ze exciteerbaar zijn bij hetzelfde pompsignaal, wat te zien is aan de uitgang van het circuit als twee afzonderlijke pulsen.

In dit doctoraat onderzoeken we nanofotonische componenten op een silicon-on-insulator (SOI) chip die het fenomenologisch gedrag van een hersencel nabootsen. Het doel is in het bijzonder om geïntegreerde optische componenten te vinden die de functionaliteit van een gepulst neuron hebben. Vermits een gepulst neuron informatie verwerkt gebruik makend van pulstreinen moeten deze componenten exciteerbaar zijn. Om communicatie tussen verschillende optische neuronen toe te laten moet de geëxciteerde outputpuls van een neuron in staat zijn om een excitatie te veroorzaken in een ander neuron. Anders verwoord: het exciteerbaarheidsmechanisme moet cascadeerbaar zijn. Om de snelheidsbeperking door elektro-optische signaalconversie te vermijden onderzoeken we componenten met een geheel optische variant van exciteerbaarheid. Hiermee bedoelen we dat zowel het ingangs- als het uitgangssignaal van de component zich in het optische domein bevinden. Dit resulteert niet alleen in een snelheidsvoordeel in vergelijking met elektronische oplossingen, maar maakt het ook mogelijk om de fase van het licht als een extra vrijheidsgraad in toekomstige optische gepulste neurale netwerken aan te wenden. Door dit concept van optische cascadeerbaarheid in geïntegreerde fotonica te demonstreren tonen we daarenboven de schaalbaarheid aan van toekomstige grootschalige ultrasnelle optische neurale netwerken.

In dit onderzoek onderzoeken we exciteerbaarheid in het SOI platform. Dit doen we omdat deze chips gefabriceerd zijn met dezelfde infrastructuur als digitale chips, wat ons toelaat om van de vooruitgang in de CMOS-fabricatietechnologie te profiteren. In het bijzonder onderzoeken we twee componenten met cascadeerbare exciteerbaarheid die beide integreerbaar zijn op het SOI platform.

Ten eerste onderzoeken we het samenspel tussen de thermische en vrijeladingsdragers niet-lineariteiten in passieve hoge-Q microring resonatoren. Het doel is exciteerbare pulsen te verkrijgen die voldoende sterk zijn om andere ringen te kunnen exciteren. Een experimentele demonstratie van dit mechanisme mondt uit in het eerste experimentele bewijs van exciteerbare pulstransfer in een geïntegreerd optisch circuit (Fig. 1).

Ten tweede onderzoeken we, door middel van simulaties, exciteerbaarheid in optisch geïnjecteerde microdisklasers (Fig. 2). Door de koppeling tussen de sterke en onderdrukte mode in de microdisklasers resulteert een excitatie van de disk door een perturbatie van de sterke mode in een puls van de onderdrukte mode. Deze puls is vergelijkbaar qua sterkte en grootte met de inputpuls. Bijgevolg is de output van een disk in staat om een andere disk te exciteren, wat de exciteerbaarheid cascadeerbaar maakt.

Samengevat demonstreren we cascadeerbare exciteerbaarheid in twee verschillende geïntegreerde fotonische componenten. Dit is een belangrijke stap op weg naar de verwezenlijking van optische gepulste neurale netwerken.

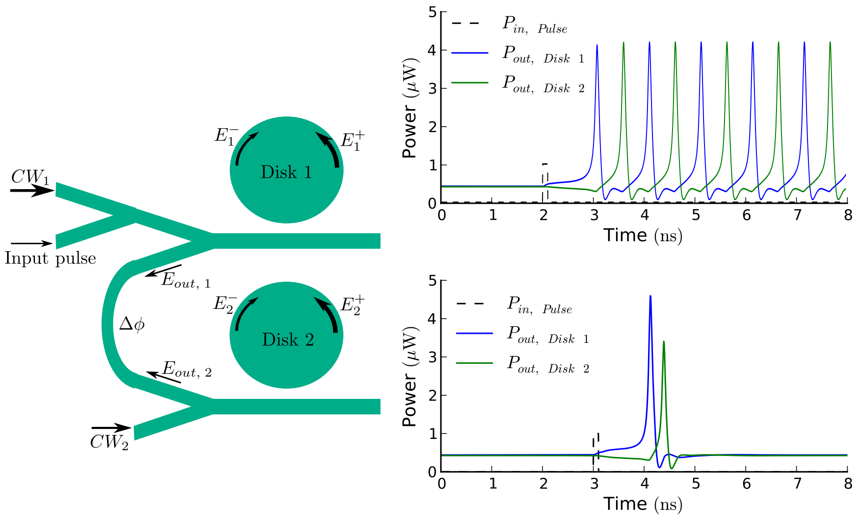

Figuur 2: (links) De gebruikte topologie om twee microdisklasers te cascaderen. De connecties tussen beide lasers komt overeen met een faseverschil $\Delta\phi$. (rechts, boven) Als een externe perturbatie de eerste disk triggert, exciteert die op zijn beurt de tweede disk. Als beide disks hetzelfde locking signaal ontvangen exciteert de tweede disk op zijn beurt terug de eerste disk door de symmetrie van het systeem. Dit proces herhaalt zichzelf en resulteert in alternerende excitaties tussen de twee disks. (rechts, onder) Symmetriebreking door het creëren van een faseverschil tussen de twee locking signalen van de disks kan de pulstransfer unidirectioneel maken: de tweede disk herexciteert de eerste disk niet.

English summary

During our life, our brain is continuously confronted with new challenges. Often it needs to learn how to solve tasks it has never solved before. Sometimes we can follow a fixed set of rules to solve such a new task. For instance, after your parents had shown you once the steps needed to open a bottle of milk, it didn't take long before you managed to do it yourself. However, our brain is also able to solve tasks without knowing in detail the rules needed to solve them. When a young child starts to walk, it does this by mimicking the example of other walking people. Fortunately, parents do not need to provide their children with a user manual of their legs.

To improve our quality of life, we feel the urge to delegate certain tasks to machines that could previously only be solved by our brain. If we have an algorithm for those tasks, the combination of a computer and a software engineer can fix this job. However, in some cases we do not have an algorithm available and we need to shift gears.

In this case, a solution is to mimic the brain. Our brain consists of neurons, which are mutually connected and communicate with each other by sending out pulses. When such a neuron receives a sufficient number of pulses from other neurons, it will - depending on its internal dynamics - send out a pulse itself. The neuron then 'spikes'. By tweaking the strengths of the connections between the neurons we are able to train a part of our brain to solve a new task.

The idea behind this PhD research is to build optical chips that mimic the biological framework of the brain. This will allow to exploit the same power efficiency and highly parallelized computational capabilities as the biological ancestor, therefore having the potential to outperform the more traditional way of serialized computing that uses the Von Neumann architecture, like current computer hardware. A neuromorphic hardware implementation in photonics has the potential to outperform an electronic one, due to the intrinsically richer dynamics and higher speeds in photonic systems.

This interdisciplinary project combines machine learning techniques, such as neuromorphic computing, with photonics.

1 Neuromorphic computing

Neuromorphic computing mimics the NNs found in our brain in hardware, as there are plenty of reasons to do so. Indeed, in everyday life, our brain functions as the central processing unit of our body. Being very versatile, it is able to execute a tremendous number of tasks, in a continuously changing environment, solely using the energy equivalent of a light bulb. The brain is able to do this because it consists of a gigantic network of neurons that can process a large amount of time-dependent information in parallel. Additionally, our brain is able to learn from examples when it tries to solve a certain task. In contrast, regular computers originally worked in a serialized manner and can only follow a predefined algorithm. Using fundamentally different computational principles, artificial NNs can outperform conventional serialized computer algorithms in a variety of tasks, such as autonomous signal generation, control functions in robotics, chaotic time series prediction and speech recognition. Although current NN techniques reach state-of-art performance on many different tasks, they are simulated on traditional computers, and hence intrinsically not leveraging the full potential of the biological design. This calls for the development of a dedicated chip.

2 Photonics

Photonics is a broad research area, in which, in general, applications of electromagnetic radiation with a wavelength close to visible light are investigated (including infrared, visible and UV-radiation). It originated with the appearence of the first laser, and its name refers both to the concept of a photon and to electronics. Thereby, its name emphasizes that in many applications the particle-wave duality of light plays an important role, while the field also envisages to follow the same road towards large-scale, cost-efficient miniaturization as chosen by the electronics industry. Besides the laser, many of its successes now play a fundamental role in our every-day life technology use: photonics has been invaluable in the development of very different applications such as state-of-the-art display technology, DVDs, laser pointers, laser printers, efficient eye surgery techniques and high-speed data transfer.

3 Neuromorphic computing using photonics

The idea to build neuromorphic chips in photonics is a fairly new one, and the first experimental demonstration of the concept still needed to be done at the start of this work. Although the technology is not yet as mature as electronics, it is a very promising platform. Indeed, the transfer of large amounts of information in the optical domain can happen at higher speed and using less power than in any electronic implementation.

Biological neurons communicate using pulses. Artificial neurons that convey information using pulse-trains are called spiking neurons. To be able to react to input spikes of other neurons they have to be excitable, i.e., a sufficiently strong perturbation of the input signal should trigger one or more pulses with a fixed output pulse shape. Fortunately, a lot of integrated optical components are excitable, both lasing and non-lasing. Therefore, these components seem suited to be used as basic building blocks for an integrated version of a Spiking Neural Network (SNN) in optics, in which the neurons are connected to each other using waveguides and power splitters. This type of implementation allows for a dense integration of the optical SNN, which would not be possible in a fiber-based setup with individual components. Additionally, in contrast to a photonic neuromorphic chip, in an electronic implementation multiple components are needed to represent a single neuron. As has been shown previously in our group, an additional advantage of a photonic implementation is that the phase corresponding to the interconnection length can play a beneficial role in computation. The latter is impossible in more traditional electronic implementations. Furthermore, photonics exhibits a whole zoo of rich dynamic effects, some of which can be extremely fast (e.g., the optical Kerr effect). Hence, it is a very interesting platform for fast and energy-efficient neuromorphic computing.

4 All-optical spiking neurons integrated on a photonic chip

In this PhD research, we investigate nanophotonic components on a Silicon-On-Insulator (SOI) chip that can closely mimic the phenomenological behaviour of a brain cell. More specifically, the objective is to bring forth integrated optical components with the functionality of a spiking neuron. As spiking neurons process information using pulse trains, these components need to be excitable. To allow for communication between different optical neurons, an excited output pulse of one neuron should be capable of triggering an excitation in another neuron. In other words, the excitability mechanism should be cascadable. To avoid the speed bottleneck of electro-optic signal conversion, we investigate components that incorporate an all-optical version of excitability, i.e., both the input and the output of the device are in the optical domain. We show that this does not only result in an advantage in speed compared to electronic solutions, but also in the potential to use the phase of light as an additional degree of freedom in future all-optical SNNs. Additionally, the demonstration of this concept in an integrated photonics platform provides scalability, opening the door to future large-scale, ultrafast all-optical SNNs.

In this research, we investigated excitability in the SOI platform, as these photonic chips are fabricated by the same infrastructure as digital chips, allowing to benefit from the advances in CMOS-fabrication technology. In particular, we analyse two different components, both integrable on the SOI platform, that show such cascadable excitability.

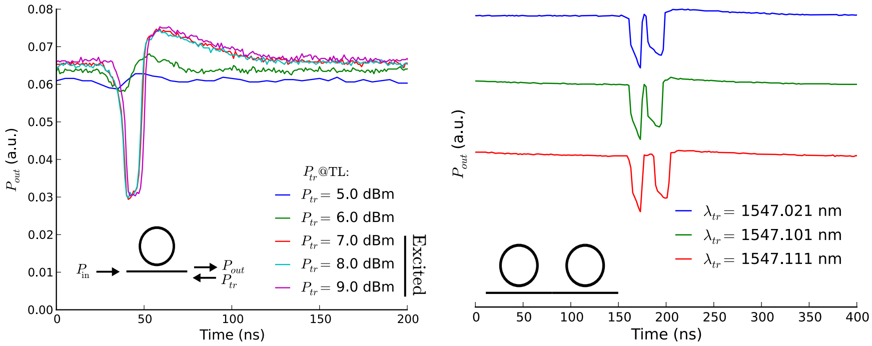

(a) (b)

Figure 1: (a) If the trigger pulse is sufficiently strong it excites the ring with a fixed pulse shape, while for lower trigger powers subthreshold oscillations are visible. (b) If the resonances of two identical AP rings with common bus waveguide are sufficiently close to each other, they will show excitability for the same pump wavelength and power, which is visible in the output of the circuit as two seperate pulses.

First, we address the interplay between thermal and free carrier nonlinearities in a passive high-Q microring resonator to obtain excitable pulses that are sufficiently strong to excite other microrings. Experimental demonstration of this mechanism results in the world's first experimental proof of excitable pulse transfer in an integrated optics circuit (Fig. 1).

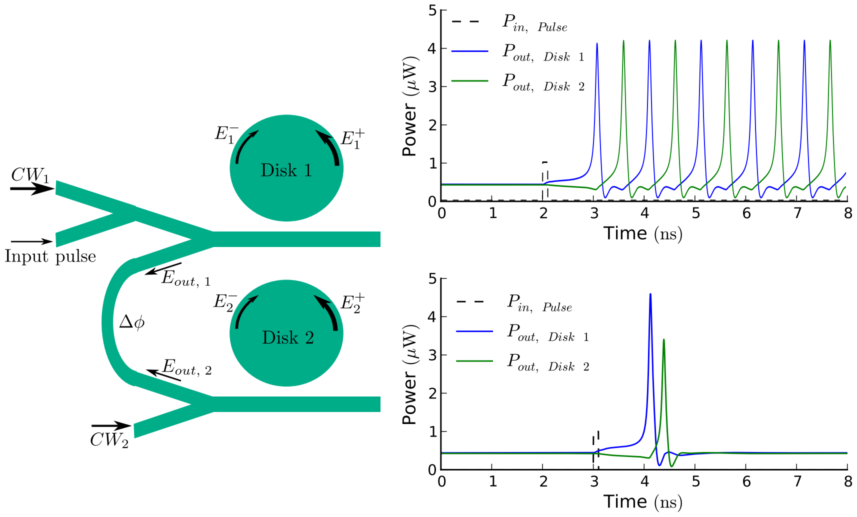

Figure 2: (left) Topology used to cascade two microdisk lasers. The connection between both lasers corresponds to a phase difference $\Delta\phi$. (right,top) If an external perturbation triggers the first disk, it excites in its turn the second disk. If both disks receive the same locking signal, due to the symmetry, the second disk excites again the first disk, and as this process repeats itself this results in alternating excitations between the two disks. (right,bottom) Symmetry breaking by inducing a difference in phase between the two locking signals of the disks can make the pulse transfer unidirectional: the second disk does not re-excite the first disk.

Second, using simulations, we investigate excitability in optically-injected microdisk lasers (Fig. 2). Due to the coupling between the strong and suppressed mode in the microdisk lasers, excitation of the disk by a perturbation of the strong mode, results in a pulse of the suppressed mode, which is comparable in strength and size to the input pulse. Consequently, the output pulse of the disk is able to excite other disks, again giving rise to cascadable excitability.

In conclusion, we demonstrate cascadable excitability in two different integrated photonic components, an important step towards the demonstration of large-scale all-optical SNNs.

1

Introduction

During our life, our brain is continuously confronted with new challenges. Often it needs to learn how to solve tasks it has never solved before. Sometimes we can follow a fixed set of rules to solve such a new task. For instance, after your parents had shown you once the steps needed to open a bottle of milk, it didn't take long before you managed to do it yourself. However, our brain is also able to solve tasks without knowing the rules needed to solve them. Day in, day out we have conversations with fellow human beings. Importantly, we do this without having access to a step-by-step list that explains us how to distinguish speech from environmental sound and how to detect words and sentences in it. Even so, in many cases, we are able to correctly interpret the message being sent by the person with whom we have a conversation. Similarly, when a young child starts to walk, it does this by mimicking the example of other walking people. Fortunately, parents do not need to provide their children with a user manual of their legs.

To improve our life quality, we feel the urge to delegate certain tasks to machines, which could previously only be solved by our brain (Fig. 1.1). If we have an algorithm for those tasks, the combination of a computer and a software engineer can fix this job. However, in some cases we do not have an algorithm available and we need to shift gears. In this case, the solution is to mimic the brain. Our brain consists of neurons, which are mutually connected and communicate with each other by sending out pulses. When such a neuron receives

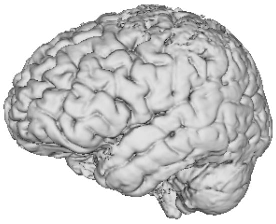

Figure 1.1: The human brain outperforms state-of-the-art computer hardware with respect to parallelization and power consumption. It processes massive amounts of time-dependent data in parallel, while its power consumption is comparable to a simple light bulb. Furthermore, by learning from previous experiences it is able to solve tasks, even without having a fixed algorithm for them.

enough pulses from other neurons, and depending on the internal dynamics of this neuron, it will spike, i.e., send out a pulse itself. By tweaking the strengths of the connections between the neurons we are able to train a part of our brain to solve a new task.

The idea of this PhD research is to build optical chips that mimic the biological framework of the brain very closely. This will allow to exploit the same power efficiency and highly parallelized computational capabilities as the biological ancestor, therefore having the potential to outperform the more traditional way of serialized computing that uses the Von Neumann architecture, like current computer hardware. A neuromorphic hardware implementation in photonics has the potential to outperform an electronic one, due to the intrinsically richer dynamics and higher speeds in photonic systems.

This interdisciplinary project combines machine learning techniques, such as neuromorphic computing, and photonics. In Sec. 1.1 and Sec. 1.2, we will provide general background on those two research fields, while in Sec. 1.3 we will make the link between both research areas. Next, in Sec. 1.4 we will explain the goal of this PhD research more in detail. Finally, in Sec. 1.5, the outline of this dissertation is discussed.

1.1 Neuromorphic computing

Neuromorphic computing mimics the NNs found in our brain in hardware, as there are plenty of reasons to do so. Indeed, in everyday life, our brain functions as the central processing unit of our body. Being very versatile, it is able to execute a tremendous number of tasks, in a continuously changing environment, solely using the energy equivalent of a light bulb. The brain is able to do this because it consists of a gigantic network of neurons that can process a large amount of time-dependent information in parallel. Additionally, our brain is able to learn from examples when it tries to solve a certain task. In contrast, regular computers work in a serialized manner and can only follow a predefined algorithm. Using fundamentally different computational principles, artificial NNs can outperform conventional serialized computer algorithms in a variety of tasks, such as autonomous signal generation, control functions in robotics, chaotic time series prediction and speech recognition [1–3]. Although current NN techniques reach state-of-art performance on many different tasks, they are simulated on traditional computers, and hence intrinsically not leveraging the full potential of the biological design. This calls for the development of a dedicated chip.

Such neuromorphic chips, currently implemented in electronics, have been studied for a few decades, but only recently has the technology become sufficiently mature and chips start to make the initial predictions on energy-efficiency come true [4]. Due to the initiation of large international research projects both in the US (BRAIN initiative [5]) and Europe (the Human Brain Project [6]), aiming for a hardware platform that can simulate a full human brain, drastic progress is to be expected in the next decade.

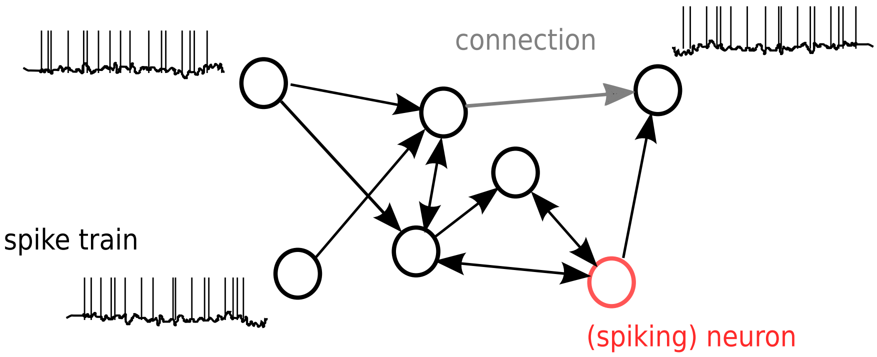

Figure 1.2: Just like its biological example, Spiking Neural Networks (SNNs) consist of interconnected neurons, that communicate with each other by sending spikes.

One subtype of NNs, the Spiking Neural Network (SNN) has become increasingly popular during the last decade [7, 8]. A SNN consists of spiking neurons, i.e., excitable (nonlinear) dynamical systems that are able to produce pulses with a fixed output shape [9]. By transferring information using pulses instead of less detailed ’activity’ levels in analog neurons, they more accurately mimic the behavior of biological neurons than previous generations of neural networks [8]. This incorporates a computational advantage, as in pulse trains in SNNs, information can not only be encoded in the average firing rate of a neuron (corresponding to the activity level of an analog neuron), but also the precise timing of the pulses can contain information, making it a more general information processing tool. The computational power of SNNs is comparable to a Turing machine [1].

Functional SNNs have recently been realized in electronics [3, 10]. Notwithstanding the potential of these electronic systems, they are subject to a fundamental bandwidth fan-in product limit. In principle, using photonics, higher speeds and bandwidths are possible. Therefore, NNs operation at time scales that are orders of magnitude faster than their biological and electronic counterparts could be achieved [11].

1.2 Photonics and the link with optical computation

Photonics is a broad research area, in which, in general, applications of electromagnetic radiation with a wavelength close to visible light are investigated (including infrared, visible and UV-radiation). It originated with the appearence of the first laser, and its name refers both to the concept of a photon and to electronics. Thereby, the name emphasizes that in many of its applications the particle-wave duality of light plays an important role, while the field also envisages to follow the same road towards large-scale, cost-efficient miniaturization as chosen by the electronics industry. Besides the laser, many of its successes now play a fundamental role in our every-day life technology use: photonics has been invaluable in the development of very different applications such as state-of-the-art display technology, DVDs, laser pointers, laser printers, efficient eye surgery techniques and high-speed data transfer.

In particular, photonic technology has a tremendous worldwide influence on the transmission speed of digital information, such as webpages, movies and music. Currently, using fibers and laser diodes, photonics provides the necessary technology to transfer digital signals over large (~ 100 km) distances, at continuously increasing bitrates (~ 100 Gbit/s and more [13]). This performance would not be possible using the more traditional electronic coax-cables. Given these successes of photonics for information transfer over large distances, there is a tendency to apply it also to information transfer over smaller distances and in the limit even to the information transfer in future generation digital chips (Fig. 1.3). There too, optical on-chip interconnections would allow to increase the information transfer rate and this transfer of large amounts of information would happen at higher speeds and using less power than using

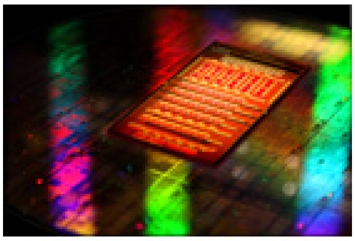

Figure 1.3: Prototype of a CMOS chip with an on-chip optical interconnect overlay (reproduced from [12]). Optical interconnects would allow to increase the information transfer rate and this transfer of large amounts of information would happen at higher speeds and using less power than using current electronic interconnects

current electronic interconnects [14–16]. In these digital chips, digital computations would be performed in the electronic domain by transistors, while the signals between these transistors would be transfered using optical links.

One could take this concept one step further, by doing the calculations in the optical domain as well, avoiding the need to transfer signals back and forth between the optical domain and the electronic domain, resulting in an additional speed increase. Hence, on-chip optical computation has the potential to outperform electronics in speed, bandwidth and power consumption. However, to perform computations, one needs nonlinearities. This can be illustrated for the calculation in one of the fundamental gates of digital logic, the 'exclusive or' (XOR) gate. The output of this XOR gate for two digital input signals x and y, is one if only one of the two input signals is one, and zero otherwise. The output can be expressed using $(x-y)^2$. Even though alternative expressions exist, they will always contains a term $\propto xy$, which is clearly nonlinear and mathematically expresses that the photons of the two different input signals need to interact with each other. As photons are bosons with a zero rest mass, they can not directly interact with each other and can only do this in an indirect way using optical nonlinearities of the surrounding material. Consequently, generally applicable optical computation requires the use of materials with optical nonlinearities. However, nonlinear photonic components still do not reach the high yield standards of their electronic counterparts, the transistors. One way of circumventing this problem is to shift the computational paradigm, using the neuromorpic approach presented in Sec. 1.1. Indeed, instead of using a photonic version of the standard Von Neumann architecture, one can, for example, try to emulate neural networks on-chip [17].

1.3 Neuromorphic computing using photonics

The idea to build neuromorphic chips in photonics is a fairly new one, and the first experimental demonstration of the concept still needed to be done at the start of this work. Although the technology is not yet as mature as electronics, it is a very promising platform. Indeed, as we discussed in the previous section, the transfer of large amounts of information in the optical domain can happen at higher speed and using less power than in any electronic implementation.

Neurons communicate using pulses. To be able to react to input spikes of other neurons they have to be excitable, i.e., a sufficiently strong perturbation of the input signal should trigger one or more pulses with a fixed output pulse shape [18]. Fortunately, a lot of integrated optical components are excitable, both lasing [11, 19–24] and non-lasing [25–27]. Therefore, these components seem suited to be used as basic building blocks for an integrated optical SNN, in which the neurons are connected to each other using waveguides and power splitters. This type of implementation allows for a dense integration of the optical SNN, which would not be possible in a fiber-based setup with individual components, such as in [28, 29]. Additionally, in contrast to a photonic neuromorphic chip, in an electronic implementation multiple components are needed to represent a single neuron [4]. As has been previously shown in our group [17, 30, 31], an additional advantage of a photonic implementation is that the phase corresponding to the interconnection length can play a beneficial role in computation. The latter is impossible in more traditional electronic implementations. Furthermore, photonics exhibits a whole zoo of rich dynamic effects, some of which can be extremely fast (e.g., the optical Kerr effect). Hence, it is a very interesting platform for fast and energy-efficient neuromorphic computing.

So far, in the field of non-linear optics, many publications about excitability deal only with single components (although there are a few exceptions, such as [11, 23, 32, 33]). The leap towards larger networks is still to be made. Although recent theoretical simulations on on-chip all-optical SNNs gave a first glimpse of the potential of these networks [11], the first experimental demonstration remains to be done and a fully-integrated approach, in which the neuron connections are also incorporated on-chip, has not yet been experimentally demonstrated. Therefore, in this PhD research, we will focus on experimentally feasible mechanisms to let neurons interact using their excitations.

Recently, feedback mechanisms are being investigated to adapt the strength of optical neuron interconnections to allow for training in optical SNNs [34].

Nonetheless, an efficient, dedicated technique for the training of an all-optical SNN is still missing. In this PhD research, we opt for integrated circuits in silicon photonics, which is compatible with CMOS-fabrication, such that in future work the chips with electronic circuits that implement control and training of the actual SNN can be easily combined with the photonics part. Since these control tasks can be performed at low speeds compared to the photonic signals, the information processing as a whole is not held back by the lack of speed in electronics as compared to optics.

In conclusion, the rationale of research on excitability in integrated photonic components is that it paves the way towards the development of a miniaturized version of a 'brain' on a photonic chip. This brain-inspired system has the potential to solve non-trivial tasks in which, e.g., many time-varying input signals have to be processed simultaneously. Similarly to our brain, which faces an equivalent computational challenge every day, it will do this in an energy-efficient way. By processing optical signals instead of electrical ones, it will also be faster than electronic solutions. Indeed, as illustrated by the recent development of optical interconnections to increase the information transfer in future generation digital chips, the transfer of large amounts of information can happen at higher speeds and using less power. Additionally, optical phenomena have much richer intrinsic dynamics, making it easier to mimic neural behaviour.

1.4 All-optical spiking neurons integrated on a photonic chip

The aim of this PhD research is to propose nanophotonic components on a SOI chip that can closely mimic the dynamical behaviour of a brain cell. More specifically, the objective is to bring forth integrated optical components with the functionality of a spiking neuron. As spiking neurons process information using pulse trains, these components need to be excitable (Fig. 1.4, top). To allow for communication between different optical neurons, an excited output pulse of one neuron should be capable of triggering an excitation in another neuron. In other words, the excitability mechanism should be cascadable (Fig. 1.4, bottom). To avoid the speed bottleneck of electro-optic signal conversion, we investigate components that incorporate an all-optical version of excitability, i.e., both the input and the output of the device are in the optical domain. We will show that this does not only result in an advantage in speed compared to electronic solutions, but also in the potential to use the phase of light as an additional degree of freedom in future all-optical SNNs. Additionally, the

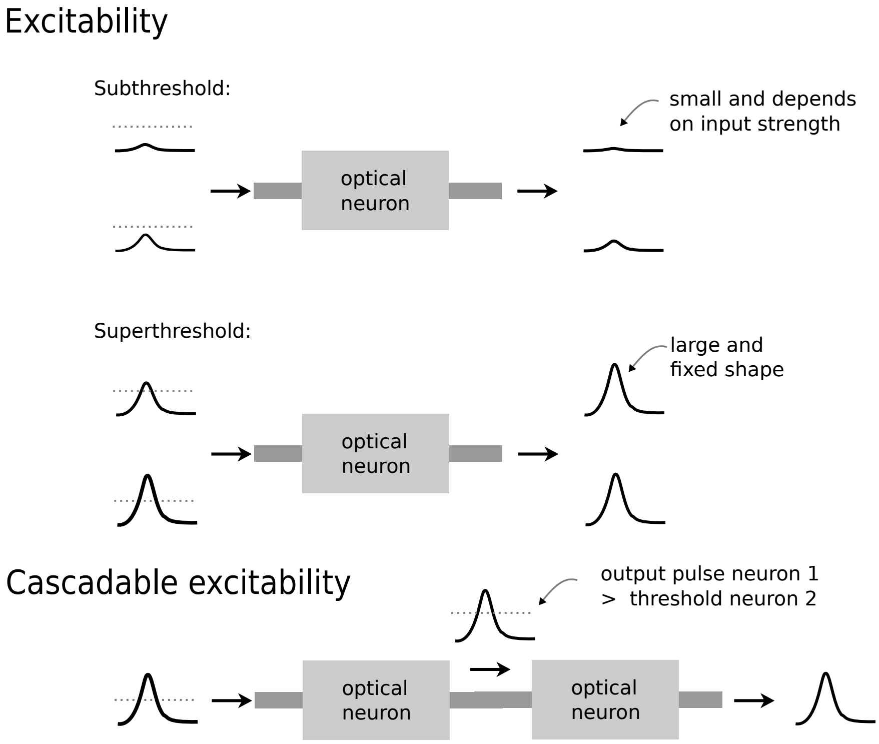
Excitability
Subthreshold:
small and depends
on input strength
optical
neuron
Superthreshold:
large and
fixed shape
optical
neuron
Cascadable excitability
output pulse neuron 1
> threshold neuron 2
optical
neuron
optical
neuron

Figure 1.4: An integrated optical neuron should be excitable and this excitability should be cascadable.

demonstration of this concept in an integrated photonics platform provides scalability, opening the door to future large-scale, ultrafast all-optical SNNs.

In our research, we investigate excitability in the SOI platform, as these photonic chips are fabricated by the same infrastructure as digital chips, allowing to benefit from the advances in CMOS-fabrication technology. In particular, we will study excitability in SOI microrings and hybrid III-V on silicon microdisk lasers. These two components have a different excitability mechanism due to the differences in underlying physics, but we will demonstrate in both components the potential for all-optical excitation transfer.

1.5 Thesis outline

In chapter 2, we place the state-of-the-art research on excitability in optical nonlinear components in the context of the quest for fast and energy-efficient hardware implementations of neuromorphic computing techniques such as SNNs. In addition, to be able to analyse excitable systems in an adequate way, we discuss some suitable mathematical tools from the field of nonlinear dynamical system theory.

To study the dynamics in circuits of excitable optical components, we need to be able to simulate the time-domain behaviour of those circuits. Therefore, in chapter 3, we introduce Caphe, an in-house software framework that we have developed to simulate this type of circuits of nonlinear dynamical components. Scalable simulation tools for nonlinear photonic circuits will be crucial during the design of future large-scale optical SNNs.

The transfer of an excitation from one neuron to another one is a key requirement when building SNNs using these neurons. In this dissertation we focus on an all-optical excitation transfer. The demonstration of this feature in integrated optical circuits is the most important innovation discussed in this dissertation. In chapters 4 and 5, we will discuss two different components, both compatible with the SOI platform, that show such cascadable excitability.

More specifically, in chapter 4, the interplay between thermal and free carrier nonlinearities in a passive high-Q microring resonator will be addressed to obtain excitable pulses that are sufficiently strong to excite other microrings. Experimental demonstration of this mechanism results in the world's first experimental proof of excitable pulse transfer in an integrated optics circuit.

In chapter 5, using simulations, we investigate excitability in optically-injected microdisk lasers. Due to the coupling between the strong and suppressed mode in the microdisk lasers, excitation of the disk by a perturbation of the strong mode, results in a pulse of the suppressed mode, which is comparable in strength and size to the input pulse. Consequently, the output pulse of the disk is able to excite other disks, giving again rise to cascadable excitability.

Finally, in chapter 6 we will summarize the conclusions of the preceding chapters and give an outlook on promising future research.

1.6 Publications

Publications in international journals

1. K. Vandoorne, P. Mechet, **T. Van Vaerenbergh**, G. Morthier, D. Verstraeten, B. Schrauwen, J. Dambre, and P. Bienstman, *Experimental demonstration of reservoir computing on a silicon photonics chip,* Nature communications, (tbp)
2. M. Fiers, **T. Van Vaerenbergh**, F. Wyffels, D. Verstraeten, B. Schrauwen, J. Dambre, P. Bienstman, *Generating Periodic Patterns Using Optical Resonators*, IEEE Transactions on Neural Networks and Learning Systems, **25**, p.344 - 355 (2014)
3. **T. Van Vaerenbergh**, K. Alexander, J. Dambre, and P. Bienstman, *Excitation transfer between optically injected microdisk lasers,* Optics Express **21**, p.28922-28932 (2013).
4. K. Alexander, **T. Van Vaerenbergh**, M. Fiers, P. Mechet, J. Dambre, and P. Bienstman, *Excitability in optically injected microdisk lasers with phase controlled excitatory and inhibitory response,* Optics Express **21**, 20292–20308 (2013).
5. **T. Van Vaerenbergh**, J. Dambre, P. Bienstman, J.A. Levenson, A. Yacomotti, *Lumped circuit heat model of photonic crystal membrane nanocavities,* IEEE Journal of Quantum Electronics, p.967 - 969 (2013)
6. **T. Van Vaerenbergh**, M. Fiers, J. Dambre, P. Bienstman, *Simplified description of self-pulsation and excitability by thermal and free-carrier effects in semiconductor microcavities*, Physical Review A, 86(6), p.063808 (2012)
7. **T. Van Vaerenbergh**, M. Fiers, P. Mechet, T. Spuesens, R. Kumar, G. Morthier, B. Schrauwen, J. Dambre, P. Bienstman, *Cascadable Excitability in microrings*, Optics Express, 20(18), p.20292-20308 (2012)
8. M. Fiers, **T. Van Vaerenbergh**, K. Caluwaerts, D. Vande Ginste, B. Schrauwen, J. Dambre, P. Bienstman, *Time-domain and frequency-domain modeling of nonlinear optical components on circuit-level using a node-based approach,* Journal of the Optical Society of America B, 29(5), p.896-900 (2012)

9. W. Bogaerts, P. De Heyn, **T. Van Vaerenbergh**, K. De Vos, S. Selvaraja, T. Claes, P. Dumon, P. Bienstman, D. Van Thourhout, R. Baets, *Silicon microring resonators*,Lasers & Photonics Reviews, 6(1), p.47-73 (2012)

Publications in international conferences

1. **T. Van Vaerenbergh**, K. Alexander, M. Fiers, P. Mechet, J. Dambre, P. Bienstman, Cascadable excitability in optically injected microdisks, Proc. SPIE 9134, Belgium, 91341W-91341W-15 (2014).
2. **T. Van Vaerenbergh**, M. Fiers, P. Bienstman, J. Dambre, *Towards integrated optical spiking neural networks: delaying spikes on chip* , Sixth 'RIO DE LA PLATA' Workshop on Laser Dynamics and Nonlinear Photonics (invited), Uruguay, p. 9-2013 (2013)
3. P. Bienstman, K.T. Vandoorne, **T. Van Vaerenbergh**, M. Fiers, B. Schneider, B. Schrauwen, J. Dambre, *Using silicon nanophotonics for digital and analog signal processing with reservoir computing*,Progress In Electromagnetics Research Symposium (PIERS 2013), Sweden, p.64 (2013)
4. P. Bienstman, K.T. Vandoorne, **T. Van Vaerenbergh**, M. Fiers, B. Schneider, B. Schrauwen, J. Dambre, *Using silicon nanophotonics for digital and analog signal processing with reservoir computing*,Horizons de l' optique, Belgium, p.12 (2013)
5. **T. Van Vaerenbergh**, M. Fiers, P. Mechet, T. Spuesens, R. Kumar, G. Morthier, K.T. Vandoorne, B. Schneider, B. Schrauwen, J. Dambre, P. Bienstman, *Characterization of cascadable excitability in a silicon-on-insulator microring*, Proceedings of the 2012 Annual Symposium of the IEEE Photonics Society Belenux Chapter, Belgium, p.119-122 (2012)
6. P. Bienstman, K.T. Vandoorne, **T. Van Vaerenbergh**, M. Fiers, B. Schneider, D. Verstraete, B. Schrauwen, J. Dambre, *Reservoir computing on nanophotonic chips*, 2012 International symposium on Nonlinear Theory and its Applications (NOLTA 2012), Spain, p.506-508 (2012)
7. **T. Van Vaerenbergh**, M. Fiers, P. Mechet, T. Spuesens, R. Kumar, G. Morthier, K.T Vandoorne, B. Schneider, B. Schrauwen, J. Dambre, P. Bienstman, *Self-pulsation and excitability mechanism in silicon-on-insulator microrings*, 2012 Asia Communications and Photonics Conference (ACP) (2012)
8. M. Fiers, K.T Vandoorne, **T. Van Vaerenbergh**, J. Dambre, B. Schrauwen, P. Bienstman, *Optical Information Processing: Advances in Nanophotonic*

Reservoir Computing, International Conference on Transparent Optical Networks (invited), United Kingdom, (2012)

9. M. Fiers, **T. Van Vaerenbergh**, K. Caluwaerts, J. Dambre, P. Bienstman, *CAPHE: Time-domain and Frequency-domain Modeling of Nonlinear Optical Components*, Advanced Photonics Congress, 2012 OSA, United States, p.paper IM2B.3 (2012)

10. **T. Van Vaerenbergh**, M. Fiers, K.T. Vandoorne, B. Schneider, J. Dambre, P. Bienstman, *Towards a photonic spiking neuron: excitability in a silicon-on-insulator microring*, accepted for publication in NOLTA, (to be published).

11. P. De Heyn, D. Vermeulen, **T. Van Vaerenbergh**, B. Kuyken, D. Van Thourhout, *Ultra-high Q and finesse all-pass microring resonators on Silicon-on-Insulator using rib waveguides*,16th European Conference on Integrated Optics and technical exhibition, Spain, p.paper 195 (2012)

12. K.T Vandoorne, **T. Van Vaerenbergh**, M. Fiers, P. Bienstman, D. Verstraeten, B. Schrauwen, J. Dambre, *Photonic reservoir computing and information processing with coupled semiconductor optical amplifiers*, Fifth 'RIO DE LA PLATA' Workshop on Laser Dynamics and Nonlinear Photonics (invited), Uruguay, p.1-3 (2011)

13. M. Fiers, **T. Van Vaerenbergh**, P. Dumon, K. Caluwaerts, B. Schrauwen, J. Dambre, P. Bienstman, *CAPHE: a circuit-level time-domain and frequency-domain modeling tool for nonlinear optical components.*, 16th Annual Symposium of the IEEE Photonics Benelux Chapter, (2011)

14. D. Vermeulen, P. De Heyn, **T. Van Vaerenbergh**, W. Bogaerts, G. Roelkens, *Silicon-on-Insulator polarization rotating micro-ring resonator*,IEEE Photonics Conference (IPC), United States, p.875-876 (2011)

15. K.T Vandoorne, M. Fiers, **T. Van Vaerenbergh**, D. Verstraeten, B. Schrauwen, J. Dambre, P. Bienstman, *Advances in photonic reservoir computing on an integrated platform*, International Conference on Transparent Optical Networks (ICTON) (invited), Sweden, p.Mo.B5.5 (2011)

Publications in national conferences

1. **T. Van Vaerenbergh**, M. Fiers, K.T Vandoorne, J. Dambre, P. Bienstman, *Photonic Reservoir Computing using thermal nonlinearities in microrings*, 12th FEA PhD Symposium (2011)

References

[1] W. Maass, T. Natschläger, and H. Markram. *Real-time Computing Without Stable States: A New Framework for Neural Computation Based on Perturbations.* Neural Computation, 14(11):2531–2560, 2002.

[2] H. Jaeger. *Harnessing Nonlinearity: Predicting Chaotic Systems and Saving Energy in Wireless Communication.* Science, 304:78–80, 2004.

[3] J. Schrauwen, D. Van Thourhout, and R. Baets. *Trimming of silicon ring resonator by electron beam induced compaction and strain.* Optics Express, 16(6):3738–3743, 2008.

[4] Swadesh Choudhary, Steven Sloan, and Sam Fok. *Silicon neurons that compute.* Artificial Neural Networks and Machine learning - ICANN 2012, 7552:121–128, 2012.

[5] `http://www.nih.gov/science/brain/`.

[6] `https://www.humanbrainproject.eu/nl_BE`.

[7] Samanwoy Ghosh-Dastidar and Hojjat Adeli. *Spiking neural networks.* International Journal of Neural Systems, 19(04):295–308, 2009.

[8] Wolfgang Maass. *Networks of spiking neurons: The third generation of neural network models.* Neural Networks, 10(9):1659 – 1671, 1997.

[9] Eugene M. Izhikevich. *Dynamical Systems in Neuroscience: The Geometry of Excitability and Bursting (Computational Neuroscience).* The MIT Press, 1 edition, nov 2006.

[10] Paul Merolla, John Arthur, Filipp Akopyan, Nabil Imam, Rajit Manohar, and Dharmendra S Modha. *A digital neurosynaptic core using embedded crossbar memory with 45pJ per spike in 45nm.* In Custom Integrated Circuits Conference (CICC), 2011 IEEE, pages 1–4. IEEE, 2011.

[11] Mitchell A Nahmias, Bhavin J Shastri, Alexander N Tait, and Paul R Prucnal. *A Leaky Integrate-and-Fire Laser Neuron for Ultrafast Cognitive Computing.* Selected Topics in Quantum Electronics, IEEE Journal of, 19:1800212, 2013.

[12] IBM. *Made in IBM Labs: Breakthrough Chip Technology Lights the Path to Exascale Computing.* 2010.

[13] Xiang Liu, A. R. Chraplyvy, P. J. Winzer, R. W. Tkach, and S. Chandrasekhar. *Fast physical random bit generation with chaotic semiconductor lasers.* Nature Photonics, 7:560–568, 2013.

[14] D.A.B. Miller. *Physical reasons for optical interconnection.* International Journal of optoelectronics, 168(11):155–168, 1997.

[15] D.A.B. Miller. *Rationale and challenges for optical interconnects to electronic chips.* Proceedings of the IEEE, 88(6):728–749, 2000.

[16] D. A. B. Miller. *Optical interconnects to electronic chips.* Applied optics, 49(25):F59–70, 2010.

[17] Kristof Vandoorne, Joni Dambre, David Verstraeten, Benjamin Schrauwen, and Peter Bienstman. *Parallel reservoir computing using optical amplifiers.* IEEE transactions on neural networks, 22(9):1469–1481, 2011.

[18] Eugene M Izhikevich. *Neural Excitability , Spiking and Bursting.* International Journal of bifurcation and chaos, 10(6):1171–1266, 2000.

[19] Sebastian Wieczorek, Bernd Krauskopf, and Daan Lenstra. *Multipulse excitability in a semiconductor laser with optical injection.* Physical review letters, 88(6):063901, 2002.

[20] Sylvain Barbay, Robert Kuszelewicz, and Alejandro M Yacomotti. *Excitability in a semiconductor laser with saturable absorber.* Optics letters, 36(23):4476–8, dec 2011.

[21] M. Turconi, B. Garbin, M. Feyereisen, M. Giudici, and S. Barland. *Control of excitable pulses in an injection-locked semiconductor laser.* Physical Review E, 88(2):022923, aug 2013.

[22] L. Gelens, L. Mashal, S. Beri, W. Coomans, G. Van der Sande, J. Danckaert, and G. Verschaffelt. *Excitability in semiconductor microring lasers: Experimental and theoretical pulse characterization.* Physical Review A, 82(6):1–9, December 2010.

[23] W. Coomans, L. Gelens, S. Beri, J. Danckaert, and G. Van der Sande. *Solitary and coupled semiconductor ring lasers as optical spiking neurons.* Physical Review E, 84(3):1–8, sep 2011.

[24] Mitchell A Nahmias, Alexander N Tait, Bhavin J Shastri, and Paul R Prucnal. *An Evanescent Hybrid Silicon Laser Neuron.* IEEE journal of selected topics in quantum electronics, 4:93–94, 2013.

[25] Stéphane Barland, Oreste Piro, Massimo Giudici, Jorge Tredicce, and Salvador Balle. *Experimental evidence of van der Pol-Fitzhugh-Nagumo dynamics in semiconductor optical amplifiers.* Physical Review E, 68(3):036209, September 2003.

[26] A. M. Yacomotti, P. Monnier, F. Raineri, B. Ben Bakir, C. Seassal, R. Raj, and J. A. Levenson. *Fast Thermo-Optical Excitability in a Two-Dimensional Photonic Crystal.* Phys. Rev. Lett., 97:143904, Oct 2006.

[27] Maia Brunstein, Alejandro M. Yacomotti, Isabel Sagnes, Fabrice Raineri, Laurent Bigot, and Ariel Levenson. *Excitability and self-pulsing in a photonic crystal nanocavity.* Phys. Rev. A, 85:031803, Mar 2012.

[28] David Rosenbluth, Konstantin Kravtsov, Mable P Fok, and Paul R Prucnal. *A high performance photonic pulse processing device.* Optics express, 17(25):22767–72, December 2009.

[29] Konstantin Kravtsov, Mable P Fok, David Rosenbluth, and Paul R Prucnal. *Ultrafast all-optical implementation of a leaky integrate-and-fire neuron.* Optics Express, 19(3):211–221, 2011.

[30] Kristof Vandoorne, Wouter Dierckx, Benjamin Schrauwen, David Verstraeten, Roel Baets, Peter Bienstman, and Jan Van Campenhout. *Toward optical signal processing using Photonic Reservoir Computing.* Opt. Express , 16(15):11182–11192, JUL 21 2008.

[31] Martin Fiers, Thomas Van Vaerenbergh, Francis Wyffels, David Verstraeten, Benjamin Schrauwen, Joni Dambre, and Peter Bienstman. *Nanophotonic reservoir computing with photonic crystal cavities to generate periodic patterns.* IEEE Transactions on Neural Networks and Learning Systems, 25(1):344–355, 2014.

[32] Alejandro Yacomotti, Gabriel Mindlin, Massimo Giudici, Salvador Balle, Stephane Barland, and Jorge Tredicce. *Coupled optical excitable cells.* Physical Review E, 66(3):036227, September 2002.

[33] B. Kelleher, C. Bonatto, P. Skoda, S. P. Hegarty, and G. Huyet. *Excitation regeneration in delay-coupled oscillators.* Physical Review E, 81(3):036204, March 2010.

[34] Mable P Fok, Yue Tian, David Rosenbluth, and Paul R Prucnal. *Pulse lead-/lag timing detection for adaptive feedback and control based on optical spike-timing-dependent plasticity.* Optics letters, 38(4):419–21, February 2013.

2

Optical Spiking Neural Networks

In Spiking Neural Networks (SNNs), information is processed by excitable neurons, that communicate with each other using pulses. Theoretically, they outperform the computational power of non-spiking artificial neural network types [1]. Given the natural appearance of excitability in many different non-linear optical components, both lasing [2–7] and non-lasing [8, 9], there is an intrinsic advantage to implementing such networks in photonic hardware, as this would allow to operate at timescales that are orders of magnitude faster than typical biological and electronic implementations [10]. In this introductory chapter, we will provide some additional background on Neural Networks (NNs) and excitability, and explain how those two concepts can be emulated in photonic hardware.

In Sec. 2.1, we start this chapter with a general introduction on neural networks. Next, in Sec. 2.2, state-of-the-art implementations of neural networks in photonics are discussed. Subsequently, in Sec. 2.3, we introduce the concept of excitability, while in Sec. 2.4, we discuss the appearance of excitability in optics.

2.1 Neural networks

In machine learning, one tries to construct computational systems that can learn from data [11]. Artificial neural networks belong to this category and are heavily inspired by our brain. Similarly to their biological counterparts, they consist of a collection of computational units, called ’neurons’, that send information to each other through their ’connections’. The purpose of this network is to solve a certain task, i.e., to obtain desired output signals, for given input signals. The neurons in a NN process information inherently in a parallel way.

In contrast to sequential computational systems based on the Von Neumann architecture, which are programmed using a predefined step-by-step algorithm, a NN is ’trained’ to solve a task. During training the behaviour of a NN is compared with the desired behaviour, and if the performance is not satisfactory, the NN is adapted to improve it. Throughout this training process, representative example data is fed to the network.

Ideally, after training, the network should be able to ’generalize’ what it has learned from the training examples to unseen data. This ability to generalize does not only depend on the complexity of the task and the capacity of the NN, but also on the quality of the training set. For instance, if a network is trained to distinguish pictures of fruit from pictures of vegetables using a collection of typical pictures of lemons, tomatoes, potatoes and apples, it should have no problems to identify a new picture of a lemon as a type of fruit. Nonetheless, it might have problems with the classification of a picture of a carrot, as the training data did not contain any representative carrot-like vegetables.

An important asset of a NN is its flexibility: the very same NN topology can be trained to solve different tasks. In the previous fruit/vegetable example, the same NN could as well be trained to return the color of the item on the picture.

In this section we will explain some of the properties of a NN in more detail. As an extensive survey on NN theory is outside the scope of this work, we refer to [11–13] for more elaborate and rigorous introductions to this topic.

NN techniques exist in many flavours, and can be subdivided on the basis of the training algorithm, the type of neurons and the connection topology.

2.1.1 Training

Training of a NN allows it to learn from input data. Training techniques can be subdivided according to the availability of the desired behaviour during training.

For instance, in supervised learning, the reaction of a network to the input is compared to the target output, and the network is adapted based on the difference between the current output and the desired output. To achieve this, for each data sample of the training set, one needs to have the corresponding desired output. For instance, in a classification task, the samples of the different classes need to be labeled. In the previous example, in which fruit pictures need to be distinguished from vegetable pictures, each picture would have a label ’fruit’ or ’vegetable’.

In contrast, during unsupervised learning, the NN only sees input data, without any information about the desired output. In the aforementioned example, the training data would contain the same set of pictures, but without the labels. Unsupervised learning would allow to group those pictures into different classes, in which the members of a given class are more similar to its class members than to members of other classes. In the fruit/vegetable example, applying supervised learning with a predefined number of four classes to a training set of pictures of lemons, tomatoes, potatoes and apples, would result in four classes of pictures of food with a similar shape. Most likely, those four classes will more-or-less correspond to lemon-, tomato-, potato- or apple-like pictures, even though the unsupervised learning algorithm had no access to these labels. It is even possible to let the algorithm determine the optimal number of classes. This type of training techniques are applied to find structure and similarity in high-dimensional input data sets.

Finally, for some tasks, one does not know the desired output in advance, and defining structure in the input data is not sufficient. For instance, if one wants to steer a remote-controlled helicopter such as in [14], initially, no examples of successful flights are available. However, we can still tell whether the training was succesful (there is no crash) or not (the helicopter crashes). In this case, one should resort to reinforcement learning in which, during training, the NN is rewarded when it performs good on a task and/or punished when it performs badly.

The precise optimization algorithm depends on the choice of neuron and topology, but in general, similar to our brain, most techniques focus on the adaptation of the connection strengths of the neurons. Furthermore, the parameters of a NN can be optimized using general-purpose optimization algorithms, such as Covariance Matrix Adaptation Evolution Strategy (CMA-ES), but as we will explain in Sec. 2.1.3, faster convergence can be obtained using algorithms that are dedicated to the neuron type and topology.

2.1.2 Neuron type

The basic computational building block of a NN is the neuron. This can be seen as a mathematical entitity that incorporates the phenomenological behaviour of a biological neuron. Different levels of detail in the approximation of the biological behaviour result in different neuron types. A biological neuron communicates with other neurons by sending and receiving pulses, also called ’spikes’. These spikes are considered to be more-or-less identical, such that information needs to be encoded in the presence of the spike or, more precisely, its timing. A neuron 'fires' when it sends out spikes. Typically, in a network, a single neuron receives many different signals from other neurons, and the importance of each corresponding input signal of this neuron is weighted by the strength of this connection. Consequently, the activity level, i.e., the firing of a neuron, depends on this weighted sum of the input signals.

In the most conceptually reduced model, the neuron is static, and given the activity levels of its preceding neurons, a neuron can only take a binary output: a neuron either fires or not. A neuron with this behaviour is called a perceptron. On the other side of the spectrum of neuron complexity, dependent on the input spike trains, a time-dependent neuron model can generate individual spikes. Such a model does not only reveal whether the neuron fires or not, but also tells at which precise moments in time this neuron fires. This is the spiking-neuron description of a neuron, the description which will be used throughout the subsequent chapters. Finally, in between those two extremes, one can average the number of spikes over a short period of time, and represent the overall activity of a neuron by its average firing rate. This analog model can be used both in a static or non-static version. In the latter model type, this firing rate is a rather smooth and continuous signal, in contrast to the output signal of spiking neurons, which is closer to an event-based model.

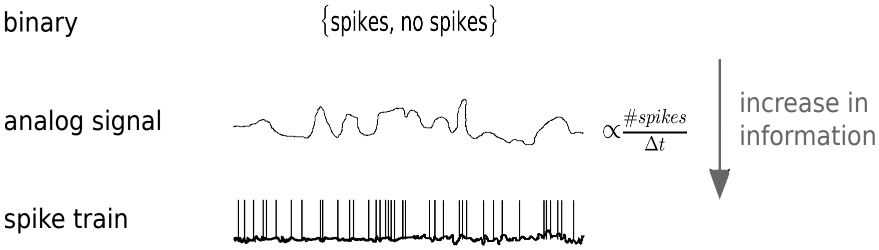

Figure 2.1: Different neuron models have different types of output signals. Due to the increase in temporal detail, there is an increase in information content from the binary output of the perceptron, over the analog output of an analog neuron, to the spike-trains produced by a spiking neuron.

In the transition from a perceptron, over an analog neuron, towards a spiking neuron, the neuron's activity level incorporates an increasing amount of temporal detail (Fig. 2.1). This gives rise to an increase in the potential of a neuron to encode information. As a consequence, for a neural network with a fixed number of neurons, the computational capacity rises with an increase in neuron complexity. For instance, since an analog NN can be seen as a spike-rate encoded version of a SNN, one can conceptually understand that a SNN with an identical connection scheme can solve all the tasks that are solvable by this analog NN. In addition, as information in a SNN can not only be encoded in the average firing rate, but also in the precise timing of the pulses [15], theoretically, a SNN can outperform an analog NN in computational capacity. This can be mathematically proven [1, 16, 17].

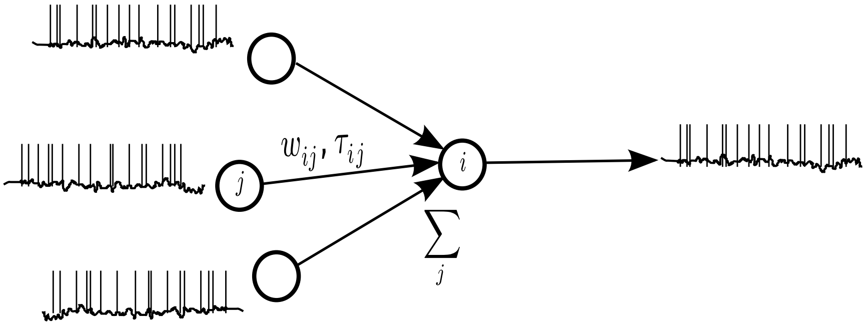

Figure 2.2: The input of a neuron is a linearly combination of the output signals of the other neurons. A connection from neuron j to i has a weight w_{ij}. If the NN is time-dependent, then the connection also has a delay τ_{ij}.

Usually, for the three neuron model types, one assumes that the signals travelling between the neurons are linearly weighted by the connections (Fig. 2.2). Additionally, in a time-dependent neuron model, a connection can also have a delay. Consequently, for a time-dependent neuron model the input $z_i(t)$ of a neuron i, that recieves input of a set S_i of preceding neurons, can be described by:

$$z_i(t) = \sum_{j \in S_i} w_{ij} y_j(t - \tau_{ij}). \tag{2.1}$$

In this, $y_j(t)$ is the output of neuron j, while w_{ij} is the weight and τ_{ij} the delay of the connection from neuron j to i.

A spiking neuron reacts to this input by firing spikes. To do so, the intrinsic dynamics of the model need to able to create such a spike. This can be done by describing a spiking neuron as a nonlinear dynamical system, with a corresponding set of rate equations [18], or by using a phenomenological description of the spiking behaviour, such as in a spike-response model [19]. In this case, $y_j(t)$ represents the amplitude as a function of time of the output spike train of neuron j. In contrast, as previously explained, for analog neurons $y_j(t)$ corresponds to the average firing rate of neuron j, and the model only needs to generate an average fire-rate as output for neuron i instead of a detailed spike train.

In a static neuron model, one often uses an activation function f to calculate the output of a neuron using $y_i = f(z_i)$ and, therefore:

$$y_i = f\left(\sum_{j\in S_i} w_{ij} y_j\right). \tag{2.2}$$

This activation function depends on the application. It can be, e.g., a linear function, a piecewise linear function, a tanh or a sigmoid function. In the case of a sign or threshold function, a perceptron is obtained. Apart from the linear function, for all those functions the output remains bounded for large input values. This sublinear increase of the output as a function of the input is a representation of the behaviour in a biologic spiking neuron. In those neurons, the internal timescale that is responsable for the spike generation will result in an effective upper limit on the firing rate, as it takes some time for a neuron to recover from the effort needed to create a spike. As a consequence, if the input firing rate is too high, the neuron can only respond with an output firing rate that is substantially lower. In chapter 5, we will demonstrate in Sec. 5.4.5 how a microdisk, as an optical spiking neuron, can indeed reproduce this trend. For non-stationary analog neurons, one sometimes uses $y_i(t) = f(z_i(t))$, in which case the neuron has no intrinsic memory. Memory can be added to this description by using $\tau\frac{dy_i}{dt} = f(z_i)$, with τ the internal timescale of the neuron.

Although a SNN is theoretically the most powerful tool from a computational point-of-view, currently, in most engineering applications, analog NNs are used. If the activation function is differentiable, gradient-descent techniques can be used for training, making the convergence during training less cumbersome than in perceptron networks or SNNs. Additionally, the simplicity of an analog neuron model makes it easier to simulate the temporal evolution of these networks. Furthermore, when using a SNN, information is encoded using spikes. However, in many real-life applications the input signals are analog signals, such that conversion of these input signals to spike trains is needed. Different methods can be used to do this, but they all have their own advantages and disadvantages. Furthermore, as the output signal, too, is in most cases an analog signal, algorithms to construct an analog signal from a spike train or population encoding techniques, in which one can average the activity of a certain subset of spiking neurons to obtain an analog value, could be used. For the latter option large-size SNN are needed, again increasing the computational effort to simulate those networks. In summary, apart from the difficulty to train SNNs, we currently do not leverage their full computational potential due to the increased complexity to simulate them. In fact, this is part of the rationale of this work, as we investigate the possibility to implement neural networks directly in hardware to avoid the need to simulate them.

2.1.3 Network topology

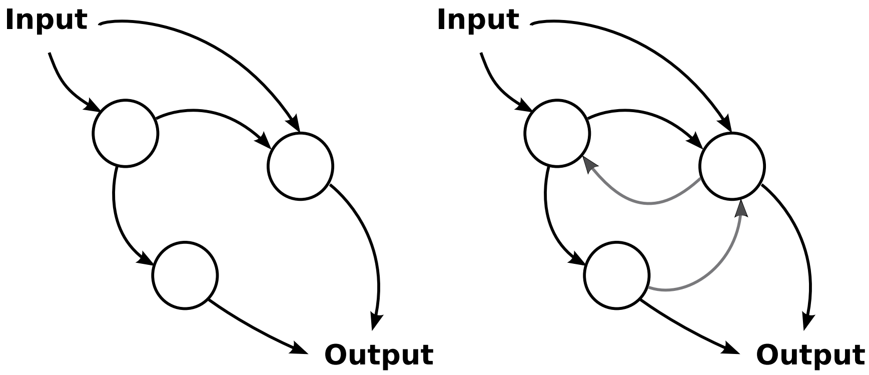

Figure 2.3: (left) A feedforward Neural Network (FNN) has no feedback loops, which makes it relatively easy to train (right) A Recurrent Neural Network has feedback, providing memory, but is more difficult to train.

Another very important network property is its connectivity, and more in particular, the presence of feedback. If a network does not contain neurons that send their output to preceding neurons, it is a Feedforward Neural Network (FNN), while in the other case, in which the connections between neurons do make loops, it is a Recurrent Neural Network (RNN) (Fig. 2.3). The choice of connectivity has an important influence on the trainability and memory behaviour of the network.

2.1.3.1 Feedforward versus recurrent neural networks

The advantage of a FNN over a RNN is that it is easier to train. A famous example of this case is a static and analog FNN, which is often referred to as a multilayer perceptron (even though the neurons are no binary perceptrons, but analog). If the neurons have a differentiable activation function, the combination of supervised learning and gradient-descent techniques, such as stochastic gradient descent, leads to the well-known error-backpropagation algorithm [11], which is due to its efficiency and simplicity one of the most-used techniques in contemporary applications. As the optimization of a FNN already encounters a non-convex error landscape, the convergence of training techniques for RNN, such as backpropagation through time, is even more peculiar due to local optima, bifurcations and sensitivity to initial conditions [12, 20, 21]. Techniques to circumvent these problems do exist, but are non-trivial to apply and have a high computational cost [12, 21–23].

However, due to the lack of feedback loops, a FNN can not retain information from the input signals for a long time, making it less suitable to apply to input signals in which the information is spread over a certain amount of time, encountered in, e.g., speech recognition and robot or machine control. In principle, the information of previous time-steps can be fed externally to the network by additional delayed versions of the input signals such as in [24]. Nonetheless, this technique has as a disadvantage the finite and artificial length of the delay and the need for many additional parameters if long delays are needed. Consequently, it would be useful if the network has intrinsic access to memory. The delay of the neuron interconnections in the feedback loops in RNNs provide such an intrinsic memory on the network level, as the information of the input signals can circulate in those loops. So, while their training is more difficult, the use of RNNs is inevitable when dealing with tasks in which memory is required.

2.1.3.2 The combination of feedforward and recurrent neural network properties using reservoir computing

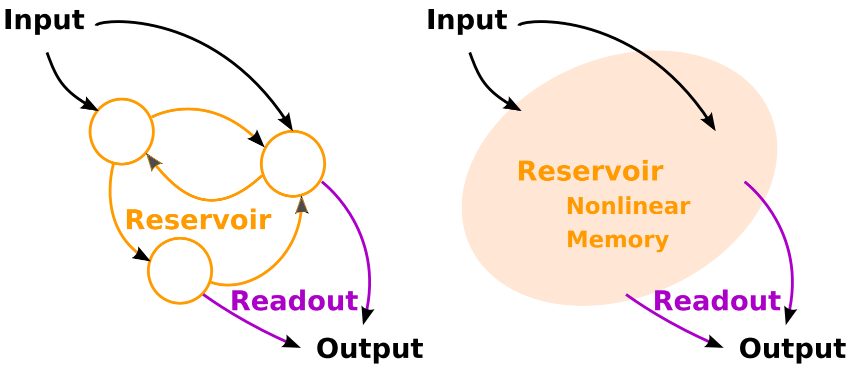

Figure 2.4: (left) The Reservoir Computing paradigm combines the easy trainability of a FNN in the readout layer with the dynamic richness of a RNN in the reservoir. (right) the RNN in the reservoir can be replaced by another nonlinear dynamic system, paving the way towards hardware implementations.

To obtain the best of both worlds, the Reservoir Computing (RC) paradigm has been proposed as a golden mean [25, 26]. In this decade-old machine learning technique, a NN is subdivided into two parts: the reservoir layer, and the readout layer (Fig. 2.4). The reservoir consists of a randomly connected RNN that is left untrained. In contrast, the readout layer is a simple FNN neural network that is trained to map the states of the reservoir to the desired output. Importantly, as the readout layer is a FNN, it has no intrinsic memory, but is easily trainable. In most cases, the output of the readout is just a linear combination of the input signals and reservoir states, such that standard linear regression techniques can be used for training. On the other side, the recurrence in the reservoir allows for memory, making the network suitable for processing time-dependent input signals. In conclusion, RC combines the advantages of both feedforward neural networks (easy trainability) and recurrent neural networks (memory, processing of time domain information) into one single network.

Before the term RC was proposed, the concept to separate a network in a highly dynamic recurrent part and an easy trainable output layer, was almost simultaneously proposed in the context of discrete-time analog NNs [21] and continuous-time SNNs [12], and the same idea appeared shortly afterwards in [27], before it was unified under the RC umbrella in [25, 26]. These different backgrounds elucidate that the precise nature of the reservoir is less important. Indeed, the reservoir only needs to project the input signals into a higher dimensional space (in both space — i.e., number of neurons of the reservoir — and time), in such a way that it becomes easier for the readout layer to calculate the desired system output using the information of the states than using the inputs directly. The reservoir makes feature extraction for the readout layer easier, and hence behaves similarly to the kernels in regular classification theory, in which input vectors are transformed to a higher dimensional space, using nonlinear functions, allowing an easy linear classification algorithm to perform nonlinear separation of the different classes [11]. Consequently, in principle, many nonlinear dynamical systems with intrinsic memory can function as a reservoir. Researchers have proven this by even using a bucket of water as a reservoir to do speech recognition [28]. While a bucket of water is not such a practical solution, the flexibility in reservoir choice opens possibilities towards hardware implementations of the reservoir, as we will see in the next section. Additionally, because only the readout layer is trained, different readouts can use the same reservoir and can consequently solve different tasks on the same input, making the concept even more flexible. Finally, RC networks are not only easy to use, but they also offer state-of-the-art performance on many tasks [15, 21, 26].

2.2 Optical implementations of neural networks

In the previous section, we described how a NN consists of interconnected neurons. All those neurons process the input information in parallel. However, when these NNs are executed on a regular microprocessor, the neuron states are calculated sequentially, making the calculation less efficient. In a hardware implementation of the NN, this disadvantage can be circumvented, resulting in higher speeds, a better power efficiency and intrinsic parallelism.

Although electronic hardware implementations of, e.g., SNNs exist [29–34], we will focus on optical implementations, as this allows to map one neuron onto one single component, instead of a small circuit, and, due to the efficiency of data transfer in the optical domain, in a potential speed increase [35–37]. These hardware networks could be used for event detection, chaotic time-series generation, massive parallel classification problems of large amounts of data, such as radar information related to traffic safety, LIDAR and the processing of data of the Large Hadron Collider. Due to the analog nature of the hardware implementation it can also be used in the context of brain-machine interfaces [38]. Additional applications are those in which the input signals are already in the optical domain, processing telecom signals or video-streams.

In early implementations, free-space configurations, using a spatial light modulator to implement the weighting by the neuron interconnections, were proposed [39, 40]. Another approach is the all-optical neural network proposed in [41], in which ring lasers, each on a separate lasing wavelength, are coupled with each other using fibers and directional couplers. However, these approaches are rather bulky, and hence have a limited scalability towards large network sizes. In the next two subsections, we will summarize some state-of-the-art results related to analog neuron implementations of Photonic Reservoir Computing (PRC) (Sec. 2.2.1), as it gives a good example of an integrated neural networks implementation and, optical SNNs (Sec. 2.2.2), as this is the final goal of the research presented in this work.

2.2.1 Photonic reservoir computing

PRC offers a very promising road for the implementation of neural networks with state-of-the-art performance in optical hardware. In this approach one uses the RC paradigm and applies it to photonics. More specifically, the reservoir is replaced by an optical dynamical system. In some applications this is done by combining a single optical nonlinear component with a long delay-line, using time-multiplexing and masking techniques of the input signal to obtain an effective multi-neuron-like behaviour [42, 43].

However, an approach more related to our work, is the integrated version of PRC, as proposed in simulations for circuits of Semiconductor Optical Amplifiers (SOAs) [35, 36], or Photonic Crystals (PhCs) with a Kerr nonlinearity [37]. In this framework, the neurons from the photonic reservoir are emulated by optical nonlinear components, connected by waveguides. Due to the planar nature of integrated photonics, waveguide crossings need to be avoided,

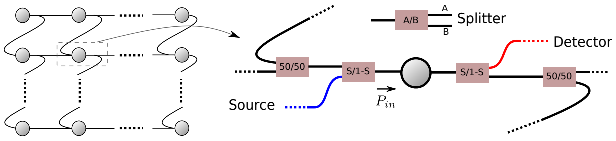

Figure 2.5: The details of the local connection topology of a fully connected optical neuron (grey circle) embedded in a 2D-mesh implementation of a PRC network. The power division over the different output branches of the splitter is determined by the splitting ratio S. Adopted from [37, 44].

resulting in restrictions on the connection topology. As a consequence, this connection topology is more regular than in the original software version of RC. Although intentional predefined length differences of the waveguides between the optical neurons are in principle possible, the currently proposed topology designs use identical interneuron waveguide lengths. Hence, the only irregularity is due to the process variations caused by fabrication imperfections, which result in small offsets between the experimental waveguides and the design target.

An additional issue that is not present in the software version of RC is the effective power loss in the splitters (combiners) that are needed to send (collect) the output (input) of a neuron to (from) several other neurons. Due to a fundamental physical limitation, a symmetric splitter (combiner) that divides (collects) a signal over (from) N-ports diminishes the amplitude of the light at each of those channels with a factor $\frac{1}{\sqrt{N}}$. Consequently, to avoid the need to compensate these losses with additional (power consuming) amplification, the number of splitters and combiners is kept limited, resulting in additional connectivity restrictions. Therefore, in the current implementations the nonlinear optical neurons are placed in a 2D-grid, in which each neuron receives (sends) input (output) from (to) maximal two other neurons. If in addition a neuron receives an external input signal, and the output of the neuron is send to a detector, additional splitters and combiners need to be incorporated (Fig. 2.5). In those power dividers and combiners, the splitting ratio can be optimized, such that the power loss in the neuron connections is reduced. Two-channel splitters and combiners can be easily defined in integrated photonics, using standard components such as multi-mode interferometers, directional couplers or Y-junctions. Advantageously, a small fan-in and fan-out per neuron also reduce the design complexity of the network topology.

Recently, the concept of integrated PRC was demonstrated in Silicon-On-Insulator (SOI) using a ’passive’ reservoir [45]. In this case, the same connection topology is used as in the previously mentioned simulations, but no nonlinear components are included. The neuron corresponds to the waveguide part on the places of the original nonlinear component positions. Hence, the whole reservoir solely consists of waveguides, splitters, combiners and grating couplers to couple light into and out of the chip. In this case, the nonlinearity of the system, needed to do computations, is shifted to the readout layer, as the output of the system consist of a linearly weighted sum of the output power of the passive neurons. By reading out the optical power, the square of the optical field is taken, resulting in the desired nonlinearity. Using this nonlinearity in the readout layer, the passive network is able to perform different calculations on bit-streams, and in simulation a larger network shows to be able to do speech recognition. Further research is needed to investigate which set of tasks can be succesfully solved by this reservoir type.

2.2.2 Optical Spiking Neural Networks

Although the RC paradigm can also be applied to SNNs, no spiking PRC networks have thus far been proposed. As we will show in Sec. 2.4, optical nonlinearities are very suitable to exhibit excitability, a property that is necessary for emulating a spiking neuron. However, even though there is a large amount of literature on excitability in single components, the research towards optical SNNs is still in its initial stage. Indeed, even though the dynamics in coupled excitable components have been studied [46–48], the devices in these experimental setups were coupled through fibers or free space optics and not much attention was spent on future prospects for scalability and training.

A first promising technology platform for optical SNNs was the excitability found in integrated InP-based multi-quantum-well Semiconductor Ring Lasers (SRLs) [2, 3, 49]. In [3], simulations demonstrated how pulse transfer between two optical excitable units is allowed. However, an experimental demonstration of this pulse transfer is still missing, and the excitability mechanism has no straight-forward analogon in biological NNs or currently used software-based versions of SNNs. In chapter 5, we will propose how optically injection in this type of structure results in a more well-known excitability behaviour. We do this for a microdisk laser on hybrid III-V on SOI, but as the physical behaviour in this component is identical to a SRL, the results should be transferable to the SRL platform as well.

During this PhD research, the first real attempt towards optical SNNs was taken by the Lightwave Communications Research Lab at Princeton in the research on what they call ’Lightwave Neuromorphic Signal Processing’. A review of this work can be found in [50]. Initially, they worked with fiber-based systems, in which different filters and nonlinear optical components were used to emulate Leaky-Integrate and Fire (LIF) behaviour all-optically, with a 10^8 speed-up compared to biological neurons [51–55]. The LIF model is an ad-hoc description of excitable behaviour in biological (integrating) neurons, and, due to its simplicity and strength, it is currently used in a lot of the SNN-related theory and applications [19, 56]. Before we proceed to their implementation of this behaviour, we will first explain this model.

In the LIF neuron model, the state of the neuron is represented by its membrane potential V. The capacitance C of the membrane, and the parallel resistance R of the current channels through this membrane, make that this neuron is a simple RC-circuit:

$$C\frac{dV}{dt} = -V + RI(t). \tag{2.3}$$

Without external input pulses the neuron resides at its rest potential V_L. If the neuron receives pulses from the outside world through its input current I, they charge the potential until a certain threshold V_{th} is reached. If this threshold is reached, nonlinear processes change the behaviour of the current channels through the membrane, resulting in an output spike. After the spike the membrane potential is reset to the value $V_R < V_L$, making it temporarly harder for external perturbations to reach the threshold. This period in which external perturbations have less influence is called the relative refractory period. In principle, the model can also be extended with an absolute refractory time, where it is completely insensitive to external inputs by fixing the membrane potential during a period Δ_{rf} after the spike, before restarting the integration of V using Eq. (2.3) at V_R.

In [51–55, 57, 58] the behaviour of this model is conceptually subdivided into different stages that can be emulated by a single optical unit. For instance, to emulate the integration by Eq. (2.3), they used cross-gain saturation in a commercial SOA or in a Electro-Absorption Modulator (EAM) (due to interaction with a device in which four-wave mixing takes place), while threshold behaviour can be obtained in Germanium-doped nonlinear loop mirror. These different stages are then connected using fibers and filters, resulting in a rather bulky setup. Furthermore, the material nonlinearities that are needed in the different units are not straightforward to obtain on a single integrated chip. However, this type of system was succesfully used to experimentally mimic the crayfish tail-flip escape response [54]. This is the world's first demonstration of a signal feature recognition task using an all-optical SNN-based methodology. Moreover, using the combination of an Electro-Optic Modulator (EOM) and an EAM even the potential for synaptic plasticity in this optical system was experimentally demonstrated, offering a technique to allow training in optical SNNs. So, even though we aim for an integrated optical SNN, the literature on this fiber-based network is a valuable source of inspiration.

Recently, using simulations, the same group has proposed other optical SNN platforms in which an optical neuron is represented by only one component instead of a circuit of components, making it more suitable for integration [58–60]. In this work the excitability mechanism related to Q-switching in a Vertical Cavity Surface-Emitting Laser (VCSEL) with intra-cavity saturable absorber [7], is adapted such that it mimics the behaviour of Eq. (2.3). In [60] VCSELs are assumed as well, while [58] is based on nonlinearities in graphene whithin a fiber-based set-up, hence, both approaches need additional off-chip components to connect the neurons. In contrast, in [59] hybrid III-V on SOI integrated lasers are proposed, which can be connected using waveguide circuitry, clearly paving the way for all-optical integration. Furthermore, [58, 60] show how small all-optical circuits with these optical spiking neurons can mimic the functionality of real-life biological circuits, such as the implementation of a circuit emulating the auditory localization algorithm seen in the barn owl. The experimental demonstration of these integrated all-optical SNNs still remains to be done.

2.3 Excitability in nonlinear dynamical systems

To emulate spiking neuron behaviour using a single optical device, this device should be excitable, i.e., sufficiently strong (but still small) input perturbations can trigger a fixed-shape large-amplitude response, after which it returns to its initial state. During its response the system is relatively insensitive to new perturbations. This is called the refractory time. Excitability is related to the concept of a threshold: if the input perturbations are below threshold, the system linearly relaxes to the rest state, and the amplitude of this response is proportional to the strength of the input perturbation. However, above threshold, the system reacts with a characteristic nonlinear response (e.g., one or more pulses) and the amplitude of this response is rather independent of the input perturbation strength. As we will see in the subsequent chapters of this dissertation, some properties of the system's reaction, such as the latency of the pulse compared to the input perturbation, can be dependent on this perturbation strength.

Nonlinear dynamical systems theory offers the mathematical tools to analyse the appearence of excitability in a device, based on its rate equations. We will explain some important concepts from this field in Sec. 2.3.1. Next, in Sec. 2.3.2, these concepts will be used to explain the origin of excitability and we will introduce classification schemes of excitability in biological neurons, allowing to link the behaviour in optical neurons with their biological counterparts. For detailed and more exhaustive introductions to nonlinear dynamical systems and excitability, we refer to [18, 61, 62].

2.3.1 Nonlinear dynamical systems theory

The dynamics in many optical components can be described using a first order Ordinary Differential Equation (ODE), describing the time evolution of a N-dimensional real state vector $\mathbf{x}$ (in the case of complex fields, it is always possible to represent this field by the combination of its real and imaginary part):

$$\frac{d\mathbf{x}}{dt} = \mathbf{f}(\mathbf{x})\,. \tag{2.4}$$

Based on a geometrical study of $\mathbf{f}(\mathbf{x})$, nonlinear dynamic system theory often allows to predict the behaviour for $t \to \infty$ of the system for a given initial condition $\mathbf{x}(t = 0) = \mathbf{x}_0$, without explicitly integrating Eq. (2.4). To achieve this, the attractors of the system are calculated, and their corresponding basins of attraction. These attractors of a dynamic system are the (stable) types of dynamic behaviour to which the system can evolve. A nonlinear system can have more than one attractor, and the initial condition determines to which attractor $\mathbf{x}(t)$ will converge, depending on in which attractor's basin it starts. A system can relax to a single 'steady-state' point, a self-sustained periodic oscillation (if $N \geq 2$) or even a chaotic state (if $N \geq 3$).

In the study of excitability, especially the interplay between steady-state points and oscillations is important, so we will limit our discussion to those two phenomena. Points for which

$$\frac{d\mathbf{x}}{dt} = \mathbf{f}(\mathbf{x}) = 0 \tag{2.5}$$

holds are called Fixed Points (FPs). A FP $\mathbf{x}_{FP}$ is stable if, after a small perturbation, the system relaxes back to the same point. Hence, stable FPs are attractors of the system. If the real part of all the eigenvalues of the Jacobian $\frac{\partial \mathbf{f}}{\partial \mathbf{x}}|_{\mathbf{x}_{FP}}$ evaluated at $\mathbf{x}_{FP}$ is purely negative, this FP is stable. FPs can also be unstable, i.e., even for very tiny perturbations the system will never relax back to its initial state. This will happen if the real part of at least one of the eigenvalues of the Jacobian in this FP is positive. If the real parts of one of the eigenvalues is equal to zero, higher-order terms in the Taylor expansion around the $\mathbf{x}_{FP}$ might provide more information on the stability. Importantly, the latter condition is often an indication that the system is in a transition between two dynamic regimes. Indeed, suppose that the system also depends on a parameter vector μ, then Eq. (2.4) can be rewritten to:

$$\frac{d\mathbf{x}}{dt} = \mathbf{f}\big(\mathbf{x}, \mu\big)\,. \tag{2.6}$$

Changes in μ can affect the dynamic behaviour of the system. For instance, due to a changing μ a stable FP can become unstable, causing the system to diverge or to relax to another attractor. At the transition between those two regimes, the real part of at least one of the eigenvalues of the Jacobian will become zero. We say that the system bifurcates at this special value of the parameter vector $\mu = \mu_c$. These bifurcations incorporate a lot of information on the system, as they help us to identify the boundaries between different dynamic behaviour.

A similar story holds for the attractors that are periodic self-sustained oscillations. One can define a Limit Cycle (LC) as a non-constant solution of Eq. (2.4) for which a $T > 0$ exists such that

$$\forall t: \ \mathbf{x}(t+T) = \mathbf{x}(t). \tag{2.7}$$

The smallest T for which the previous equation holds, is called the period of the oscillation. As with the FPs, after a small perturbation the system can relax back to the LC, or diverge from it, resulting in a stable and unstable LC, respectively.

In general, a bifurcation occurs when a change in the parameters of the system results in a qualitative change in the dynamic behaviour of this system. We will now illustrate this concept a bit more in-depth for some bifurcations that are relevant to excitability, explaining how bifurcations can give birth to LCs.

2.3.1.1 Saddle-node or fold bifurcation

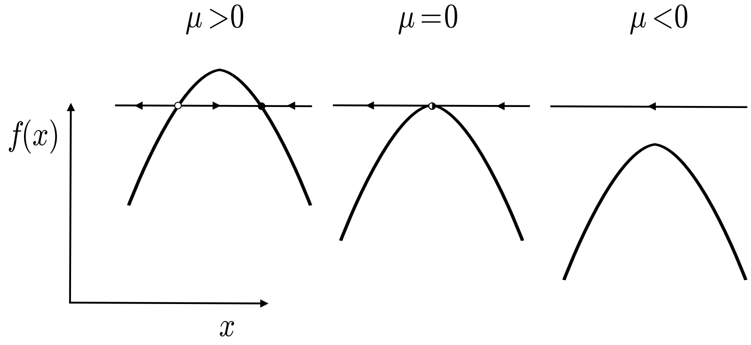

Figure 2.6: In a saddle-node bifurcation a stable FP (black circle) and unstable FP (white circle) collide and disappear. Arrows indicate the direction of the flow on the x-axis.

Consider the one dimensional system:

$$\frac{dx}{dt} = \mu - x^2. \tag{2.8}$$

If $\mu > 0$, the system has two FPs, one stable at $x_1 = \sqrt{\mu}$ and one unstable at $x_2 = -\sqrt{\mu}$. At $\mu = 0$ those two FPs collide, and for $\mu < 0$ the FPs have disappeared. This bifurcation is a saddle-node or fold bifurcation (Fig. 2.6). Any system that shows this bifurcation is topologically identical to Eq. (2.8) in the proximity of this bifurcation, which we call the normal form corresponding to this bifurcation. This bifurcation can also appear in systems with $N > 1$.

Importantly, the stable FP disappears by colliding with an unstable FP. It can be proven that a FP can only change its stability by interaction with another invariant set (e.g., an unstable FP or LC).

2.3.1.2 Andronov-Hopf bifurcation

If the dimensionality of the system $N \geq 2$, then LCs can appear. This can be easily seen in the following example:

$$\frac{dx}{dt} = \mu x - \omega y - x(x^2 + y^2), \tag{2.9}$$

$$\frac{dy}{dt} = \omega x + \mu y - y(x^2 + y^2). \tag{2.10}$$

This system can be expressed in its polar coordinates:

$$\frac{dr}{dt} = r(\mu - r^2), \tag{2.11}$$

$$\frac{d\theta}{dt} = \omega. \tag{2.12}$$

The phenomenological behaviour of this system in the xy-plane is shown in the upper part of Fig. 2.7. If $\mu < 0$, the system has a stable FP at $r = 0$, while for $\mu > 0$ this FP looses stability and a stable LC appears with oscillation frequency ω, and amplitude $r = \sqrt{\mu}$. The bifurcation at $\mu = 0$ is a supercritical Andronov-Hopf bifurcation. In this case, a stable FP is converted in an unstable FP and a stable LC. If in a physical system that resides in its stable FP for $\mu < 0$, μ is slowly increased, such that it crosses the bifurcation, noise will let the system diverge from the unstable FP to the stable LC. The amplitude of this oscillation grows $\propto \sqrt{\mu}$, resulting in very small oscillations above threshold.

Another type of Andronov-Hopf bifurcation is the subcritical Andronov-Hopf bifurcation, in which a stable FP coexists with an unstable LC, and after the bifurcation this unstable LC is converted to an unstable FP. In physical systems, due to energy conservation, the unstable LC is normally surrounded by another stable LC (Fig. 2.7, bottom). An example of this type of system is:

$$\frac{dr}{dt} = r(\mu + r^2 - r^4), \tag{2.13}$$

$$\frac{d\theta}{dt} = \omega. \tag{2.14}$$

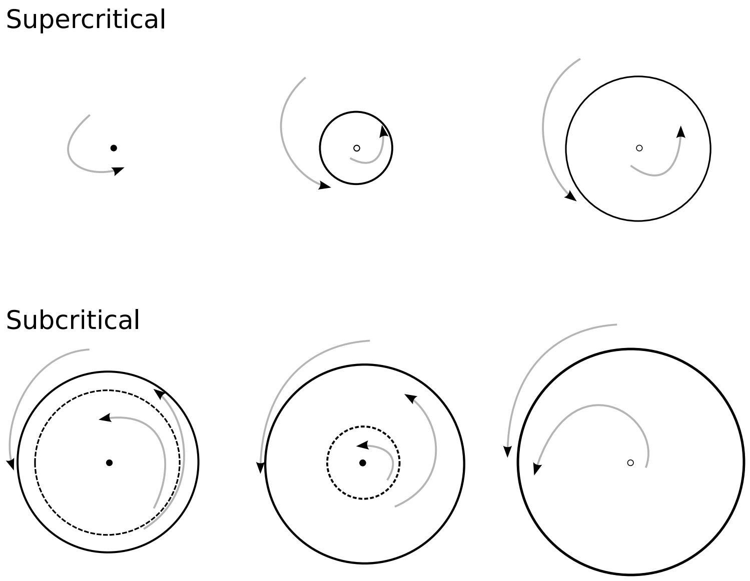

Figure 2.7: Two different types of Andronov-Hopf bifurcations: in a supercritical Andronov-Hopf bifurcation a stable LC originates from a stable FP, while in a subcritical Andronov-Hopf bifurcation an unstable LC collides with a stable FP, resulting in an unstable FP. In most physical systems with subcritical Andronov-Hopf bifurcation the unstable FP is surrounded by another stable LC.

The contrast between this system and the one describing the supercritical Andronov-Hopf bifurcation, can be observed by slowly increasing the parameter μ from $\mu < 0$ to $\mu > 0$, starting in the stable FP. In this case, after the bifurcation, noise kicks the system out of the equilibrium to oscillations which have immediately a large amplitude ($r \approx 1$). Even more, for negative μ-values close to zero, sufficiently large noise can bring the system in an initial condition outside the amplitude of the unstable LC (which has a small amplitude $\propto \sqrt{-\mu}$), and the system can switch as well to the large amplitude oscillations of the surrounding stable LC. It can be calculated that at $\mu_f = -\frac{1}{4}$ the unstable LC that originates from the subcritical Andronov-Hopf bifurcation and the surrounding stable LC collide and disappear for $\mu < -\frac{1}{4}$. This is a LC fold bifurcation. In the μ-region between the LC fold bifurcation and the subcritical Andronov-Hopf bifurcation, the system is bistable: x can converge to two different attractors, the FP at the origin, or the surrounding stable LC.

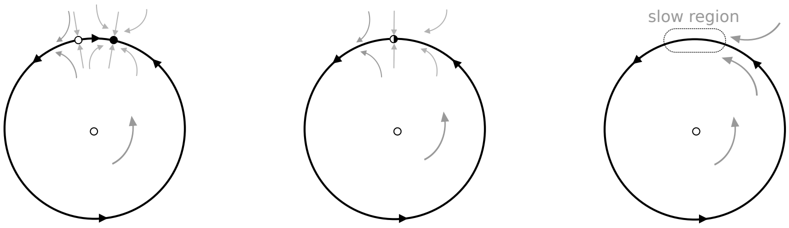

Figure 2.8: A saddle-node on a invariant circle bifurcation gives rise to a LC.

2.3.1.3 Saddle-node on an invariant circle bifurcation

In the previous example we discussed how a small-amplitude LC can originate from a change in stability of a FP. Another mechanism of LC creation is shown in Fig. 2.8. It occurs in the following example:

$$\frac{dr}{dt} = r(1-r^2), \tag{2.15}$$

$$\frac{d\theta}{dt} = \alpha - \sin(\theta). \tag{2.16}$$

This system has an unstable FP at the origin, and trajectories are attracted to the circle with $r = 1$. If $\alpha \in]-1,1[$ the system has one stable FP and one unstable FP on this circle, at $\theta_1 = \arcsin(\alpha)$ and $\theta_2 = \pi - \arcsin(\alpha)$, respectively. At $\alpha = 1$ and $\alpha = -1$ these FPs collide in $\frac{\pi}{2}$ and $-\frac{\pi}{2}$, respectively, and the circle $r = 1$ becomes a stable LC. This bifurcation is called a saddle-node on an invariant circle, as during this bifurcation a saddle-node bifurcation takes place in the θ-dimension. Interestingly, in this case, the oscillation had immediately a large amplitude $r = 1$, and for values close to the bifurcation, an infinite period is obtained. Indeed, close to the bifurcation at $\alpha = 1$, due to continuity, for $\theta \approx \frac{\pi}{2}$, the derivative $\frac{d\theta}{dt}$ will still be very small, slowing down the dynamics, so for $\alpha \to 1$ this period will diverge. This type of slowing down, is sometimes also called a 'ghost' effect of the nearby bifurcation.

2.3.2 The origin of excitability and its classification

In most cases, a superthreshold perturbation of an excitable system results in a single pulse. In the previous subsection, we have explained how bifurcations can give rise to LCs, which can be considered as periodic pulse or spike trains. Most excitable behaviour is linked to the presence of such spiking behaviour. Before the arrival of the perturbation, the system resides in a stable rest state, and the perturbation kicks the system into a large amplitude trajectory, of which the shape is a reminiscent of the dynamics of the nearby periodic spiking regime. Rougly said, the perturbations triggers a ghost pulse from the nearby spike train.

This explains why excitability in biological neurons is often characterized using the bifurcation-type that causes self-sustained oscillations. Four typical examples of such onsets are:

- Supercritical Andronov-Hopf bifurcation
- Subcritical Andronov-Hopf bifurcation
- Saddle-node on an invariant circle
- Saddle-node off an invariant circle

A saddle-node off an invariant circle is a normal saddle-node bifurcation, in the presence of a LC. After the stable FP has lost its stability, noise will kick the system to this stable LC. Both the saddle-node off an invariant circle and the subcritical Andronov-Hopf bifurcation have a parameter range for which there is bistability between a stable FP and a stable LC. Another important criterium to classify those bifurcations is considering the reaction to (subthreshold) perturbations near the oscillation onset. Both Andronov-Hopf bifurcations will respond with subthreshold oscillations, i.e., a damped oscillatory response, that relaxes to the FP, with a frequency related to the nearby self-sustained oscillation. A neuron with this behaviour is called a 'resonator'. On the contrary, for the two saddle-node bifurcations, small perturbations do not result in subthreshold oscillations, only in an exponential relaxation. A neuron with this type of bifurcation is an 'integrator'.

Apart from the difference in reaction to subthreshold pulses, integrators and resonators differ in the type of threshold. In the case of an integrator, the threshold is theoretically always well-defined by a threshold manifold [18]. For instance, in the case of a saddle-node on an invariant circle bifurcation, the unstable FP is a saddle point which has a stable manifold that accurately separates two regions in phase space (and is hence called a separatrix). Consequently, this stable manifold of the unstable FP serves as a threshold manifold. In the case of a resonator neuron, this threshold manifold is not always properly defined, and in many cases a continuous transition between subthreshold oscillations and excitability exists. However, sometimes the sensitivity to the perturbation strength is extremely narrow, even below the experimental noise level, such that these neurons in practical situations do exhibit proper all-or-none reactions on external perturbations. This is quasi-threshold behaviour.

The classification of neurons in resonators and integrators can be explained by another computational property of each class. Indeed, two sufficiently closely-spaced subthreshold pulses can result in an excitation if the neuron is an integrator, the neuron 'integrates' their combined perturbation. This correspons to the LIF behaviour, described in Eq. (2.3). In the case of a resonator, two subthreshold perturbations can also result in an excitation, but in this case the two pulses need to be in resonance, i.e., in phase with the intrinsic frequency related to the subthreshold perturbations. If the time spacing is too small or too large, no excitation will occur.

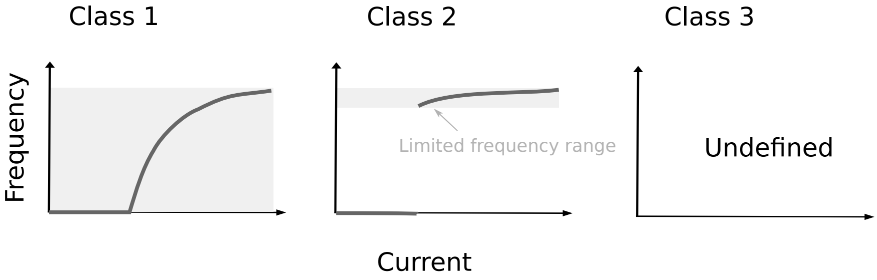

Figure 2.9: Neural excitability can be subdivided in three classes based on the frequency-current relation at the onset of spiking [18].

By experimentally slowly changing the current in biological neurons between the rest state and the spiking state of the neuron, different classes of excitability can be defined based on the frequency-current relation at the onset of spiking (Fig. 2.9). This often-used classification scheme is the one proposed by Hodgkin based on the study of squid axons. Rephrased in our terminology his classification becomes:

- Class 1 neural excitability: spike trains can be generated with arbitrarily low frequency, depending on the strength of the applied current.
- Class 2 neural excitability: spike trains are generated in a certain frequency band that is relatively insensitive to changes in the strength of the applied current.
- Class 3 neural excitability: A single spike is generated in response to a pulse of current. Repetitive spiking can be generated only for extremely strong injected currents or not at all.

In other words, the frequency-current relation for Class 1 neurons starts from zero and continuously increases, for Class 2 neurons it is discontinuous, while for Class 3 neurons it is not defined [18]. During the slow current ramp, both Class 1 and Class 2 neurons encounter a bifurcation, and it will depend on the type of bifurcation to which class a neuron belongs. For instance, Andronov-Hopf bifurcations and a saddle-node (off an invariant circle) result in Class 2 behaviour, while saddle-node on invariant circle bifurcations result in Class 1 behaviour. In some publications, all integrators are considered to be Class 1, while all resonators (even the saddle-node off invariant circle bifurcations) are considered to be Class 2, but this is in principle in contradiction with Hodgkin's original classification. As stated by [18], due to this confusion it is better to explicitly mention the bifurcation that is responsable for excitability.

In Hodgkin's scheme, Class 3 excitability is a special case, gathering neurons that do not bifurcate from rest state to self-sustained oscillations for a current ramp, and that are therefore not characterized by a nearby oscillation-onset bifurcation in the current. Hence, this class seems an apparent counter example of the statement that excitability is always related to a close bifurcation from rest state to self-sustained oscillation. However, such a bifurcation appears when other parameters of the neuron than the current are changed [18]. This class is not relevant for our dissertation.

2.4 Excitability in optics

Not only biological neurons exhibit excitability. It also occurs in other parts of our body, such as the muscle cell membrane in our heart [62, 63]. Excitability also appears in chemical reactions, in a driven mechanic pendulum or even in electronic systems (e.g., the Van der Pol oscillator we will discuss in Sec. 2.4.2). In this section, we investigate excitability in optics [5, 6, 9, 50, 64–72]. Apart from the development of optical SNNs, these different optical excitability mechanisms have interesting potential applications in photonics such as clock recovery, pulse reshaping, and optical delay lines [7, 73, 74]. However, it is not our purpose to discuss every single excitability phenomenon that appears in optics, and we will only mention the most relevant ones from the perspective of this PhD research.

Optical excitability is just as neural excitability related to a bifurcation from stationary to oscillatory behaviour, of which three generic bifurcations in the plane (i.e., a two dimensional system) exist. In optics, those three[1] types can be associated with different physical mechanisms. Therefore, in literature on optical excitability, these three types are used as another classification scheme of excitability: [7, 68, 75] (using the name conventions of [18]):

- Type 1 optical excitability: due to a saddle-node on an invariant circle bifurcation,
- Type 2 optical excitability: due to a Andronov-Hopf bifurcation,
- Type 3 optical excitability: due to a saddle homoclinic orbit bifurcation.

---

[1] In principle, a fourth mechanism to lose oscillatory behaviour, a LC Fold bifurcation could be listed as well [18], but in the following classification this is incorporated in type 2.

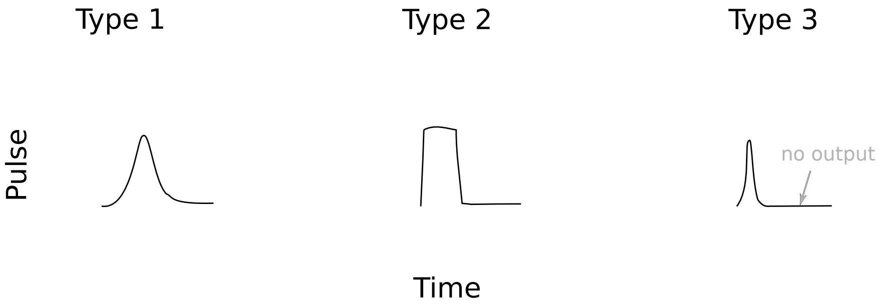

Figure 2.10: The three optical excitability types have a different characteristic pulse shape [75]. The smooth pulse shape of type 1 excitability is linked with the Adler model discussed in Sec. 2.4.1, while the block-shape of type 2 excitability is linked to slow-fast dynamics discussed in Sec. 2.4.2. Type 3 excitability will not be discussed in-depth in this dissertation, but an important feature here is that, in between the excitations, at the rest state there is no output light.

As we will explain later on in this section, type 1 appears in optically-injected lasers near the the locking threshold [64] or in lasers with optical feedback [67], while type 2 typically appears in slow-fast systems with Fitzhugh-Nagumo dynamics, often due to the interaction between thermal and free-carrier nonlinearities [9, 69], while type 3 appears in lasers with a saturable absorber near the transition to Q-switch-like pulsing [7, 75]. If we compare this with Hodgkin's classification discussed in Sec. 2.3.2, type 1 corresponds to Class 1 excitability, and type 2 is an example of class 2 excitability. However, confusingly, type 3 has nothing to do with class 3 excitability, but is an example of Class 1 excitability. The three underlying physical mechanisms related to these three excitability types bring along a characteristic pulse shape (Fig. 2.10). Importantly, in both type 1 and type 2 excitability, true to the original definition of excitability, the amplitude of the excursion is independent of the perturbation, because the slow manifold and the invariant circle determine the maximum of the pulse, respectively [75]. In contrast, type 3 excitations have a (slight) dependence on the initial perturbation strength. In [10, 59] it is claimed that the dependence on the input perturbation strength of type 3 excitability can be effectively lowered by a good choice of the lifetimes of both gain and saturable absorber lifetime, and the pump current settings, such that the model mimics more closely LIF-behaviour.

Additionally, the previous typology does not accurately describe all the different optical excitability cases. For instance, the excitability due to asymmetric intermodal coupled encountered in SRLs [2, 3, 49] is caused by a weakly broken $\mathbb{Z}_2$-symmetry close to a Bogdanov-Taken bifurcation. Even though the intermodal coupling can be seen as a version of optical feedback whithin this laser system, it shows 'resonator' behaviour, and is hence Class 2 excitable.

In this PhD research, we will study both type 1 (in microdisk lasers, chapter 5) and type 2 (in passive SOI microrings, chapter 4) excitability. We will provide additional context on both types by explaining the Adler model (Sec. 2.4.1) and by introducing slow-fast dynamics (Sec. 2.4.2), respectively.

2.4.1 Adler model

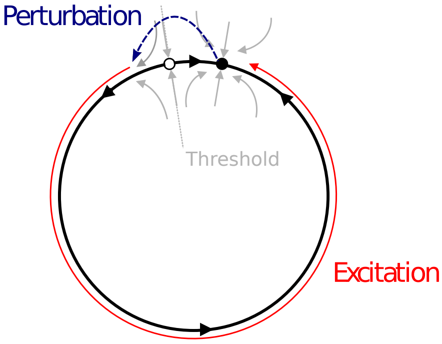

Figure 2.11: The Adler model describes how a sufficiently strong perturbation can let the system cross the stable manifold of the unstable FP (a saddle, hollow circle in the figure), and initiates as such a perturbation, as the system has the make a full round trip before it can return to the stable rest state (full circle).

An intuitive example of the appearence of a saddle-node on invariant circle bifurcation in optics, is the one of an optically injected laser. During injection locking, a laser with free-running lasing frequency ω_0 is injected with an external signal at ω_1. If the input power of the injected signal is sufficiently strong, the slave laser will phase-lock to the field of the injected signal. This can be described using the Adler model, developed to describe the coupling between two oscillators [76]:

$$\frac{d\theta}{dt} = \Delta\omega - B\sin(\theta). \tag{2.17}$$

Here, θ is the phase difference between master and slave laser, B represents the strength of the optically injected signal, while $\Delta\omega = \omega_1 - \omega_0$. This one-dimensional model corresponds to a rescaled version of Eq. (2.16), so the analysis in Sec. 2.3.1.3 can be applied to this system using $\alpha = \frac{\Delta\omega}{B}$. As the Adler-model is one-dimensional, only the phase of the oscillation is incorporated, and there is no explicit analogon of Eq. (2.15), governing the amplitude of the oscillation.

However, similar to Sec. 2.3.1.3, it is assumed that the system exhibits an invariant circle, to which the trajectory converges. Consequently, the system has a saddle-node on an invariant circle bifurcation.

Suppose that we are in a rest state close to the bifurcation at $\frac{\Delta\omega}{B} = 1$. External perturbations can kick the system state accross the stable manifold of the unstable FP (Fig. 2.11). To return to the stable FP, the laser has to make almost a full round trip, over the remaining part of the invariant circle, which will be visible as a pulse in the phase of the laser, often accompagnied by a related pulse in the amplitude. Hence, the Adler model clearly describes Class 1 excitability.

An optically injected laser is not the only system where the Adler model can be applied. For instance, this also happens in an optical torque wrench, in which the high spatio-temporal resolution of optical tweezers is combined with the angular control of tailored microscopic birefringent cylindric particles. These birefringent cylinders can be forced by a rotating linear polarization in the optical tweezer beam, resulting in a locking between the rotation of the particle and the rotation of the beam that can be mapped to Eq. (2.17). Again, we find excitability, which can be used to implement a conceptually new sensing technique capable of detecting single perturbation events, such as the detection of another particle that passes by at a certain distance [71, 77]. This technique is believed to have a high signal-to-noise ratio and a continuously adjustable sensitivity.

2.4.2 Slow-fast dynamics

In optics the large separation between the timescales of thermal effects and free-carrier effects result in slow-fast dynamics, such as self-pulsation and excitability. Already in 1994, this was observed in semiconductor resonator cavities [78]. In 2003, similar phenomena were demonstrated in semiconductor optical amplifiers and the behaviour could be explained using the simple Van der Pol-Fitzhugh-Nagumo model proposed to explain excitability in biological neurons [69]. This excitability also appears in PhC cavities, while the related self-pulsation is observed as well in silicon microrings and microdisks [79–81]. Applications of this physical effect are not only found in the field of excitability. Recently, the frequency dependence of the thermo-electrical self-pulsation to humidity changes was proposed as a sensing mechanism. Additionally, interactions with other nonlinearites with other timescales, such as the instantaneous Kerr-effect, might have similar consequences.

A two-dimensional slow-fast system can typically be rewritten in the fol-

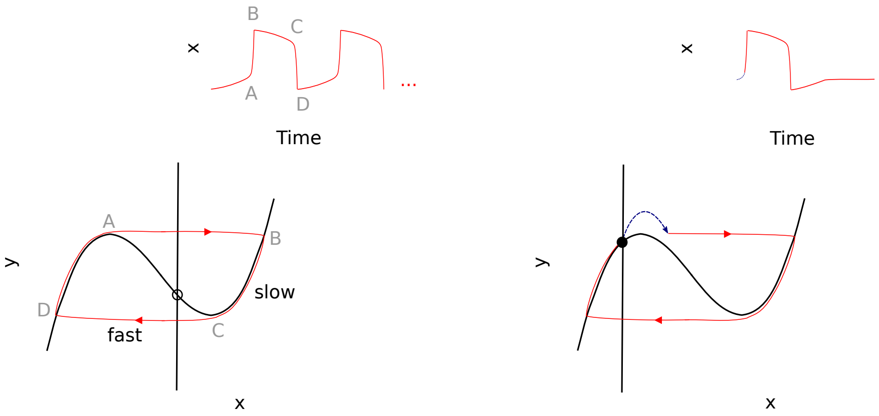

Figure 2.12: (left) If in a slow-fast system the slow (vertical) nullcline intersects the middle branch (from A to C) of the S-shaped fast nullcline, the intersection is an unstable FP and the system oscillates with a typical blockwaved pulse shape. (right) If the slow nullcline intersects the fast nullcline in one of the stable branches, near the oscillation onset, excitability appears.

lowing format:

$$\frac{dx}{dt} = f(x,y), \tag{2.18}$$

$$\frac{dy}{dt} = \epsilon g(x,y). \tag{2.19}$$

Here, the ratio of the timescales ϵ is very small, such that x is the fast variable, while y is the slow variable. Typically, the fast x-nullcline $f(x,y) = 0$, has a cubic or S-shaped form. A prototype of such a system is the forced Van der Pol model [61]. The forced Van der Pol equation describes a driven non-linear electronic circuit and can be written as [61]:

$$\frac{d^2x}{dt^2} + \mu(x^2-1)\frac{dx}{dt} + x = a, \tag{2.20}$$

We investigate the regime with $\mu >> 1$. After a coordinate transformation, this system can be converted to the first order ODE [61]:

$$\begin{aligned} \frac{dx}{dt} &= \mu\left(y - \left(\frac{x^3}{3} - x\right)\right), \\ \frac{dy}{dt} &= -\frac{1}{\mu}(x-a) \qquad (2.21) \end{aligned}$$

This could in principle be rewritten to the format of Eq. (2.19) by using a rescaled version of the time $t' = \mu t$, resulting in $\epsilon = \frac{1}{\mu^2}$, but we will continue our analysis with the current format of the equations. The x-nullcline $y = \frac{x^3}{3} - x$ is clearly cubic, while the y-nullcline $x = a$ is parallel to the y-axis (Fig. 2.12, left). This system has only one FP. If $|a| > 1$ this FP is stable, as it intersects the 'stable' branches of the fast x-nullcline. However, at $|a| = 1$, when the y-nullcline intersects the x-nulline at one of the two knees, the system has a supercritical Andronov-Hopf bifurcation. During such oscillations the system slides up along the left stable branch of the x-nullcline until it reaches the left knee, A. This requires $O(\mu)$ time. Next, it quickly jumps, nearly horizontally, to point B and then slowly slides down along the right stable branch of the x-nullcline. This requires $O(\frac{1}{\mu})$ time. When the system reaches the right knee, C, the system jumps back to the left branch and completes the oscillation by sliding down again. This type of oscillatory behaviour is called a relaxation oscillation.

If $|a| > 1$, but near the oscillation-threshold, the system is excitable, as small perturbations can kick the system accross the nearby knee of the system, after which a fast transfer to the other stable branch of the nullcline happens and the system consequently has to make a full round trip before it can return to the initial rest state again (Fig. 2.12, right).

A special feature is that the frequency of the sub-threshold oscillations is $O(1)$ (calculated from the Jacobian at the FP at the bifurcation onset), while the frequency of large-amplitude relaxation oscillation is on the order μ, because it takes $\frac{1}{\mu}$ units of time to pass up and down the stable branches of the fast nullcline. This is a difference in order of magnitude of $\epsilon^{\frac{1}{2}}$ Consequently, in a slow-fast system, the period of small subthreshold oscillations might not be on the same order of magnitude as the period of the self-sustained oscillations.

The forced Van der Pol oscillator can be seen as a restricted version of the Fitzhugh-Nagumo (FN) model of a neuron, which is a phenomenological $2D$ approximation of the $4D$ Hodgkin-Huxley neuron model obtained from experimental measurements on a squid axon [18]:

$$\begin{aligned} \frac{dV}{dt} &= V(a-V)(V-1) - w + I, \\ \frac{dw}{dt} &= bV - cw. \end{aligned} \tag{2.22}$$

In some publications an additional constant term in the $\frac{dw}{dt}$-equation is present, see, e.g., [19]. Although in the Hogdkin-Huxley model the slow nullcline is still linear, it does not need to be parallel to the w-axis anymore, allowing for the possibility to have more than one FP. For the parameter range where the nullclines have only one intersection and if b and c are both very small, relaxation oscillations will appear, and the results from the forced van der Pol oscillator still hold. However, if the w-nullcline is not parallel to the w-axis, depending on the settings of this model, the oscillation onset can now be a sub- or supercritical Andronov-Hopf bifurcation, and the bifurcation does not take place exactly at the knees of the V-nullcline, but at a position at the stable branch close to this knee [18, 19, 82–84]. If the nullclines do intersect in more than one FP, then additional phenomena can appear.

For some parameters of the FN-model, near the onset of oscillation, in a very narrow region of control parameters, special LC trajectories exist, which closely follow the unstable manifold near the unstable knee of the S-shaped nullcline. Due to their shape, this type of trajectories is called 'canards' (French for 'ducks'). In the excitable regime, canard trajectories are related to the existence of quasi-thresholds in resonator neurons [18].

2.5 Conclusion

In this chapter, we have given a general introduction on both NN theory and excitability, to put the research of the subsequent chapters in perspective.

In Sec. 2.1, we have explained how a NN consists of a collection of interconnected neurons. Furthermore, we have introduced the concept of a spiking neuron, which is the neuron type that most accurately mimics the behaviour of a biological neuron, compared to rate-coding based analog neurons or perceptrons. Later on in this work, we will emulate such a spiking neuron in optical hardware and we will study the potential to couple these neurons. Additionally, in Sec. 2.2, state-of-the-art research on the implementation of neural networks in (integrated) photonics has been discussed, of both analog and spiking NNs. These implementations can serve as a guideline for the implementation of all-optical SNNs in silicon photonics.

A spiking neuron can be described as an excitable nonlinear dynamical system. The concept of excitability was introduced in Sec. 2.3. If sufficiently strong perturbations can trigger one or more fixed-shape output pulses, a system is excitable. This dynamic behaviour often appears close to a regime with self-sustained oscillations.

Next, in Sec. 2.4, we discussed the appearance of excitability in optics. In general, three relevant categories for optical excitability can be distinguished: excitability due to slow-fast dynamics related to the interplay between thermal and electronic nonlinearities, excitability close to the onset of injection locking in optically-injected lasers and excitability close to the onset of Q-switching in a laser with a saturable absorber. In this work we will demonstrate the occurence of two such mechanisms in silicon photonics: slow-fast excitability in a microring (chapter 4) and excitability close to the onset of injection locking in a microdisk laser (chapter 5).

References

[1] Wolfgang Maass. *Networks of spiking neurons: The third generation of neural network models.* Neural Networks, 10(9):1659 – 1671, 1997.

[2] Stefano Beri, Lilia Mashall, Lendert Gelens, Guy Van der Sande, Gabor Mezosi, Marc Sorel, Jan Danckaert, and Guy Verschaffelt. *Excitability in optical systems close to Z2-symmetry.* Physics Letters A, 374(5):739–743, jan 2010.

[3] W. Coomans, L. Gelens, S. Beri, J. Danckaert, and G. Van der Sande. *Solitary and coupled semiconductor ring lasers as optical spiking neurons.* Physical Review E, 84(3):1–8, sep 2011.

[4] Sebastian Wieczorek, Bernd Krauskopf, and Daan Lenstra. *Multipulse excitability in a semiconductor laser with optical injection.* Physical review letters, 88(6):063901, 2002.

[5] D. Goulding, S. Hegarty, O. Rasskazov, S. Melnik, M. Hartnett, G. Greene, J. McInerney, D. Rachinskii, and G. Huyet. *Excitability in a Quantum Dot Semiconductor Laser with Optical Injection.* Physical Review Letters, 98(15):153903, April 2007.

[6] A. Hurtado, K. Schires, I. D. Henning, and M. J. Adams. *Investigation of vertical cavity surface emitting laser dynamics for neuromorphic photonic systems.* Applied Physics Letters, 100(10):103703, 2012.

[7] Sylvain Barbay, Robert Kuszelewicz, and Alejandro M Yacomotti. *Excitability in a semiconductor laser with saturable absorber.* Optics letters, 36(23):4476–8, dec 2011.

[8] Maia Brunstein, Alejandro M Yacomotti, Isabel Sagnes, Fabrice Raineri, Laurent Bigot, and Ariel Levenson. *Excitability and self-pulsing in a photonic crystal nanocavity.* Physical Review A, 85(3):031803, 2012.

[9] A. M. Yacomotti, P. Monnier, F. Raineri, B. Ben Bakir, C. Seassal, R. Raj, and J. A. Levenson. *Fast Thermo-Optical Excitability in a Two-Dimensional Photonic Crystal.* Phys. Rev. Lett., 97:143904, Oct 2006.

[10] Mitchell A Nahmias, Bhavin J Shastri, Alexander N Tait, and Paul R Prucnal. *A Leaky Integrate-and-Fire Laser Neuron for Ultrafast Cognitive Computing.* Selected Topics in Quantum Electronics, IEEE Journal of, 19:1800212, 2013.

[11] CM Bishop. *Pattern recognition and machine learning.* 2006.

[12] W. Maass, T. Natschläger, and H. Markram. *Real-time Computing Without Stable States: A New Framework for Neural Computation Based on Perturbations.* Neural Computation, 14(11):2531–2560, 2002.

[13] D. Verstraeten. *Reservoir Computing: Computation with Dynamical Systems.* Phd, Ghent University, 2009.

[14] Konstantinos Dalamagkidis. *Autonomous Vertical Autorotation for Unmanned Helicopters.* 2009.

[15] H Paugam-Moisy. *Computing with spiking neuron networks.* .), Handbook of Natural Computing., 2009.

[16] Wolfgang Maass. *Noisy Spiking Neurons with Temporal Coding have more Computational Power than Sigmoidal Neurons.* 1999.

[17] W. Maass and C.M. Bishop. *Pulsed neural networks.* MIT press, 2001.

[18] Eugene M. Izhikevich. *Dynamical Systems in Neuroscience: The Geometry of Excitability and Bursting (Computational Neuroscience).* The MIT Press, 1 edition, nov 2006.

[19] W. Gerstner and W. Kistler. *Spiking Neuron Models: Single Neurons, Populations, Plasticity.* Cambridge University Press, 2002.

[20] B. Hammer and J. J. Steil. *Perspectives on learning with recurrent neural networks.* In Proceedings of the 10th European Symposium on Artifical Neural Networks (ESANN), Bruges, Belgium, April 2002.

[21] H. Jaeger. *The "echo state" approach to analysing and training recurrent neural networks.* GMD Report 148, GMD - German National Research Institute for Computer Science, 2001.

[22] D.V. Prokhorov. *Training recurrent neurocontrollers for real-time applications.* Neural Networks, IEEE Transactions on, 18(4):1003–1015, 2007.

[23] G.V. Puskorius and L.A. Feldkamp. *Neurocontrol of nonlinear dynamical systems with Kalman filter trained recurrent networks.* Neural Networks, IEEE Transactions on, 5(2):279–297, 1994.

[24] Alexander Waibel and T Hanazawa. *Phoneme recognition using time-delay neural networks.* IEEE transactions on acoustics, Speech and Signal processing, 37(3):328–339, 1989.

[25] Benjamin Schrauwen, L Büsing, and RA Legenstein. *On Computational Power and the Order-Chaos Phase Transition in Reservoir Computing.* NIPS, pages 1–8, 2008.

[26] David Verstraeten, Benjamin Schrauwen, Michiel d'Haene, and Dirk Stroobandt. *An experimental unification of reservoir computing methods.* Neural Networks, 20(3):391–403, 2007.

[27] J.J. Steil. *Backpropagation-Decorrelation: Online recurrent learning with O (N) complexity.* In Neural Networks, 2004. Proceedings. 2004 IEEE International Joint Conference on, volume 2, pages 843–848. IEEE, 2004.

[28] C. Fernando and S. Sojakka. *Pattern recognition in a bucket.* Advances in Artificial Life, pages 588–597, 2003.

[29] Benjamin Schrauwen, Michiel D'Haene, David Verstraeten, and Jan Van Campenhout. *Compact hardware liquid state machines on FPGA for real-time speech recognition.* Neural Networks, page 2008, 2008.

[30] Johannes Schemmel and D Bruderle. *A wafer-scale neuromorphic hardware system for large-scale neural modeling.* Circuits and Systems (ISCAS), Proceedings of 2010 IEEE International Symposium on, pages 1947–1950, 2010.

[31] Paul Merolla, John Arthur, Filipp Akopyan, Nabil Imam, Rajit Manohar, and Dharmendra S Modha. *A digital neurosynaptic core using embedded crossbar memory with 45pJ per spike in 45nm.* In Custom Integrated Circuits Conference (CICC), 2011 IEEE, pages 1–4. IEEE, 2011.

[32] Swadesh Choudhary, Steven Sloan, and Sam Fok. *Silicon neurons that compute.* Artificial Neural Networks and Machine learning - ICANN 2012, 7552:121–128, 2012.

[33] Mantas Lukoševičius, Herbert Jaeger, and Benjamin Schrauwen. *Reservoir Computing Trends.* KI - Künstliche Intelligenz, accepted 2012.

[34] Ben Varkey Benjamin, Peiran Gao, Emmett McQuinn, Swadesh Choudhary, Anand R. Chandrasekaran, Jean-Marie Bussat, Rodrigo Alvarez-Icaza, John V. Arthur, Paul a. Merolla, and Kwabena Boahen. *Neurogrid: A Mixed-Analog-Digital Multichip System for Large-Scale Neural Simulations.* Proceedings of the IEEE, 102(5):699–716, May 2014.

[35] Kristof Vandoorne, Wouter Dierckx, Benjamin Schrauwen, David Verstraeten, Roel Baets, Peter Bienstman, and Jan Van Campenhout. *Toward optical signal processing using Photonic Reservoir Computing.* Opt. Express , 16(15):11182–11192, JUL 21 2008.

[36] Kristof Vandoorne, Joni Dambre, David Verstraeten, Benjamin Schrauwen, and Peter Bienstman. *Parallel reservoir computing using optical amplifiers.* IEEE transactions on neural networks, 22(9):1469–1481, 2011.

[37] Martin Fiers, Thomas Van Vaerenbergh, Francis Wyffels, David Verstraeten, Benjamin Schrauwen, Joni Dambre, and Peter Bienstman. *Nanophotonic reservoir computing with photonic crystal cavities to generate periodic patterns.* IEEE Transactions on Neural Networks and Learning Systems, 25(1):344–355, 2014.

[38] Julie Dethier, Paul Nuyujukian, and C Eliasmith. *A Brain-Machine Interface Operating with a Real-Time Spiking Neural Network Control Algorithm.* NIPS, pages 1–9, 2011.

[39] H Y Li, Y Qiao, and D Psaltis. *Optical network for real-time face recognition.* Applied optics, 32(26):5026–35, September 1993.

[40] a.S. Younger and E. Redd. *Design of an optical fixed-weight learning neural network.* Proceedings. 2005 IEEE International Joint Conference on Neural Networks, 2005., 2:610–615, 2005.

[41] Ying Chen, Qi-guang Zhu, and Zhi-quan Li. *A novel all-optical neural network based on coupled ring lasers.* Advances in Neural Networks-ISNN 2006, pages 1380–1385, 2006.

[42] Lennert Appeltant, Miguel Cornelles Soriano, Guy Van der Sande, Jan Danckaert, Serge Massar, Joni Dambre, Benjamin Schrauwen, Claudio R Mirasso, and Ingo Fischer. *Information processing using a single dynamical node as complex system.* Nature communications, 2:6, 2011.

[43] Y Paquot, F Duport, a Smerieri, J Dambre, B Schrauwen, M Haelterman, and S Massar. *Optoelectronic reservoir computing.* Scientific reports, 2:287, January 2012.

[44] M. Fiers. *Nanophotonic Reservoir Computing Using Photonic Crystal Cavities.* PhD thesis, Ghent University, 2012-2013.

[45] Kristof Vandoorne, Pauline Mechet, Thomas Van Vaerenbergh, Geert Morthier, David Verstraeten, Benjamin Schrauwen, Joni Dambre, and Peter Bienstman. *Experimental demonstration of reservoir computing on a silicon photonics chip.* Nature communications, tbp.

[46] Alejandro Yacomotti, Gabriel Mindlin, Massimo Giudici, Salvador Balle, Stephane Barland, and Jorge Tredicce. *Coupled optical excitable cells.* Physical Review E, 66(3):036227, September 2002.

[47] B. Kelleher, C. Bonatto, P. Skoda, S. P. Hegarty, and G. Huyet. *Excitation regeneration in delay-coupled oscillators.* Physical Review E, 81(3):036204, March 2010.

[48] Olivier Vaudel, P Nicolas, Pascal Besnard, Cnrs Foton-enssat, and De Kerampont Bp. *Synchronization on excitable pulses in optically injected semiconductor lasers.* 6997:1–9, 2008.

[49] L Gelens, S Beri, and J Danckaert. *Phase-space approach to directional switching in semiconductor ring lasers.* Applied Physics, (September 2008):1–9, 2009.

[50] Alexander N Tait, Mitchell A Nahmias, Yue Tian, Bhavin J Shastri, and Paul R Prucnal. *Nanophotonic Information Physics.* Nano-Optics and Nanophotonics. Springer Berlin Heidelberg, Berlin, Heidelberg, 2014.

[51] David Rosenbluth, Konstantin Kravtsov, Mable P Fok, and Paul R Prucnal. *A high performance photonic pulse processing device.* Optics express, 17(25):22767–72, December 2009.

[52] Konstantin Kravtsov, Mable P Fok, David Rosenbluth, and Paul R Prucnal. *Ultrafast all-optical implementation of a leaky integrate-and-fire neuron.* Optics Express, 19(3):211–221, 2011.

[53] Mable P Fok, David Rosenbluth, Konstantin Kravtsov, and Paul R Prucnal. *Lightwave Neuromorphic Signal Processing.* IEEE Signal Processing Magazine, (November):1–3, 2010.

[54] Mable P Fok, Hannah Deming, Mitchell Nahmias, Nicole Rafidi, David Rosenbluth, Alexander Tait, Yue Tian, and Paul R Prucnal. *Signal feature recognition based on lightwave neuromorphic signal processing.* Optics letters, 36(1):19–21, January 2011.

[55] Mable P Fok, Yue Tian, David Rosenbluth, and Paul R Prucnal. *Asynchronous spiking photonic neuron for lightwave neuromorphic signal processing.* 37(16):3309–3311, 2012.

[56] Eugene M Izhikevich. *Neural Excitability , Spiking and Bursting.* International Journal of bifurcation and chaos, 10(6):1171–1266, 2000.

[57] Alexander N Tait, Student Member, Bhavin J Shastri, Mable P Fok, Mitchell A Nahmias, and Paul R Prucnal. *The DREAM : An Integrated Photonic Thresholder.* 31(8):1263–1272, 2013.

[58] Bhavin J Shastri, Mitchell A Nahmias, Alexander N Tait, Yue Tian, Mable P Fok, Matthew P Chang, Ben Wu, and Paul R Prucnal. *Exploring Excitability in Graphene for Spike Processing Networks.* pages 83–84, 2013.

[59] Mitchell A Nahmias, Alexander N Tait, Bhavin J Shastri, and Paul R Prucnal. *An Evanescent Hybrid Silicon Laser Neuron.* IEEE journal of selected topics in quantum electronics, 4:93–94, 2013.

[60] Mitchell A Nahmias, Bhavin J Shastri, Alexander N Tait, and Paul R Prucnal. *A Leaky Integrate-and-Fire Laser Neuron for Ultrafast Cognitive Computing.* 2013.

[61] Steven H. Strogatz. *Nonlinear Dynamics And Chaos: With Applications To Physics, Biology, Chemistry, And Engineering (Studies in Nonlinearity).* Studies in nonlinearity. Westview Press, 1 edition, jan 2001.

[62] JD Murray. *Mathematical Biology I: An Introduction. 2002.* Springer, 2002.

[63] Werner Coomans. *Nonlinear Dynamics in Semiconductor Ring Lasers - Towards an integrated optical neuron.* PhD thesis, Vrije Universiteit Brussel, 2013.

[64] Sebastian Wieczorek, Bernd Krauskopf, and Daan Lenstra. *Full length article A unifying view of bifurcations in a semiconductor laser subject to optical injection.* 172(December):279–295, 1999.

[65] Johan L A Dubbeldam and Bernd Krauskopf. *Self-pulsations of lasers with saturable absorber : dynamics and bifurcations.* Optics communications, (January):325–338, 1999.

[66] R. Lang and K. Kobayashi. *External optical feedback effects on semiconductor injection laser properties.* IEEE Journal of Quantum Electronics, 16(3):347–355, March 1980.

[67] M. Giudici, C. Green, G. Giacomelli, U. Nespolo, and J. R. Tredicce. *Andronov bifurcation and excitability in semiconductor lasers with optical feedback.* Physical Review E, 55(6):6414–6418, June 1997.

[68] F Plaza and MG Velarde. *Excitability following an avalanche-collapse process.* EPL (Europhysics Letters), 85, 1997.

[69] Stéphane Barland, Oreste Piro, Massimo Giudici, Jorge Tredicce, and Salvador Balle. *Experimental evidence of van der Pol-Fitzhugh-Nagumo dynamics in semiconductor optical amplifiers.* Physical Review E, 68(3):036209, September 2003.

[70] Maia Brunstein, Alejandro M. Yacomotti, Isabel Sagnes, Fabrice Raineri, Laurent Bigot, and Ariel Levenson. *Excitability and self-pulsing in a photonic crystal nanocavity.* Phys. Rev. A, 85:031803, Mar 2012.

[71] Francesco Pedaci, Zhuangxiong Huang, Maarten van Oene, Stephane Barland, and Nynke H. Dekker. *Excitable particles in an optical torque wrench.* Nature Physics, 7(3):259–264, December 2010.

[72] B. Garbin, D. Goulding, S.P. Hegarty, G. Huyet, B. Kelleher, and S. Barland. *Incoherent optical triggering of excitable pulses in an injection-locked semiconductor laser.* optics letters, (January):(tbp), 2014.

[73] F. Pedaci, S. Barland, E. Caboche, P. Genevet, M. Giudici, J. R. Tredicce, T. Ackemann, a. J. Scroggie, W. J. Firth, G.-L. Oppo, G. Tissoni, and R. JaÌĹger. *All-optical delay line using semiconductor cavity solitons.* Applied Physics Letters, 92(1):011101, 2008.

[74] Maia Brunstein. *Nonlinear Dynamics in III-V Semiconductor Photonic Crystal Nano-cavities.* PhD thesis, LPN,CNRS, 2012.

[75] J L Dubbeldam, B Krauskopf, and D Lenstra. *Excitability and coherence resonance in lasers with saturable absorber.* Physical review. E, Statistical physics, plasmas, fluids, and related interdisciplinary topics, 60(6 Pt A):6580–8, December 1999.

[76] Robert Adler. *Locking Phenomena in Oscillators.* PROC. IRE, (10):351–357, 1946.

[77] Francesco Pedaci, Zhuangxiong Huang, Maarten van Oene, and Nynke H Dekker. *Calibration of the optical torque wrench.* Optics express, 20(4):3787–802, February 2012.

[78] AV Grigor'yants and IN Dyuzhikov. *Formation of a neuron-like pulsed response in a semiconductor resonator cavity with competing optical nonlinearities.* Quantum Electronics, 469:469–471, 1994.

[79] G Priem, P Dumon, W Bogaerts, D Van Thourhout, G Morthier, and R Baets. *Optical bistability and pulsating behaviour in Silicon-On-Insulator ring resonator structures.* Opt. Express , 13(23):9623–8, nov 2005.

[80] Thomas J Johnson, Matthew Borselli, and Oskar Painter. *Self-induced optical modulation of the transmission through a high-Q silicon microdisk resonator.* Opt. Express , 14(2):817–31, jan 2006.

[81] Wolfram H P Pernice, Carsten Schuck, Mo Li, and Hong X Tang. *Carrier and thermal dynamics of silicon photonic resonators at cryogenic temperatures.* Opt. Express , 19(4):3290–6, feb 2011.

[82] SM Baer and T Erneux. *Singular Hopf bifurcation to relaxation oscillations.* SIAM Journal on Applied Mathematics, 46(5):721–739, 1986.

[83] SM Baer and T Erneux. *Singular Hopf bifurcation to relaxation oscillations. II.* SIAM Journal on Applied Mathematics, 52(6):1651–1664, 1992.

[84] Peter Langfield, Bernd Krauskopf, and Hinke M Osinga. *Solving Winfree ' s puzzle : the isochrons in the FitzHugh-Nagumo model.* pages 1–25, tbp.

3

Phenomenological modeling of photonic integrated circuits

The final aim of this PhD is to design photonic integrated circuits that behave as optical Spiking Neural Networks (SNNs). For this purpose, we need to be able to model the dynamics in such a photonic system on a circuit level. In our research we often need to interchange component models to verify their influence on the circuit dynamics. Additionally, in future work, we will need to simulate very large optical SNNs. State-of-the-art software tools do not exhibit the required flexibility and scalability. For this reason, we have devoted part of our research time to the development of Caphe, an in-house nonlinear circuit simulator. In this chapter, we will discuss the underlying theoretical framework of this simulator.

Caphe is based on the definition of a node, the basic building block of the framework, representing optical components or circuits. Nodes can contain subnodes and are coupled to other nodes using ports. Every node can have an arbitrary number of ports. It can as well have its own set of state variables, described by arbitrary Ordinary Differential Equations (ODEs). In addition, each node has access to previous states or inputs.

Due to this flexibility in the definition of circuits and components, Caphe is currently applied in very different research contexts, such as the frequency-domain analysis of optical filters [1], the time-domain analysis of very large nanophotonic reservoirs [2] and finally, as discussed in the subsequent chapters, the study of the dynamics in small circuits of microrings and microdisks.

We start this chapter by comparing the simulator requirements in the context of our research to the capabilities of existing simulation tools (Sec. 3.1). We explain the need for a new software tool, and the choice of programming language in Sec. 3.2. In Sec. 3.3, we discuss the signal representation in our framework: we work with travelling-waves, using a slowly-varying envelope approximation. After that, in Sec. 3.4, we summarize the theory on scatter-matrix representation, before we propose the definition of a node, i.e., an extension of the scatter-matrix model, in Sec. 3.5. Based on this node definition, we develop the framework in Sec. 3.6-3.8. Subsequently, as the simulations in the following chapters are based on Coupled Mode Theory (CMT) models of components, we introduce this in Sec. 3.9, and make our framework in Sec. 3.10 compatible to this type of models. Next, we apply our framework to an example frequency-domain simulation in Sec. 3.11 (examples of time-domain simulations are ubiquitous in subsequent chapters). Finally, challenges for future work are discussed in Sec. 3.12.

The work discussed in this chapter has been carried out in close collaboration with dr. ir. M. Fiers, who applied the framework to perform large nonlinear circuit simulations [2, 3]. We have published the main results in [4]. Additionally, Chapter 4 from his PhD-dissertation [5] has served as an important source of inspiration during the writing of the current chapter.

3.1 Towards phenomenological models

When designing a photonic integrated circuit, it is important to validate whether the circuit processes the input signals as it should. The behaviour of optical signals is described by Maxwell's laws, and ideally, one would like to have simple analytic solutions to these equations to model the circuit behaviour. However, while such analytic solutions can be derived for some simple systems, in general such a solution is not available. When modeling large and complex circuits, even approximate analytic solutions are not sufficient, as some underlying assumptions might be violated in experimental conditions. One then has to resort to simulation algorithms. These algorithms can be classified by the level of spatial detail they include during the simulation. As a rule of thumb one can assume that an increase in spatial accuracy implies an increase in computation time and memory requirement of the simulation. Therefore, a full three-dimensional field profile as a function of time can only be calculated for relatively small circuits of a limited set of components. Due to this trade-off, when investigating circuits of increasing size and complexity, the dimension-

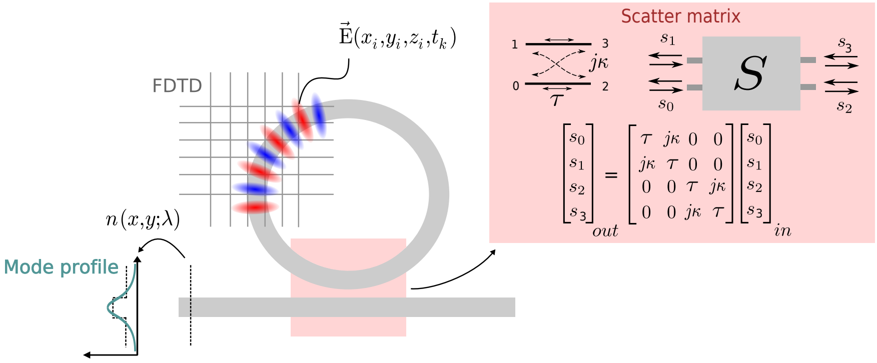
FDTD
$\vec{E}(x_i,y_i,z_i,t_k)$
$n(x,y;\lambda)$
Mode profile
Scatter matrix
1
3
0
2
$j\kappa$
τ
s_1
s_0
s_3
s_2
S
$\begin{bmatrix} s_0 \\ s_1 \\ s_2 \\ s_3 \end{bmatrix}_{out} = \begin{bmatrix} \tau & j\kappa & 0 & 0 \\ j\kappa & \tau & 0 & 0 \\ 0 & 0 & \tau & j\kappa \\ 0 & 0 & j\kappa & \tau \end{bmatrix} \begin{bmatrix} s_0 \\ s_1 \\ s_2 \\ s_3 \end{bmatrix}_{in}$

Figure 3.1: A microring can be investigated using different simulation algorithms. A full vectorial FDTD, by discretizing the Maxwell's equations both in space and time will return a detailed distribution of the electromagnetic fields. However, to reduce simulation time, one can also use an eigenmode solver to calculate the mode profile of the waveguides. One can then calculate effective refractive indices based on this mode profile, and use this information in black box models that do not incorporate any spatial information of the field distribution. For instance, the ring can be considered to be a combination of a directional coupler and a waveguide, which can be modelled using a scatter-matrix.

ality of the simulation needs to be reduced. In practical design situations, one will use a bottom-up approach: individual components will be simulated using algorithms with a high level of spatial details, and this information will be used in higher-level simulation tools that incorporate less spatial details in the models.

In this section we illustrate the relevance of different levels of spatial accuracy using the example of a microring (Fig. 3.1). The microring in this figure consists of a waveguide loop, close to a straight waveguide. Light can couple from the access waveguide into the ring and can subsequently make roundtrips in this loop. For some wavelengths, light in the loop will interfere constructively, resulting in resonance behaviour. We will reuse this example later on in this chapter, and study its nonlinear dynamic behaviour in detail in chapter 4.

For such a microring it is still feasible to calculate the full vectorial field profile of the whole structure as a function of time, by discretizing Maxwell's equations on a discrete grid both in space and time, using, e.g., Finite Element Methods (FEM) or Finite Difference Time Domain (FDTD). The dimensionality of this type of simulation can be $3D$, $2D$ (e.g., one simulates in the plane of the ring) or $1D$ (e.g., using cilinder symmetry in the plane of the ring). Possible outcomes of this type of simulation can be the resonance wavelengths of the ring and the quality factors of this device. As there are almost no restrictions on the material properties and geometry, the method is very generally applicable. However, due to its spatial accuracy it is computationally very demanding. By decreasing the discretization step size, not only the accuracy increases, but also the simulation time. Unfortunately, when performing a $3D$ simulation of a resonant structure such as the ring, in which light can make many roundtrips, a single simulation can take hours, consuming a large amount of computer memory. Hence, this technique is not appropriate to do simulations of very large circuits, containing > 100 components. The open-source software package MEEP offers an implementation example of an FDTD simulation method [6, 7].

Another way to analyse this circuit, is by interpreting it as a collection of waveguides. Indeed, the mode profile and the corresponding effective index of the guided modes in the waveguide cross-section (Fig. 3.1, bottom left) incorporates crucial information about the circuit performance. This numerical method analyses the field in the frequency-domain. In this method we only analyse a cross-section of the waveguide, making the calculation one or two dimensional. Consequently, a calculation over a reasonable frequency range only takes a few minutes. Two eigenmode solvers are CAMFR [8, 9] and FimmWave [10].

When we consider the optical component as a black box, we are not interested in the spatial field distribution of the component. A passive and linear element, such as the directional coupler of Fig. 3.1, is then described by a single scatter-matrix **S**. Later in this chapter, we will see how we can link the scatter-matrix of the directional coupler with the scatter-matrix of the ring waveguide to build the scatter-matrix of the whole microring circuit. Additionally, using, e.g., dynamic component models based on temporal CMT, the description of this building block can be further extended with nonlinear or non-passive behaviour. These extensions pave the way for simulations of nonlinear circuits, such as a nanophotonic reservoir (see the Semiconductor Optical Amplifier (SOA) and Photonic Crystal (PhC) networks in [2, 5] and [11–13], respectively) or an optical spiking neural network (this work). The scatter-matrix description and CMT are approximative in nature, but extremely fast, as they enormously reduce the dimensionality of the system by eliminating all spatial dependencies in the physical problem. In fact, considering the optical component as a black box by ignoring the spatial details of the field profiles can be seen as the core of the methodology we present in this chapter.

Other techniques, such as the Time-Domain Travelling Wave (TDTW) [14] or the Split-Step Method (SSM) [14], can be situated on the scale of spatial detail and computational effort in between the previous black box approaches and FDTD.

In the current software landscape, tools are available that use the aforementioned numeric algorithms to design complex optical circuits consisting of many components. For instance, ASPIC [15] calculates the steady-state response of optical circuits, while VPI [16] retrieves the time-domain behaviour. The TDTW optical model is applied in PicWAVE [17], and RSoft Optsim is based on SSM [18]. Some tools, e.g., OptiSPICE [19, 20], use Modified Nodal Analysis (MNA), a technique often used in the simulation of electronic circuits, therefore allowing for co-simulation of electronical and optical circuits.

In this chapter, we introduce Caphe [21], a framework that simulates networks which consist of 'nodes'. Such a node is a very generally-defined property container that represents an optical circuit or a component. It is important to note that the concept of node in our framework has nothing to do with the node definition in MNA. Our node networks can be analysed using both time or frequency-domain simulations. Each component can be naturally represented in the node format. For instance, in contrast to the MNA methods used in SPICE simulators, state variables such as the optical field, the temperature and the carrier density, do not need to be converted into a voltage and current representation. By characterizing each component using only a small set of variables, the simulation speed is considerably faster compared to methods with a higher spatial accuracy such as FDTD, TDTW and SSM.

In addition, we derive an algorithm to eliminate components with trivial time-domain behaviour from the network, reducing the number of components that need to be explicitly simulated during a time-domain simulation. The calculations are implemented in a C++ library to improve the speed of the tool, while users have access to an easy scriptable Python front-end, with allows for easy interfacing to a large collection of freely-available scientific libraries.

3.2 Implementation details

3.2.1 The need for a new software package

Given the long list of available software packages in the previous section, one might wonder whether we could not use a commercial solution to perform our simulations. We found two important limitations when using commercial packages such as VPI Photonics [16] or OptiSpice [18]. First, we would have been limited to the available building blocks. However, to investigate the behaviour of optical spiking neural networks, we regularly needed to use component models that were not yet available in the libraries of the software package. Second, the Graphical User Interface (GUI) of those programs makes it difficult to create large circuits. This is a big limitation to the scalability of the simulations, and would obstruct the research of the dynamics in large optical SNNs. Therefore, we have opted for a scriptable environment for our software package.

During this PhD research, we noticed that commercial software developers also start to make the jump towards circuit-level simulators combining both frequency and time-domain, and with scalability due to a scripting interface. For instance, VPI has also provided an interface to Python, while Lumerical has launched a new commercial software package for this purpose, called Interconnect [22], which is able to interface with Matlab. Lumerical uses a fundamentally different approach to our framework, based on digital filters with multiple timescales, but no satisfying answer is yet given about their possibility to handle nonlinear components. VPI has independently developed a similar hybrid frequency-time domain approach as the one presented in this chapter [23–25]. Given the similar rationale of those programs to ours, the need for this type of software tool is clearly illustrated. Which tool will eventually be used by the research community within five or ten years will depend largely on the ease-of-use of the tool and the interfacing possibilities with other simulation tools. Hence, the amount of manpower to create user-friendly interfaces between layouting tools, FDTD simulations and phenomenological models, will be more decisive for the succes of a specific solution than the implementation and algorithmic details of these high-level simulation tools. Given recent developments in optical interconnects and the need for proper design tools for this type of application, the possibility to interface between photonic and electonic simulation tools is also an important asset.

3.2.2 Choice of programming language

We have chosen to implement the core of our algorithm in C++, while we have provided a Python scripting interface for the end user. Just like Matlab, Python is an interpreted language, allowing for a more intuitive, easily-readable style of programming. Being open source it is heavily used in academic research, and one can consequently fall back on well-established scientific libraries. Unfortunately, as the language is an interpreted language, each line of code poses an overhead in calculation time. A good Python programmer will, if possible, try to combine for-loops into vector or matrix operations as this considerably improves the speed of the program. Unfortunately, when different optical components need to be combined, the component-specific computations can not be combined into one single vector operation without loosing generality. For this reason, we have implemented the actual calculations in C++, as this tremendously reduces up the computation time. The end-user does not directly have to interact with this C++ core. He or she can write the ODEs of his component in a Pythonic format. Behind the scenes these equations are converted on the fly to a piece of compiled C++ code in a format usable by the Caphe core.

An additional advantage of the usage of Python is that it paves the way for the integration of Caphe with IPKISS [26–29], a software package developed in our group for designing photonic integrated circuits, which can already interact with other simulation tools such as CAMFR or MEEP.

3.3 Signal representation

In this section we explain why we represent electromagnetic signals using travelling-waves (Sec. 3.3.1) in the envelope approximation (Sec. 3.3.2).

3.3.1 Travelling waves

The framework we will develop is a high level description of the Maxwell's equations for travelling-wave-based systems. In electronics, such a high-level description is often based on applying Kirchhoff's current and voltage laws to a lumped-element representation of the circuit. The underlying assumption of the voltage law (the sum of voltage differences in a closed loop is zero) is that the electric field $\vec{\mathbf{E}}$ can in this case be considered to be conservative due to the absence of significant changes in the magnetic field $\vec{\mathbf{H}}$. The underlying assumption of the current law (the sum of all currents entering a junction is zero) is that current only flows through conductors, and that it does this without charge accumulation in the lumped element version of conductors. These laws are implemented very efficiently in the famous electronic circuit simulator SPICE [30]. Nonlinear electronic circuits can be implemented using the Modified Nodal Analysis (MNA) [31]. For low-frequency signals in electronic circuits the representation using currents I_i and voltages V_i does not violate the underlying assumptions of Kirchhoff's law in a significant way. However, for high-frequency simulations the wave nature of electromagnetic fields appears and, for instance, due to the large and fast variations in time of $\vec{\mathbf{H}}$, $\vec{\mathbf{E}}$ is not conservative anymore. Consequently, given the high-frequency nature of light in our circuits, the propagation of energy in waveguide modes is better represented using forward and backward travelling-waves [19]. More specifically, the total electric field $\vec{\mathbf{E}}(x,y,z,t)$ in a lossless waveguide corresponding to a monochromatic signal with frequency $\omega = \frac{2\pi c}{\lambda}$ (wavelength λ), propagating in an optical mode i with transversal mode profile $\vec{\mathbf{S}}_{i,\alpha}$ is then a sum of a forward (f) and a backward (b) contribution (an analog expression is valid for the magnetic field $\vec{\mathbf{H}}$):

$$\vec{\mathbf{E}}_{i,f}(x,y,z,t) = \Re\left\{E_f \vec{\mathbf{S}_{i,f}}(x,y)e^{j(\omega t - \beta_i z)}\right\}, \tag{3.1}$$

$$\vec{\mathbf{E}}_{i,b}(x,y,z,t) = \Re\left\{E_b \vec{\mathbf{S}_{i,b}}(x,y)e^{j(\omega t + \beta_i z)}\right\}. \tag{3.2}$$

The propagation constant $\beta_i = n_{eff,i}\frac{2\pi c}{\lambda}$, determining the effective wavelength $\frac{\lambda}{n_{eff,i}}$ in the z-direction, depends on the effective refractive index $n_{eff,i}$ for the optical eigenmode. We use a phasor notation for the complex amplitudes $E_{i,\alpha} = |E_{i,\alpha}|e^{\phi_{i,\alpha}}$ ($\alpha \in \{f,b\}$), determining the amplitude and phase of the light, and normalize $\mathbf{S}_{i,\alpha}$ in such a way that $|E_{i,\alpha}|^2$ represents the optical power passing through the cross-section of the waveguide. Starting from the symmetry properties of the Maxwell's equations with respect to the propagation direction, it can be proven that in the plane of the cross-section $\vec{\mathbf{S}}_{i,f;T} = \vec{\mathbf{S}}_{i,b;T}$, while in the direction of the waveguide $S_{i,f;z} = -S_{i,b;z}$.

Both the transversal mode profile $\vec{\mathbf{S}}_{i,\alpha}$ and the propagation constant β_i can be determined using other software tools. In the phenomenological framework presented in this chapter, we are only interested in the power and phase of light (represented by $E_{i,\alpha}$) at some well-chosen waveguide cross-sections in the circuit (see Sec. 3.4).

As explained in [19], in principle, a mathematical mapping of the travelling-wave representation onto the voltage and current based equations in the MNA is possible, such that every optical component is represented by an equivalent 'electronic' circuit. However, this mapping is non-trivial for the end-user. Hence, in this chapter we propose a framework in which the equations are intrinsically consistent with the travelling-wave nature of light, resulting in some important simplifications of the system description and improvements in simulation speed. The drawback is that it becomes more difficult to use the optimized algorithms incorporated in SPICE to do efficient and fast opto-electronic co-simulations. As in future-generation photonic integrated circuits a close interaction between electronic and photonic systems will be required, in future work this issue will need to be addressed. However, for the tasks in this PhD research, these opto-electronic simulations are not yet required.

3.3.2 Envelope approximation

From now on, we represent an optical signal at a given waveguide cross-section travelling in a certain direction as a time-varying complex amplitude $s(t)$. The actual real-valued optical field at this cross-section is then the real part of the product of the very fast carrier (with frequency ω), modulated by a complex-valued envelope $s(t)$:

$$\mathrm{E}(t) = \Re\left\{s(t)e^{j\omega t}\right\}. \tag{3.3}$$

The representation of the signal by the *envelope* $s(t)$ instead of $\mathrm{E}(t)$ is numerically advantageous. Indeed, $s(t)$ varies much slower than $\mathrm{E}(t)$, such that a much larger integration step can be used, while preserving the same accuracy. Of course, an increase of the bandwidth of the input signal $s(t)$ still implies that more samples per time unit are needed for an accurate simulation of the system.

This choice to use the envelope of the signals is based on the slowly-varying envelope approximation, i.e., the assumption that the envelope of a travelling-wave pulse with narrow bandwidth varies slowly in both time and space compared to the period and wavelength of the carrier. In high-speed electronics, this approach is sometimes entitled the circuit envelope simulation [19, 32, 33], and extensions of it, based on underlying SPICE models, such as the Envelope Transient Harmonic Balance technique [34] can even model the transfer of energy to higher order terms in ω due to nonlinearities. However, as such higher order terms of signals at the telecom wavelength are absorbed in the Silicon-On-Insulator (SOI) platform, we did not incorporate an equivalent to the latter technique in our approach.

In principle, if the waveguide transfers multi-wavelength signals in a mode i, in direction α, on K clearly separated frequency bands, one could define an envelope $E^k_{i,\alpha}(t)$ with carrier frequency ω_k for each of these K frequency bands. Additionally, each carrier frequency has its own transversal mode profile $\vec{\mathbf{S}}^{\omega_k}_{i,\alpha}$ and propagation constant $\beta_{i,k}$, such that the optical field becomes:

$$\vec{\mathbf{E}}_{i,\alpha}(x,y,z,t) = \Re\left\{\sum_{k=0}^{K-1} E^k_{i,\alpha}(t)\vec{\mathbf{S}}^{\omega_k}_{i,\alpha}(x,y)e^{j(\omega_k t \mp \beta_{i,k} z)}\right\}, \tag{3.4}$$

However, in this dissertation we will only use signals with a single carrier frequency. Although there are no mathematical limitations that inhibit the extension of our framework to multiple carrier frequencies, the implementation in software will be rather tedious and is considered to be future work. The implementation of this extension would allow for simulation of (experimentally often encountered) pump-probe based circuits, needed to perform, e.g., all-optical wavelength conversion or switching [35–38]. The extension to multi carrier wavelength simulations would also allow for simulations of four-wave mixing process [14, 39].

3.4 Scatter matrices

In this section we consider an optical structure to be a black box that exchanges energy with the outside world through N optical ports (Fig. 3.2). These ports can correspond to an optical waveguide mode, or even a free space electromagnetic beam. Each port carries only one mode, but different ports are allowed to physically coincide to describe waveguides with multiple modes (e.g., in a waveguide with both Transverse-electric (TE) and Transverse-magnetic (TM) polarized light two ports might coincide with one waveguide cross-section). Additionally, we will often choose port positions that simplify the description of the

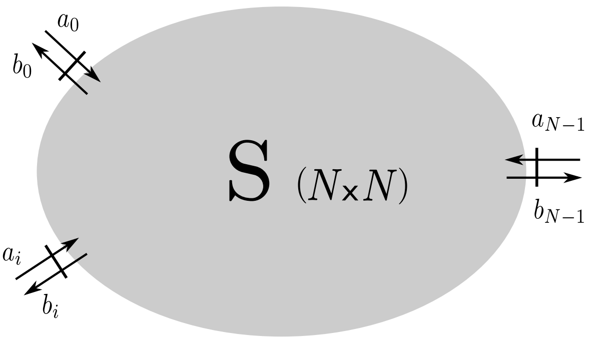

Figure 3.2: In scatter-matrix theory a linear N-port optical component is treated as a black box. Its input-output relationship is fully determined by the scatter-matrix **S**.

component. For this purpose, if the position of a port corresponding to a cross-section of a waveguide is moved over a distance ΔL, the scatter-matrix can be adapted by incorporating a compensating factor $e^{j\beta\Delta L}$ on the appropriate row and column.

We define a_i and b_i as the complex amplitude of the ingoing and outgoing normalized electromagnetic mode at port i, respectively. If no sources are present and if the component only contains materials with a linear and instantaneous response to the applied fields, the relationship between the outputs $\mathbf{b} = (b_0, ..., b_{N-1})$ and the inputs $\mathbf{a} = (a_0, ..., a_{N-1})$ can be described in a simple matrix equation:

$$\mathbf{b} = \mathbf{S} \cdot \mathbf{a} \tag{3.5}$$

Here, the $N \times N$ dimensional matrix **S** is the scatter-matrix of the component, sometimes also called scattering matrix. By normalization $||\mathbf{a}||^2$ and $||\mathbf{b}||^2$ represent the input power and output power, respectively. Furthermore, material properties of the structure, such as being passive or reciprocal induce constraints on this matrix.

3.4.1 Passive component

If a component does not generate energy it is called passive. This implies that $||\mathbf{b}||^2 \leq ||\mathbf{a}||^2$, for all possible values of **a**. Given $||\mathbf{v}||^2 = \mathbf{v}^H\mathbf{v}$ (with $\mathbf{v}^H$ being the Hermitian transpose of **v**), this is equivalent to:

$$\forall \mathbf{a}: \; \mathbf{a}^H \left(\mathbf{I} - \mathbf{S}^H\mathbf{S}\right) \mathbf{a} \geq \mathbf{0}, \tag{3.6}$$

Consequently, the matrix $\left(\mathbf{I} - \mathbf{S}^H\mathbf{S}\right)$ is semi-positive definite.

In a lossless component, no power is absorbed and the equality holds. In this case, this implies that **S** is an unitary matrix, i.e.,

$$\mathbf{S}^H\mathbf{S} = \mathbf{1}. \tag{3.7}$$

However, we derived Eq. (3.5) for a ciruit consisting of instantaneously reacting materials. The conditions for being passive are more complicated when noninstantaneous materials are involved. Apart from the condition that the component should absorb more energy than it generates, causality should be respected, such that the release of a certain amount of energy only happens *after* a corresponding amount of energy is first absorbed by the component [40].

3.4.2 Reciprocal component

A component is reciprocal if only it consists of materials with symmetrical constitutive parameters, i.e., with both permittivity $\epsilon=\epsilon^T$ and permeability $\mu=\mu^T$, as Lorenz' reciprocity theorem will hold. Almost all materials are reciprocal, except for magnetic materials in the presence of a magnetic field. Starting from Maxwell's equations, it can be proven that for a reciprocal component, **S** is a symmetrical matrix,

$$\mathbf{S} = \mathbf{S}^T. \tag{3.8}$$

This result has important consequences, as it implies that the transmission through the component between two different ports does not depend on the propagation direction. Counterintuitively, no symmetry of the actual geometry of the component is required to obtain a symmetric **S**; the fact that a component is made out of reciprocal materials is sufficient. As a consequence, a non-magnetic, linear and time-invariant component can never be used as an optical isolator [41], i.e., a component that transmits light in one direction but blocks it in the other direction.

3.4.3 Example scatter matrices

For future reference, we conclude the current section with the inclusion of the scatter matrices of two components that are very important to the silicon photonics platform. First, we discuss the scatter-matrix of an optical waveguide. This device is used to guide light between different places on the chip and can be considered as the main information carrier in a photonic integrated circuit. Second, we discuss a directional coupler, a component that can be used to transfer light from one waveguide to another. Both components can be used to form a microring, the component studied in the next chapter.

3.4.3.1 Scatter matrix of a waveguide

For any geometry, a waveguide without reflection can be represented by the following S-matrix:

$$\mathbf{S}_{wg} = \begin{bmatrix} 0 & A(\lambda)\exp(-j\frac{2\pi}{\lambda}n_{eff}(\lambda)L) \\ A(\lambda)\exp(-j\frac{2\pi}{\lambda}n_{eff}(\lambda)L) & 0 \end{bmatrix}. \tag{3.9}$$

In this, $\lambda = \frac{2\pi c}{\omega}$ is the wavelength of the light in vacuum. The effective index $n_{eff}(\lambda)$ can be determined using an eigenmode solver. The loss in the waveguide is defined by the term $A(\lambda)$, but in SOI this is usely almost constant around the telecom wavelengths. The parameters of this scatter-matrix can be obtained from measurements or from simulation tools such as eigenmode solvers.

3.4.3.2 Scatter matrix of a directional coupler

A directional coupler can be implemented using a 2 × 2 multimode interferometer, or by bringing two waveguides sufficiently close to each other, such that they couple through the evanescent fields of the waveguide eigenmodes. Regardless of the geometrical implementation, the scatter-matrix of an ideal lossless directional coupler can be described by the following scatter-matrix (if the port positions are chosen approperiately):

$$\mathbf{S}_{DC} = \begin{bmatrix} 0 & 0 & \tau & j\kappa \\ 0 & 0 & j\kappa & \tau \\ \tau & j\kappa & 0 & 0 \\ j\kappa & \tau & 0 & 0 \end{bmatrix} \tag{3.10}$$

In this matrix τ and κ are real numbers and, if the device is lossless, $|\tau|^2+|\kappa|^2 = 1$. The phenomenological parameters τ and κ only describe the input-output behavior of this component. How these phenomenological parameters are related to the geometric parameters is determined by the physics of the device. This can be studied in, e.g., a FDTD simulation or by calculating supermodes using an eigenmode solver. In principle, this model can be extended to include reflections as well [42].

3.5 Beyond the scatter-matrix: the node description

An optical component that is linear, instantaneous and does not generate energy when there is no incident light, can be perfectly described using only a scatter-matrix. However, if we want to efficiently describe cavity resonances, nonlinear optical components, lasers or the delay in long waveguides or fibers, this description is not sufficient or optimal. Here we extend the description to an optical component with different state variables and differential equations for these states. For instance, the evolution of the optical field in a cavity, or the temperature and carrier density can be modeled in this way. We will consider the union of the scatter-matrix and the state variable description to be a 'node' model of the optical component. Furthermore, each node has access to its input history, which allows us to create delay lines. Additionally, a node can also be a representation of a circuit as it can contain subnodes, allowing the creation of hierarchical networks.

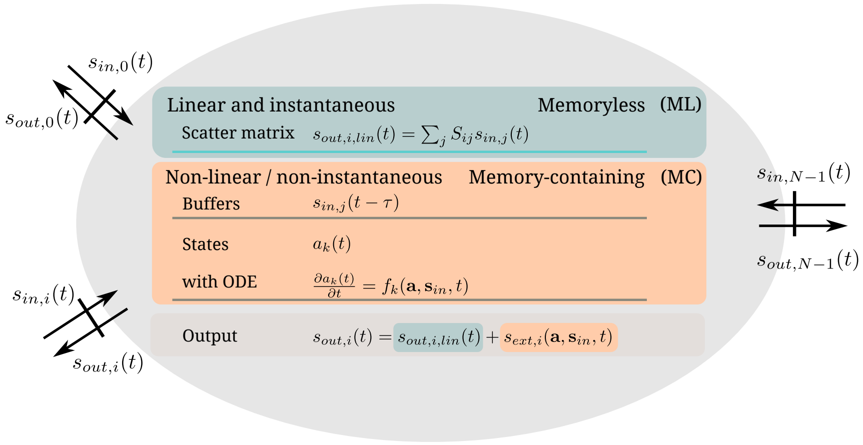
$s_{in,0}(t)$
$s_{out,0}(t)$
Linear and instantaneous
Memoryless (ML)
Scatter matrix $s_{out,i,lin}(t) = \sum_j S_{ij} s_{in,j}(t)$
Non-linear / non-instantaneous
Memory-containing (MC)
Buffers $s_{in,j}(t-\tau)$
States $a_k(t)$
with ODE $\frac{\partial a_k(t)}{\partial t} = f_k(\mathbf{a}, \mathbf{s}_{in}, t)$
Output $s_{out,i}(t) = s_{out,i,lin}(t) + s_{ext,i}(\mathbf{a}, \mathbf{s}_{in}, t)$
$s_{in,N-1}(t)$
$s_{out,N-1}(t)$
$s_{in,i}(t)$
$s_{out,i}(t)$

Figure 3.3: Properties of a node with N ports in Caphe. A linear and instantaneous node is described by its scatter-matrix $\mathbf{S}$. State variables (e.g., temperature and free carriers), accompanied by the corresponding (nonlinear) ODEs, can be added to this description. This makes the node non-instantaneous.

Figure 3.3 illustrates the representation of a Node in Caphe. Similarly to the optical components described in Sec. 3.4, a node can exchange optical energy with the outside world using N ports. The linear instantaneous transmission between port i (input $s_{in,i}$) and j (output $s_{out,j}$) is defined through the scatter-matrix-element S_{ij}.

As discussed earlier, two optional time-domain related features can be added to enrich this component (see Fig. 3.3, bottom): a component can have states and buffers.

First, we can add internal *states* a_k to the node. These are time-dependent and can be used to describe, e.g., the gain in an SOA or the complex amplitude of a resonator. A set of ODE equations describes the component as a function of its internal variables and input. The equations are not restricted in their format, allowing for the inclusion of nonlinear terms.

Second, one can add *buffers* to have access to the values of the inputs $s_{in,i}$ or states a_k at previous timesteps. For instance, this is relevant when modeling a delayed waveguide. To decrease memory use in long simulations, we implement the buffers using a cyclic buffer approach. Each buffer has a fixed number of timesteps it can remember, and data will be stored in a cyclic way, overwriting the oldest inputs.

Because of these two additions, as will be described in Sec. 3.6, the *output* $s_{out,i}$ of a node is a sum of the linear part and a term describing the temporal, possibly nonlinear behavior of the component.

3.6 Generalized source term

For each component we can add the influence of its (optional) buffers or state variables to its output signal. The corresponding general input-output relation has the following format:

$$s_{out,i}(t) = \sum_{j=0}^{N-1} S_{ij} s_{in,j}(t) + s_{ext,i}(\mathbf{a}, \mathbf{s}_{in}, t) \tag{3.11}$$

$$s_{out,i}(t) = s_{out,i,lin}(t) \qquad + s_{ext,i}(\mathbf{a}, \mathbf{s}_{in}, t) \tag{3.12}$$

In this, $s_{ext,i}$ is a 'generalized' source term. For instance, for a continuous wave source with complex amplitude A, we get $s_{ext} = A$, while for a two-port waveguide with delay τ, we get $s_{out,i}(t) = s_{ext,i}(t) = Bs_{in,1-i}(t-\tau)$ (with $i \in [0,1]$). Here, the transmission is complex-valued and combines the loss and phase change in the waveguide. Importantly, this description does not take waveguide dispersion into account: both the transmission B and the delay τ are fixed and calculated for the carrier frequency ω. By approximating the continuous time impulse response of a waveguide by a digital filter, of which the output is stored in the generalized source term, it is in principle possible to incorporate dispersion effects. Alternatively, we are currently investigating how we could use vector fitting techniques [43] to transfer the model of a dispersive waveguide in a state space model, instead of the memory-consuming digital filter approach.

From the moment an external source term appears in (3.11), the component can show non-instantaneous behaviour. We call this type of nodes the memory-containing (MC) nodes (Fig. 3.3, bottom), as opposed to the the memoryless (ML) nodes, which are fully characterized solely by their S-matrix. For instance, depending on whether the delays in a waveguide are important for a simulation, a waveguide can be modeled with delay (which makes it MC), or without delay (as a ML component). As will be explained in Sec. 3.7, the latter option has the advantage that the waveguide can be eliminated from the total network representing the circuit.

3.7 Generalized connection matrix of a circuit

In the previous subsection we have made a distinction between ML and MC nodes. If, apart from sources and detectors, a circuit only contains ML nodes, the output of the circuit at the detectors is a weighted sum of the input signals at the sources, with coefficients determined by the scatter matrices of the individual components. In this section we will take advantage of the linearity of the response of the ML nodes for any external input signal, by absorbing their influence in the system equations of the MC nodes. This corresponds to an elimination of the ML nodes from the list of components that needs to be tracked during time-domain simulations. This is allowed as long as a ML component has no significant dispersion effects for the bandwidth of the envelope under interest. Consequently, for networks that contain both instantaneous and non-instantaneous components, the dimensionality of the system can be reduced, resulting in both an effective speed-up and a decrease in the memory use of the time-domain simulations. This possibility to eliminate components from the simulation equations is actually the main novelty of our framework (and a similar framework discussed in [23–25]), compared to other optical simulation tools. As a side effect, when considering a system containing only ML nodes, sources and detectors, the same approach can also be applied to do frequency-domain simulations.

To achieve the elimination of the ML nodes, we start from the representation of a node shown in Fig. 3.3, and derive in Sec. 3.7.1 a matrix called the generalized connection matrix. This describes how all inputs s_{in} of the MC nodes are related to the generalized source term s_{ext} (which is by definition only nonzero for the MC nodes). This generalized connection matrix is the result of the elimination of the ML nodes from the circuit. Subsequently, in Sec. 3.7.2, we illustrate the physical meaning of the generalized connection matrix by calculating it for a microring, indicating how it can be useful in both time-domain and frequency-domain simulations. Finally, in Sec. 3.7.3, we describe how we can significantly improve the scalability of the software by using sparse matrices for the calculation of the generalized connection matrix, and we perform a test to check the speed improvements.

3.7.1 Derivation of the generalized connection matrix

To eliminate the ML nodes, we split the input/output vector $\mathbf{s}_{in/out}(t)$ into a part for the MC nodes ($\mathbf{s}_{in/out,MC}(t)$) and a part for the ML nodes ($\mathbf{s}_{in/out,ML}(t)$). For notational simplicity, we do not explicitly include the time dependency (t) in the following derivation. We can describe the connection of the different components in the circuit using a matrix product:

$$\begin{pmatrix} \mathbf{s}_{in,MC} \\ \mathbf{s}_{in,ML} \end{pmatrix} = \mathbf{C}_{tot} \begin{pmatrix} \mathbf{s}_{out,MC} \\ \mathbf{s}_{out,ML} \end{pmatrix} = \begin{pmatrix} \mathbf{C}_{MC,MC} & \mathbf{C}_{MC,ML} \\ \mathbf{C}_{ML,MC} & \mathbf{C}_{ML,ML} \end{pmatrix} \begin{pmatrix} \mathbf{s}_{out,MC} \\ \mathbf{s}_{out,ML} \end{pmatrix}. \tag{3.13}$$

In Eq. (3.13), $\mathbf{C}_{tot}$ is a binary connection matrix with $C_{tot,ij}$ equal to 1 if port i is connected to port j and equal to 0 if not. Hence, $\mathbf{C}_{tot}$ is symmetric and contains at most one element per row and at most one element per column, with zeros on the diagonal.

Based on the definition of ML and MC nodes, Eq. (3.11) can be reorganized into the following two equations:

$$\mathbf{s}_{out,MC} = \mathbf{S}_{MC,MC}\mathbf{s}_{in,MC} + \mathbf{s}_{ext,MC} \,, \tag{3.14}$$

$$\mathbf{s}_{out,ML} = \mathbf{S}_{ML,ML}\mathbf{s}_{in,ML} \tag{3.15}$$

Here, we define the scatter matrices $\mathbf{S}_{ML,ML}$ and $\mathbf{S}_{MC,MC}$, as two subparts of the total scatter-matrix of the circuit S_{tot}, a block diagonal matrix that contains all the individual scatter matrices of the components. Both are block diagonal matrices, with each block representing the scatter-matrix of a ML and a MC node, respectively. The second term in Eq. (3.14), $\mathbf{s}_{ext,MC}$, is the generalized source term described in Eq. (3.11).

Using Eq. (3.13), (3.14) and (3.15) we can derive the input at the MC ports $\mathbf{s}_{in,MC}$, as a function of $\mathbf{s}_{ext,MC}$. Eliminating $\mathbf{s}_{out,ML}$ in Eq. (3.13) using Eq. (3.15) and subsequently solving for $\mathbf{s}_{in,MC}$ results in

$$\begin{aligned} \mathbf{s}_{in,MC} = \Big(&\mathbf{C}_{MC,MC} + \\ &\mathbf{C}_{MC,ML}\mathbf{S}_{ML,ML}\left(\mathbf{I} - \mathbf{C}_{ML,ML}\mathbf{S}_{ML,ML}\right)^{-1}\mathbf{C}_{ML,MC}\Big)\mathbf{s}_{out,MC} \,, \end{aligned} \tag{3.16}$$

$$= \widehat{\mathbf{C}}_{MC,MC}\,\mathbf{s}_{out,MC} \,. \tag{3.17}$$

While $\mathbf{C}_{MC,MC}$ only considers the direct connections between ports of MC nodes, $\widehat{\mathbf{C}}_{MC,MC}$ extends this matrix with the connections between ports of MC nodes that are indirectly linked by connections with intermediate ML nodes. Furthermore, this matrix does not only indicate the presence of such a connection with a binary 1 or 0 at the appropriate place, but also takes the amplitude change and phase change into account that is caused by the transmission through those intermediate ML nodes. As a consequence, we do not need to track $\mathbf{s}_{in,MC}$ during time-domain simulations, resulting both in a reduced memory use and a reduced number of calculations per simulation time step.

As our final aim is to express $\mathbf{s}_{in,MC}$ as a function of $\mathbf{s}_{ext,MC}$, we substitute

Eq. (3.14) in Eq. (3.16):

$$\mathbf{s}_{in,MC} = \left(\mathbf{I} - \widehat{\mathbf{C}}_{MC,MC}\mathbf{S}_{MC,MC}\right)^{-1}\widehat{\mathbf{C}}_{MC,MC}\mathbf{s}_{ext,MC} \ , \tag{3.18}$$

$$= \mathbf{C}_{in,ext}\,\mathbf{s}_{ext,MC} \ . \tag{3.19}$$

We end up with a matrix $\mathbf{C}_{in,ext}$, the generalized connection matrix of the circuit. Importantly, this matrix has a smaller size than $\mathbf{C}_{tot}$ or $\mathbf{S}_{tot}$. Additionally, whereas $\widehat{\mathbf{C}}_{MC,MC}$ incorporates the influence of the ML nodes in the circuit equations, $\mathbf{C}_{in,ext}$ also takes the effect of the instantaneous linear transmission through the MC nodes, included in $\mathbf{S}_{MC,MC}$, into account. It transfers the signals in the generalized source term $\mathbf{s}_{ext,MC}$ directly to the input signal vector $\mathbf{s}_{in,MC}$. As a result, during a time-domain simulation, we do not need to explicitly calculate the matrix product $\mathbf{S}_{MC,MC}\mathbf{s}_{in,MC}$ in Eq. (3.14) at every time step, reducing again the number of calculations per time step.

Note that $\mathbf{S}_{ML,ML}$ is a block diagonal matrix and $\mathbf{C}_{ML,ML}$ only permutes the rows of $\mathbf{S}_{ML,ML}$. Consequently, $\left(\mathbf{I} - \mathbf{C}_{ML,ML}\mathbf{S}_{ML,ML}\right)$ is a sparse matrix. However, depending on the topology of the original circuit and on the individual scatter matrices of the ML nodes, the inversion of the latter matrix in Eq. (3.16), can make $\widehat{\mathbf{C}}_{MC,MC}$ nonsparse, therefore also affecting the sparseness of $\mathbf{C}_{in,ext}$. Fortunately, in many circuits $\mathbf{C}_{in,ext}$ is still a rather sparse matrix.

In Sec. 3.7.3, we will show how the sparseness of the circuit matrices, combined with an appropriate choice of scientific libraries, can tremendously increase the speed of the calculations. Before we get to this point, we will first illustrate the physical meaning of the matrix elements in $\mathbf{C}_{ML,ML}$ by calculating them for a microring circuit in the next subsection.

3.7.2 Application of the framework to a microring resonator

To illustrate the process of ML node elimination we will apply it to the microring resonator circuit of Fig. 3.4. A microring consists of the combination of a directional coupler and a bent waveguide (the S matrices of these components were defined in section 3.4). The bent waveguide connects the two top ports of the directional coupler, making a loop. Additionally, two MC nodes are present in the circuit, a source (the laser) and a detector (the OSA). Caphe calculates the transmission through this ring using Eq. (3.16) and (3.18), but we will use analytic calculations for this purpose, as this is more instructive.

If monochromatic light (having a frequency ω) couples into a microring resonator (with coupling coefficient $j\kappa$), it starts to circulate inside this ring. At the end of a roundtrip through the ring waveguide the amplitude of the signal is multiplied by the complex propagation factor $\alpha = A\exp(-j\beta L)$ (with $\beta = \frac{2\pi}{\lambda}n_{eff}(\lambda)$. We assume that the loss A is independent of the wavelength, which is a reasonable assumption for SOI around telecom wavelengths. Light then

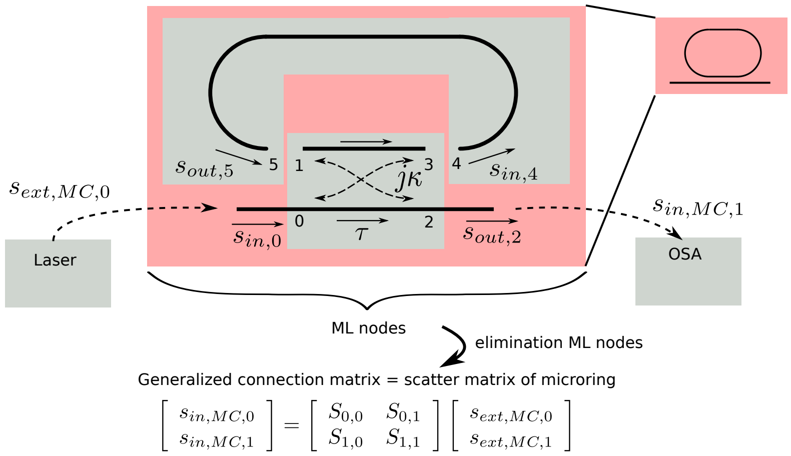
$s_{ext,MC,0}$
Laser
$s_{out,5}$
5
1
3
4
$s_{in,4}$
$j\kappa$
0
2
$s_{in,0}$
τ
$s_{out,2}$
$s_{in,MC,1}$
OSA
ML nodes
elimination ML nodes
Generalized connection matrix = scatter matrix of microring
$\begin{bmatrix} s_{in,MC,0} \\ s_{in,MC,1} \end{bmatrix} = \begin{bmatrix} S_{0,0} & S_{0,1} \\ S_{1,0} & S_{1,1} \end{bmatrix} \begin{bmatrix} s_{ext,MC,0} \\ s_{ext,MC,1} \end{bmatrix}$

Figure 3.4: A microring resonator consists of two parts: a directional coupler and a bent waveguide. In Caphe, we would probe this component with two memory-containing components, a source (the laser) and a detector (the OSA) each having only one port. If the memoryless nodes are eliminated from the circuit, the transmission of the ring is summarized in a small (2×2) generalized connection matrix $\mathbf{C}_{in,ex}$, being equal to the scatter-matrix S of this microring.

again encounters the directional coupler, and, while some part of the light will couple out of the ring, a fraction τ of this light will start a new roundtrip (we will assume the directional coupler to be lossless, i.e., $|\tau|^2 + |\kappa|^2 = 1$). Hence, the field at port 3 is an infinite sum of all the roundtrip contributions:

$$s_{out,3} = j\kappa s_{in,0} \left(1 + (\tau\alpha) + (\tau\alpha)^2 + \ldots\right), \tag{3.20}$$

This infinite sum only converges if $|\tau\alpha| < 1$, and is equal to:

$$s_{out,3} = j\kappa s_{in,0} \frac{1}{1 - \alpha\tau}, \tag{3.21}$$

which leads us to the the well-known amplitude transmission for a microring resonator [27]:

$$s_{in,MC,1} = s_{ext,MC,0} \frac{\tau - \alpha}{1 - \alpha\tau}. \tag{3.22}$$

Note that if we would have followed the derivation of Eq. (3.16) and (3.18) to calculate $C_{in,ext;1,0}$ we would obtain the same solution. Hence, importantly, our framework naturally incorporates the influence of closed loops in the geometrical layout of the circuit on the transmission. Moreover, if one would combine the directional coupler and ring waveguide into a single component, representing the microring as a whole, the elements of the scatter-matrix of this component would in this case be equal to the corresponding elements of $\mathbf{C}_{ML,ML}$. In general, if the circuit contains only ML nodes, sources and detectors, $\mathbf{C}_{ML,ML}$ can be interpreted as the scatter-matrix of the circuit formed by the ML nodes.

The case $|\tau\alpha| > 1$ is unphysical, as this would imply $A > 1$ or $\tau > 1$. If $\alpha\tau = 1$, the complex roundtrip amplitude in the ring is 1 and as $det\left(\mathbf{I} - \mathbf{C}_{ML,ML}\mathbf{S}_{ML,ML}\right) = 0$ the inversion of $\left(\mathbf{I} - \mathbf{C}_{ML,ML}\mathbf{S}_{ML,ML}\right)$ in Eq. (3.16) becomes impossible. This problem can only occur in the limit case $\tau = 1$, which describes a directional coupler without coupling, if the ring is at resonance (i.e., $\beta L = 2\pi$, see Sec. 3.7.2.1). In this rather academic limit situation, the analytic result is $s_{in,MC,1} = s_{ext,MC,0}$, while the field in the ring should be zero. As we will discuss in Sec. 3.7.3, some numeric algorithms will still be able to retrieve part of this solution (more specifically, $s_{in,MC,1} = s_{ext,MC,0}$), but if one would monitor not only the output at the detector, but also the power level in the ring, the results might be unphysical.

In the next paragraphs, we discuss how the elimination of the ML nodes in this microring system can be relevant for both frequency-domain and time-domain simulations.

3.7.2.1 Frequency-domain simulations

As the circuit presented in Fig. 3.4 only contains a source, a detector and ML nodes, it is suited to do frequency-domain simulations. Indeed, by evaluating $\mathbf{C}_{in,ext;1,0}$ using Eq. (3.22) at a grid of different wavelengths, the frequency dependency of the (complex-valued) linear steady-state transmission of the microring at the pass port can be probed. In contrast, if MC nodes would be present in the circuit, the elements in $\mathbf{C}_{in,ext}$ could differ from the physical transmission. For instance, if the instantaneous waveguide model would be replaced by one that incorporates delay, the delay model would have a zero scatter-matrix, resulting in $\mathbf{C}_{in,ext;1,0} = 0$.

Figure 3.5 shows an example transmission spectrum of the ring circuit from Fig. 3.4, calculated by Caphe. We will now discuss some characteristic features of a such a ring spectrum and introduce some new definitions as the corresponding concepts will be useful throughout the remainder of this dissertation. We can calculate the power transmission analytically starting from $T_P = \left|\frac{s_{in,MC,1}}{s_{ext,MC,0}}\right|^2$ and Eq. (3.22):

$$T_P(\phi) = \frac{A^2 + \tau^2 - 2A\tau\cos(\phi)}{1 + A^2\tau^2 - 2A\tau\cos(\phi)}. \tag{3.23}$$

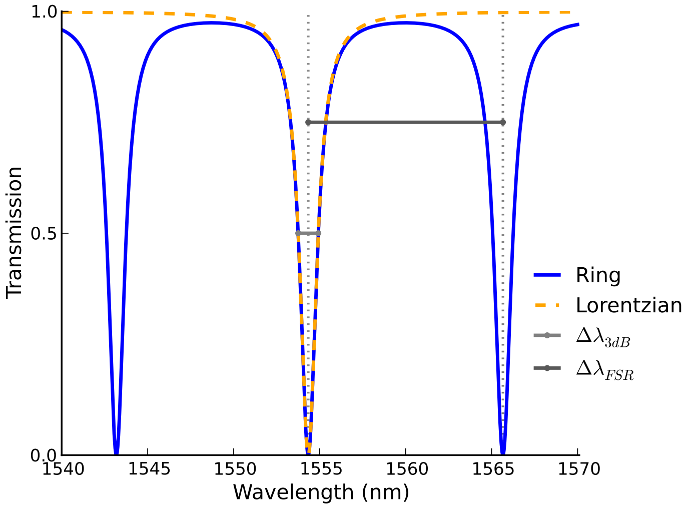

Figure 3.5: The power transmission of a critical coupled ring as a function of wavelength, calculated by Caphe. The ring properties are $A = \tau = 0.85$, $L = 50\,\mu$m, $n_{eff}(1550\,\text{nm}) = 2.43$ and $n_g = 4.3$. We also show the Lorentzian approximation of the spectrum of one of the resonance peaks, calculated using Eq. (3.28).

Here, $\phi = \beta L = \frac{2\pi n_{eff}(\lambda)L}{\lambda}$ is the single pass phase change. It is easy to check that for a lossless ring ($A = 1$) the transmission will always be one. In this case the ring only imposes a wavelength-dependent phase change of the input light. Equation (3.23) can be rewritten in a more intuitive format:

$$T_P(\phi) = \frac{T_{min} + 4F^2 \sin^2\left(\frac{\phi}{2}\right)}{1 + 4F^2 \sin^2\left(\frac{\phi}{2}\right)} \tag{3.24}$$

$$T_{min} = \frac{(\tau - A)^2}{(1 - \tau^2 A^2)^2} \tag{3.25}$$

$$F = \frac{\sqrt{\tau A}}{(1 - \tau A)} \tag{3.26}$$

The ring is 'on resonance' when the phase is an integer multiple of 2π. This happens when the wavelength of the light fits a whole number of times inside the optical length of the ring: $\lambda_r = \frac{n_{eff}(\lambda_r)L}{m}$, $m \in 1, 2, 3, \ldots$. If $\tau = A$, the transmission at resonance is zero. This condition is called 'critical coupling' (the ring in Fig. 3.5 is an example of this situation).

In the remainder of this dissertation, we will often assume linear dispersion, resulting in a constant group index $n_g = n_{eff}(\lambda) - \frac{dn}{d\lambda}\lambda$. Using this linear approximation of the dispersion curve of n_{eff}, the Free Spectral Range (FSR), i.e., the distance between subsequent resonance peaks, is in the wavelength domain given by [27]

$$\Delta\lambda_{FSR} = \frac{\lambda_r^2}{n_g L} \tag{3.27}$$

A similar expression can be defined in frequency-domain using $\frac{\Delta\omega}{\omega} = \frac{\Delta\lambda}{\lambda}$. This spectral distance is related to the roundtrip time $T_r = \frac{n_g L}{c}$ of the light in the ring. In this dissertation, we are mostly interested in the behaviour near one resonance. In this regime, one often uses a first order approximation in ϕ of Eq. (3.24):

$$T_P(\phi) = \frac{T_{min} + F^2\Delta\phi^2}{1 + F^2\Delta\phi^2}. \tag{3.28}$$

This is called the Lorentzian approximation of the ring resonance [27], and appears in a rescaled version as a function of wavelength, or as a function of frequency. Starting from this approximation it is easy to characterize the shape of the resonance more in detail. The 3dB-bandwidth of the resonance is in the wavelength domain defined as:

$$\Delta\lambda_{3dB} = \frac{(1-\tau A)\lambda_r^2}{\pi\sqrt{\tau A} n_g L}. \tag{3.29}$$

This definition of $\Delta\lambda_{3dB}$ corresponds to the wavelength range around resonance for which the optical energy in the cavity is still higher than half of the optical energy that circulates in the cavity at λ_r. Only if the ring is critically coupled, $\Delta\lambda_{3dB}$ can be interpreted as well as the wavelength range around resonance for which the transmission is less than $\frac{1}{2}$. The corresponding quality factor $Q = \frac{\lambda_r}{\Delta\lambda_{3dB}}$ of the resonance is:

$$Q = \frac{\pi\sqrt{\tau A} n_g L}{(1-\tau A)\lambda_r}, \tag{3.30}$$

while the finesse $\mathfrak{F} = \frac{\lambda_{FSR}}{\lambda_{3dB}}$ is:

$$\mathfrak{F} = \frac{\pi\sqrt{\tau A}}{(1-\tau A)}, \tag{3.31}$$

In Sec. 3.9.1 the physical meaning of both the Q-factor and the finesse will be discussed.

3.7.2.2 Time-domain simulations

In a time-domain simulation, if the bandwidth of the input signal is significantly smaller than the bandwidth of the ring resonator, the ML nodes (i.e., the waveguide and the directional coupler) can be eliminated. We then need to evaluate Eq. (3.22) solely at the wavelength of the input signal, before starting the actual time-domain simulations. In a ring resonator, the phase change over the 3dB bandwidth is $\pi/2$ radians, making the dispersion not negligible. For a ring with a Q-factor of 62500 (as the one we will model with CMT in chapter 4), if the ring has a resonance around 1550 nm, the photon lifetime is 103 ps (in Sec. 3.9.1 we will show how this can be derived from the Q-factor), which corresponds to an upper limit for the signal bandwidth of ~ 9.7 GHz. If the ML nodes can be eliminated we would only incorporate 2 ports of the circuit in the simulation, instead of using 8 ports. If the signal bandwidth is not negligible, one could take the wavelength dependency in $\mathbf{C}_{in,ext}$ into account by constructing a digital filter, or, alternatively, as we will show in Sec. 3.9.1, a CMT model can be used to convert the combination of the directional coupler and the waveguide to a MC node with a differential equation. If the input signal bandwidth is negligible, the elimination of the directional coupler and the waveguide from the circuit avoids that the signals that travel through the six ports of those two components (two for the waveguide, four for the directional coupler) need to be calculated or stored.

3.7.3 Speeding up the matrix calculations

In Sec. 3.7.1 we have derived the matrix product to calculate $\mathbf{s}_{in,MC}$ from $\mathbf{s}_{in,ML}$. In this section we will optimize this calculation with respect to speed. As $\mathbf{C}_{MC,MC}$ is independent of $\mathbf{s}_{in,ML}$, we can calculate this matrix in advance. For this purpose, we need to solve two times a linear system that can be rewritten in the form

$$\mathbf{AX} = \mathbf{B}, \tag{3.32}$$

and needs to be solved for $\mathbf{X}$. Indeed, to calculate $\left(\mathbf{I} - \widehat{\mathbf{C}}_{MC,MC}\mathbf{S}_{MC,MC}\right)^{-1}\widehat{\mathbf{C}}_{MC,MC}$ in Eq. (3.18) we need to solve

$$\left(\mathbf{I} - \widehat{\mathbf{C}}_{MC,MC}\mathbf{S}_{MC,MC}\right)\mathbf{X} = \widehat{\mathbf{C}}_{MC,MC} \tag{3.33}$$

for $\mathbf{X}$ and a similar calculation needs te be done in Eq. (3.16). At first sight, one would be tempted to solve Eq. (3.32) by first calculating $\mathbf{A}^{-1}$ and subsequently calculating the matrix product $\mathbf{A}^{-1}\mathbf{B}$. However, this is not necessary. This system can also be solved by first LU factorizing $\mathbf{A}$, followed by the calculation of $\mathbf{X}$ using forward and backward substitution. Using this approach instead of the matrix inversion results in an improvement of both speed and stability [44].

Since these matrices are sparse, we can use sparse matrix algorithms to solve this system. One software package, the Clark Kent sparse LU factorization (KLU) algorithm, is perfect for our framework, as it is optimized for circuit-like matrices [45–48].

Interestingly, the scientific library that implements KLU in our code returns the correct output at the detector if we choose $\tau = 1$ in the directional coupler of the microring circuit discussed in Sec. 3.7.2, in spite of a version of Eq. (3.32) needs to be solved in which **A** is not invertable (but subparts of it still are). The solution of the system using standard Python or Matlab libraries would result in an error, or NaN. More generally, even if non-invertable matrices appear during the calculation, e.g., due to the appearance in the circuit of lossless light-loops with zero phase change, we see that the current KLU-implementation in the chosen library still returns correct $\mathbf{C}_{ext,in}$-values at the port positions where signals pass that did not interact with those problematic light loops. In the case of the aforementioned microring circuit, the user does not even notice the convergence issue in the ring loop, as only the light at the pass port is dedected, and this signal does not interact with the ring loop. At the other ports, where $\mathbf{C}_{ext,in}$ would also theoretically be ill-defined, by convention, a zero is returned. Of course, the results for these limit cases should always be investigated very carefully.

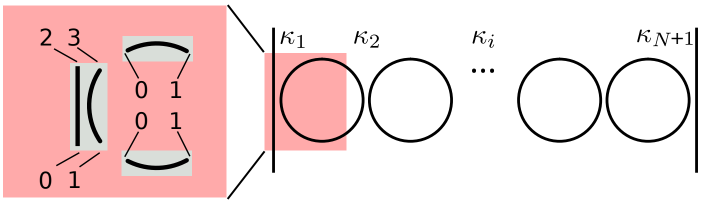

Figure 3.6: A Coupled Ring Optical Waveguide (CROW) circuit can be subdivided in multiple sections that consist of a directional coupler and two waveguides. Port numbers in such a section are shown in the left. A N ring CROW circuit contains $N+1$ coupling sections.

To benchmark the speed improvement by using KLU compared to other scientific libraries, we simulate the frequency response of an optical filter called a Coupled Ring Optical Waveguide (CROW) using LAPACK, MKL and KLU. A CROW is a sequence of optical rings as shown in Fig. 3.6. Each section is made of a directional coupler (with coupling values κ_i) and two waveguides, which then couples to the next section. Here we will only perform a speed test, whereas in section 3.11 we consider a real-world use case.

The directional coupler and the waveguide are ML components with four

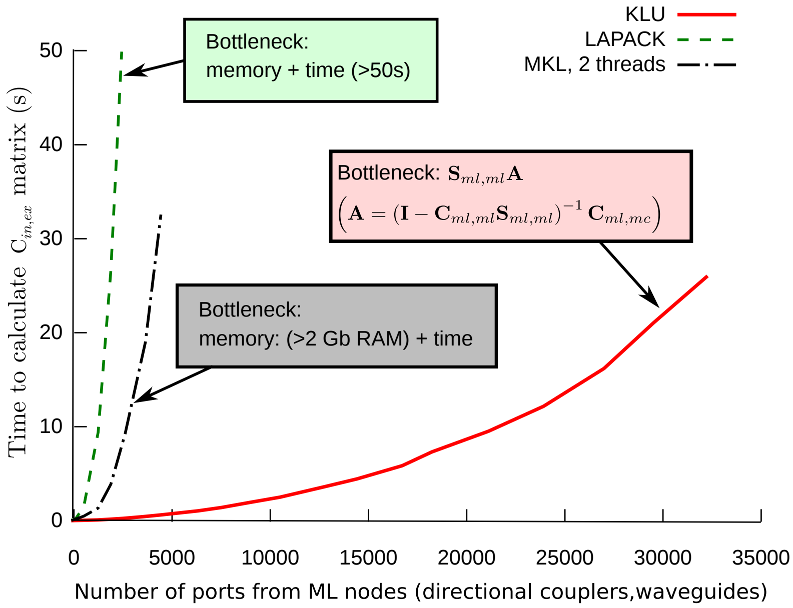

Figure 3.7: Calculating the frequency response of a passive circuit. Using KLU, a sparse matrix solver suited for circuit-like matrices, we can easily calculate scatter matrices of very large circuits.

and two ports, respectively. This means there are eight ports per CROW section. By plotting the simulation time as a function of the number of ports in the circuit, we observe how scalable our software framework is for the frequency-domain. This is shown in Fig. 3.7, where we compare the time spent by different scientific libraries on the matrix calculations as a function of the number of ML ports. As can be seen in the figure, a large number of CROW sections can easily be handled with the KLU algorithm in a fast way. This proves the technique is useful for analyzing very complex systems in steady-state regime.

3.8 Integration of the state variables

A key ingredient of the node model presented in Fig. 3.3 is the vector with the internal states of the node. Those are stored in the total state variable vector $\mathbf{a}(t)$. This vector describes some internal variables of components in the circuit, e.g., the temperature and number of free carriers in a laser, or the complex amplitude of light in a cavity. The evolution of this vector as a function of time and inputs is described by a first-order ODE system:

$$\frac{d\mathbf{a}}{dt} = \mathbf{f}(\mathbf{a}, \mathbf{s}_{in}, t) \tag{3.34}$$

In fact, the ODE system presented here is the core part of the simulator, as it delivers the basic mechanism to advance time in the simulation. In Sec. 3.8.1 we will discuss an efficient approach to evaluate $\frac{d\mathbf{a}}{dt}$ for a given input vector $\mathbf{s}_{in}$, based on the use of the generalized connection matrix. Next, in Sec. 3.8.2 we will discuss the numeric integration of Eq. (3.34).

3.8.1 Node elimination during time-domain simulations

Just like in the frequency-domain, if a circuit network contains both ML and MC nodes, one can eliminate the ML nodes prior to starting the time-domain simulation, reducing the calculation time needed for the evaluation of $\frac{d\mathbf{a}}{dt}$. The speed of the time-domain simulation depends on the size of the matrix $\mathbf{C}_{in,ext}$ after eliminating the ML nodes. We will explain how this matrix is used in the flow of the calculation in Sec. 3.8.1.1, and demonstrate the speed improvement due to node elimination for an example in Sec. 3.8.1.2.

3.8.1.1 Efficient evaluation of the time derivative of the system

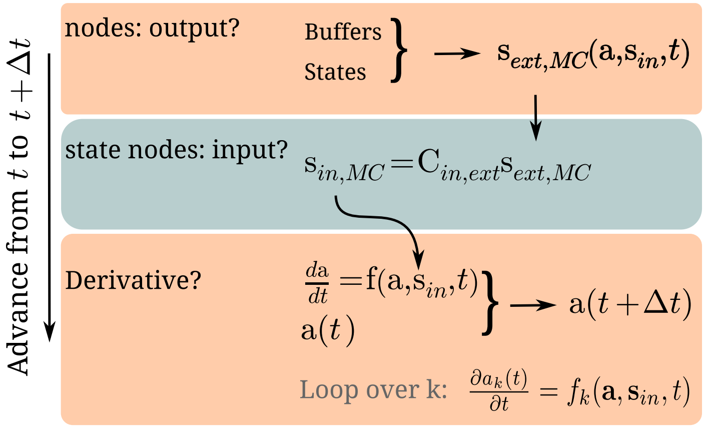
Advance from t to $t+\Delta t$
nodes: output?
Buffers
States
$s_{ext,MC}(a,s_{in},t)$
state nodes: input?
$s_{in,MC}=C_{in,ext}s_{ext,MC}$
Derivative?
$\frac{da}{dt}=f(a,s_{in},t)$
$a(t)$
$a(t+\Delta t)$
Loop over k: $\frac{\partial a_k(t)}{\partial t}=f_k(\mathbf{a},\mathbf{s}_{in},t)$

Figure 3.8: At every time step Eq. (3.34) needs to be evaluated. For this purpose we first calculate $\mathbf{s}_{ext,MC}$. Next we calculate $\mathbf{s}_{in,MC}$. And finally $\mathbf{s}_{in,MC}$ is used $\mathbf{s}_{in,MC}$ in the evaluation of $\mathbf{f}(\mathbf{a},\mathbf{s}_{in},t)$.

By definition, only the MC nodes can have state variables. Consequently, we only need to know the input of the MC nodes to evaluate Eq. (3.34). Additionally, in the previous sections we described how the input signals for the MC nodes $\mathbf{s}_{in,MC}$ can be calculated, without explicitly calculating the input signals $\mathbf{s}_{in,ML}$ that correspond to the ML nodes. As argued in Sec. 3.7, elimination of these variables from the equations can make the algorithm faster.

More precisely, in order to perform the integration, we have to be able to evaluate the function $\mathbf{f}$ at every timestep (Fig. 3.8). We do this by looping over all MC nodes to calculate their contribution to the generalized source term $\mathbf{s}_{ext}$, based both on the current state or the history of the state variables and external driving signals. Subsequently, we can calculate the input to each MC node, $\mathbf{s}_{in}$, using the matrix product defined in Eq. (3.18). Importantly, $\mathbf{C}_{in,ext}$ should only be calculated once at the beginning of the simulation. Finally, based on the input for each node individually, we can evaluate the ODEs, $\frac{da_k}{dt}=f_k(\mathbf{a},\mathbf{s}_{in},t)$, and combine them into the derivative of the full system $\frac{da}{dt}$.

3.8.1.2 Node elimination in a nanophotonic reservoir

To benchmark the speed improvement by using ML node elimination when integrating Eq. (3.34), we perform a time-domain simulation of a large network of photonic components. For this purpose we choose the nanophotonic reservoir consisting of SOAs studied in [49]. The topology in this simulation is a regular 2D grid of SOAs. Each SOA is connected to its nearest neighbours, in a structure called a swirl topology [49], see Fig. 3.9(a). To connect the SOAs, we used a combination of splitters and waveguides. The details about the circuit are described in [49], while additional details on the implementation of such a nanophotonic reservoir in Caphe are given in [5]. We use Euler integration with timestep 0.1 ps, while the input signal was a 10 ns long noise signal, equally distributed over all the SOAs.

We compare two systems. In the first system the ML nodes behave as MC nodes (such that their port positions are incorporated in $\mathbf{C}_{in,ext}$), in the second system we first eliminate all ML nodes. In the first case, we need to calculate the input at each splitter and waveguide, which means the simulation will take longer, and consume more memory, compared to the second case, in which only the input at the SOAs is calculated (Fig. 3.9(b)).

The main contribution to the total simulation time is the evaluation of the ODEs of the individual SOAs and the matrix multiplication from Eq. (3.18). This explains why elimination of the ML nodes can approximately double the simulation speed (Fig. 3.9(b), top), even though the calculation time for evaluating the ODEs is the same for both systems. In the bottom graph of Fig. 3.9(b) we show the dependency of the total memory usage of the program (i.e., the sum of the memory allocated in C++ and in Python) on increasing circuit size. Initialization overhead in Python results in a fixed offset. During the simulations, for each port of a MC containing component a buffer that stores 500 timesteps is used. Consequently, elimination of the ML nodes drastically reduces the memory use. The linearity of both the calculation time and memory as a function of the circuit size is a result of the sparse matrix algorithms used in our framework.

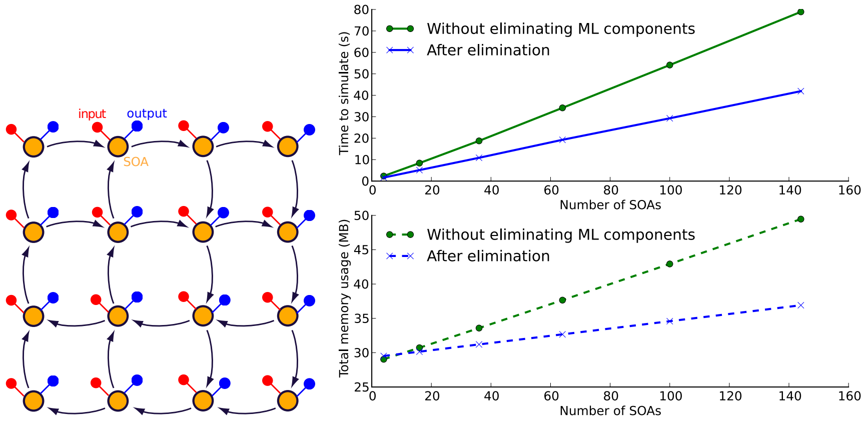

(a) (b)

Figure 3.9: (left) Topology of a nanophotonic reservoir, containing both ML and MC nodes. Each circle represents a SOA (MC), which are connected via waveguides (ML) and splitters (ML, not shown) to other SOAs, detectors and sources (MC) (right) Due to the nearest neighbour connection topology of the network and sparse implementation of the matrix products, both the simulation time and memory use increase linearly with the number of SOAs, but this increase is less steep if the ML nodes are eliminated. The offset in the memory consumption graph is related to initialization overhead in Python.

3.8.2 Choice of integration algorithm

3.8.2.1 Stability, accuracy and speed

For the numeric integration of the system in Eq. (3.34) several types of integration routines can be used, each with their own advantages and disadvantages. For instance, forward Euler integration with a fixed timestep Δt allows to calculate the next state based on the current state of the system using:

$$\mathbf{a}(t+\Delta t) = \mathbf{a}(t) + \Delta t \mathbf{f}(\mathbf{a}, \mathbf{s}_{in}, t) \tag{3.35}$$

This method is based on a first-order Taylor expansion of Eq. (3.34). Hence, the error per step is on the order of $O(\Delta t^2)$, while the total error accumulation is on the order of $O(\Delta t)$ (as the total number of steps is $\propto \frac{1}{\Delta t}$). This slow convergence of the error as a function of Δt, combined with stability issues, make this integration method less suited for some of the more complicated equations encountered in nonlinear optics.

To improve stability, two advanced integration routines are implemented in the current framework. The first method is the fourth-order Runge-Kutta method, which has an error per step on the order of $O(\Delta t^5)$, resulting in a total error accumulation on the order of $O(\Delta t^4)$. Compared to the first-order Euler integration it is much more accurate for a given Δt, but it requires more function evaluations. The second integration routine is based on Bulirsch-Stoer, and as it is in most cases a better choice than Runge-Kutta (caveats on this rule of thumb can be found in [44]), it is this one we will use most throughout this dissertation. We have implemented this algorithm in combination with an adaptive stepsize method. In such an adaptive stepsize algorithm, the internal integration step Δt is continuously optimized during the integration, trying to make it as large as possible, while maintaining a given accuracy. As some photonic components contain very different timescales, their ODEs are sometimes stiff (i.e., some numeric integration algorithms are numerically unstable or prohibitively slow). Hence, in future work, other integration methods such as backward Euler and other implicit methods might be implemented to improve stability of such stiff equations.

In our current implementation of Eq. (3.34), we use complex state variables, using the default C++ package for complex numbers. This implies that the complex field $E = |E|e^{j\phi}$ is represented by its real (E_r) and imaginary (E_i) part. In contrast, in [19] one argues that in the case of, e.g., steady-state chirp in a solid state laser this choice might result in the need to take very small stepsizes. Representing the signals by the amplitude $|E|$ and the phase ϕ might circumvent this problem, even though it has a larger computational complexity, as for a constant chirp $|E|$ is fixed, while ϕ is changing linearly (so a larger stepsize can be taken to model this). Given the advantages of representing E in the complex domain, demonstrated in Sec. 3.7.1, we stick to the more natural (E_r,E_i) signal representation choice. However, in future implementations of the framework we will incorporate the option to integrate systems of real variables, such that users have the possibility to efficiently integrate the ODE equations of a component of which the derivatives are expressed in the ($|E|$,ϕ)-representation, while the transfer of signals would still happen in the optimal (E_r,E_i)-representation.

3.8.2.2 Numeric integration of coupled nonlinear cavity dynamics

We will conclude this subsection with a comparison of two integration routines for an example nonlinear photonic circuit. The first integration scheme is a simple forward Euler with fixed time step Δt. The second one is an advanced stepping routine based on Bulirsch-Stoer [44], in a version with adaptive stepsize, to guarantee accuracy and stability. As example circuit, we simulate a system of two coupled inline photonic crystal cavities. An inline cavity is a two port component that reflects all the power, if the input wavelength is off resonance. As proven in [50], this system can be described using CMT. The background on

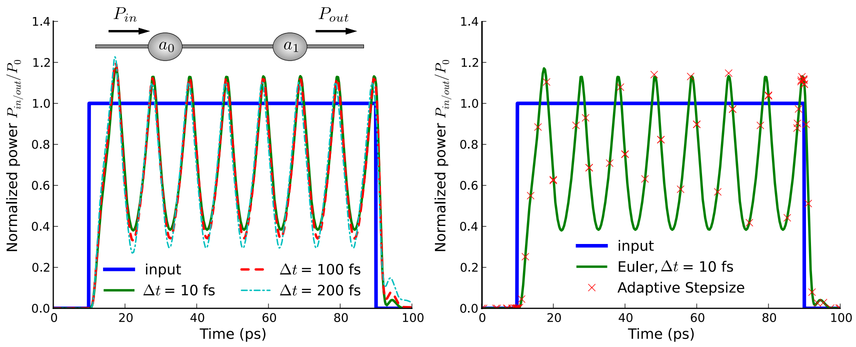

(a) Fixed steps

(b) Adaptive stepsize

Figure 3.10: (left) When using forward Euler integration, larger timesteps decrease the accuracy. (right) An adaptive stepsize integration algorithm automatically uses the optimal dt when targeting a given accuracy level. Indeed, during the sudden jump in the input the integration step is clearly decreased. Parameters are identical as in [50].

the CMT-equations will be provided in Sec. 3.9, but we include them here to illustrate the choice to work with complex variables a_j ($j = 0, 1$):

$$\frac{\mathrm{d}a_j}{\mathrm{d}t} = \left[i\left(\omega_0 + \delta\omega_j - \omega\right) - \frac{1}{\tau} \right] a_j + d s_{j;0,+} + d s_{j;1,+}, \tag{3.36}$$

$$s_{j;0,-} = \exp(i\phi) s_{j;0,+} + d a_j, \tag{3.37}$$

$$s_{j;1,-} = \exp(i\phi) s_{l;1,+} + d a_j, \tag{3.38}$$

In this, τ is the lifetime of the cavity and ϕ represents the phase that depends on the waveguide length and the resonator mirror reflection properties. The coupling between the cavity and its access waveguide is governed by $d = i\exp(i\phi/2)/\sqrt{\tau}$. The nonlinear frequency shift is $\delta\omega_j = -|a_j|^2/(P_0\tau^2)$, with P_0 the 'characteristic nonlinear power' of the cavity [51]. As is common in CMT, $|a_j|^2$ is the energy in the cavity mode, while $|s_{j;k,+}|^2$ ($|s_{j;k,-}|^2$) represents the power flowing in (out) port k (for $k = 0, 1$) of cavity j (for $j = 0, 1$). Port 1 of cavity 1 is connected with port 0 of cavity 2. Consequently, $|s_{0;0,+}|^2 \equiv P_{in}$ is the input power, $|s_{1;1,-}|^2 \equiv P_{out}$ is the transmitted power. There is no input from the right, $s_{1;1,+} = 0$. This system exhibits self-pulsation for certain pump settings [50].

The waveforms obtained by simulating these CMT-equations approximate very accurately the output of a full-wave FDTD simulation of the same system [50] . The difference in simulation time motivates the use of a phenomenological, high-level simulator as the one presented in this chapter. Indeed, while it takes ~ 10 hours to simulate this system in 2D FDTD, only a few milliseconds are required when using CMT.

Despite the highly nonlinear equations, the numerics remain very stable (Fig. 3.10). Furthermore, by using an adaptive stepsize the most important details of the simulation are taken into account, due to an optimal choice of Δt at every time step. Whereas for a fixed stepsize algorithm, like forward Euler, accuracy over the whole simulation domain can only be obtained by choosing a very small stepsize (Fig. 3.10(a)), this is not required for the adaptive stepsize algorithm: during switch-on and switch-off, there are a lot of discretization steps, while in-between the adaptive stepsize solution can follow the reference solution with fewer discretization steps (Fig. 3.10(b)).

3.9 Temporal Coupled Mode Theory

As illustrated in Sec. 3.8.2.2, the Coupled Mode Theory (CMT) is often used to describe the temporal behaviour of a resonator with monochromatic input light near resonance [50–55]. This theory is developed by Haus and co-workers [56–58] and describes the coupling of the resonator modes between each other or between the modes and external excitations (Fig. 3.11 schematically depicts the information flow in a CMT resonator). It will be heavily used in the subsequent chapters, therefore we give a brief introduction.

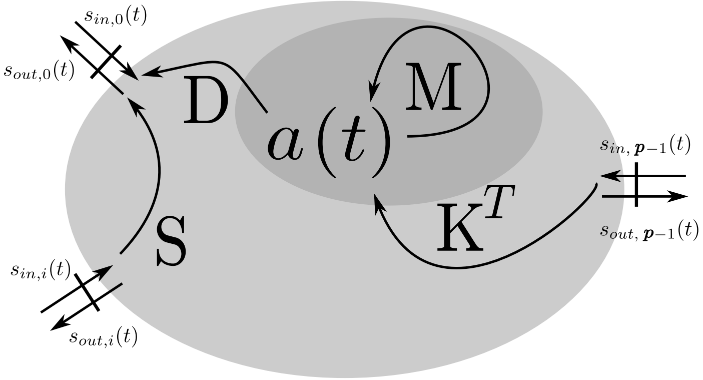

Figure 3.11: Structure of a CMT resonator with p ports and m modes. The matrix S couples light directly from input to output ports, the matrix K^T couples light from the input to the modes, the matrix M contains information about the resonance frequencies, losses and intermodal coupling and the matrix D couples light from the states to the output.

The coupled-mode equations describe the relation between the input signal s_{in} and the output signal s_{out}, depending on the temporal evolution of the modes **a**. For a lossless and reciprocal linear resonator with m modes and p ports these equations become [55]:

$$\frac{d\mathbf{a}}{dt} = \mathbf{Ma} + \mathbf{K}^T \mathbf{s}_{in}, \tag{3.39}$$

The mode amplitudes a_k are scaled such that $|a_k|^2$ represents the optical energy in mode k. The $m \times p$ matrix $\mathbf{K}^T$ describes the coupling from the p input signals to the states. The $m \times m$ matrix $\mathbf{M}$ consists of two parts:

$$\mathbf{M} = j\Omega - \Gamma_c, \tag{3.40}$$

The matrix Ω incorporates the resonance frequencies of the uncoupled modes on the diagonal, while the off-diagonal elements represent (lossless) optical coupling between these modes (of which the strenght is determined by the overlap integrals between the modes). The matrix Γ_c represents the energy loss due to coupling to the output ports. Both Ω and Γ_c are Hermitian, and the real part of the eigenvalues of the matrix $\mathbf{M}$ satisfies $\Re\{\lambda_{\mathbf{M}}\} \leq 0$ (if one of the eigenvalues is equal to zero, this implies that one of the modes does not couple to the output ports). For instance, for a unimodal PhC cavity (Sec. 3.8.2.2) or, as we will derive in Sec. 3.9.1, a unidirectional microring model with a single mode, $m = 1$ and $\mathbf{M}$ is a scalar: $M = j(\omega_r - \omega) - \frac{1}{\tau}$, hence, $\Omega = (\omega_r - \omega)$ (the term $-\omega$ is due the envelope approximation), while $\Gamma_c = \frac{1}{\tau}$.

The output of the resonator is given by:

$$\mathbf{s}_{out} = \mathbf{S}\mathbf{s}_{in} + \mathbf{Da}, \tag{3.41}$$

where the the $p \times p$ symmetric (reciprocity) and unitary (no loss) matrix $\mathbf{S}$ is the scatter-matrix of the resonator, describing the direct optical coupling between the ports, while the $p \times m$ matrix $\mathbf{D}$ describes the coupling from the states to the output.

Since the overall system, including both the resonances and the ports, is energy conserving, the decay process described by the matrix Γ_c, can only originate from the coupling from the resonances to the ports. Consequently, these matrices are related to each other. Indeed, for a lossless and reciprocal cavity containing only standing wave modes, using time-reversal symmetry and energy conservation arguments, the following relationships can be derived [55]:

$$\mathbf{D}^H\mathbf{D} = 2\Gamma_c \tag{3.42}$$

$$\mathbf{D} = \mathbf{K} \tag{3.43}$$

$$\mathbf{SD}^* = -\mathbf{D} \tag{3.44}$$

For cavities containing travelling-wave modes, Eq. (3.42) is also applicable. Similar equations to Eq. (3.43) and (3.44) can be derived using the same symmetry and conservation arguments, provided that for each travelling-wave mode also its counterpropagating version is included in the system description [59]. Alternatively, one can of course convert the system description to a standing wave mode eigenbase and directly apply Eq. (3.42)-(3.44).

While the previous formalism is constructed for lossless cavities, intrinsic losses can be easily incorporated by adding an extra loss matrix Γ_l to $\mathbf{M}$, corresponding to the intrinsic loss of the modes and their coupling:

$$\mathbf{M} = j\Omega - \Gamma_c - \Gamma_l. \tag{3.45}$$

The latter does not affect the evaluation of Eq. (3.42)-(3.44).

Additionally, by adding nonlinear contributions to the resonance frequencies incorporated in Ω and Γ_l, also nonlinear effects, such as the Kerr effect or Two Photon Absorption (TPA) can be incorporated. For instance, the conservative part of nonlinear effects that changes the resonance frequency can be interpreted as a result of a change in refractive index, which is often easy to analyse using phenomenological reasoning and can be transferred back to the value of the resonance frequency using $\frac{\delta\omega_{nl}}{\omega_r} = -\frac{\delta n_{nl}}{n_g}$.

In principle, the format of the CMT equations can be justified by deriving them directly from Maxwell's equations [53, 56–58], by expanding the fields in terms of the eigenmodes of the access waveguides and cavity modes. The resulting overlap integrals can be used to calculate the coupling between the cavity modes or between the cavity modes and the access waveguides. Even the nonlinear extensions of the CMT equations can be derived starting from the original Maxwell equations, resulting in the proper propertionality terms for each type of nonlinearity [39, 60, 61].

As the previous overlap integrals are rather tedious to calculate, we will use another approach to clarify the format of the equations. In the next subsection, we will use the example of a microring to illustrate how the temporal CMT formalism can be derived starting from the transmission derived in Sec. 3.7.2.1. In fact, the derivation in Sec. 3.7.2.1 can be seen as an application of 'spatial' coupled mode theory. Relationships between the parameters of these two coupled mode theory versions are presented in [52]. An advantage of deriving the *temporal* coupled mode theory equations based on the *spatial* version of coupled mode theory is that we naturally obtain these intuitive relationships, making it possible to transfer parameters of one model to the other.

3.9.1 Derivation of CMT equations for a microring resonator

In this subsection we will derive the CMT equations for the microring discussed in Sec. 3.7.2, illustrating the approximations that are made when modeling an optical resonator with a CMT model. These equations will be the basis of the equations used in chapter 4 to describe a microring. We start from the field at port 3 as calculated in Eq. (3.21). First, we assume the losses in the ring waveguide to be low, such that $A = e^{-\alpha L} \approx 1 - \alpha L$. Second, we assume the coupling between the access waveguide and the ring waveguide to be low, such that $\tau = \sqrt{1-\kappa^2} \approx 1 - \frac{\kappa^2}{2}$. Those two conditions result in high-Q rings and are satisfied in the ring described in chapter 4.

As the losses are low, the power level in the ring waveguide does not change much. Hence, we will describe the dynamics of the optical field in the ring, using a complex amplitude a representing the phase and energy of the light in the ring. By convention we choose the phase of this variable equal to the phase of the light at port 3 in Fig. 3.4. Futhermore, during one roundtrip period $T_R = \frac{n_g L}{c}$, all the energy stored in the ring has to pass through port 3, hence $|s_{out,3}|^2 = \frac{|a|^2}{T_R}$. Consequently, based on Eq. (3.21), we can derive the dependence of a on $s_{ext,MC,0}$:

$$a = \sqrt{T_R}(j\kappa) s_{in,0} \frac{1}{1 - \alpha\tau}. \tag{3.46}$$

In CMT one investigates the dynamics of the resonator for frequencies ω near one of the resonance frequencies. Hence, to begin this derivation, we calculate the output of the ring for a steady-state monochromatic input signal with frequency ω, near a resonance frequency ω_r. Furthermore, we approximate $\alpha = Ae^{-j\phi}$ as $A(1 - j\Delta\phi)$, with $\Delta\phi = (\omega - \omega_r) T_R$. Additionally, it will prove to be benificial to temporarily work with unmodulated fields $\widehat{a} = ae^{j\omega t}$ and $\widehat{s} = se^{j\omega t}$. Substituting all aforementioned approximations and conventions in Eq. (3.46), results in:

$$\widehat{a} = \frac{\sqrt{T_R}(j\kappa)}{j(\omega - \omega_r) T_R + \alpha L + \frac{\kappa^2}{2}} \widehat{s}_{in,0}. \tag{3.47}$$

We now define an intrinsic loss term $\frac{1}{\tau_l} = \frac{\alpha L}{T_R}$, a coupling loss term $\frac{1}{\tau_c} = \frac{\kappa^2}{2T_R}$ and a new coupling term $\widetilde{\kappa} = j\frac{\kappa}{\sqrt{T_R}} = j\sqrt{\frac{2}{\tau_c}}$. We can use these definitions to reorganize Eq. (3.47) to:

$$j\omega\widehat{a} = \left(j\omega_r - \frac{1}{\tau_l} - \frac{1}{\tau_c}\right)\widehat{a} + \widetilde{\kappa}\widehat{s}_{in,0}. \tag{3.48}$$

This expression is derived for a monochromatic input signal with frequency ω and can be interpreted as an equation in Fourier space. Hence, we can inverse Fourier transform this to the time-domain:

$$\frac{d\widehat{a}}{dt} = \left(j\omega_r - \frac{1}{\tau_l} - \frac{1}{\tau_c}\right)\widehat{a} + \widetilde{\kappa}\widehat{s}_{in,0}. \tag{3.49}$$

Using the slowly-varying envelope approximation, the differential equation becomes:

$$\frac{da}{dt} = \left(j(\omega_r - \omega) - \frac{1}{\tau_l} - \frac{1}{\tau_c} \right) a + \widetilde{\kappa} s_{in,0}. \tag{3.50}$$

Based on the definition of the directional coupler, and the complex roundtrip amplitude α of the cavity we can now calculate $s_{in,MC,1}$:

$$\begin{aligned} s_{in,MC,1} =& \tau s_{ext,MC,0} + j\kappa\alpha \frac{a}{\sqrt{T_R}} \qquad (3.51) \\ \approx& s_{ext,MC,0} + j\widetilde{\kappa} a \qquad (3.52) \end{aligned}$$

In steady-state, $\frac{da}{dt} = 0$ and hence:

$$s_{in,MC,1} = \frac{\left(j(\omega_r - \omega) - \left(\frac{1}{\tau_l} - \frac{1}{\tau_c} \right) \right)}{\left(j(\omega_r - \omega) - \left(\frac{1}{\tau_l} + \frac{1}{\tau_c} \right) \right)} s_{ext,MC,0} \tag{3.53}$$

Consequently, the transmission $T_P(\omega) = \frac{s_{in,MC,1}}{s_{ext,MC,0}}$ at the pass port of the ring is:

$$T_P(\omega) = \frac{\left((\omega - \omega_r)^2 + \left(\frac{1}{\tau_l} - \frac{1}{\tau_c} \right)^2 \right)}{\left((\omega - \omega_r)^2 - \left(\frac{1}{\tau_l} + \frac{1}{\tau_c} \right)^2 \right)} \tag{3.54}$$

This is the frequency dependent version of the Lorentzian approximation of a resonance given in Eq. (3.28), implying that the CMT-model of the ring is a dynamic extension of the Lorentzian approximation of a ring resonance. If we define the photon lifetime τ_{ph} of the cavity to be $\frac{1}{\tau_{ph}} = \frac{1}{\tau_l} + \frac{1}{\tau_c}$, the Q-factor can easily be seen to be $\frac{\omega\tau_{ph}}{2}$. One would obtain the same expression for the Q-factor if one would introduce the approximation $A = 1 - \alpha L$ and $\tau = 1 - \frac{\kappa^2}{2}$ directly into Eq. (3.30). Furthermore, due to Eq. (3.50), the optical energy $|a|^2$ of the cavity decays with $\frac{2}{\tau_{ph}}$. Consequently, the Q-factor is not only a spectral feature, but also has a physical meaning, as it is equal to 2π times the number of oscillations made by the light in the ring, before the optical energy decays to $1/e$ of its initial state. Similarly, the finesse F of a ring is 2π times the number of roundtrips light in the ring makes, before the optical energy decays to $1/e$ of its initial state.

3.10 Extending the framework to CMT-models

Many optical resonators can be described using a CMT-like format for the equations concerning the optical field. For instance, the models that we will use to describe the dynamics of a passive nonlinear microring (chapter 4) or a microdisk laser (chapter 5), are CMT-based. In this section we will point out how the framework presented in Sec. 3.5-3.8 can be adapted to CMT-style models, and how this adaptation can in some cases result in an additional increase in simulation speed. For instance, the large circuit simulations done in [2] could take advantage of this speed up. Additionally, it will allow for frequency-domain simulations in the case of circuits that contain linear CMT components. Indeed, as a CMT component is a MC component, the optical resonances, being represented by differential equations, would not appear in the transmission characteristic if one would use the approach described in Sec. 3.7.2 for this purpose.

3.10.1 Reshaping the system equation towards CMT

By calculating the generalized connection matrix $\mathbf{C}_{in,ex}$, we model the linear and instantaneous transmission of the waves that originate from a generalized 'external' sources vector and travel through the components of the circuit. This connection matrix speeds up the time-domain simulations when the inputs of all the MC components need to be calculated for a given $\mathbf{s}_{ext}(t)$. This happens not only because the ML can be eliminated from the circuit, but also because we can use one single sparse matrix product $\mathbf{s}_{in}(t) = \mathbf{C}_{in,ex}\mathbf{s}_{ext}(t)$ to efficiently execute this calculation simultaneously for all the nodes. As this improvement in speed is clearly due to the *linearity* of the signal transfer encoded in the scatter-matrix, we will now investigate how additional linear behaviour in the MC node can be exploited to make the framework even more efficient.

As we saw in Sec. 3.9, in CMT models, the light coupling between the optical modes of the cavity and the access waveguides is also linear. Typically, the CMT equations of a nonlinear resonator i are given by:

$$\frac{d\mathbf{a}_i}{dt} = \mathbf{M}_i\mathbf{a}_i + \mathbf{K}_i^T\mathbf{s}_{i,in} + \mathbf{N}_i(\mathbf{a}, t, ...) \tag{3.55}$$

The function $\mathbf{N}_i$ describes the nonlinear contribution, e.g., due to changes in absorption or refractive index by the Kerr nonlinearity. If the cavity model contains additional dynamic variables, such as the number of free carriers, or the temperature, these extra equations can as well be shoehorned in the previous matrix format, by extending $\mathbf{K}_i^T$ in the appropriate places with zeros and $\mathbf{M}_i$ with linear contributions of the corresponding ODE, while the remaining nonlinear terms can be incorporated in $\mathbf{N}_i(\mathbf{a}, t, ...)$. More generally, every MC component can be trivially transferred into this format, by extending the original ODE system with additional $\mathbf{M}_i$, $\mathbf{K}_i^T$ and $\mathbf{D}_i$ matrices equal to zero. As we will use sparse matrix representations, these additional zeros will have no significant influence on the simulation speed.

Even if the resonator is nonlinear, the coupling of the modes and input signals to the output stays linear:

$$\mathbf{s}_{i,out} = \mathbf{S}_i \mathbf{s}_{i,in} + \mathbf{D}_i \mathbf{a}, \tag{3.56}$$

We now define the linear coupling matrices $\mathbf{M}$, $\mathbf{K}^T$ and $\mathbf{D}$ for the circuit as a whole. These matrices are block matrices, constructed from the submatrices $\mathbf{M}_i$, $\mathbf{K}_i^T$ and $\mathbf{D}_i$ for all the MC nodes $i \in \{0, ..., N-1\}$. Using the same syntax as before, $\mathbf{M}$ linearly couples the states to the states, $\mathbf{K}^T$ couples the input to the states, while $\mathbf{D}$ couples the states to the output. If we suppose the system has s states, then $\mathbf{M}$ is $s \times s$ dimensional, while $\mathbf{D}$ and K are both $p \times s$ dimensional. Using those matrices, we can rewrite Eq. (3.34) as:

$$\frac{d\mathbf{a}}{dt} = \mathbf{M}\mathbf{a} + \mathbf{K}^T \mathbf{s}_{in,MC} + \mathbf{N}(\mathbf{a}, t, ...) \tag{3.57}$$

As derived in Sec. 3.7, $\mathbf{s}_{in,MC} = \mathbf{C}_{in,ex}\mathbf{s}_{ext}$. However, the generalized source term can be split into two parts: a linear part, related to the linear coupling by D_i of the resonators in the circuit, and an external source term $\mathbf{s}'_{ext}(t)$ of which the linear coupling terms are substracted (e.g., containing the input signals of the sources in the circuit, or the outputs of waveguides with delay or SOAs):

$$\mathbf{s}_{in,MC} = \mathbf{C}_{in,ex}\left(\mathbf{D}\cdot\mathbf{a} + \mathbf{s}'_{ext}\right). \tag{3.58}$$

Interestingly, by doing this we have created a framework that is already a bit more powerful than before. Indeed, whereas $\mathbf{M}$ is originally considered to be a block-diagonal matrix, coupling only states within a node, we can in principle also extend it to couple states between different nodes. This was not possible in the previous formalism, as only optical coupling through the ports was allowed. However, the current formalism, e.g., allows for a more generic way of implementing optical coupling between cavity modes, using the theory developed in [52]. Also the implementation of thermal coupling between nearby resonators is conceptually simplified by this extension.

3.10.2 Calculation of the linear transmission

Suppose our circuit contains only ML nodes, CMT-modeled resonators, sources and detectors. To gain a first insight into the potential dynamics in such a circuit it is often valuable to look at the linear transmission of the system. Using the equations defined in the previous subsection it becomes possible to calculate this. Combining the equations from the previous subsection into one master equation for the ODE system yields:

$$\frac{d\mathbf{a}}{dt} = \left(\mathbf{M} + \mathbf{K}^{\mathbf{T}}\mathbf{C}_{in,ex}\mathbf{D}\right)\mathbf{a} + \mathbf{K}^{\mathbf{T}}\mathbf{C}_{in,ex}\mathbf{s}'_{ext} + \mathbf{N}(\mathbf{a}, t, ...) \tag{3.59}$$

As $\mathbf{N}(\mathbf{a}, t, ...)$ is the nonlinear part, we will ignore this in the remainder of the derivation in this subsection. Starting from $\frac{d\mathbf{a}}{dt} = 0$, we can calculate $\mathbf{a}_{ss}$:

$$\mathbf{a}_{ss} = -\left(\mathbf{M} + \mathbf{K}^T \mathbf{C}_{in,ex} \mathbf{D}\right)^{-1} \mathbf{K}^T \mathbf{C}_{in,ex} \mathbf{s}'_{ext}. \tag{3.60}$$

Using Eq. (3.56) the inputs to all components can be calculated:

$$\mathbf{s}_{in} = \mathbf{C}_{in,ex} \left[\mathbf{I} - \left(\mathbf{M} + \mathbf{K}^T \mathbf{C}_{in,ex} \mathbf{D}\right)^{-1} \mathbf{K}^T \mathbf{C}_{in,ex}\right] \mathbf{s}'_{ext}. \tag{3.61}$$

Given the similarity in physical meaning between the previous equation and Eq. (3.18), we can define a new version of the generalized connection matrix $\mathbf{C}^{CMT}_{in,ex}$:

$$\mathbf{C}^{CMT}_{in,ex} = \mathbf{C}_{in,ex} \left[\mathbf{I} - \left(\mathbf{M} + \mathbf{K}^T \mathbf{C}_{in,ex} \mathbf{D}\right)^{-1} \mathbf{K}^T \mathbf{C}_{in,ex}\right]. \tag{3.62}$$

This new matrix models the linear steady-state transmission through the circuit, taking the resonances due to the ODEs of the optical modes into account.

As the circuit only consists out of sources and detectors, s'_{ext} will only be different from zero at the port positions corresponding to the sources, while $\mathbf{s}_{in}$, only needs to be known at the port positions of the detectors. Consequently, often only a subset of this matrix needs to be calculated. This might seem a trivial remark, but in Sec. 3.10.3 we will see how a similar reasoning about the equations governing the time-domain simulations in some cases can result in a speed up in simulation time.

In principle, we could try to solve $\frac{d\mathbf{a}}{dt} = 0$, even if $\mathbf{N}(\mathbf{a}, t, ...)$ is included. Indeed, one could iteratively solve this system until it reaches steady-state, e.g., using Newton Rhapson techniques to solve the nonlinear equation (as done in SPICE-simulators) combined with continuation techniques to follow both stable and unstable steady-state solutions (as applied in [62]). However, preliminary simulations show that it is difficult to scale these techniques to larger circuits.

3.10.3 Increasing sparseness

In this subsection, we will use the knowledge of the positions of resonators, detectors and sources in a circuit to make the matrices in the system equations sparser, resulting in a speed improvement of the calculation time.

If a circuit contains cavities with a CMT model (in the remainder of this section we will always consider a cavity to be modeled by a CMT model), then we know that s'_{ext} will be equal to zero at those port positions. Similarly, port positions of detectors in the circuit will also correspond to additional zeros in s'_{ext}. We will now introduce a diagonal $p \times p$ matrix $\mathbf{I}^M_{ex}$, that contains a zero on the diagonal for each port that corresponds to a resonator or a detector. Using this matrix and Eq. (3.58), assuming that the rows of $\mathbf{D}$ are only nonzero at the port positions of resonators we can rewrite Eq. (3.16) to:

$$\mathbf{s}_{in,MC} = \mathbf{C}_{in,ex}\left[\left(\mathbf{I}-\mathbf{I}^{M}_{ex}\right)\mathbf{D}\mathbf{a}+\mathbf{I}^{M}_{ex}\mathbf{s}'_{ext}\right]. \tag{3.63}$$

The presence of $\mathbf{I}^{M}_{ex}$ in the previous equation generates additional zeros in the matrix products, making them sparser and hence potentially speeding up the calculations. Hence, $\mathbf{I}^{M}_{ex}$ can be considered to be some kind of 'mask' matrix.

Additionally, when doing a time-domain simulation, it is not necessary to calculate $\mathbf{s}_{in,MC}$ at the port positions that contain sources (assuming that these sources are not influenced by reflected signals from the circuit, as is the case in most simulations). We will now introduce a second diagonal $p \times p$ mask matrix $\mathbf{I}^{M}_{in}$, that contains a zero on the diagonal for each port that corresponds to a resonator or a source. By defining $\mathbf{s}'_{in,MC} = \mathbf{I}^{M}_{in}\mathbf{s}_{in,MC}$ as the vector that monitors the inputs of all the ML nodes, except for the sources and the resonators, we can rewrite $\mathbf{s}_{in,MC}$ to:

$$\mathbf{s}_{in,MC} = \mathbf{s}'_{in,MC} + \left(\mathbf{I}-\mathbf{I}^{M}_{in}\right)\mathbf{s}_{in,MC}. \tag{3.64}$$

Assuming that only the columns of $\mathbf{K^T}$ corresponding to the resonators are different from zero, $\mathbf{K^T}\mathbf{s}'_{in,MC} = 0$ and introduction of Eq. (3.64) in Eq. (3.57) results in:

$$\frac{d\mathbf{a}}{dt} = \mathbf{M}\mathbf{a} + \mathbf{K^T}\left(\mathbf{I}-\mathbf{I}^{M}_{in}\right)\mathbf{s}_{in,MC} + \mathbf{N}(\mathbf{a}, t, \ldots). \tag{3.65}$$

Substitution of Eq. (3.63) gives:

$$\begin{aligned}\frac{d\mathbf{a}}{dt} = {} & \left[\mathbf{M} + \mathbf{K^T}\left(\mathbf{I}-\mathbf{I}^{M}_{in}\right)\mathbf{C}_{in,ex}\left(\mathbf{I}-\mathbf{I}^{M}_{ex}\right)\mathbf{D}\right]\mathbf{a} \\ & + \left[\mathbf{K^T}\left(\mathbf{I}-\mathbf{I}^{M}_{in}\right)\mathbf{C}_{in,ex}\mathbf{I}^{M}_{ex}\right]\mathbf{s}'_{ext} + \mathbf{N}(\mathbf{a}, t, \ldots),\end{aligned} \tag{3.66}$$

while $\mathbf{s}'_{in,MC}$ can be calculated to be:

$$\mathbf{s}'_{in,MC} = \left[\mathbf{I}^{M}_{in}\mathbf{C}_{in,ex}\left(\mathbf{I}-\mathbf{I}^{M}_{ex}\right)\mathbf{D}\right]\mathbf{a} + \left[\mathbf{I}^{M}_{in}\mathbf{C}_{in,ex}\mathbf{I}^{M}_{ex}\right]\mathbf{s}'_{ext}. \tag{3.67}$$

In the previous two equations, we encounter four new matrices:

$$\left[\mathbf{M} + \mathbf{K^T}\left(\mathbf{I}-\mathbf{I}^{M}_{in}\right)\mathbf{C}_{in,ex}\left(\mathbf{I}-\mathbf{I}^{M}_{ex}\right)\mathbf{D}\right], \tag{3.68}$$

$$\left[\mathbf{K^T}\left(\mathbf{I}-\mathbf{I}^{M}_{in}\right)\mathbf{C}_{in,ex}\mathbf{I}^{M}_{ex}\right], \tag{3.69}$$

$$\left[\mathbf{I}^{M}_{in}\mathbf{C}_{in,ex}\left(\mathbf{I}-\mathbf{I}^{M}_{ex}\right)\mathbf{D}\right], \tag{3.70}$$

$$\left[\mathbf{I}^{M}_{in}\mathbf{C}_{in,ex}\mathbf{I}^{M}_{ex}\right]. \tag{3.71}$$

Dependent on the connection topology of the circuit, the first matrix can be dense, but the last three will generally be rather sparse. These matrices can be calculated in advance. Hence, in a time-domain simulation, integration of Eq. (3.66) can be done by updating only $\mathbf{s}'_{ext}$ instead of $\mathbf{s}_{ext}$. Advantageously, $\mathbf{s}'_{ext}$ will be sparser, and additionally, the output signals at the resonators do not need to be tracked anymore, as their influence on the inputs of other non-resonator MC components is incorporated by the matrix product with $\mathbf{a}$ in Eq. (3.67). Similarly, in circuits with a lot of resonators and sources, $\mathbf{s}'_{in,MC}$ is a lot sparser than $\mathbf{s}_{in,MC}$.

3.10.4 Applicability of the extended framework

It is important to note that the previous derivation considers general circuits, that can contain other components than sources, detectors and resonators. Hence, components such as waveguides with delay or SOAs can still be part of the circuit, making this extended framework very flexible.

Interestingly, the replacement of $\mathbf{C}_{in,ex}$ in Eq. (3.18) with its equivalent in Eq. (3.71) already offers a speed improvement in circuits without resonators, but with a significant number of detectors and sources. In this case, the matrices in Eq. (3.68)-(3.70) are dimensionless (i.e., the number of rows and/or columns is equal to zero), so their appearance in the equations does not slow down the calculation.

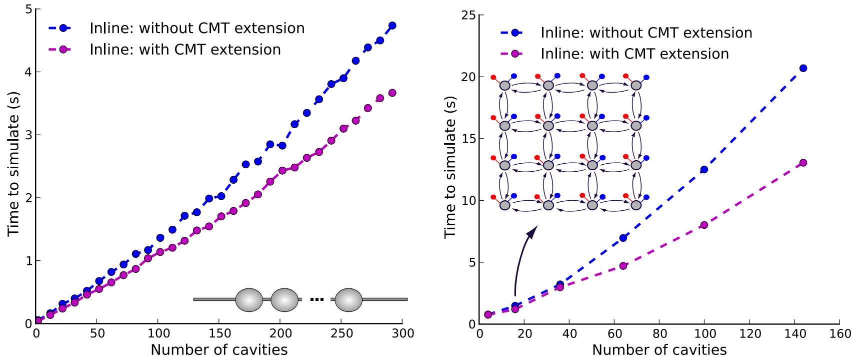

(a)

(b)

Figure 3.12: (left) In a long chain of inline PhC cavities, incorporation of the CMT formalism improves the simulation speed. In this simulation we used an equally long input signal as in Fig. 3.10(a). (right) A similar improvement can be seen in a simulation of a nanophotonic reservoir of inline PhC cavities in the topology of Fig. 3.9(a). In the latter simulation we used the same input signals as in Fig. 3.9(b), and this time the signals travel in two directions through the connections.

However, if we now consider circuits with a significant number of resonators, it depends on the circuit details how much the extended framework improves the simulation speed. In Fig. 3.12 we illustrate this using two examples. In Fig. 3.12(a) we simulate a chain of the inline PhC cavities discussed in Sec. 3.8.2.2. For large chains, using the extended framework results in a 25%-reduction in the number of non-zero elements in the matrix products. As a large part of the simulation time is spent in the calculation of these matrix products, this results in an almost equally large decrease of the total simulation time. In Fig. 3.12(b) we repeat the simulation of Fig. 3.9(b) for a nanophotonic reservoir of PhC cavities instead of SOAs. In this case, the relative reduction in calculation time is even stronger than for the cavity chain simulation. This is mainly due to the large number of sources and detectors in the nanophotonic reservoir, which brings along a lot of unnecessary calculations per time step in the original framework (e.g., propagating nonexistent output signals of the detectors to the sources).

3.11 Example: frequency simulation of a Coupled Resonator Optical Waveguide circuit

In the previous sections we have developed a framework that is suitable to do both time and frequency-domain simulations. In the subsequent chapters we will use this framework to do time-domain simulations and study the dynamics of nonlinear coupled systems. In this section we illustrate the other use-case of the framework with an example of a frequency-domain simulation. We will elucidate an approach to design a CROW (Fig. 3.7) with a flat pass-band filter of about 1 nm wide at 1.545 μm. Although we have shown in Fig. 3.7 that large circuits can be simulated, we will restrict the demonstration of the tool to only four rings. Standard optimization algorithms implemented in the scientific libraries in Python can be applied to optimize this circuit.

The transmission characteristic of a CROW is heavily dependent on the coupling strengths κ_i, $i \in [1,5]$, of the different coupling sections. Hence, these parameters can be adapted to retrieve the desired filter shape. Our filter should be centered around 1.545 μm. The resonance wavelength of the rings is determined by their roundtrip length, which we will keep fixed for all the rings. To optimize the κ_i-values we use the Covariance Matrix Adaptation Evolution Strategy (CMA-ES), a powerful evolutionary algorithm [63]. Due to the Python front-end of Caphe, we have easy access to a Python optimization library that implements this algorithm. During the optimization, we keep $\kappa_1 = \kappa_5$ and $\kappa_2 = \kappa_4$. The cost function that we feed to the algorithm is the integrated mean square error between the version of the filter for the current set of κ_i and the target filter. We applied CMA-ES with 33 generations and a population size of 14. As each simulation takes about 200 ms, this whole procedure takes a few minutes on a desktop computer. Figure 3.13 shows that the algorithm returns a solution that closely mimics the desired function. The optimized coupling values are $\kappa = [0.285, 0.017, 0.009, 0.017, 0.285]$.

Additional optimization generations would only result in small improvements, that will in practice not result in better performance. Indeed, during fabrication statistical variations in the device geometry appear, changing the κ values and effective indices of the waveguides. Hence, the fabricated and the designed filter will differ. Unfortunately, these variations have an important influence on the performance of the filter. In the simulation in Fig. 3.13(b), a random variation on the resonance wavelength of 0.5 nm of the original designed circuit on the simulated filter output decreases the filter performance enormously .

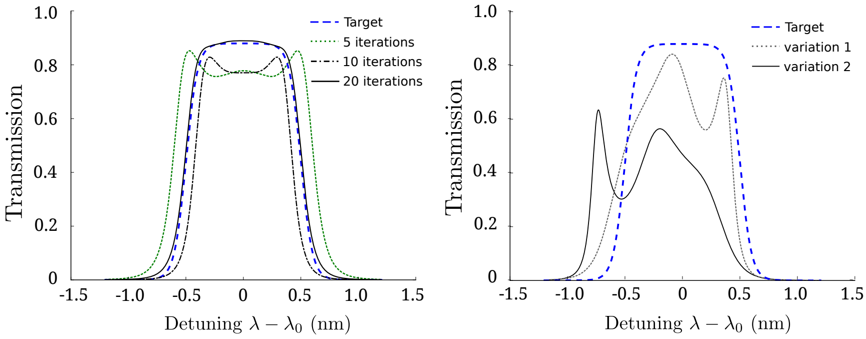

(a) Optimizing the filter (b) Process variations

Figure 3.13: (left) The the κ_i of a Coupled Ring Optical Waveguide (CROW) can be optimized to match a desired filter characteristic. (right) If realistic process variations are added to the original design specifications, performance deteriorates.

The process variations can be compensated by using heaters on top of the rings. Indeed, these heaters change the refractive index locally. In SOI the resonance wavelength of rings due to process variations varies over ~ 1 nm [64]. The refractive index change required to compensate this is approximately 0.0022. As $dn_{eff}/dT \simeq 1.86 \cdot 10^{-4}$ [65], the heater needs to change the temperature by 12 °C. Well designed heaters can achieve this using less than 1 mW [66, 67]. Assuming a uniform distribution of the resonance variations, approximately 6 °C thermal tuning per ring is needed. Consequently, each heater will consume on average ~ 0.5 mW.

3.12 Future work

As discussed in Sec. 3.2.1, the future use of Caphe will not only depend on its intrinsic capabilities (i.e., speed, user-friendliness, general applicability, ...), but also on its integration with other simulation and design tools. Nonetheless, some improvements of the proposed framework still need to be made, to make the software package even more attractive to the end-user. The most important challenges are discussed briefly in the following subsections.

3.12.1 Multiwavelength simulations

We have developed the whole framework using an envelope approximation with one common carrier for the whole circuit. Nonetheless, as discussed in Sec. 3.3.2, the choice of multiple carrier frequencies is compatible to our framework. Indeed, in principle, one could extend the S-matrix of a component to a larger multiwavelength scatter-matrix. This matrix would be a block diagonal matrix, in which each block would correspond to the different carrier frequencies. The derivation of the generalized connection matrix could then be done, starting from this extended scatter-matrix. The CMT-based matrices defined in Sec. 3.10.3, can be extended in a similar way, assuming that the optical modes in the resonators are also subdivided in frequency bands that correspond to the envelope frequencies.

3.12.2 Time-domain model of dispersion

In time-domain simulations, if the bandwidth of an input signal becomes very large, dispersion effects might appear for some components. Indeed, if the phase change over this bandwidth becomes significant, different frequency bands of the signal will have different delays. We have discussed this maximal bandwidth issue in Sec. 3.7.2.2 for a microring, and in Sec. 3.9.1 we have shown how a CMT model of a ring can take such effects into account near a given resonance frequency.

When simulating long waveguides, used as, e.g., delay lines, we can model such a waveguide using the cyclic buffers incorporated in our framework (they can be accessed in the calculation of the general source term in Sec. 3.6). As long as the dispersion is linear, it is sufficient to take the group index of the material into account when calculating the delay of such a waveguide given its length. However, in the SOI-platform, higher-order dispersive terms need to be taken into account. The implementation using a digital filter approach is a memory-consuming one, and will slow down simulations of large circuits. That is why we believe other techniques, such as vector fitting can form a valuable alternative (see Sec 3.6 and [43]).

3.12.3 Co-simulation of electronic and photonic circuits

In Sec. 3.3.1 we have discussed how a travelling-wave representation of the signals in the equations is an optimal choice from the physics point-of-view, resulting in simplifications of the calculations. Another choice is the one chosen in [19], where the variables are still expressed as travelling-waves, but the equations are mapped onto SPICE-circuits. When simulating circuits with both photonic and electronic components, the latter approach has the advantage that the simulations of the electronic components can be done using the default SPICE libraries for electronic circuits.

In the previous sections we did not yet mention that electronic circuits can also be represented in our framework. Using the link between the scatter-matrix formalism and bond-graph theory, as presented in [68], we can model electronic circuits in a bond-graph formalism, and map this into our scatter-matrix formalism, with the potential to reuse all the optimizations for the electronic circuit simulations. Currently, we did not yet benchmark this approach with native electronic circuit solvers. However, if speed limitations due to this mapping approach would appear, we could still opt for a simulation in which our framework interfaces with a default SPICE simulator.

3.12.4 Noise modeling

Thus far, we did not discuss how noise can be included in the simulations. In this dissertation we will not include noise terms, but literature shows that there are many reasons to investigate its implementation in future work. Noise can have many different origins. It occurs both in experimental electronic and photonic systems. Hence, in some cases it is a significant term in the rate equations of an optical component as it can severely influence the dynamics. For instance, when modeling lasers or optical amplifiers, often a noise term, the Langevin force, related to amplified spontaneous emission, is necessary to model the dynamics accurately [69–71]. Furthermore, in excitable optical components, related to the ones we will study in the subsequent chapters, noise induces many interesting effects such as coherence or stochastic resonance [72–74]. In summary, including noise in the framework will make the gap between simulations and experiments even smaller.

In principle, white noise can be simulated with the current framework, when using a fixed stepsize. One could consider the noise term to be an external source and fill one of the cyclic buffers at every timestep with a data point sampled from, e.g., a Gaussian distribution. However, in future work, it might be better to include a native random number generation in the core of the framework, to allow for an implementation that is compatible with the faster adaptive stepsize integration algorithms, using the algorithms used in, e.g., [75, 76].

3.12.5 Variability and yield analysis

Deviations due to process variations between experimental integrated components and the corresponding design target, influence the performance of larger circuits. Hence, it is important to analyse the robustness of circuit dynamics to such variations of component parameters in order to optimize the fabrication yield of the circuits [29]. Similar to Sec. 3.11, one can use Monte Carlo sweeps, in which the parameters of the components are varied within a realistic range by sampling a probablistic distribution. This implies that one has to resimulate the circuit many times, for all the different parameter values. At the end of such a Monte Carlo sweep, statistics are done on the performance of the circuit. More advanced techniques have been proposed for variability analysis of on-chip (electronic) interconnects [77]. As these techniques are computationally more efficient and given the similarity between electronic interconnects and photonic integrated systems it is worthwhile to study the applicability of these techniques to photonic circuit simulations. Preliminary algebraic calculations show that these technique seem indeed compatible to our framework.

3.13 Conclusion

The framework proposed in this chapter allows for the modeling of optical circuits both in the time-domain and in the frequency-domain. In the frequency-domain, it can be used to calculate the (linear) steady-state characteristics of very large circuits. In the time-domain it enables the efficient simulation of highly nonlinear systems by eliminating those components that can be fully described using only a scatter-matrix. The elimination of this type of components reduces the effective size of the circuit, and consequently speeds up the time-domain simulations. Due to a very flexible definition of the properties of the basic building block of the framework, we believe it can be used for other dynamical systems such as electrical systems and neural networks.

As the optical components in the subsequent chapters are modeled using CMT, we have introduced the concepts of this formalism, and have shown how our framework can be extended with a CMT-compatible matrix formalism.

While the software framework was originally developed for time-domain simulations of nonlinear dynamics in nanophotonic integrated circuits, it is already frequently being used for other applications in photonics, such as in optical filter design. The software framework Caphe is therefore a very promising tool, as it is very fast, flexible, and can be combined with other scientific libraries which are readily available in Python.

References

[1] Sarvagya Dwivedi, Herbert D'heer, and Wim Bogaerts. *A Compact All-Silicon Temperature Insensitive Filter for WDM and Bio-Sensing Applications.* IEEE Photonics Technology Letters, 25(22):2167–2170, November 2013.

[2] Martin Fiers, Thomas Van Vaerenbergh, Francis Wyffels, David Verstraeten, Benjamin Schrauwen, Joni Dambre, and Peter Bienstman. *Nanophotonic reservoir computing with photonic crystal cavities to generate periodic patterns.* IEEE Transactions on Neural Networks and Learning Systems, 25(1):344–355, 2014.

[3] M Fiers, T Van Vaerenbergh, Pieter Dumon, Ken Caluwaerts, Benjamin Schrauwen, Joni Dambre, and Peter Bienstman. *CAPHE: a circuit-level time-domain and frequency-domain modeling tool for nonlinear optical components.* 16th Annual Symposium of the IEEE Photonics Benelux Chapter, 2011.

[4] Martin Fiers, Thomas Van Vaerenbergh, Ken Caluwaerts, Dries Vande Ginste, Benjamin Schrauwen, Joni Dambre, and Peter Bienstman. *Time-domain and frequency-domain modeling of nonlinear optical components on circuit-level using a node-based approach.* J. Opt. Soc. Am. B , 29(5):896–900, 2011.

[5] M. Fiers. *Nanophotonic Reservoir Computing Using Photonic Crystal Cavities.* PhD thesis, Ghent University, 2012-2013.

[6] Ardavan F. Oskooi, David Roundy, Mihai Ibanescu, Peter Bermel, J. D. Joannopoulos, and Steven G. Johnson. *MEEP: A flexible free-software package for electromagnetic simulations by the FDTD method.* Computer Physics Communications, 181:687–702, January 2010.

[7] Emmanuel Lambert, Martin Fiers, Shawkat Nizamov, Martijn Tassaert, and Wim Bogaerts. *Python bindings for the open source electromagnetic simulator MEEP.* Computing in Science and Engineering, 2010.

[8] P. Bienstman and R. Baets. *Optical Modelling of Photonic Crystals and VCSELs Using Eigenmode Expansion and Perfectly Matched Layers.* Opt. Quantum Electron., 33:327–341, 2001. CAMFR simulation software is freely available from http://camfr.sourceforge.net/.

[9] http://camfr.sourceforge.net.

[10] http://www.photond.com/products/fimmwave.htm.

[11] Kristof Vandoorne, Wouter Dierckx, Benjamin Schrauwen, David Verstraeten, Roel Baets, Peter Bienstman, and Jan Van Campenhout. *Toward optical signal processing using Photonic Reservoir Computing.* Opt. Express , 16(15):11182–11192, JUL 21 2008.

[12] Kristof Vandoorne, Joni Dambre, David Verstraeten, Benjamin Schrauwen, and Peter Bienstman. *Parallel reservoir computing using optical amplifiers.* IEEE transactions on neural networks, 22(9):1469–1481, 2011.

[13] Kristof Vandoorne. *Photonic reservoir computing with a network of coupled semiconductor optical amplifiers.* PhD thesis, Ghent University, 2010-2011.

[14] Govind Agrawal. *Nonlinear Fiber Optics, Third Edition (Optics and Photonics).* 2007.

[15] http://www.aspicdesign.com/.

[16] http://www.vpiphotonics.com/optical_systems.php.

[17] http://www.photond.com/products/picwave.htm.

[18] http://www.rsoftdesign.com/products.php?sub=System+and+Network&itm=OptSim.

[19] P. Gunupudi, T. Smy, J. Klein, and Z.J. Jakubczyk. *Self-Consistent Simulation of Opto-Electronic Circuits Using a Modified Nodal Analysis Formulation.* Advanced Packaging, IEEE Transactions on, 33(4):979 –993, nov. 2010.

[20] Tom Smy, Pavan Gunupudi, Steve Mcgarry, and Winnie N Ye. *Circuit-level transient simulation of configurable ring resonators using physical models.* America, 28(6):1534–1543, 2011.

[21] http://www.caphesim.com.

[22] https://www.lumerical.com/tcad-products/interconnect/.

[23] Sergei Mingaleev, Eugene Sokolov, Cristina Arellano, Igor Koltchanov, and Andre Richter. *Hybrid Time-and-Frequency-Domain approach for modeling photonic integrated circuits.* 2011 Numerical Simulation of Optoelectronic Devices, pages 183–184, September 2011.

[24] C. Arellano, S. F. Mingaleev, E. Sokolov, I. Koltchanov, and A. Richter. *Time-and-frequency-domain modeling (TFDM) of hybrid photonic integrated circuits.* 8265:82650K, February 2012.

[25] C. Arellano, S. Mingaleev, I. Koltchanov, A. Richter, J. Pomplun, S. Burger, and F. Schmidt. *Efficient design of photonic integrated circuits (PICs) by combining device- and circuit- level simulation tools.* 8627:862711, March 2013.

[26] Wim Bogaerts, Paul Bradt, Lieven Vanholme, Peter Bienstman, and Roel Baets. *Closed-loop modeling of silicon nanophotonics from design to fabrication and back again.* Optical and Quantum Electronics, 40(11-12):801–811, January 2009.

[27] Wim Bogaerts, Pieter Dumon, Emmanuel Lambert, Martin Fiers, Shibnath Pathak, and Antonio Ribeiro. *IPKISS: A parametric design and simulation framework for silicon photonics.* The 9th International Conference on Group IV Photonics (GFP), 2:30–32, August 2012.

[28] Martin Fiers, Emmanuel Lambert, Shibnath Pathak, Bjorn Maes, Peter Bienstman, Wim Bogaerts, and Pieter Dumon. *Improving the design cycle for nanophotonic components.* Journal of Computational Science, 4(5):313–324, September 2013.

[29] Wim Bogaerts, Martin Fiers, and Pieter Dumon. *Design Challenges in Silicon Photonics.* 14(4):1–8, 2014.

[30] LW Nagel and DO Pederson. *SPICE: Simulation program with integrated circuit emphasis.* Memorandum No. ERL-M382, University of California, Berkeley, 1973.

[31] A. Ruehli and P. Brennan. *The modified nodal approach to network analysis.* IEEE Transactions on Circuits and Systems, 22(6):504–509, June 1975.

[32] How-Siang Yap. *Designing to digital wireless specifications using circuit envelope simulation.* In Microwave Conference Proceedings, 1997. APMC'97, 1997 Asia-Pacific, volume 1, pages 173–176. IEEE, 1997.

[33] Shmuel Ben-Yaakov, Stanislav Glozman, and Raul Rabinovici. *Envelope simulation by SPICE-compatible models of linear electric circuits driven by modulated signals.* Industry Applications, IEEE Transactions on, 37(2):527–533, 2001.

[34] Nuno B Carvalho, José C Pedro, Wonhoon Jang, and Michael B Steer. *Nonlinear RF circuits and systems simulation when driven by several modulated signals.* Microwave Theory and Techniques, IEEE Transactions on, 54(2):572–579, 2006.

[35] R Dekker, a Driessen, T Wahlbrink, C Moormann, J Niehusmann, and M Först. *Ultrafast Kerr-induced all-optical wavelength conversion in silicon waveguides using 1.55 mum femtosecond pulses.* Optics express, 14(18):8336–46, September 2006.

[36] L Stampoulidis, K Vyrsokinos, K Voigt, L Zimmermann, F Gomez-Agis, H J S Dorren, D Van Thourhout, L Moerl, J Kreissl, B Sedighi, J C Scheytt, A Pagano, and E Riccardi. *The European BOOM Project: Silicon Photonics for High-Capacity Optical Packet Routers.* IEEE Journal of Selected Topics in Quantum Electronics, 16(5):1422–1433, September 2010.

[37] Rajesh Kumar, Thijs Spuesens, Pauline Mechet, Pragati Kumar, Oded Raz, Nicolas Olivier, Marc Fedeli, Gunther Roelkens, Roel Baets, Dries Van Thourhout, and Geert Morthier. *Ultra-fast and Bias-free All-Optical Wavelength Conversion Using III-V on Silicon Technology.* pages 9–11, 2011.

[38] S Malaguti, G Bellanca, and S Trillo. *Optimizing pump-probe switching ruled by free-carrier dispersion.* 21(13):15859–15868, 2013.

[39] Thomas James Johnson. *Silicon microdisk resonators for nonlinear optics and dynamics.* PhD thesis, California Institute of Technology, 2009.

[40] Piero Triverio, Stefano Grivet-Talocia, Michel S Nakhla, Flavio G Canavero, and Ramachandra Achar. *Stability, causality, and passivity in electrical interconnect models.* Advanced Packaging, IEEE Transactions on, 30(4):795–808, 2007.

[41] Dirk Jalas, Alexander Petrov, Manfred Eich, Wolfgang Freude, Shanhui Fan, Zongfu Yu, Roel Baets, Miloš Popović, Andrea Melloni, John D. Joannopoulos, Mathias Vanwolleghem, Christopher R. Doerr, and Hagen Renner. *What is - and what is not - an optical isolator.* Nature Photonics, 7(8):579–582, July 2013.

[42] Jirí Čtyroký, Ivan Richter, and Milan Šinor. *Dual resonance in a waveguide-coupled ring microresonator.* Optical and Quantum Electronics, 38(9-11):781–797, January 2007.

[43] Francesco Ferranti and Yves Rolain. *Variance weighted vector fitting for noisy frequency responses.* Microwave and wireless components letters, 20(4):187–189, 2010.

[44] William H. Press, Saul A. Teukolsky, William T. Vetterling, and Brian P. Flannery. *Numerical Recipes: The Art of Scientific Computing.* 2007.

[45] Timothy A. Davis and Ekanathan Palamadai Natarajan. *Algorithm 8xx: KLU, a direct sparse solver for circuit simulation problems.*

[46] Timothy A. Davis. *Direct methods for sparse linear systems.* 2006.

[47] Ken Stanley. *KLU: a Clark Kent sparse LU factorization algorithm for circuit matrices.* 2004 SIAM Conference on Parallel Processing for Scientific Computing (PP04), 2004.

[48] TA Davis and E Palamadai Natarajan. *Algorithm 907: KLU, a direct sparse solver for circuit simulation problems.* ACM Transactions on Mathematical software, 37(3), 2010.

[49] Kristof Vandoorne, Joni Dambre, David Verstraeten, Benjamin Schrauwen, and Peter Bienstman. *Parallel reservoir computing using optical amplifiers.* IEEE Transactions On Neural Networks, 22(9):1469–1481, 2011.

[50] Bjorn Maes, Martin Fiers, and Peter Bienstman. *Self-pulsing and chaos in series of coupled nonlinear micro-cavities.* Physical Review B11, 7911(111), 200911.

[51] Mehmet Fatih Yanik, Shanhui Fan, and Marin Soljacic. *High-contrast all-optical bistable switching in photonic crystal microcavities.* Applied Physics Letters, 83(14):2739 –2741, oct 2003.

[52] B.E. Little, S.T. Chu, H.A. Haus, J. Foresi, and J.-P. Laine. *Microring resonator channel dropping filters.* Journal of Lightwave Technology, 15(6):998–1005, June 1997.

[53] C Manolatou, MJ Khan, SH Fan, PR Villeneuve, HA Haus, and JD Joannopoulos. *Coupling of modes analysis of resonant channel add-drop filters.* IEEE Journal of Quantum Electronics, 35(9):1322–1331, 1999.

[54] S. Fan, W. Suh, and JD Joannopoulos. *Temporal coupled-mode theory for the Fano resonance in optical resonators.* JOSA A, 20(3):569–572, 2003.

[55] W. Suh, Z. Wang, and S. Fan. *Temporal coupled-mode theory and the presence of non-orthogonal modes in lossless multimode cavities.* Quantum Electronics, IEEE Journal of, 40(10):1511–1518, 2004.

[56] HA Haus. *Waves and fields in optoelectronics.* 1984.

[57] H. Haus, W. Huang, S. Kawakami, and N. Whitaker. *Coupled-mode theory of optical waveguides.* Journal of Lightwave Technology, 5(1):16–23, 1987.

[58] H.A. Haus and W. Huang. *Coupled-mode theory.* Proceedings of the IEEE, 79(10):1505–1518, 1991.

[59] Thomas Van Vaerenbergh. *Photonic reservoir computing op basis van thermische niet-lineariteiten in ring resonatoren.* Master's thesis, UGent, 2010.

[60] Marin Soljačić, Mihai Ibanescu, Steven G. Johnson, Yoel Fink, and J. D. Joannopoulos. *Optimal bistable switching in nonlinear photonic crystals.* Phys. Rev. E, 66:055601, Nov 2002.

[61] Mohammad Soltani. *Novel Integrated Silicon Nanophotonic Structures using Ultra-high Q Resonators A Thesis COPYRIGHT 2009 BY MOHAMMAD SOLTANI Novel Integrated Silicon Nanophotonic Structures using Ultra-high Q Resonators.* Technology, (December), 2009.

[62] R. H. Clewley, W. E. Sherwood, M. D. LaMar, and J. M. Guckenheimer. *PyDSTool, a software environment for dynamical systems modeling.* 2007.

[63] N. Hansen. *The CMA evolution strategy: a comparing review.* In J.A. Lozano, P. Larranaga, I. Inza, and E. Bengoetxea, editors, Towards a new evolutionary computation. Advances on estimation of distribution algorithms, pages 75–102. Springer, 2006.

[64] S.K. Selvaraja, W. Bogaerts, P. Dumon, D. Van Thourhout, and R. Baets. *Subnanometer Linewidth Uniformity in Silicon Nanophotonic Waveguide Devices Using CMOS Fabrication Technology.* Selected Topics in Quantum Electronics, IEEE Journal of, 16(1):316–324, jan.-feb. 2010.

[65] F. De Leonardis, A. V. Tsarev, and V. M. N. Passaro. *Optical properties of new wide heterogeneous waveguides with thermo optical shifters.* Optics Express, 16(26):21333–21338, 2008.

[66] Daoxin Dai, Liu Yang, and Sailing He. *Ultrasmall Thermally Tunable Microring Resonator With a Submicrometer Heater on Si Nanowires.* Lightwave Technology, Journal of, 26(6):704–709, march15, 2008.

[67] Ciyuan Qiu, Jie Shu, Zheng Li, Xuezhi Zhang, and Qianfan Xu. *Wavelength tracking with thermally controlled silicon resonators.* Optics Express, pages 5143–8, 2011.

[68] RG Longoria. *Wave-scattering formalisms for multiport energetic systems.* Journal of the Franklin Institute, 333(4):539–564, 1996.

[69] GP Agrawal. *Fiber-optic communication systems.* 6:0–471, 1997.

[70] B. Kelleher, C. Bonatto, P. Skoda, S. P. Hegarty, and G. Huyet. *Excitation regeneration in delay-coupled oscillators.* Physical Review E, 81(3):036204, March 2010.

[71] Sylvain Barbay, Robert Kuszelewicz, and Alejandro M Yacomotti. *Excitability in a semiconductor laser with saturable absorber.* Optics letters, 36(23):4476–8, dec 2011.

[72] Weiping Lu, Dejin Yu, and Robert G Harrison. *Excitability in a nonlinear optical cavity.* 58(2):809–811, 1998.

[73] Francesco Marino, Massimo Giudici, Stéphane Barland, and Salvador Balle. *Experimental Evidence of Stochastic Resonance in an Excitable Optical System.* Physical Review Letters, 88(4):040601, January 2002.

[74] Stéphane Barland, Oreste Piro, Massimo Giudici, Jorge Tredicce, and Salvador Balle. *Experimental evidence of van der Pol-Fitzhugh-Nagumo dynamics in semiconductor optical amplifiers.* Physical Review E, 68(3):036209, September 2003.

[75] V. Flunkert and E. Schöll. *pydelay – a python tool for solving delay differential equations.* `arXiv:0911.1633 [nlin.CD]`, 2009.

[76] PM Burrage and K Burrage. *A variable stepsize implementation for stochastic differential equations.* SIAM Journal on Scientific Computing, 24(3):848–864, 2003.

[77] Dries Vande Ginste, Daniel De Zutter, Dirk Deschrijver, Tom Dhaene, Paolo Manfredi, and Flavio Canavero. *Stochastic modeling-based variability analysis of on-chip interconnects.* IEEE transactions on components, packaging and manufacturing technology, 2(7):1182–1192, 2012.

4

Cascadable excitability in microrings

To emulate a spiking neuron, a photonic component needs to be excitable. In this chapter, we theoretically simulate and experimentally demonstrate cascadable excitability near a self-pulsation regime in high-Q-factor silicon-on-insulator microrings. For the theoretical study we use Coupled Mode Theory (CMT). We show that if we neglect the fast energy and phase dynamics of the cavity light, we can still preserve the most important microring dynamics by only keeping the temperature difference with the surroundings and the concentration of free carriers as dynamical variables of the system. As a result we can analyse the microring dynamics in a 2D phase portrait. For some wavelengths, when changing the input power, the microring undergoes a subcritical Andronov-Hopf (AH) bifurcation at the self-pulsation onset. As a consequence the system shows Class 2 excitability. Experimental single-ring excitability and self-pulsation behaviour follows the theoretic predictions. Moreover, simulations and experiments show that this excitation mechanism is cascadable.

The rest of this chapter is structured as follows. We first give some additonal background on the link between slow-fast dynamics in optical systems with thermo-electrical nonlinearities and excitability in Sec. 4.1. In Sec. 4.2, we write down the CMT-equations for a microring, as this formalism allows to incorporate the contributions of all the relevant physical effects in a very intuitive way. In Sec. 4.3 we use standard nonlinear dynamical phase-planes and bifurcation diagrams to analyse those rate equations. In this section, we not only demonstrate how we can simplify the CMT-equations while still preserving the relevant physics of the problem, but also identify the exact bifurcation type at the oscillation onset. Subsequently, in Sec. 4.4, we analyse some time-traces to illustrate how the microring can be excited. In addition, we demonstrate that this excitability is cascadable. In Sec. 4.5, we confirm with some experimental results the predictions from the simulations. All the time-traces in this chapter are simulated with Caphe, the nonlinear component circuit simulator introduced in chapter 3, while PyDSTool [1] is used to continue the limit cycles during the bifurcation analysis.

The results have been published in two articles in peer-reviewed journals [2, 3].

4.1 Excitability in thermo-electrical nonlinear photonic components

A high Q/V-ratio enhances light-matter interaction in a microcavity and accordingly reduces the required input power for nonlinear behaviour. Consequently, in a passive microcavity with a high Q/V-ratio, if the resonance wavelength of light with sufficiently high input power is detuned close to the resonance wavelength of the cavity, both self-pulsation and excitability can be observed [4–8].

In Silicon-On-Insulator (SOI) cavities, Two Photon Absorption (TPA) generates both free carriers and heat. Other heating mechanisms are Surface State Absorption (SSA) and Free Carrier Absorption (FCA). The presence of the free carriers induces a blueshift of the resonance wavelength, known as Free Carrier Dispersion (FCD), while the heating of the cavity induces a red-shift due to the thermo-optic effect. The difference between the timescales of the fast free carrier dynamics and the slow heating effects results in self-pulsation in whispering gallery mode cavities such as microdisks and microrings [4–6]. In Indium Phosphide (InP)-based 2D Photonic Crystal (PhC) resonators or PhC nanocavities a similar type of self-pulsation is visible [7, 8], even though the main heating and free carrier generation mechanism in this material system is Single Photon Absorption (SPA) instead of TPA. Moreover, excitability is perceived in InP PhC cavities, close to the self-pulsation region, mainly at the blue side of the resonance [7, 8].

In this chapter, we focus on a simple SOI microring. Similar to [7, 8], we will demonstrate in this chapter how this self-pulsation is linked with excitability.
In literature the mechanism behind this self-pulsation (or excitability) in microrings, microdisks and similar passive cavities is often explained using CMT. Time-domain simulations in this formalism show a good correspondence with

experiments [5, 6, 9]. Moreover, the steady state equations are still analytically tractable, both for varying power and wavelength of the input light. For SOI microdisks no hysteresis in the threshold of the input wavelength for the onset of oscillations is found, which indicates a supercritical AH bifurcation [6]. As we explained in Sec. 2.3.1.2, in such a supercritical AH, a stable Fixed Point (FP) bifurcates to an unstable FP together with a stable Limit Cycle (LC), as opposed to a subcritical AH, where an unstable FP bifurcates into a stable FP together with a stable LC (with an unstable LC in-between) [10]. Both subtypes correspond to Class 2 excitability in which the order of magnitude of the nearby self-pulsation period will be relatively insensitive to the power or wavelength of the pump signal.

Additionally, the CMT-equations can be rewritten into the mean-field model used in [7, 8]. Using the steady state curves and corresponding 2D projections of nullclines of this model, the Class 2 excitability of a 2D InP PhC can be explained [8]. There as well, a sweep of the input wavelength indicates an AH bifurcation, but the exact subtype is not specified. Similar behaviour appears in PhC nanocavities [7].

Besides the theoretical work that has been done to explain the dynamics in the aforementioned integrated nonlinear cavities using CMT-like models, it is worthwhile to mention the research related to excitability and self-pulsation due to the interaction between free carriers and heating in Semiconductor Optical Amplifiers (SOAs) [11]. The slow-fast dynamics due to thermo-electrical nonlinearities are equivalent to the dynamics observed in the integrated devices mentioned above. In contrast to the cavity-based devices, there is no resonance mechanism in a SOA. However, by changing the input power strength or the electrical injection, this component can be put in similar dynamic regimes. As described in Sec. 2.4.2, the excitability mechanism in this component was explained using the analogy with the well-known forced Van der Pol oscillator [11]. This is a special case of the Fitzhugh-Nagumo equations, a two-dimensional differential equation system that is often used to explain the dynamical behaviour in biological neurons [10]. In this case, excitability is proven to appear by the presence of a supercritical Hopf-bifurcation, accompagnied by a nearby canard explosion, just as in the default Van der Pol system [12]. In this canard explosion, the small amplitude oscillations of the stable LC near the AH-bifurcation are blown up to large amplitude oscillations within a tiny control parameter range, as a consequence of the slow-fast dynamics of the system. This results in nice large pulses when the system is excited from an equilibrium position near the self-pulsation onset.

As the computational properties of the microring used as a spiking neuron are linked to the relevant bifurcation types [10], we will focus on the bifurcation type at the onset of self-pulsation, for varying input power and fixed input wavelength. This takes into account that, on a photonic chip, information is encoded in the amplitude and phase of the light, while the wavelength rather corresponds to the choice of channel the information is transferred in. Classifying this bifurcation allows us to predict how the microring can be excited by input signals [10]. This helps to understand how it could process information in a (photonic) spiking neural network. Furthermore, we focus on the cascadability of these optical spiking neuron units, as this is a crucial feature when building networks.

4.2 Silicon-on-insulator microring resonator

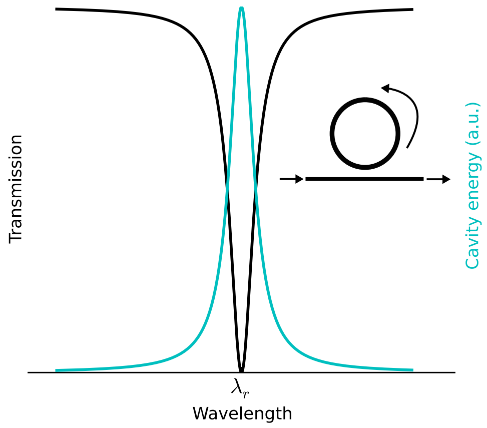

Figure 4.1: The transmission of an all-pass ring is minimal at the resonance wavelength, while the energy in the cavity is maximal. For high input powers, this implies that nonlinear interactions will be enhanced in the ring for wavelengths near the resonance wavelength.

To enhance the nonlinear interactions in SOI-waveguides, we use a microring as resonant structure. Using one or two directional couplers we couple light in and out of a waveguide loop. For wavelengths that fit exactly an integer number of times in the optical roundtrip length of the ring, the resonance condition is fullfilled, i.e., after one roundtrip light interferes constructively with itself [13]. Hence, if the waveguide and coupling losses in the ring are low and the input wavelength is near this resonance condition, light can make multiple roundtrips before it couples out of the ring, is absorbed or is scattered away. This results in an increase of the optical field in the ring waveguide with respect to, e.g., the access waveguides, intensifying the nonlinear interactions between light and the silicon core of the ring waveguide. Figure 4.1 schematically depicts the spectral behaviour of an all-pass ring near resonance: the energy in the cavity is maximal at resonance, while the transmission is minimal. Here, we have used the linear CMT-model of a microring derived in the previous chapter in Sec. 3.9.1.

In this section we will introduce the model for this nonlinear SOI microring, together with the numerical parameters that we use during the simulations.

4.2.1 CMT-equations of a nonlinear microring

In previous research in our group, optical bistability and self-pulsation in a SOI-microring has experimentally been demonstrated [4]. Hence, we need a model that is sufficiently rich to explain this behaviour. For this purpose, we use the CMT-description of a microring, in which we can include several physical effects in a limited number of rate equations.

A first important effect in bulk silicon is TPA, which generates free carriers. These free carriers are then able to absorb light by FCA. In addition, the presence of free carriers causes a blueshift in the wavelength by FCD. In SOI microrings also (linear) SSA at the silicon-silica interface is present, and at the same time some light is lost due to surface scattering and radiation loss [4]. The absorbed optical energy is mainly lost by thermalization, which generates heating. Due to the thermo-optic effect this heat results in a redshift in the resonance wavelength. The free carriers typically relax at least one order of magnitude faster than the temperature.

When the backscattering in the microring is neglected, the dynamics of the ring can be described in CMT with one complex variable (the mode amplitude $a = |a|e^{j\phi}$, with $|a|^2$ the energy in the cavity and ϕ the phase), and two real variables (the mode-averaged temperature difference with the surroundings ΔT and the concentration of free carriers N). In this chapter, we study an All-Pass (AP) filter with one input: a single ring coupled with only one bus waveguide. The CMT-equations are then [5, 6, 9, 14]:

$$\frac{\mathrm{d}a}{\mathrm{d}t} = \left[j\left(\omega_r + \delta\omega_{nl} - \omega\right) - \frac{\gamma_{loss}}{2} \right] a + \kappa s_{in}, \tag{4.1}$$

$$\frac{\mathrm{d}\Delta T}{\mathrm{d}t} = -\frac{\Delta T}{\tau_{th}} + \frac{\Gamma_{th}\gamma_{abs}|a|^2}{\rho_{Si} c_{p,Si} V_{th}}, \tag{4.2}$$

$$\frac{\mathrm{d}N}{\mathrm{d}t} = -\frac{N}{\tau_{fc}} + \frac{\Gamma_{FCA}\beta_{Si} c^2 |a|^4}{2\hbar\omega V_{FCA}^2 n_g^2}, \tag{4.3}$$

$$s_{out} = e^{j\phi_c} s_{in} + \kappa a, \tag{4.4}$$

with s_{in} the amplitude of the input light (input power $P_{in} = |s_{in}|^2$), s_{out} the amplitude of the output light (output power $P_{out} = |s_{out}|^2$), ϕ_c the phase propagation in the bus waveguide, κ the coupling from waveguide to ring, $\omega_r = \frac{2\pi c}{\lambda_r}$ the resonance frequency of the cavity and $\omega = \frac{2\pi c}{\lambda}$ the frequency of the input light. τ_{th} and τ_{fc} are the relaxation times for resp. the temperature and the free carriers. β_{Si} is the constant governing TPA, $c_{p,Si}$ the thermal capacity, ρ_{Si} the density of silicon and n_g is the group index. We neglect dispersion and take $n_g = n_{Si}$, with n_{Si} the refractive index of bulk silicon. We also use the effective volumes V_α and confinements Γ_α corresponding to a physical effect α defined in [6]. In Eqs. (4.1) and (4.2) γ_{loss} and γ_{abs} are resp. the total loss and absorption loss in the cavity, with:

$$\gamma_{loss} = \gamma_{coup} + \gamma_{rad} + \gamma_{abs}, \tag{4.5}$$

where we have introduced the coupling loss into the waveguide γ_{coup} (with $\kappa = j\sqrt{\gamma_{coup} e^{j\phi_c}}$) and the radiation loss γ_{rad}. In the ring we have absorption by linear surface absorption, TPA and FCA :

$$\gamma_{abs} = \gamma_{abs,lin} + \Gamma_{TPA} \frac{\beta_{Si} c^2 |a|^2}{n_g^2 V_{TPA}} + \Gamma_{FCA} \frac{\sigma_{Si} c}{n_g} N, \tag{4.6}$$

σ_{Si} is the absorption cross section of FCA and $\gamma_{abs,lin}$ the linear absorption constant. In SOI $\eta_{lin} = \frac{\gamma_{abs,lin}}{\gamma_{abs,lin} + \gamma_{rad}} \approx 0.4$ [4, 14], so we use this value throughout the chapter. The thermo-optic effect and FCD both cause a relevant shift in the resonance frequency ω_r, while the shift caused by the Kerr-effect is negligible. In first order perturbation theory, this gives:

$$\frac{\delta\omega_{nl}}{\omega_r} = -\frac{1}{n_g}\left(\frac{\mathrm{d}n_{Si}}{\mathrm{d}T}\Delta T + \frac{\mathrm{d}n_{Si}}{\mathrm{d}N} N\right). \tag{4.7}$$

4.2.2 Numerical details of the simulations

In high-Q rings ($Q > 2 - 3 \times 10^4$) TPA generates enough free carriers to make FCD prominent for sufficiently high input powers. We will illustrate the concepts of this chapter with simulations for such a high-Q SOI microring with a geometry that is inspired by the one measured in [4]. Our ring prototype has a $4\,\mu$m-radius with $540\,$nm × $220\,$nm cross section waveguides. This ring has a resonance width $\lambda_{3dB} = 25\,$pm at the resonance wavelength $\lambda_r = 1552.770\,$nm. We consider a critically coupled ring with $\gamma_{coup} = \gamma_{abs,lin} + \gamma_{rad}$.

The effective volumes and confinements are calculated using Meep FDTD

[15], while the other material parameter values are based on [4, 6, 14]. This results in the parameter values in Table 4.1. In most of the simulations in this chapter we will assume an AP filter that is critically coupled. If we simulate the dynamics for an Add-Drop (AD) filter, the two coupling sections both have the same τ_{coup} as the coupling section in the AP filter.

Parameter	Value	Magnitude
β_{Si}	8.4×10^{-12}	$m \cdot W^{-1}$
$\frac{dn_{Si}}{dT}$	1.86×10^{-4}	K^{-1}
$\frac{dn_{Si}}{dN}$	-1.73×10^{-27}	m^3
σ_{Si}	10^{-21}	m^2
ρ_{Si}	2.33	$g \cdot cm^{-3}$
$c_{p,Si}$	0.7	$J \cdot g^{-1} \cdot K^{-1}$
$n_g = n_{Si}$	3.476	
η_{lin}	0.4	
λ_r	1552.770	nm
AP ring: λ_{3dB}	25	pm
AD ring: λ_{3dB}	37.5	pm
$\tau_{abs,lin} = \frac{2}{\gamma_{abs,lin}}$	$\frac{205}{\eta_{lin}}$	ps
$\tau_{coup} = \frac{2}{\gamma_{coup}}$	205	ps
τ_{th}	65	ns
τ_{fc}	5.3	ns
Γ_{th}	0.9355	
Γ_{TPA}	0.9964	
Γ_{FCA}	0.9996	
V_{th}	3.19	μm^3
V_{TPA}	2.59	μm^3
V_{FCA}	2.36	μm^3

Table 4.1: Parameter values used in the simulations.

4.3 Nonlinear dynamical analysis of bistability and self-pulsation

In this section we show how, for sufficiently high input power and an input wavelength sufficiently close to the resonance wavelength of the ring, the CMT-model predicts bistability and self-pulsation regions.

Before diving into the mathematical details and simulations, we use the spectral picture of Fig. 4.1 to explain how bistability (Sec. 4.3.1) and self-pulsation (Sec. 4.3.2) originate in a microring. In Sec. 4.3.3, we will identify hysteresis behaviour of the output power as a function of the input power during an input power sweep with fixed input wavelength. Additionally, we show how unstability of some FPs corresponds to self-pulsation. In Sec. 4.3.4, we explain how this behaviour can be analysed using an intuitive phase-plane portrait. In sec. 4.3.5 we will introduce an adiabatic elimination of the fast light dynamics (loading and unloading of the ring resonator). This simplifies the model and will extensively be used at the end of this chapter in Sec. 4.6. We end this section with a bifurcation analysis of the bistability and self-pulsation onset in Sec. 4.3.6. The bifurcation classification of the self-pulsation onset will provide us with a tool to identify the regions where we can expect excitability. This will be studied more in-depth in the next section.

We include the calculation details that support our findings in appendices of the previous subsections. As these technicalities are not necessary to understand the general messages in the next subsections, they can be easily omitted during a first reading.

4.3.1 Physical origin of bistability in a ring

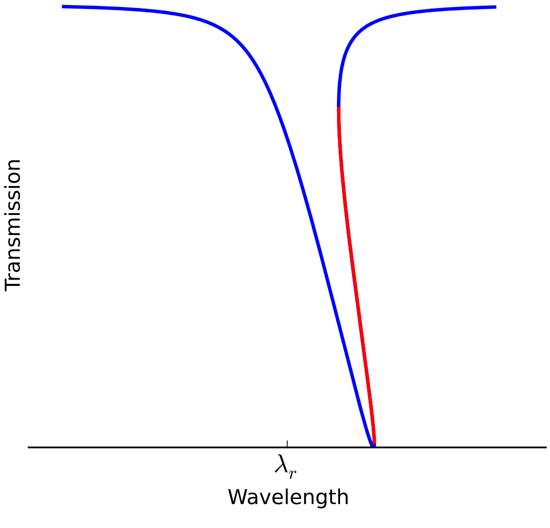

Figure 4.2: The transmission of an all-pass ring with $(\lambda_{r,eff} - \lambda_r) \propto \Delta T \propto |a|^2$ gets skewed to the right for higher input powers. This results in bistability (blue points are stable FPs, while red points are unstable).

Figure 4.1 showed the linear transmission of an all-pass microring. This transmission spectrum can be experimentally obtained using a tunable laser, by doing a wavelength sweep for fixed input power. However, for higher input powers, the absorption of the light in the ring waveguide will generate heat, and an increase in temperature will induce a shift in effective resonance wavelength, proportional to the temperature difference. In Fig. 4.2 we assume $\Delta T \propto |a|^2$, and hence $(\lambda_{r,eff} - \lambda_r) \propto |a|^2$. Importantly, at the dip of the resonance, the amount of optical energy in the ring cavity is largest, resulting in the largest ΔT increase and thus largest shift in $\lambda_{r,eff}$, while the ΔT-induced shift is less strong for detunings for which less light couples into the cavity. Consequently, the transmission dip is skewed due to these nonlinearities. For sufficiently high input powers this can result in bistability. As $\frac{dn}{dT} > 0$, we see that the linear transmission dip is tilted towards longer wavelengths.

In our actual ring model, we need to include nonlinear absorption terms such as TPA and FCA, and the free carrier effects also need to be taken into account. However, the main conclusion that a high input power will result in bistability at the red side of the resonance will still hold.

4.3.2 Physical origin of self-pulsation in a ring

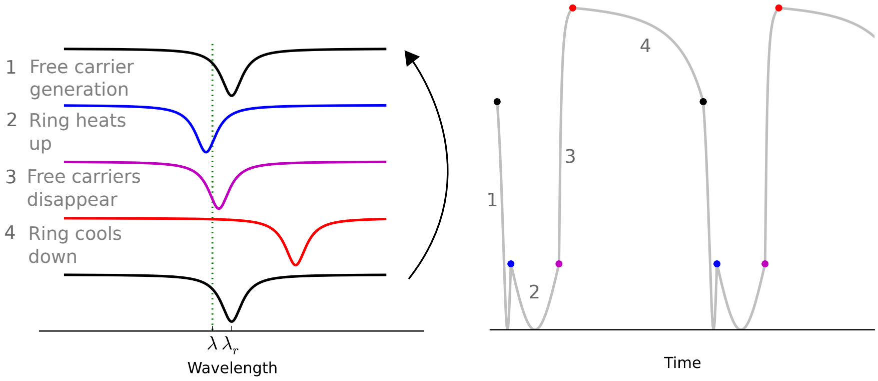

Figure 4.3: Changes in temperature or free carrier concentration change the effective resonance wavelength, resulting in different detuning scenarios with respect to an input signal at a fixed wavelength. This can result in self-pulsation.

By tracking $\lambda_{r,eff}$ as a function of time, and by incorporating the effect of changes in the resonance frequency due to changes in the concentration of free carriers, it can be understood how self-pulsation can arise in a ring (Fig. 4.3). Indeed, suppose we apply an input signal with high input power, with a fixed input wavelength close to λ_r. As the ring is close to resonance, the optical field in the ring will generate additional free carriers, resulting in a blue shift of $\lambda_{r,eff}(t)$, within a ~ ns time scale. Due to this blueshift, the detuning of the input wavelength with respect to $\lambda_{r,eff}(t)$ is less strong, resulting in heating of the ring, and consequently, on a slower timescale (~ $12-20\,\text{ns}$) $\lambda_{r,eff}(t)$ is pushed to higher wavelengths. As we will show in Sec. 4.6 the influence of the heat generation on the resonance wavelength $\delta\lambda_{r,\Delta T}(t)$ is stronger than the influence of the free carriers $\delta\lambda_{r,N}(t)$. Consequently, at a certain point in time, the redshift $\delta\lambda_{r,\Delta T}(t)$ will become sufficiently large to compensate for the blueshift $\delta\lambda_{r,N}(t)$, and the increase in detuning of the input wavelength with respect to $\lambda_{r,eff}(t)$ will decrease the amount of light that couples into the ring. As a consequence, the additional concentration of free carriers will disappear, and $\delta\lambda_{r,N}(t)$ will tend to zero. As a result $\lambda_{r,eff}(t) = \lambda_r + \delta\lambda_{r,N}(t) + \delta\lambda_{r,\Delta T}(t) \approx \delta\lambda_{r,\Delta T}(t)$ will increase, resulting in a stronger total redshift. As the input wavelength is now completely out of resonance with the ring, no light will couple into the ring and the heated ring will slowly cool down within ~ $50-60\,\text{ns}$. Finally, when sufficiently cooled down, the input signal is again in resonance with the ring, and the whole process will repeat.

In the actual system of this ring, FCA and TPA also need to be taken into account, resulting in changes of the resonance width. However, this does not result in qualitative differences in the dynamics.

4.3.3 Power sweep for fixed wavelength

Figure 4.4 shows the relation between input and output power for the full microring model (calculation in App. 4.3.3.A). We clearly see bistable behaviour. This bistability is mainly caused by the thermo-optic effect, whereas free carrier effects influence the appearance of self-pulsation. Indeed, in agreement with the explanation in Sec. 4.3.2, as the optical energy both heats up the cavity and generates free carriers, and as the thermo-optic and FCD have an opposite influence on the effective resonance wavelength (and thus the amount of light coupled into the cavity), self-pulsation arises with a mostly asymmetric pulse shape, caused by the difference in timescale between the fast free carrier generation and absorption of optical power and the slow relaxation of the temperature in the cavity. For lower input powers, in the bistability region, there can be two stable FPs in combination with an unstable one ($P_{in} = 167-191\,\mu\text{W}$) or one stable FP together with two unstable FPs and a stable LC ($P_{in} > 191\,\mu\text{W}$, LC not included in the figure). For higher input powers there are no stable FPs and the ring will always self-pulsate.

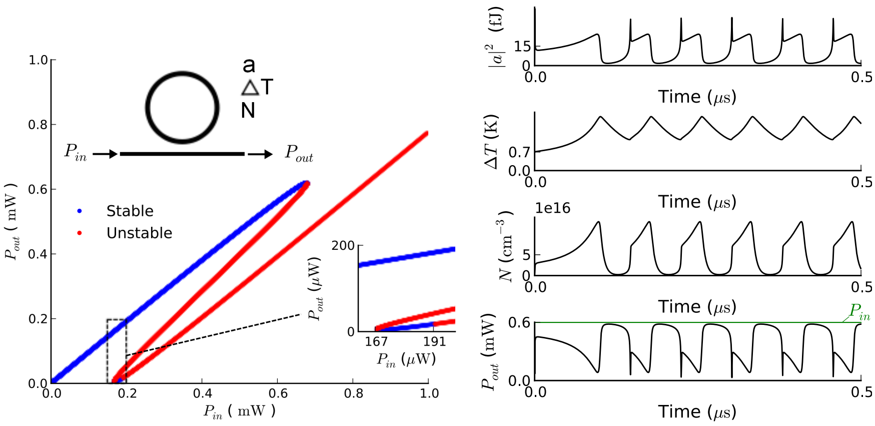

Figure 4.4: For a detuning $\lambda - \lambda_r = 62\,\text{pm}$, $P_{out}(P_{in})$ is bistable (left figure), for $P_{in} > 191\,\mu\text{W}$ the lower P_{out}-branch becomes unstable, which is an indication of self-pulsation. For $P_{in} = 0.6\,\text{mW}$ and $(a, \Delta T, N)(t{=}0){=}(0, 0.7, 0)$ this gives the self-pulsation time-traces on the right.

4.3.3.A Calculation of the steady state equations

In this appendix of Sec. 4.3.3, we present the calculation details of the simulation in Fig. 4.4. Setting the derivatives to zero in Eqs. (4.1)-(4.3) results in the steady state equations. These can be solved analytically. From Eq. (4.3) N is easy to calculate if we know $|a|$, which can, together with $|a|$, be used to calculate ΔT. If we keep the input wavelength λ fixed and put $\frac{\mathrm{d}a}{\mathrm{d}t} = 0$ in Eq. (4.1), we can rewrite the result as:

$$\left[j\left(\omega_r + \delta\omega_{nl}(\Delta T, N)\right) - \omega) - \frac{\gamma_{loss}(|a|, N)}{2} \right] a = -\kappa s_{in}. \tag{4.8}$$

If we now take the square of the modulus of both sides we get, independent of ϕ:

$$\left[(\omega_r + \delta\omega_{nl}(\Delta T, N) - \omega)^2 + \left(\frac{\gamma_{loss}(|a|, N)}{2} \right)^2 \right] |a|^2 = |\kappa s_{in}|^2. \tag{4.9}$$

As $P_{in} = |s_{in}|^2$, the right hand side of Eq. (4.9) is linear in the input power. Given that Eq. (4.6) and (4.7) are linear in ΔT and N, the left hand side is a quadratic function of ΔT and N and a higher order polynomial in $|a|^2$. To obtain the steady state curves we can thus simply parameterize ΔT, N and P_{in} as a function of $|a|^2$. When we substitute those values in Eq. (4.8), we can calculate ϕ.

The stability of the steady state solutions can be analysed by evaluating the eigenvalues of the Jacobian of the real version of the system equations for a given FP (cfr. Sec. 2.3.1). For this purpose, we split Eq. (4.1) in its real and imaginary part, and take the derivative of the right hand side of both equations together with the right hand sides of Eq. (4.2) and (4.3) with respect to $\Re(a)$, $\Im(a)$, ΔT and N. This results in a system of four differential equations of four real variables, and, hence, this Jacobian has four eigenvalues. If all eigenvalues of a FP have a negative real part, it is stable. If at least one of them has a positive real part, the FP is unstable, while a real part equal to zero indicates a bifurcation.

4.3.4 Phase-plane analysis

Similar to [8], to gain more insight in the CMT-equations, we now construct 2D-phase portraits, which will be heavily used in the remainder of this chapter. For this purpose, we project the $(a,\Delta T,N)$-time-traces for a given input power and wavelength onto the $(\Delta T,N)$-plane. Moreover, we calculate the $d(\Delta T,N)/dt = 0$, $d(\Delta T,a)/dt = 0$ and $d(N,a)/dt = 0$ nullclines (details in App. 4.3.4.A). Where the three curves intersect we have steady state FPs.

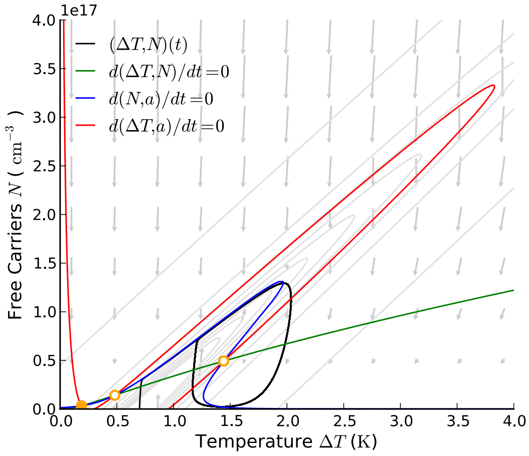

Figure 4.5: On the phase portrait for $P_{in} = 0.6\,\mathrm{mW}$ and a 62 pm detuning, the $d(N,a)/dt = 0$, $d(\Delta T,a)/dt = 0$ nullclines only intersect at the three FPs (orange circles). In correspondence with Fig. 4.4 two of those FPs are unstable (open circle), while one is stable (filled circle). The example time-trace from Fig. 4.4 (black line) clearly follows both the $d(\Delta T,N)/dt$ directions on the $da/dt = 0$-surface (grey arrows) and the corresponding direction changes indicated by the nullclines. Moreover, (grey) contour lines of $da/dt = 0$ for $|a|^2 = 1\,\mathrm{fJ} - 31\,\mathrm{fJ}$ are elliptic and do not overlap (Sec. 4.3.4.B).

$d(N,a)/dt = 0$ and $d(\Delta T,a)/dt = 0$ only intersect in the $(\Delta T,N)$-plane in those FPs (Fig. 4.5, proof given in App. 4.3.4.B).

Moreover, both the temperature time constant ($\tau_{th} = 65\,\text{ns}$) and the free carrier relaxation time ($\tau_{fc} = 5.3\,\text{ns}$) are larger than the time constants governing the dynamics of the light ($\eta_{lin}\tau_{abs,lin} = \tau_{coup} = 2/\gamma_{coup} = 205\,ps$, and the detuning of the light corresponds to a time constant of the same order of magnitude). After a very short transient period $\approx 100\,ps\ da/dt \approx 0$, the $(a,\Delta T,N)(t)$ solutions converge to the $da/dt = 0$ surface. We can thus use the projections of the $d(\Delta N, a)/dt = 0$ and $d(\Delta T, a)/dt = 0$ nullclines on the $(\Delta T,N)$-plane to do standard 2D phase-plane analysis.

The time-traces follow both the $d(\Delta T, N)/dt$ directions on the $da/dt = 0$-surface and the corresponding direction changes indicated by the nullclines (Fig. 4.5). As N reacts faster than ΔT, the time-traces fastly relax towards the $d(N, a)/dt = 0$ nullcline. Consequently, during the self-pulsation the ring makes steep transitions between the upper and lower $d(N, a)/dt = 0$-branches.

4.3.4.A Calculation of the nullclines

For the solution of $d(\Delta T, N)/dt = 0$ we can use the same parameterization of ΔT and N as a function of $|a|$ as for the steady state case. When solving $d(N, a)/dt = 0$ we use Eq. (4.3) to parameterize N as a function of $|a|$, substitute this in Eq. (4.9) and solve the quadratic equation for ΔT. $d(\Delta T, a)/dt = 0$ can be obtained by solving Eq. (4.2) for ΔT (which is then dependent both on $|a|$ and N), substituting this in Eq. (4.3) and solving the corresponding quadratic equation for N (which gives us $N(|a|)$) and resubstituting this in the expression for ΔT (finally only dependent on $|a|$). In all three cases it is thus possible to find a suitable parameterization of both ΔT and N as a function of $|a|$.

4.3.4.B Proof of the bijection between (ΔT,N)-plane and $da/dt = 0$-surface

That $d(N, a)/dt = 0$ and $d(\Delta T, a)/dt = 0$ only intersect in the $(\Delta T,N)$-plane in the FPs can be geometrically understood by considering the projection of the $da/dt = 0$ surface on the $(\Delta T,N)$-plane. Eq. (4.9) is quadratic both in ΔT and N, and defines an ellipse for each $|a|$-value. As the coefficients for ΔT^2, N^2 and ΔTN are all proportional to $|a|^2$, the orientation of the principal axes is independent of $|a|$. However, the center of this ellipse and the global scaling factor of the axes are both monotonically $|a|$-dependent, so the size of the ellipse, e.g., shrinks for higher $|a|^2$. Apparently, in Fig. 4.5, this dependence is in such a way that ellipses corresponding to different $|a|$-values do not overlap. This has as a consequence that the projection of the $da/dt = 0$ surface on the $(\Delta T,N)$-plane is a bijection. Both $d(\Delta T, a)/dt = 0$ and $d(N, a)/dt = 0$ lie on the $da/dt = 0$ surface and only intersect in the FPs. The intersections of their projections therefore uniquely correspond to those FPs. From Eq. (4.9) it can be proven that this bijection is valid for general P_{in} and ω settings. Indeed, for a given $(\Delta T,N)$ pair, Eq. (4.9) is a third order equation in $|a|^2$. Applying, e.g., Descartes' rule of signs, on the coefficients of this third order $|a|^2$-polynomial one can determine that, independent of P_{in} and ω, there always exists just one single real positive root, which implies that the projection of $da/dt = 0$ on the $(\Delta T, N)$-plane is indeed a bijection. Consequently, for general P_{in} and ω settings, we can identify the FPs only by looking at the intersections of $d(N,a)/dt = 0$ and $d(\Delta T, a)/dt = 0$ in the $(\Delta T, N)$-plane.

4.3.5 2D approximation

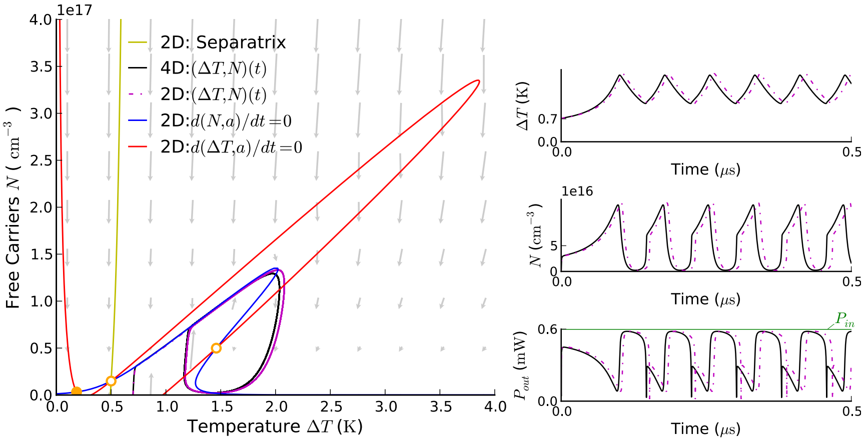

Figure 4.6: The phase portrait obtained by neglecting the TPA-contribution in γ_{loss} in Eq. (4.6), looks similar to Fig. 4.5 and still explains (approximately) the dynamic behaviour of the time-trace of the 4D-system from Fig. 4.4 (black line). Furthermore, the time-trace with a corresponding initial condition in the 2D-approximation (dashed magenta lines) follows qualitative the 4D-behaviour, both in phase-plane and in time-domain, although the shape of the limit cycle (LC) is slightly different. The yellow line is the separatrix of the simplified system.

In section 4.3.4 we have explained why we can do phase-plane analysis in the $(\Delta T, N)$-space. The same arguments can now be used to do a dimensionality reduction, by doing an adiabatic elimination of the field variable a (a basic center manifold projection technique [16]). To simplify the equations we neglect the TPA-contribution in γ_{loss} in Eq. (4.6) (details included in App. 4.3.5.A). In this system we still see self-pulsation (Fig. 4.6), so at longer timescales (above 100 ps) the most relevant dynamical properties are conserved.

This 2D system can be used to calculate the separatrix of the microring, by starting close to the unstable saddle and integrating backwards in time (Fig.

4.6). As will be explained in Sec. 4.6, this separatrix is the boundary between the basins of attraction of the low-energy FP and the high-energy FP or its surrounding LC (in Fig. 4.6 the case of surrounding LC is depicted). It can be considered as a threshold for switching.

This reduction of the number of variables not only simplifies the phase-plane analysis, but in addition allows a speed-up of simulations of huge circuits containing these microrings. By eliminating the fast timescale from the system, the integration step can increase without significant accuracy loss. In addition, fewer variables need to be stored. Finally, this 2D-approximation is an extra justification for our 2D phase-plane analysis. Although qualitatively similar results are obtained with this 2D-approximation, the simulations in the body of this chapter are still done with the full 4D-system. Only at the end of this chapter, in Sec. 4.6 we will use this simplification to calculate the scaling laws of the microring dynamics.

4.3.5.A Calculation details of the 2D approximation

Most of the time $da/dt \approx 0$, and $|a|$ is completely determined by the instantaneous value of ΔT and N. From Sec. 4.3.4.B we know that, for a given $(\Delta T, N)$ pair, Eq. (4.9) has only one positive real root, such that this third order equation can be solved unambiguously for $|a|$. However, in this chapter we simply neglect the TPA-contribution in γ_{loss} in Eq. (4.6), as its effect on the broadening of the resonance width is $1-2$ orders of magnitude smaller than the other relevant physical effects. This makes Eq. (4.9) linear in $|a|^2$. If we substitute $|a|$ in Eq. (4.2) and (4.3) with this approximative $|\hat{a}|(\Delta T, N)$, we get a 2D dynamical system as a function of ΔT and N.

4.3.6 Bifurcation analysis of the onset of bistability and the onset of self-pulsation

In the previous subsections we discussed how the dynamics of a microring can be analysed using a phase plane representation, and how this representation is linked with the possibility to adiabatically eliminate the fast light dynamics. In this subsection we will analyse the evolution of the number of FPs of the system. By doing a bifurcation analysis we will investigate how these FPs depend on the input signal, and how the system can be tuned in a regime that is suitable for excitability.

For a given input power the microring can have one, two or three FPs (Fig. 4.4 and Fig. 4.7). The microring undergoes a Saddle-Node bifurcation (SN) if it has two FPs. If it has three FPs, at least one (at low-$|a|$) is stable.When two of the three FPs are unstable, there is a stable LC around the high-$|a|$ FP. The middle FP will always be unstable, and is a saddle point. It has an unstable manifold

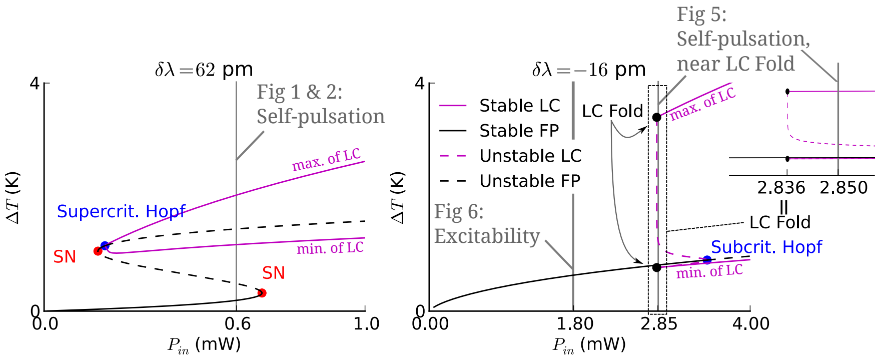

Figure 4.7: At the red side of the resonance (e.g., left: $\delta\lambda = 62\,\text{pm}$) the Andronov-Hopf (AH) bifurcation (blue dot) tends to be supercritical, while it can be subcritical at the blue side of the resonance (e.g., right: $\delta\lambda = -16\,\text{pm}$). FPs (black) and both maximum and minimum values of the LCs (magenta) in a $\Delta T(P_{in})$-bifurcation diagram, calculated using PyDSTool [1], illustrate this. Moreover, at $\delta\lambda = 62\,\text{pm}$ the ring is bistable in-between two Saddle-Node (SN) bifurcations (red dots), while at $\delta\lambda = -16\,\text{pm}$ a stable and unstable LC annihilate in a LC Fold bifurcation at $P_{in} = 2.836\,\text{mW}$ (black dots indicate the maximum and minimum of the LC at this bifurcation). Relevant P_{in}-values used in the other figures are indicated.

which ends at the low-$|a|$ stable FP and, if there is one, at the upper LC, or else, at the high-$|a|$ stable FP. A stable manifold or separatrix divides the basins of attraction of the lower FP and the higher-$|a|$ FP/LC. If there is only one FP and it is unstable, then there is a stable LC around it.

For some wavelengths, the onset of oscillation shows hysteresis in the input power, which is a sign of a subcritical AH bifurcation, in contrast to the regions without this hysteresis which correspond to a supercritical AH bifurcation. Given the previous ring parameters, typically a subcritical AH bifurcation appears, if the input light is detuned towards the blue, where there is no bistability. However, if the input light is detuned towards the red, in the bistability region, a supercritical AH bifurcation appears (this corresponds to the supercritical AH bifurcation reported in [6]). In the case of the subcritical AH bifurcation, a stable LC coexists with a stable FP centered in this LC. This can be proved explicitly with time-traces for, e.g., $P_{in} = 2.85\,\text{mW}$ at a $\delta\lambda = -16\,\text{pm}$ detuning, where we have one stable FP and a stable LC. By choosing the initial conditions within a subregion of the region defined by the LC on the $da/dt = 0$ surface we can end up in the central FP or in the LC (Fig. 4.8). The basin of attraction of the stable FP is determined by an unstable LC (not included in figure) in-between

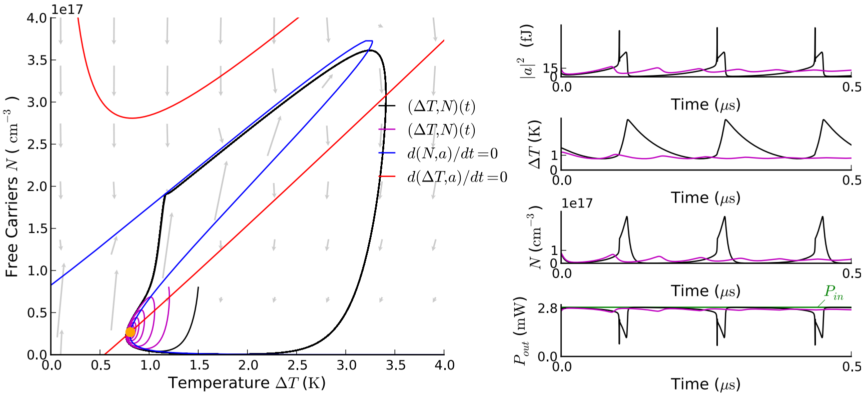

Figure 4.8: For some input powers and wavelength settings the LC encloses a stable FP (filled circle) in the $(\Delta T, N)$ phase-plane. This indicates a subcritical AH bifurcation. We illustrate this here for $P_{in} = 2.85\,\mathrm{mW}$ and $\delta\lambda = -16\,\mathrm{pm}$. Depending on the initial conditions, the trajectory will converge to the LC (black curve $(\Delta T, N)(t{=}0) = (1.5\,\mathrm{K}, 8\mathrm{e}16\,\mathrm{cm}^{-3})$) or to the FP (magenta curve $(\Delta T, N)(t{=}0) = (1.2\,\mathrm{K}, 8\mathrm{e}16\,\mathrm{cm}^{-3})$).

the stable LC and this FP. The stable and unstable LCs annihilate in a fold LC bifurcation for lower input powers (e.g., at $P_{in} = 2.836\,\mathrm{mW}$ for $\delta\lambda = -16\,\mathrm{pm}$ in Fig. 4.7).

The qualitative difference between the amplitude growth of the stable LC near the supercritical AH bifurcation and of the unstable LC near the subcritical AH bifurcation in Fig. 4.7 plays an important role in the excitability presented in the subsequent section. In the case of the supercritical AH bifurcation, the oscillation amplitude grows rather smoothly, without abrupt changes. This corresponds to the default behaviour of an AH-bifurcation, but is less useful if the system needs to be excitable. In contrast, the oscillation amplitude of the subcritical AH bifurcation, after an initial smooth growth, explodes at a certain point, within a very small P_{in}-range, to large amplitude oscillations. This can be related to the canard explosions observed in excitable SOAs [12], and is a result of the difference in timescale between τ_{th} and τ_{fc}. The combination of the subcritical AH-bifurcation with the amplitude growth of the unstable LC due to slow-fast dynamics will result in excitability with well-defined pulses.

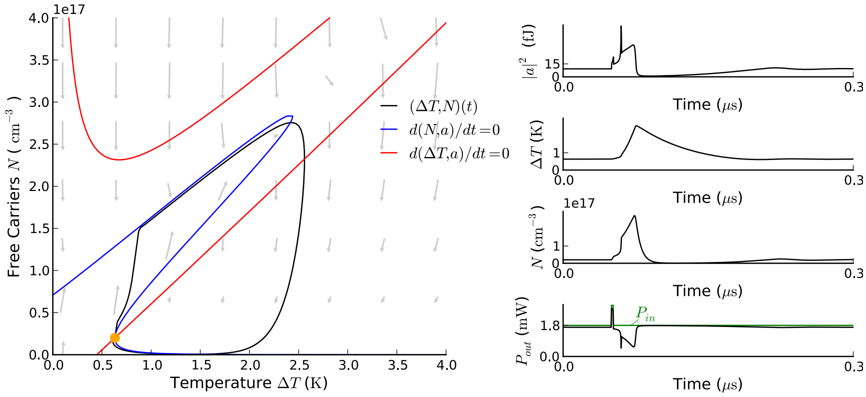

Figure 4.9: A temporary increase from $P_{in} = 1.8$ mW to 2.9 mW at $\delta\lambda = -16$ pm, during 2 ns, triggers an excitation. Although for this input power no LC is present, the excitation can be seen as a reminiscent of the nearby LC from Fig. 4.8.

4.4 Excitability: single and double ring configuration

In the wavelength region where the self-pulsation hysteresis is present, the microring is excitable if the input power is below, but close to, the fold LC bifurcation (Fig. 4.9, with a $T_{tr} = 2$ ns long power increase of P_{in} from 1.8 mW to 2.9 mW as perturbation, modelled by making s_{in} time-dependent in Eq. (4.1)). For these input settings a small perturbation will kick the ring out of its rest state, into a 'ghost' of a LC pulse, whereafter the system will return to the initial rest state. In this power region there does not yet exist a stable LC, but the phase-plane already incorporates similar dynamics, as we are close to the bifurcation point. A look at the pulse-trajectory in the phase-plane clearly illustrates this similarity (Fig. 4.9). Being close to an AH bifurcation, similar to the excitability reported in [7], this is Class 2 excitability (cfr. Sec. 2.3.2 or [10]).

Although the presence of this AH bifurcation can be considered sufficient for this mechanism to be classified as Class 2 excitability, it is important to note that the fact that this bifurcation is subcritical is in agreement with excitability in the Hogdkin-Huxley model, as well as many other biophysical models [17]. Additionally, this subcategory of Class 2 excitability is also emulated succesfully in a Metal-Oxide-Semiconductor Field-Effect Transistor (MOSFET) circuit [18]. In contrast, the Class 2 excitability due to thermo-electronic nonlinear dynamics in SOAs is generated by a canard explosion near a supercritical Hopf bifurcation [12], resulting in slightly other dynamics. For instance, whereas in the latter system excitations can be triggered on a background of small-amplitude oscillations, this is not the case for the system investigated in this chapter. However, as can be inferred from Sec. 4.3.6, in a microring there is no canard explosion for the wavelengths where a supercritical AH bifurcation appears. As a consequence, for a ring that is pumped in this wavelength region by an input signal with P_{in} below the self-pulsation onset, the ring's output does not show threshold behaviour as a function of the input perturbation strength, in contrast, even for strong input pulses, the amplitude of the ring's response still increases smoothly with the perturbation strength. This implies that excitability does not appear in this wavelength range.

In the current section we will analyse this excitability mechanism further using simulations, while in the subsequent section, i.e., in Sec. 4.5, we will validate those simulations experimentally. In Sec. 4.4.1 and Sec. 4.4.2, we will discuss two typical features of excitability: threshold behaviour and the refractory period, respectively. In Sec. 4.4.3 we will introduce the cascadability of this excitable microring. In Sec. 4.4.4, we discuss the performance of the microring with respect to speed and energy consumption.

4.4.1 Threshold behaviour

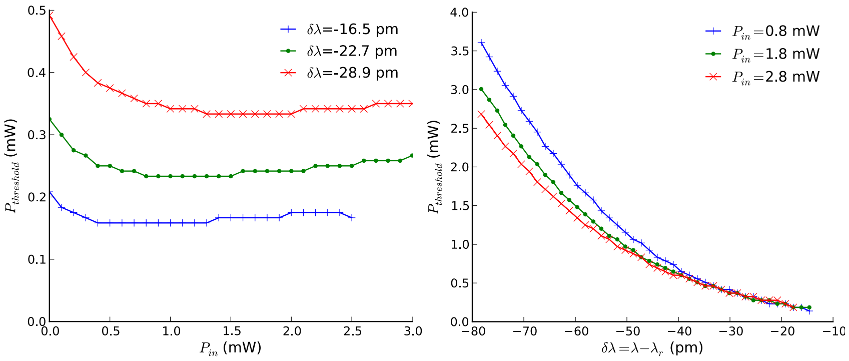

Figure 4.10: The excitability-threshold power $P_{threshold}$ is more λ than P_{in}-dependent. Trigger pulses are T_{tr} = 10 ns long and have been sent in the opposite direction as the pump light.

Characteristic for this kind of excitability is that the precise shape of the perturbation is rather unimportant. As long as the perturbation is sufficiently strong, the shape of the ring's excitation is not influenced by the input-pulse shape. In contrast to Class 1 excitability the threshold of Class 2 excitable system is theoretically less well-defined [17]: there is a continuum between an excitation and a subthreshold oscillation. Fortunately, in practice, the transition between those two regimes happens in a very narrow input pulse strength range, such that one effectively observes quasi-threshold behaviour. In this section we will determine this 'effective' threshold.

For a given $T_{tr} = 10\,\mathrm{ns}$ we can determine the threshold $P_{threshold}$ in the trigger power P_{tr}. Below this threshold no excitation will be triggered (and the response to the perturbation will be trigger pulse dependent), above this threshold the ring is excited. We simulate this by sending pulses with varying P_{tr}-height, with the trigger wavelength $\lambda_{tr} = \lambda$, in the opposite direction of the pump light (this simplifies the comparison of $P_{threshold}$ for different P_{in}). This can be easily modelled by incorporating an extra version of Eq. (4.1) for the counterpropagating mode in the ring, and incorporate its influence on ΔT and N [9]. We neglect backscattering in the ring. As a consequence, no interference effects due to coupling between pump light and injected trigger pulse are possible, and the dynamics will be independent of the phase of the trigger pulse. Additionally, the behaviour of this type of triggering is phenomenologically identical to what would happen if one would inject trigger pulses at the other resonance wavelengths of the rings, instead of using the same resonance wavelength as is used for the pump light.

To approximate $P_{threshold}$, we calculate the peak temperature after a pulse, i.e., $h = max(\Delta T(t > t_{pulse}))$ (cfr. the example temperature timetrace of an excitation in Fig. 4.9, right), and keep track of the P_{tr}-value for which dh/dP_{tr} is maximal. This algorithm to determine the threshold is based on the observation that perturbations above threshold induce a remarkably stronger temperature increase than sub-threshold perturbations. Below threshold the peak temperature of the microring's response to the input slightly increases for increasing trigger pulses, while above threshold the peak temperature remains almost constant, such that the large jump in peak temperature at the threshold results in a maximal dh/dP_{tr}. In the low-P_{in} region there is no 'real' excitability, as the shape of the system's output pulse again becomes dependent of P_{tr}. However, as this transition between excitability and no excitability is rather smooth, the used threshold-approximation algorithm can still detect a 'threshold', which apparently slightly increases. For small detunings high values of P_{in} generate a stable LC, we therefore exclude those points from the graphs.

In principle, $P_{threshold}$ should increase if the distance to the LC fold bifurcation increases. This effect is rather negligible for a fixed λ if P_{in} decreases, but is present for a fixed P_{in} if λ decreases (Fig. 4.10). The more λ is detuned from λ_r, the higher the input power needed to reach this bifurcation point, and thus the higher the threshold.

4.4.2 Refractory period

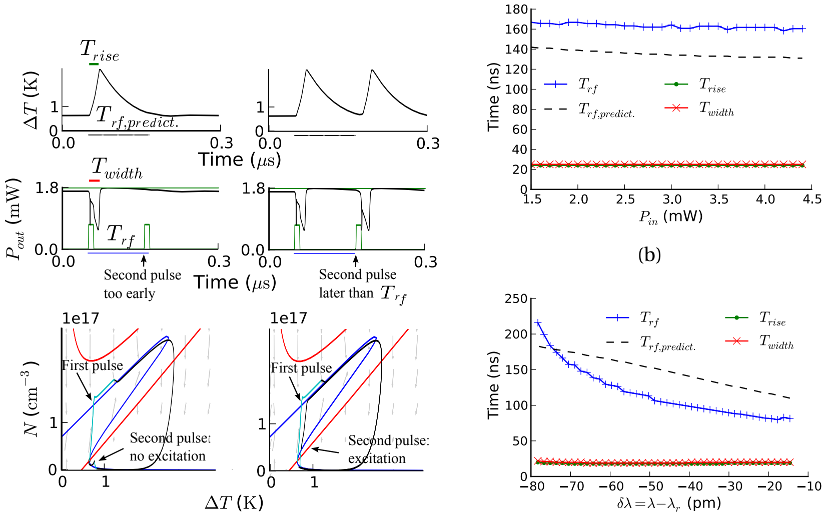

(a)

(b)

(c)

Figure 4.11: The refractory period T_{rf} is the time after a pulse during which the ring is insensitive to a second perturbation (a). It is on the order of magnitude of τ_{th}, and is not much power dependent for $\delta\lambda = -35\,\text{pm}$ (b), while there is a clear wavelength dependency for $P_{in} = 1.8\,\text{mW}$ (c). $P_{tr} = 1.65\,\text{mW}$ for (b) and $P_{tr} = 3.42\,\text{mW}$ for (c) (the need for the high P_{tr}-value of the latter is necessary to be above threshold for all wavelengths in the sweep range, as can be inferred from Fig. 4.10(b)). The refractory period can be predicted by looking at the time needed for $\Delta T(t)$ to relax to the rest state ($T_{rf,predict.}$). Moreover, the width of the pulse T_{width} is proportional to the rise time of the temperature, i.e., the time needed to reach the maximum temperature after a pulse. In the phase portrait we indicate the trajectory the ring makes during the external perturbations with cyan, while we use black for the rest of the response.

If, after an excitation, the microring did not yet relax to the rest state, it is temporarily insensitive to new excitations of the same strength (Fig. 4.11). This is a known feature of excitable systems and corresponds to the refractory period of the system of which there are two types:

1. the absolute refractory period: during this period a second pulse can not initiate a perturbation, no matter its strength,

2. the relative refractory period: during this period a second excitation is

inhibited, but not completely forbidden.

The absolute refractory period will in our system be on the order of the pulse width T_{width}. It will also be shorter than the relative refractory period. Indeed, an increase in the strength of the second input pulse with respect to the first one, would decrease the time needed to trigger a second excitation, and for an 'extremely' strong input pulse this time would converge to the absolute refractory period. In this section we will approximately determine the relative refractory period, and identify its power and wavelength dependence. For this purpose, we use input pulses that are above threshold for wide wavelength and power ranges, but still not too strong to end up in the absolute refractory regime. We keep the strength of the second pulse equal to the strength of the first pulse, and see from which moment on a second excitation can be triggered. So, the refractory period T_{rf} corresponding to the latter definition is the time during which the microring is insensitive to new pulses of the same strength after an excitation, given a certain trigger pulse power. In principle, this simulation can be refined by sweeping the height of the perturbing pulses for each setting of the input power and wavelength to find a pulse height that is just above threshold. However, the behaviour will qualitatively be the same as what we obtain with the current approach.

Figure 4.11 shows a power and wavelength dependency that is comparable to the one observed in Fig. 4.10: T_{rf} is rather insensitive to P_{in}, but increases with decreasing λ. As $\Delta T(t)$ is the slowest variable of the system, we can link the order of magnitude of T_{rf} to the thermal relaxation time τ_{th}: after an excitation, the ring is only sensitive to new perturbations if its temperature has sufficiently decreased, so it is sufficiently close to its rest state. Consequently, T_{rf} can be more-or-less predicted by the time needed for a ring to return to the initial rest state after a pulse ($T_{rf,predict.}$). In Fig. 4.11(c), we have used a rather high $P_{tr} = 3.42\,\mathrm{mW}$ to guarantee that the pulse is above threshold over the whole wavelength range of the sweep. As a consequence, for detunings close to resonance (i.e., $\delta\lambda$ close to zero) P_{tr} is significantly more above threshold than for detunings far from resonance. In the region with smaller detunings this results in the simulated T_{rf} value to be an underestimate of the actual relative refractory period, partly explaining the strong wavelength dependence of Fig. 4.11(c) and the larger deviation with $T_{rf,predict.}$ in this region.

Finally, T_{width} seems to be proportional to the rise time, i.e., the time the temperature needs after an excitation to reach the maximum value (Fig. 4.11). It is important to note that as the latency between the excitation and the perturbing input pulse is almost zero, this behaviour is to be expected for excitatory input pulses for a Class 2 excitable neuron [10]. Finally, we do not see the proportionality of T_{rf} with T_{width}, with a slope approximately equal to one, as is measured in PhC nanocavities [7]. We assume that the input pulses in the latter experiment are relatively stronger, with respect to the threshold, than the input pulses in our simulations. This brings T_{rf} closer to the absolute refractory time, which should indeed scale with T_{width}.

4.4.3 Cascadability

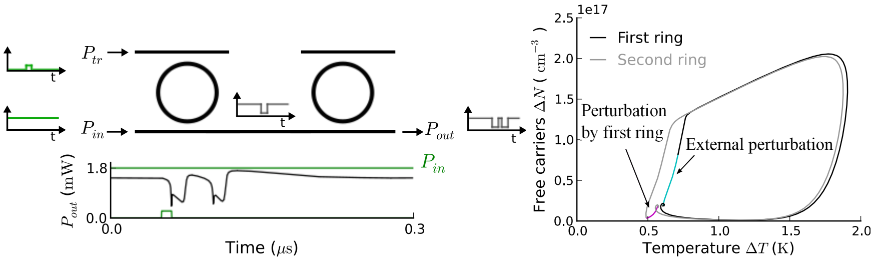

Figure 4.12: If a ring is excited by a trigger signal, this excitation can excite another ring. To demonstrate this we send a CW pump signal with $P_{in} = 1.8\,\text{mW}$ and $\delta\lambda = -16\,\text{pm}$ through the common bus of a series of two AD filters. By exciting the first ring via the drop port (with a 10 ns trigger with $P_{tr} = 250\,\mu\text{W}$, $\lambda_{tr} = \lambda$) we guarantee that the external trigger pulse never reaches the second ring. The second pulse in the circuit's output, which corresponds to the second ring's excitation, is thus triggered by the first pulse, originating from the first ring. In contrast to the perturbation of the first ring (caused by the trigger), the second ring is initially perturbed (by the first ring) towards lower ΔT and N (right phase portrait). This causes the delay between the two excitations to be bigger than the delay between the trigger and the first pulse (time-trace bottom left).

Since the precise shape of the trigger pulse is less important, the output pulse of a ring can serve as a trigger pulse of another ring. If the trigger pulse is on the common bus waveguide, it is impossible to distinguish whether the last ring is excited by the input trigger or by the first ring's excitation. To distinguish between both situations we use a circuit with two AD filters with common bus waveguide and excite the first ring in such a way that the input pulse never reaches the second ring. The two rings have identical settings, and the extra coupling section has the same τ_{coup} as in the previous simulations. In this setup the first ring clearly excites the second one, which makes this excitability mechanism cascadable (Fig. 4.12). Moreover, the second ring is perturbed in a different manner than the first one: the trajectory is initially kicked towards lower ΔT and N (phase portrait Fig. 4.12). This results in a longer time-lapse between this pulse and its perturbation (the first ring's excitation) than the time-lapse between the first ring's pulse and its perturbation (the external trigger).

Other simulations (not included) indicate that for this pump signal the resonance wavelength of both rings can slightly differ ($\sim 0.2\delta\lambda_{3dB,AD}$).

4.4.4 Energy consumption and speed

Typically, biological neurons operate at a speed of ~ 10 Hz. While some electronic hardware implementations of Spiking Neural Networks (SNNs) (e.g., the chips developed at the IBM SyNAPSE project [19] and the Neurogrid project [20]), opt to operate at this biological timescale, the fastest electronic implementation (i.e., the chip developed by the Heidelberg University BrainScales project [21]) accelerates the biological neuronal timescale with a factor 10^4. As the refractory period of the microring is determined by the thermal timescale, the microring neuron can process input spike trains with a spike frequency on the order of ~ 10 MHz, which is $10^6\times$ faster than a biological neuron and, as a consequence, still 100× faster than the current fastest electronic SNN-implementation. By combining the speed of the neuron with the ~ 1mW power that is required to pump the microring in the excitable regime, an energy/spike estimation of 100 pJ is obtained. At first sight this seems to be comparable with the energy/spike-values obtained in electronic implementations, where a record dynamic energy/spike-value of 45 pJ is obtained [19], and, if the static power is included as well, values of about $100-1000$ pJ are reported [20]. However, in contrast to the energy/spike-value we mention for the microring, the numbers mentioned for those electronic implementations incorporate the energy needed to transfer the spike through the synaptic connections between the neurons. In addition, the electronic neurons have a very large fan-in and fan-out (at least on the order of several 100s), while the fan-in/fan-out of the microring circuit in the previous subsection was only one, making the comparison unfair. In principle, photonics is a perfect platform to perform high bandwidth data transmission at low energies, but it will definitely be a non-trivial challenge to obtain an equally large fan-in and fan-out as in the electronic implementations. For instance, in the monochromatic photonic reservoir computing circuits discussed in Sec. 2.2.1, the fan-in/fan-out was increased with power splitters and combiners, but these components have the disadvantage that they result in additional losses in the neuron interconnections.

4.5 Measurement of the microring neurons

In the previous sections we have analysed the dynamics of a prototype of a ring in simulations. In this section we will verify those simulation results experimentally. In Sec. 4.5.1 we explain both the ring design and fabrication and the measurement set-up, in Sec. 4.5.2 we show timetraces of self-pulsation, in Sec. 4.5.3

we demonstrate excitability in a single ring, while in Sec. 4.5.4 we demonstrate its cascadability.

4.5.1 Fabrication, design and measurement setup

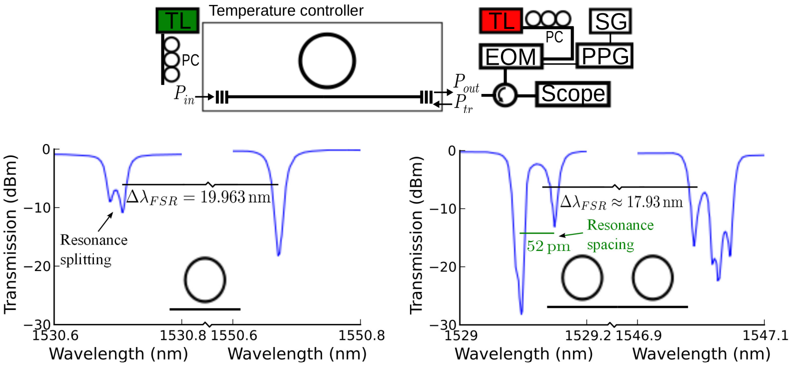
TL
Temperature controller
PC
P_{in}
P_{out}
P_{tr}
TL
PC
SG
EOM
PPG
Scope
Transmission (dBm)
0
−10
−20
−30
$\Delta\lambda_{FSR} = 19.963\,\mathrm{nm}$
Resonance splitting
1530.6
1530.8
1550.6
1550.8
Wavelength (nm)
Wavelength (nm)
Transmission (dBm)
0
−10
−20
−30
$\Delta\lambda_{FSR} \approx 17.93\,\mathrm{nm}$
52 pm
Resonance spacing
1529
1529.2
1546.9
1547.1
Wavelength (nm)
Wavelength (nm)

Figure 4.13: Schematic of the setup for a single-ring measurement. Light of a tunable laser (TL), polarized with polarization controllers (PC) is coupled in and out the chip via grating couplers (GC). The ring output is measured with a 10 GHz photodiode and visualized with a 1 GHz real-time scope. In the excitability experiment a second TL is used, mostly coupled in the opposite direction via a circulator. The pulses are created using a signal generator (SG) and a pulse pattern generator (PPG) and an electro-optical modulator (EOM). At the bottom, spectral details of both the single-ring (left figure) and double-ring resonances (right figure), used in this chapter, are included.

To test the previous simulation results we designed the corresponding ring circuits on the SOI platform. The designs were fabricated at imec using deep UV litography on a 200 mm SOI wafer with a 2 μm buried oxide (BOX) layer. The waveguides of the circuits are produced in a 220 nm crystalline silicon layer on top of that BOX layer. Typically, there is a choice between an air cladding or an oxide cladding of the waveguides. All the measurements in this PhD research were performed using samples with an oxide cladding. Reported losses for TE-modes in typical strip waveguides (i.e., with a rectangular waveguide cross-sections of 450 nm × 220 nm) with an oxide cladding are below 2 dB/cm [22]. The rings in the fabricated circuits have a geometry that approximates the geometry of the ring prototype described in Sec. 4.2.2. However, as extensively discussed in [23], the losses in such small footprint TE-microrings, with small radii on the order of ~ 5μm are typically higher than the losses in straight waveguides, due to excess loss mechanisms. For instance, due to the sharp bend radius of the ring waveguide the mode is pushed outwards, making it more sensitive to surface scattering at the sidewalls and, consequently, increasing the losses. Additionally, as some part of the light will be reflected due to the surface roughness, the clockwise and counterclockwise propagating mode in the ring waveguide will couple and, as a consequence, for very high Q-factors resonance splitting can appear [13, 24]. In future designs this might be circumvented by using the TM-mode of the waveguide. Indeed, due its decreased sensitivity to the sidewall roughness, the level of backreflection and corresponding resonance splitting is drastically improved [25].

The AP ring used to experimentally demonstrate the dynamical behaviour encountered in the single-ring simulations was nominally designed to have a 550 nm × 220 nm cross section, a 4.5 μm radius, a 250 nm gap, with a bus waveguide bent with the same curvature as the ring, but with a default 450 nm × 220 nm cross section. The broader cross section of the ring waveguide with respect to the bus waveguide was chosen to increase the confinement in the ring waveguide, to reduce the losses and hence improve the intrinsic Q-factor of the ring. The gap was chosen to obtain a sufficiently high-Q, near the critical coupling regime. The resulting ring has a resonance at 1530.708 nm with $\delta\lambda_{3dB} \approx 20$ pm (with resonance splitting $\delta\lambda_{ps} \approx 20$ pm) and an 8 dB extinction ratio (Fig. 4.13, bottom left). The design specifications of the double ring circuit used to demonstrate cascadability will be discussed in Sec. 4.5.4.

During the measurements of these ring circuits, a temperature controller, which guarantees the chip temperature deviations to be below ±0.03 K, is used to prevent drift of the resonance wavelength (Fig. 4.13, top). Light of a tunable laser (TL) is coupled in and out the chip via grating couplers [26]. The ring output is measured with a 10 GHz photodiode and visualized with a 1 GHz real-time scope, as we expect a ~ 10 MHz signal.

4.5.2 Single microring self-pulsation

Both the input power and wavelength clearly change the pulse shape and period of the self-pulsation in a ring (Fig. 4.14). The self-pulsation period is on the order of ~ 50 ns, which is a little bit shorter than the period in our simulations. We therefore expect τ_{th} to be slightly smaller. The on-chip powers needed for these self-pulsation traces are on the order of ~ 0.6 – 1 mW, as predicted by our simulations. These input powers are hence comparable to those needed for self-pulsation in PhC nanocavities, while this ring self-pulsates one order of magnitude faster [7].

The experimental pulse shape differs slightly from the simulated one due to a different ring geometry and pump setting, but adapting the simulation parameters to the experimental chip design can eliminate this difference [6, 9].

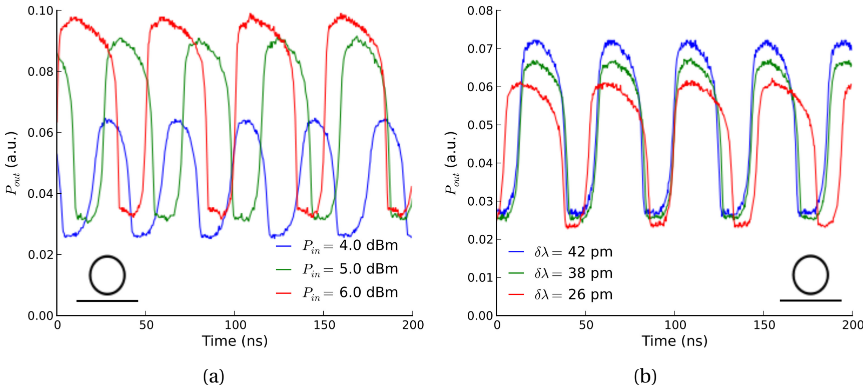

(a) (b)

Figure 4.14: Both the input power and wavelength clearly change the pulse shape and period of the self-pulsation in an AP ring with a 550 nm × 220 nm cross section, a 4.5 μm radius, near the resonance wavelength at 1530.708 nm. (a) Input power sweep with pump wavelength detuning $\delta\lambda = \lambda - \lambda_r = 40$ pm. Power values are those at the output of the laser. Due to the grating coupler the on-chip input power of the ring is expected to be ~ 6 dB lower. (b) Detuning sweep of the same ring with 5.0 dBm output power at the TL laser. The self-pulsation period is on the order of ~ 50 ns.

Furthermore, the limited range of the self-pulsation period, which is finite at the self-pulsation onset confirms the presence of the AH-bifurcation.

4.5.3 Single microring excitability

To verify the excitability of the rings we detune the pump wavelength at the blue side of the resonance with an input power near the self-pulsation onset. If we are too close to this onset, excitations triggered by noise can be perceived, but the purpose is to trigger the excitations by an external optical signal. For instance, sending rectangular trigger pulses with a 15.625 ns width and 250 ns period at a wavelength 'close' to one of the resonances of the ring can excite the ring (in this chapter we trigger at another ring resonance, as this allows to filter out the trigger light, but triggering at the same resonance also works). To create these trigger pulses another TL is modulated with an electro-optical modulator (EOM), we generate a 16-bit signal (a single 1 and 15 0's, unless mentioned otherwise) with a pulse pattern generator (PPG) of which the clock is fixed by a signal generator (SG) at 64 MHz. Although the pulse width of the trigger signal is rather big compared to the thermal timescale, experiments show that the pulse shape is independent of this width. The on-chip pulse-energy threshold for ex-

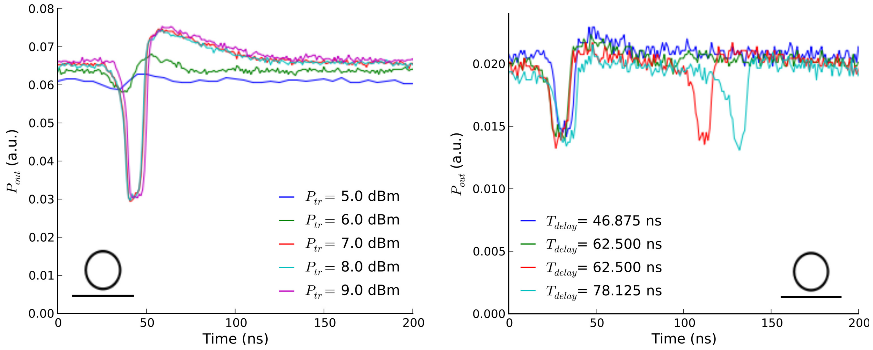

(a) (b)

Figure 4.15: (a) If the trigger power is sufficiently high (≥ 7 dBm@TL) the ring excites with a fixed pulse shape, while for lower trigger powers subthreshold oscillations are visible. The 4 dBm pump light is detuned at $\delta\lambda = -4$ pm from the $\lambda_r = 1530.708$ nm resonance. The trigger light is tuned $\delta\lambda_{tr} = 9$ pm near another ring resonance at $\lambda_{r'} = 1550.671$ nm. (b) The refractory period is on the order of magnitude of the self-pulsation period. The pump settings are similar to (a), while the trigger pulse settings are $\delta\lambda_{tr} = 9$ pm and $P_{tr} = 5$ dBm. Mentioned power values are those at the output of the lasers, due to GCs and EOM the on-chip input power of the ring is expected to be ~ 6 dB lower for the pump light and ~ 14 dB lower for the trigger signal.

citability is ~ 3 pJ (Fig. 4.15(a)).

If the delay between two trigger pulses (T_{delay}) is too small, the second pulse does not excite the ring (Fig. 4.15(b)). Therefore we can infer the relative refractory period to be somewhere around 60 ns, i.e. on the order of magnitude of the self-pulsation period. This all confirms the initial assumption in our simulations that τ_{th} is ~ 60 ns. It is difficult to measure this refractory period more accurately with this setup, as noise makes the ring response ambiguous: e.g., at a 62.5 ns delay the second pulse can sometimes excite the ring, but sometimes fails to do so.

In Fig. 4.15(b) an extra optical tunable filter with passband at 1530 nm is placed before the photodiode. The comparison with Fig. 4.15(a) confirms that reflection of the trigger pulses in the circulator to the photodiode can be neglected.

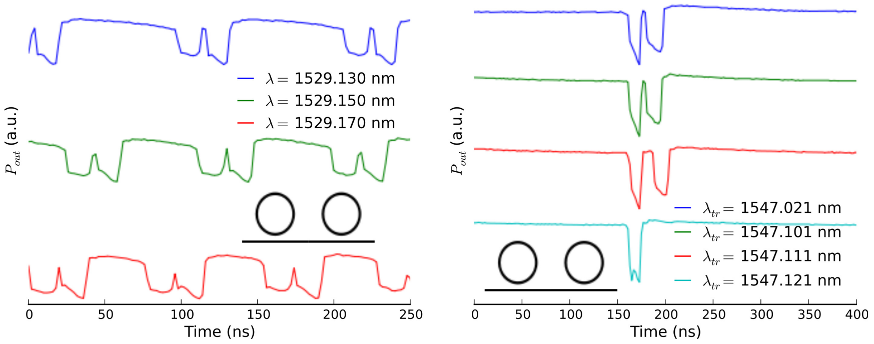

(a) (b)

Figure 4.16: If the resonances of two identical AP rings with common bus waveguide are sufficiently close to each other, they will show self-pulsation (a) and excitability (b) for the same pump wavelength and power. Both rings have a 5.0 μm radius. The self-pulsation is measured at 10.5 dBm@TL (this starts at ~ 1529.120 nm and ends around 1529.260 nm in hysteresis with single-ring self-pulsation), the excitability with the pump at λ = 1529.007 nm and P_{in} = 13.60 dBm, while P_{tr} = 12.00 dBm. Trigger pulse and pump light are now co-directional. On-chip powers are therefore expected to be resp. 10.00 dB and 18.00 dB lower, as ~ 4 dB is lost in a splitter used to combine pump and trigger signals.

4.5.4 Cascadable microring excitability

To experimentally investigate the cascadability of ring excitability, we did similar measurements of two identical AP rings with a 550 nm × 220 nm cross section, a 5.0 μm radius, and a 225 nm gap, connected to the same bus waveguide. The spacing of the ring resonances at ~ 1529 nm is 52 pm, while $\lambda_{3dB} \approx 30$ pm (Fig 4.13). Similar rings on this chip sometimes had a > 1 nm spacing, as this value is determined by the process variation statistics. For some pump settings (λ = 1529.130 – 1529.170 nm in Fig 4.16(a)) the rings self-pulsate in a synchronized way, with one fixed period. Moreover, for some pump settings they are both excitable for the same input power and wavelength (e.g., over a ~ 90 pm λ_{tr}-region in the upper three curves in Fig 4.16(b)). Indeed, given the small (compared to the relative refractory period) and rather fixed time-lapse between the two pulses, comparison to the single-ring excitability experiments suggests that the second pulse is not triggered by noise and the two pulses therefore originate from different rings. This illustrates the experimental feasability of the simulation result from Fig. 4.12, where an AD ring circuit is used.

However, in contrast to the AD-configuration from Fig. 4.12, in the currently measured AP-configuration it is impossible to unambiguously trigger the first ring without directly perturbing the second one, even if we change the wavelength of the trigger pulse. Indeed, both rings have nominally the same radius and thus the same free spectral range. Therefore, if the excitability regions and regions where the ring is sensitive to trigger pulses overlap at one resonance, they also overlap at all the other resonances. Subsequently, it is nontrivial to identify to which rings the resonances belong and trigger them individually. A difference in ring radius or the usage of AD rings can circumvent this problem.

The second ring thus feels both the external trigger pulse and the excitation of the first ring. From Fig. 4.12 we know that the external trigger will result in an initial ΔT and N increase, while the first ring's excitation kicks the second ring's trajectory initially towards lower ΔT and N, which results in a longer time-lapse between the two excitations. The $\sim 15-20\,\text{ns}$ delay between the excitations in the upper three curves from Fig. 4.16(b) indicates that the excitation of the first ring is strong enough to sufficiently perturb the trajectory of the second ring to induce this longer time-lapse, clearly showing the cascadable transfer of information from the excitation of the first ring to the second ring. Indeed, the $47.1\,\mu\text{m}$ center-to-center distance of the rings results in a $0.7\,\text{ps}$ latency between the two rings, so if the last ring was only perturbed by the trigger pulse the two excitations should almost coincide.

Furthermore, we can simulate a similar trigger situation by cascading two AP rings and trigger them with a small P_{in} perturbation through the common bus (Fig. 4.17). The trigger pulse excites both rings, but the excitation of the first ring kicks the trajectory of the second ring back to lower N. Consequently, the excitation of the second ring is delayed and therefore does not coincide with the first ring's excitation.

If the trigger wavelength is in a $< 10\,\text{pm}$ region around $1547.121\,\text{nm}$ (bottom curve Fig. 4.16(b)), only one pulse is visible. This pulse can correspond to a single-ring excitation (the trigger excites only one ring), or with a coincident double ring excitation (the trigger excites both rings directly and the first ring had no influence on the second one). Further research is needed to explain this time-trace more thoroughly, but in all likelihood the trigger signal is detuned too far from resonance for the excitability to be cascadable.

Measurements of similar ring pairs with a $> 100\,\text{pm}$ resonance spacing reveal regions with synchronized self-pulsation, but no regions with coexisting excitability. Measurements of ring pairs with a $> 1\,\text{nm}$ resonance spacing even fail to show synchronized self-pulsation.

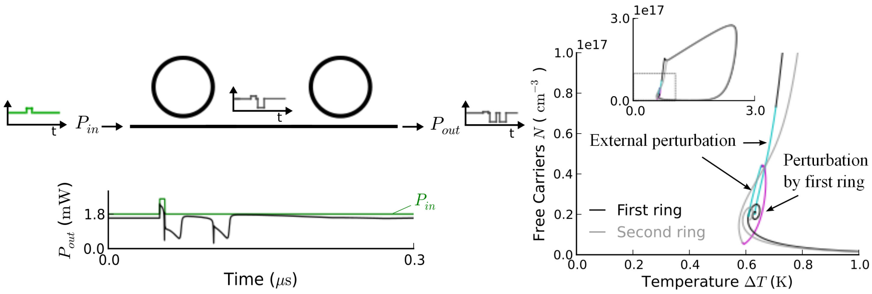

Figure 4.17: In simulations, triggering two cascaded AP rings through the common bus with a 5 ns power increase from 1.8 mW to 2.59 mW at $\delta\lambda = -16$ pm results in a similar time-lapse between two pulses in the time-trace (left) as in Fig 4.12. The phase-plane (right) clearly illustrates how the excitation of the first ring delays the excitation of the second ring, by kicking its trajectory towards lower N.

4.6 Derivation and analysis of the scaling laws of the cavity dynamics

In Sec. 4.5 we have experimentally demonstrated the existance of the excitability mechanism theoretically predicted in Sec. 4.4. So far, in our theoretical analysis, we have assumed a typical small-footprint SOI microring, that can be produced with current state-of-the-art Complementary Metal Oxide Semiconductor (CMOS) fabrication techniques. However, fabrication technology is continuously improving, resulting in, e.g., lower loss waveguides. Consequently, it is important to determine how we have to adapt our design to chips with improved quality. Hopefully, this results in excitability in SOI microrings at higher speed and for lower power consumption.

In this section, we analyse the dependency of the excitability mechanism on the material constants and cavity design, by deriving some relevant scaling laws. The semi-analytic approach used in this section, will not only result in design guidelines for future generation SOI chips, but will also be usable in other material platforms. Furthermore, we will also be able to explain why excitability has currently only been measured at the blue side of the resonance wavelength. As the content of this section is rather mathematical, readers not interested in the technical details can restrict themselves to Sec. 4.6.1, in which we explain the motivation of our approach, and Sec. 4.6.6, in which we summarize the main results of the derivation.

Throughout this section, we will use parameter values that are based on the ones mentioned in Table 4.1, representing a typical critically coupled all-pass

SOI microring with self-pulsing behaviour, unless mentioned otherwise. However, we emphasize again that the proposed approach is also usable for other material systems and cavity types.

4.6.1 Context of the calculation method

The dynamic behaviour demonstrated in Sec. 4.5 or other related experiments on both disks [6] and rings [5] in SOI or PhC cavities in InP [7, 8], can be described accurately using mean field models such as the temporal CMT model we presented in Sec. 4.2.1. However, a thorough analysis of the influence of the cavity design and different material parameters on the oscillation and excitability onset is still missing, as it is not straightforward to analyze this 4D-system (consisting of one complex variable a and two real variables ΔT and N) and the influence of its many parameters in a systematic manner.

Therefore, several simplified models have been proposed. For instance, recent publications show how in nonlinear cavities in which the (slow) thermal heating effects are neglected, bistability, self-pulsation and even chaos can appear provided the remaining cavity nonlinearities (e.g., the free carrier effects) have a sufficiently fast relaxation time compared to the photon lifetime [27–29]. Of course, due the absence of heating effects, this self-pulsation is caused by other physical mechanisms than the one discussed in this chapter. Importantly, bifurcation diagrams of the onset of bistability and self-pulsation can be calculated for the reduced models of those cavities.

In this section, we show how a similar calculation method can be applied on a simplified model that, besides the free carrier nonlinearities, does incorporate the thermal heating effects. For this purpose, we start from the equations of motion proposed in Sec. 4.2.1 and, based on the argumentation in Sec. 4.3.5, adiabatically eliminate the fast light dynamics (build up time of the cavity light), so that we end up with a 2D system. The remaining dynamic variables represent ΔT and N, respectively. This dimensionality reduction allows for a semi-analytic calculation of bifurcation diagrams of the simplified system. We use this calculation, e.g., to explain why excitability has until now been observed mainly at the blue side of the resonance.

4.6.2 Dimensionless version of simplified rate equations

In this subsection, we derive the equations of motion of the cavity. First, we rescale both ΔT and N to a dimensionless variable:

$$\Theta = \frac{2Q\frac{d\mathrm{n}}{dT}}{\mathrm{n}_g}\Delta T, \qquad n = \frac{2Q|\frac{d\mathrm{n}}{dN}|}{\mathrm{n}_g}N. \tag{4.10}$$

Here, $d\mathrm{n}/dT > 0$ is the thermal index change, $d\mathrm{n}/dN < 0$ is the free carrier index change and n_g is the group index. As $\delta = (\omega - \omega_r)\tau_{ph}$ is the (normalized) detuning of the input light to the resonance frequency ω_r of a cavity with photon lifetime τ_{ph} (and thus $Q = \omega_r \tau_{ph}/2$), Θ and n can be interpreted as the absolute value of the (normalized) induced detuning shift caused by ΔT and N, respectively.

As explained in Sec. 4.3.5.A, in SOI, the influence of TPA is at least one or two orders of magnitude smaller than the other nonlinear effects. If we neglect this influence, both on the broadening of the resonance width and the heating of the cavity, the simplified and rescaled version of Eqs. (4.1), (4.2) and (4.3), describing the time evolution of the optical field a in the cavity and these nonlinear detunings Θ and n become:

$$\frac{\mathrm{d}a}{\mathrm{d}t} = \frac{1}{\tau_{ph}}\left[j\left(-\delta - \Theta + n\right) - \left(1 + fn\right)\right]a + j\sqrt{\frac{2}{1+k}\frac{P_{in}}{\tau_{ph}}}e^{j\alpha}, \tag{4.11}$$

$$\frac{\mathrm{d}\Theta}{\mathrm{d}t} = \frac{1}{\tau_{th}}\left[-\Theta + \frac{|a|^2}{P_0^{th}\tau_{ph}}\left(1 + efn\right)\right], \tag{4.12}$$

$$\frac{\mathrm{d}n}{\mathrm{d}t} = \frac{1}{\tau_{fc}}\left[-n + \frac{|a|^4}{\left(P_0^{el}\tau_{ph}\right)^2}\right], \tag{4.13}$$

where we introduced the thermal and electric characteristic intrinsic power of the cavity [30]:

$$P_0^{th} = \frac{\rho_{Si}c_{p,Si}}{4\frac{\frac{d\mathrm{n}}{dT}}{\mathrm{n}_g}\tau_{th}\eta_{lin}\Gamma_{th}}\frac{V_{th}}{Q_i}\left(\frac{1+k}{k}\right)^2, \tag{4.14}$$

$$P_0^{el} = \sqrt{\frac{\hbar\omega_r^3}{4\frac{|\frac{d\mathrm{n}}{dN}|}{\mathrm{n}_g}\tau_{fc}\Gamma_{FCA}\beta_{Si}v_g^2}}\frac{V_{FCA}}{Q_i^{3/2}}\left(\frac{1+k}{k}\right)^{3/2}. \tag{4.15}$$

Here, $Q_i = \frac{\omega_r \tau_l}{2}$ is the intrinsic Q-factor of this cavity. Similar to [14], $k = \frac{\tau_c}{\tau_l}$ is the ratio of 'good' loading (lifetime τ_c) to the parasitic and intrinsic loss channels (lifetime τ_l) of the resonator. The loaded Q-factor of the cavity is then $Q = Q_i k/(1+k)$. For a critically coupled cavity $k = 1$, for an undercoupled cavity $k > 1$ and for an overcoupled cavity $k < 1$. In Eq. (4.11), α is the phase of the input light. In Eq. (4.11) and Eq. (4.12),

$$f = \frac{\frac{\sigma_{Si}c}{\mathrm{n}_g}}{2\frac{\omega_r}{\mathrm{n}_g}\frac{d\mathrm{n}}{dN}} \tag{4.16}$$

is the ratio of the broadening of the resonance width due to FCA (σ_{Si} is the absorption cross section of FCA) to the shift of the resonance peak due to FCD. Finally, $e = \frac{1+k}{k\eta_{lin}}$, while ef represents the additional heating due to FCA.
By putting $\frac{\mathrm{d}a}{\mathrm{d}t} = 0$ in Eq. 4.11, the steady state value of the optical energy in the cavity, normalized to $\sqrt{P_0^{th}\tau_{ph}}$ ($a' = a/\sqrt{P_0^{th}\tau_{ph}}$), can be calculated:

$$|a'_{ss}|^2 = \frac{p}{(1+fn)^2 + (\delta + \Theta - n)^2}, \tag{4.17}$$

where $p = P_{in}/(P_0^{th}\frac{1+k}{2})$ is the normalized version of the input power. As τ_{ph} is considerably smaller than τ_{fc} and τ_{th}, we do an adiabatic elimination of the optical field, i.e., for a given $\Theta(t)$ and $n(t)$, we approximate $|a'|^2(t)$ with its 'steady state' value $|a'_{ss}|^2$. Expressing time τ in units τ_{th} ($\tau = t/\tau_{th}$), the equations of motion of (Θ,n) are then:

$$\frac{d\Theta}{d\tau} = -\Theta + \frac{p(1+efn)}{(1+fn)^2 + (\delta + \Theta - n)^2}, \tag{4.18}$$

$$\frac{dn}{d\tau} = \frac{1}{\epsilon}\left[-n + \left(\frac{pq}{(1+fn)^2 + (\delta + \Theta - n)^2}\right)^2\right]. \tag{4.19}$$

In those equations, $\epsilon = \tau_{fc}/\tau_{th}$, while $q = \frac{P_0^{th}}{P_0^{el}}$ determines the relative importance of the thermo-optic effect versus FCD. If FCD is absent, $q = 0$ (as $P_0^{el} = \infty$), while if the thermo-optic effect is absent $q = \infty$ (as $P_0^{th} = \infty$). Therefore, a relatively strong FCD corresponds to a large q-value. For the convenience of the reader, we summarize the previous model parameters, together with their formulas and a short description of their meaning in Table 4.2.

These simplified equations still incorporate both self-pulsation (Fig 4.18, top) and excitability (Fig 4.18, bottom). In the remainder of this section, unless mentioned otherwise, we use $q = 0.397$, $\epsilon = 0.0815$, $f = 0.0714$, $e = 5$ as ring parameters. P_{out} is calculated based on Eq. (4.17) and power is normalized to ($P_0^{th}\frac{1+k}{2}$).

Eq. (4.18) and (4.19) are independent of the optical phase α of the input light, which can be in principle time-dependent. Consequently, the dynamics of Θ and n are independent of temporal changes in the global phase of its input signal, due to, e.g., interference between the pump light and a co-directional trigger pulse with a certain phase offset, but is only sensitive to the effective change in input power due to such interference effects. This is a crucial difference with the microdisk system that we will present in chapter 5, in which even pure phase pulses might result in excitable behaviour.

Similar to Sec. 4.3.4, a phase-plane analysis of the time-traces is useful to explain the dynamics of the system (Fig. 4.19). The time-traces from Fig. 4.18 follow the direction changes indicated by the the nullclines ($\mathrm{d}\Theta/\mathrm{d}\tau$=0,$\mathrm{dn}/\mathrm{d}\tau$=0).

Name	Description	Formula	Value
p	normalized input power	$P_{in}/(P_0^{th}\frac{1+k}{2})$	
δ	normalized detuning of the input light	$(\omega-\omega_r)\tau_{ph}$	
q	ratio thermo-optic shift (due to SSA-induced heating) to FCD	$\frac{P_0^{th}}{P_0^{el}}$	0.397
ϵ	timescale ratio of the thermal effects to the free carrier effects	$\frac{\tau_{fc}}{\tau_{th}}$	0.0815
e	related to FCA-induced heating	$\frac{1+k}{k\eta_{lin}}$	5
f	ratio FCA to FCD	Eq. (4.16)	0.0714
k	fraction of 'good' loading to losses	$\frac{\tau_c}{\tau_l}$	1
P_0^{th}	thermal characteristic intrinsic power (related to SSA)	Eq. (4.14)	$320\,\mu$W
P_0^{el}	free carrier characteristic intrinsic power (related to FCD)	Eq. (4.15)	$804\,\mu$W
Q	loaded quality factor	$\frac{\omega_r\tau_{ph}}{2}=Q_i\frac{k}{1+k}$	6.25×10^4
τ_{ph}	photon lifetime	$(\tau_l^{-1}+\tau_c^{-1})^{-1}$	103 ps
τ_{th}	thermal relaxation time		65 ns
τ_{fc}	free carrier relaxation time		5.3 ns

Table 4.2: Description and formula of the model parameters and, if appropriate, their default value.

Moreover, the rectangular-like pulse shape of both the self-pulsation and excitation pulses is caused by fast relaxations ($\sim\tau_{fc}$) of the trajectory towards the $dn/d\tau$=0 nullcline, alternated with a period in which the trajectory slowly ($\sim\tau_{th}$) follows this nullcline.

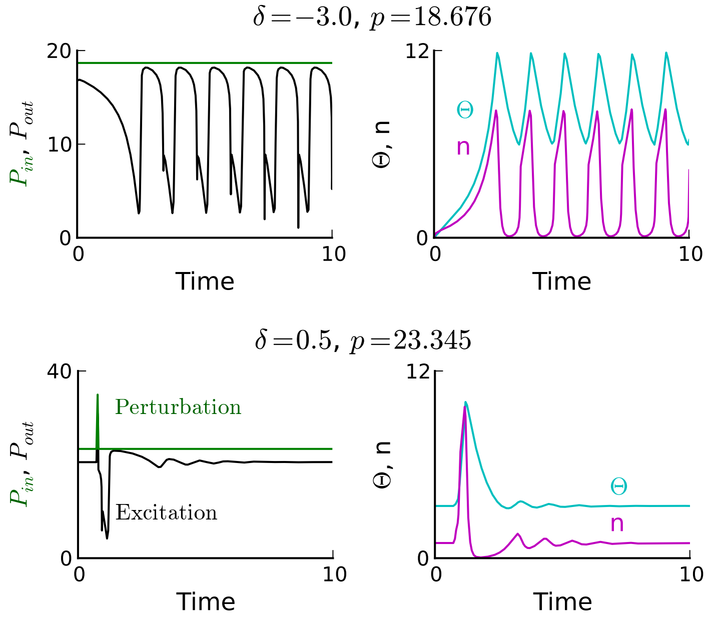

Figure 4.18: At $\delta = -3$ and $p = 18.676$ the microring self-pulsates, while at $\delta = 0.5$ and $p = 23.345$ the ring is excitable: a sufficiently strong perturbation can trigger a pulse. Ring parameters are $q = 0.397$, $\epsilon = 0.0815$, $f = 0.0714$ and $e = 5$. Simulations are done with Caphe.

4.6.3 Influence of cavity design on nonlinearity enhancement

The cavity design enhances the input power for the different physical effects with different scaling laws of the design parameters of the cavity (Q_i, V, k, ...). In other words, for a given P_{in}, a good choice of (Q_i, V, k, ...) can optimize p (SSA-induced heating), ep (FCA-induced heating) and/or qp (free carrier generation).

Therefore, in this subsection, we study how the cavity design can affect the values of the model parameters p, q and e (Table 4.2 summarizes some relevant definitions).

4.6.3.1 Influence of Q_i and k on p, ep and qp

From Eq. (4.14) we obtain $P_0^{th} \propto \frac{1}{\eta_{lin}}\frac{V}{Q_i}\left(\frac{1+k}{k}\right)^2$, and thus $p \propto \left(2\eta_{lin}\frac{k^2}{(1+k)^3}\right)\frac{Q_i}{V}P_{in}$. This proportionality expresses how the cavity enhances the thermal nonlinearity for a given input power P_{in}. Given the cavity losses, the optimization of the light coupling into the cavity (i.e., k) can enhance the nonlinearities. In-

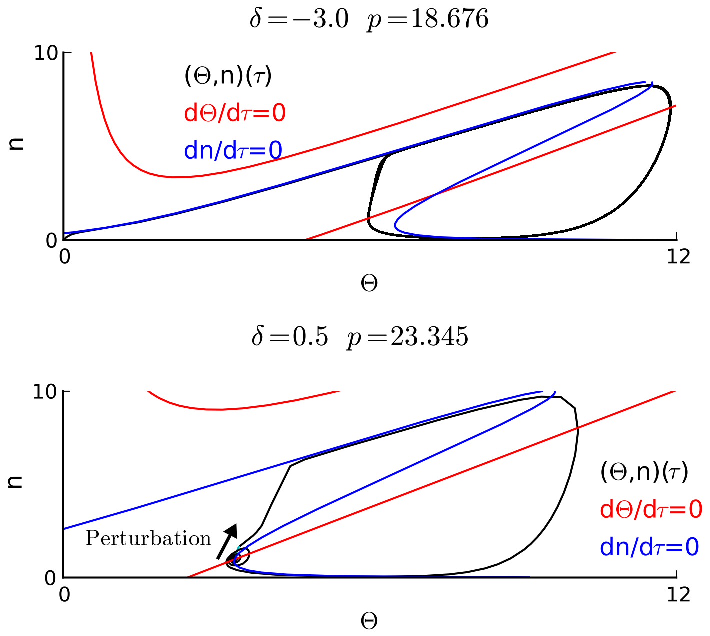

Figure 4.19: In phase plane, the signal makes, both for the self-pulsation time-trace ($\delta = -3$ and $p = 18.676$, top) and the excitability time-trace ($\delta = 0.5$ and $p = 23.345$, bottom) from Fig 4.18, a fast transition between the upper and lower branch of the $dn/d\tau$=0 nullcline, while in between these transitions it slowly follows those branches.

deed, if the cavity is drastically overcoupled ($k << 1$) or undercoupled ($k >> 1$), the cavity-enhancement of the light is rather small and high input powers will be needed to reach thermal nonlinearity. However, near critical coupling the cavity-enhancement is optimal. Similarly, as FCA-induced heating depends on $ep \propto \left(2\frac{k}{(1+k)^2}\right)\frac{Q_i}{V}P_{in}$ and FCD depends on $qp \propto \left(2\frac{k^{3/2}}{(1+k)^{5/2}}\right)\frac{Q_i^{3/2}}{V}P_{in}$, the cavity-enhancement is also optimal for the free carrier effects near critical coupling.

4.6.3.2 Influence of V on p, ep and qp

Additionally, we study the influence of the volume V of the cavity. The necessary scaling laws as a function of V are already derived in Sec. 4.6.3.1. However, the cavity in our chapter is a microring, such that V is proportional to the roundtrip length L of this microring. Therefore, we rephrase the previous scaling laws as a function of L.

In a microring with average waveguide loss $\alpha_{dB/m}$ (with bend loss included) and L not too large ($<< 1/\alpha_{dB/m}$), $Q_i = \frac{2\pi n_g}{\alpha_{dB/m}\lambda_r}\frac{10}{\ln 10}$ is independent of L. However, a coupling section with power coupling K has $Q_c = \frac{\omega_r \tau_c}{2} = \frac{2\pi n_g L}{K\lambda_r}$, such that[1] $k \propto L$. Furthermore, $V \propto L$. Hence, for a given $\alpha_{dB/m}$ and power coupling K, the cavity-enhancement for both the thermal and free carrier effects (cfr. p, qp and ep) reaches an optimum at a value of L close to the one needed for critical coupling (i.e., $L_{crit.} = \frac{K}{\alpha_{dB/m}} \frac{10}{\ln 10}$). However, if we optimize K for a given $\alpha_{dB/m}$ and L, the optimal choice for K will result in an optimal value for k that is independent of the precise value of L. Hence, the scaling factors that depend on k are effectively independent of L. Consequently, the $1/V \propto 1/L$ dependence in the previous scaling laws for p, qp and ep results in an improvement of the nonlinearity enhancement for smaller L (provided the bend losses stay negligible). The critical coupling condition for rings with small L results in small K, which physically corresponds to larger gaps. This is an advantage, as these small rings are a better alternative than racetrack resonators (with corresponding losses on the interface between rounded and straight waveguides) or the fabrication of rings with small gap features (which are difficult to process).

4.6.3.3 Influence of Q_i and k on q and e

Finally, given the scaling laws calculated in subsection 4.6.3.1, we can also analyze how a changing cavity-enhancement changes the relative importance of the corresponding different physical effects. This is reflected in the scaling laws of q and e. Indeed, as discussed in Sec. 4.6.2, q expresses the relative importance of free carrier generation versus heat generation by SSA.

Given $q \propto \frac{1}{\eta_{lin}} Q_i^{1/2} \left(\frac{1+k}{k}\right)^{1/2}$, free carrier effects will dominate in low-loss (high-Q_i) cavities. Also, if $k << 1$, the light only stays in the cavity for a very short time, and in this limit the free carrier effects dominate the heating due to linear absorption. Moreover, q decreases monotonically for increasing k and reaches a global minimum for $k \to \infty$.

As $e \propto \frac{(1+k)}{k}$, similar conclusions are valid for the k-dependence of e, representing the relative importance of the heating induced by FCA versus the heating induced by SSA.

4.6.4 Linear stability analysis

We now explain how the bistability, self-pulsation and excitability regions can be calculated for the model presented in Sec. 4.6.2. The bistability and self-pulsation region boundaries can be calculated analytically, while the excitability domain can be determined using numerical continuation techniques. In the next subsection we will then analyze how the different model parameters change the size of these regions.

---

[1] A change in roundtrip length L can of course imply a change in the curvature at the coupling section (reflected in a change in K), but this is an indirect dependence which is not important for the current reasoning

The steady state curves of Θ and N can be analytically calculated. Indeed, from Eq. (4.18)-(4.19) it can be seen that $\Theta_{ss} = \frac{\sqrt{n}_{ss}}{q}(1+efn_{ss})$. Hence, at steady state:

$$p = \frac{\sqrt{n}_{ss}}{q}\left[\left(1+efn_{ss}\right)^2 + \left(\delta + \frac{\sqrt{n}_{ss}}{q}(1+efn_{ss}) - n_{ss}\right)^2\right]. \tag{4.20}$$

$p(n_{ss})$ is a 7th-order polynomial in $\sqrt{n_{ss}}$, while $\Theta_{ss}(n_{ss})$ is a 3rd order polynomial. As $ef > 0$, Θ_{ss} is a monotonically increasing function of n_{ss}. Moreover, this steady state is independent of ϵ, i.e., the ratio between the free carrier and the thermal timescales.

We now substitute $\Theta(t) = \Theta_{ss} + \delta\Theta(t)$ and $n(t) = n_{ss} + \delta n(t)$ in Eq. (4.18)-(4.19) and only retain the terms linear in $(\delta\Theta(t),\delta n(t))$. This results in a 2×2 Jacobian J_{ss}, with a quadratic characteristic equation:

$$\lambda^2 + tr(J_{ss})\lambda + det(J_{ss}) = 0. \tag{4.21}$$

This equation has two roots λ_1, λ_2. If $det(J_{ss}) = 0$ and $tr(J_{ss}) \neq 0$ one of the roots will be 0 (a sign of a saddle-node bifurcation, resulting in bistability), if additionally $tr(J_{ss}) = 0$ both roots are 0. If $det(J_{ss}) > 0$ and $tr(J_{ss}) = 0$, both roots are purely imaginary, with $\lambda_2 = \lambda_1^*$ (a sign of a Hopf-bifurcation). By substituting both $p(n_{ss})$ and $\Theta(n_{ss})$ into $det(J_{ss})$ and $tr(J_{ss})$, $det(J_{ss}) = 0$ and $tr(J_{ss}) = 0$ result in two 6th order polynomial equations as a function of $\sqrt{n_{ss}}$. Hence, the corresponding 6 roots can be numerically tracked. Of course, only the real, positive roots have a physical meaning.

From Eq. (4.18)-(4.19) it can be inferred that the only ϵ-dependence of $det(J_{ss})$ is a global $\frac{1}{\epsilon}$ scaling factor. Hence, as can be expected from Eq. (4.20), the solutions of $det(J_{ss}) = 0$ are ϵ-independent. This implies that the saddle-node bifurcation, i.e., the bistability onset, is also ϵ-independent. However, the roots of $tr(J_{ss}) = 0$, are ϵ-dependent. This implies that the Hopf-bifurcation does depend on ϵ, and a good ϵ-setting is therefore crucial in obtaining self-pulsation.

Using PyDSTool as numerical continuation software [1], starting from the Hopf-bifurcations, we perform a limit cycle continuation. That is, we track the change in limit cycle shape caused by sweeping a certain parameter. Figure 4.20 illustrates for both $\delta = 0.5$ and $\delta = -3$ how the previously mentioned mathematical and numerical tools not only allow the calculation of the steady state response of n_{ss} for fixed δ and changing p, but also help to indicate the stability regions and to calculate the extreme values of n_{ss} corresponding to the branch of limit cycles, originating from the Hopf bifurcation. While for $\delta = -3$, the curve is bistable, in the $\delta = 0.5$ case it is not. Moreover, for $\delta = 0.5$ the Hopf bifurcation is subcritical (i.e., nearby, a stable fixed point coexists with

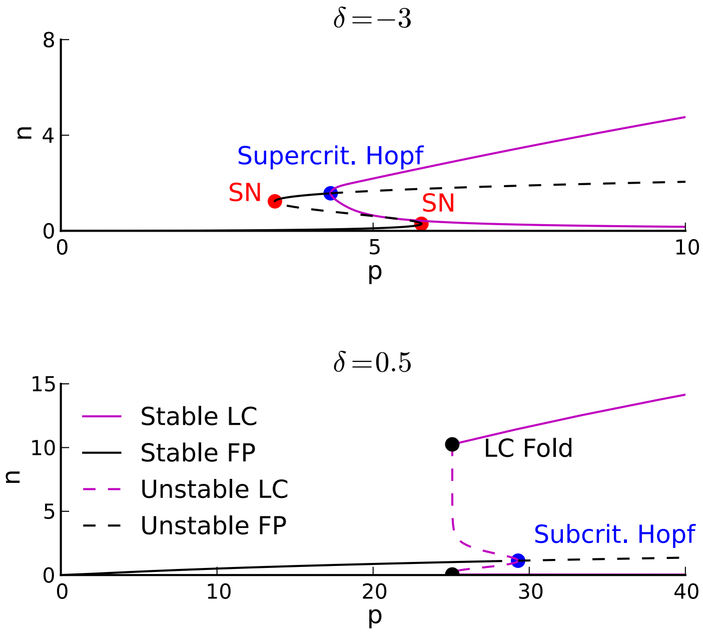

Figure 4.20: The steady state response at $\delta = -3$ is, in between two saddle-node (SN) bifurcations, bistable and has also a supercritical Hopf-bifurcation. At $\delta = 0.5$ no bistability is present, but an unstable limit cycle branch (LC) originates from a subcritical Hopf-bifurcation and annihilates with a stable limit cycle branch in a limit cycle fold (LC Fold). To visualize the limit cycles, both the minimum and maximum values of the cycles are plotted. Stable and unstable Fixed Points (FP) or limit cycles are indicated with resp. solid or dashed lines.

a surrounding unstable limit cycle), while for $\delta = -3$ the Hopf bifurcation is supercritical (i.e., nearby, an unstable fixed point coexists with a surrounding stable limit cycle).

As discussed in Sec. 4.4, the subcritical Hopf bifurcation at $\delta = 0.5$ implies that, for lower input powers, the ring is excitable (Fig. 4.18, right). For a given cavity, the only free variables are the detuning δ and the input power p. In the (δ, p)-plane (Fig. 4.21), the bistability (BI) onset disappears in a Cusp bifurcation, while the Hopf bifurcation transits at a Generalized Hopf (GH) bifurcation from supercritical ($\delta < \delta_{GH}$) to subcritical ($\delta > \delta_{GH}$). Hence, a fold bifurcation of limit cycles curve starts from a Generalized Hopf bifurcation ($\delta_{GH} = -1.077, p_{GH} = 4.317$), towards $\delta > \delta_{GH}$. Subsequently, for $\delta > \delta_{GH}$ and p sufficiently large, but still smaller than the limit cycle fold curve, the microring is

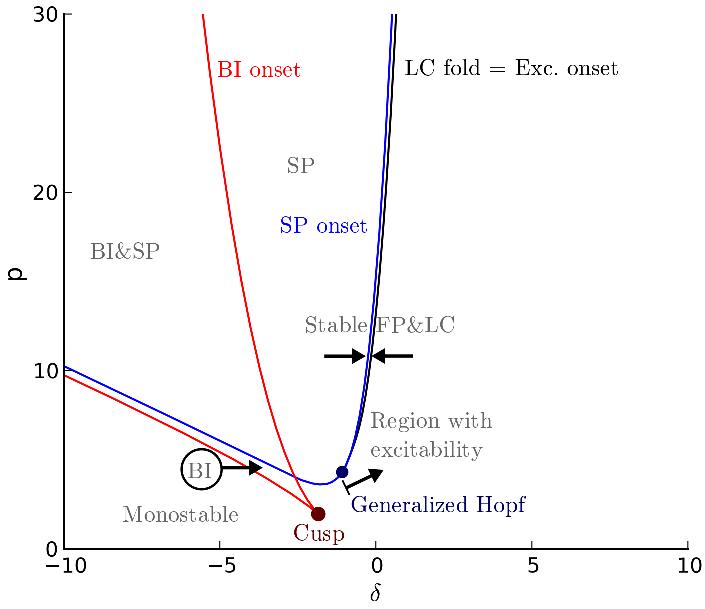

Figure 4.21: By tracking both the saddle-node bifurcations (BI onset) and Hopf bifurcation (SP onset) in the (δ, p)-plane we can determine resp. the bistability (BI) and self-pulsation (SP) region, which partly overlap (BI&SP). A limit cycle fold (LC Fold) originates from a Generalized Hopf bifurcation on the self-pulsation onset, for higher δ excitability is present, if p is below, but sufficiently close, to this limit cycle fold. In between the self-pulsation onset and limit cycle fold a stable fixed point coexists with an unstable limit cycle, surrounded by a stable one (Stable FP&LC).

excitable. The subcritical region of the Hopf bifurcation is mainly centered at the blue side ($\delta > 0$) of the resonance. This explains why excitability has until now only been measured in this wavelength region [2, 7, 8], instead of at the red side ($\delta < 0$) of the resonance. Furthermore, the steep power dependency of the LC fold bifurcation as a function of wavelength at the blue side of the resonance also explains the threshold behavior observed in Fig. 4.10. Indeed, an input pulse corresponds to a kick in power. Hence, the threshold depends on the vertical distance of the equilibrium state to the LC Fold bifurcation. Consequently, Fig. 4.21 geometrically explains why a small change in wavelength can have a drastic influence on the excitability threshold, while a small change in input power has a rather negligible influence.

4.6.5 Influence of model parameters on bistability, self-pulsation and excitability

In Sec. 4.6.3, we analyzed how optimizing the volume, the loss and coupling of a cavity can reduce the required input power needed for nonlinear behaviour and additionally changes the relative importance of the different physical effects (e.g., by changing q). In this subsection, using the techniques presented in Sec. 4.6.4, we will investigate the influence of a change in q, ϵ, τ_{fc} and f on the cavity dynamics in the (δ,p)-plane or the (δ,n)-plane.

4.6.5.1 Influence of q: FCD versus SSA

Whereas the bistability region only shifts slightly for changing $q = \frac{P_0^{th}}{P_0^{el}}$ (as the bistability is mainly caused by the thermal nonlinearity and, consequently, is rather insensitive to moderate changes in P_0^{el}), it should not be surprising that the self-pulsation region (and corresponding excitability onset) is heavily dependent on q (as they are caused by the interplay between thermal and free carrier nonlinearities). We verify this in Fig. 4.22, for different q-values, all with a predominant thermal nonlinearity (i.e., $q < 1$). A higher q-value implies a shift of the self-pulsation region towards higher δ, such that the excitability region stops coinciding with the bistability region. As discussed in Sec. 4.6.3, q can be changed by changing the cavity design. In principle, for $q = 0.5q_0$ (with $q_0 = 0.397$) we expect excitability at the red side of the resonance. However, the region is rather small and coincides with the bistability region. Hence, it will not be trivial to detect this experimentally. For $q = 0$, both the self-pulsation and excitability regions disappear, as in this case only the thermal nonlinearity is present.

4.6.5.2 Influence of timescale ratio ϵ

Slightly adapting the analysis method proposed in [27, 28] to Eq. (4.18) and (4.19), the influence of ϵ on the self-pulsation (SP) and bistability (BI) region can be analyzed. We illustrate the calculation method together with some relevant definitions for $\delta = -3$ (where a Generalized Hopf bifurcation appears) and $\delta = 0.5$ (in which case the Hopf bifurcation is always subcritical) in Fig. 4.23, and summarize the most interesting results in (ϵ,δ)-plane in Fig. 4.24.

We start by calculating the ’on’ and the ’off’ free carrier detuning for self-pulsation ($n_{H,-}$ and $n_{H,+}$, resp.) and bistability ($n_{b,-}$ and $n_{b,+}$, resp.). Note that $n_{H,-/+}$ can be found by solving $tr(J_{ss}(p = p(n))) = 0$, while $n_{b,-/+}$ can be found by solving $det(J_{ss}(p = p(n))) = 0$ (Sec. 4.6.4).

Furthermore, for a given δ, self-pulsation is only possible below a critical value ϵ_{sp}. The curve $(\epsilon_{sp},\delta_{sp})$ can be calculated by tracking the fold bifurcation

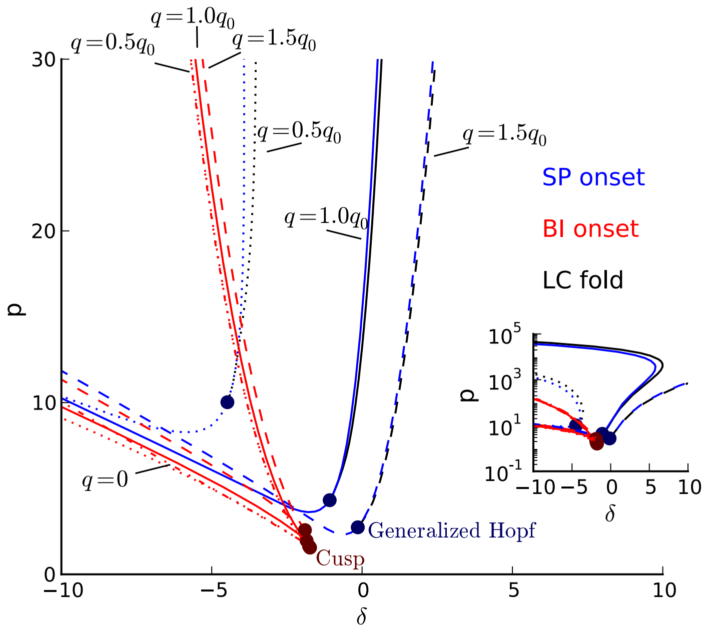

Figure 4.22: While the bistability region is only slightly dependent on the exact q-value, the self-pulsation region and the corresponding excitability region shifts clearly to higher δ for increasing q. Calculation done for $q = 0.5q_0$ (dotted line), $q = q_0$ (solid line) and $q = 1.5q_0$ (dashed line), with $q_0 = 0.397$, i.e., the value from Fig. 4.18. For reference we also included the bistability curve for $q = 0$ (dash-dotted line), i.e., without any free carrier effects.

of $tr(J_{ss}(p = p(n))) = 0$ (using PyDSTool). Similarly (ϵ_b, δ_b) encloses the region with bistability ($BI \neq \emptyset$). In this case, δ_b is ϵ-independent and thus needs to be calculated only once (using PyDSTool). Finally, the curve $p(n_{H,-}) = p(n_{b,-})$ divides the region where $BI \neq \emptyset$ into a domain where $BI \cap SP = \emptyset$, where self-pulsation sets in only for powers above the bistable knee for up-switching, and a domain where $BI \cap SP \neq \emptyset$, where self-pulsation is present at the upper branch of the bistability curve. $p(n_{H,-}) = p(n_{b,-})$ can be parameterized, for a given δ, by first solving $det(J_{ss}(p = p(n))) = 0$ for $n_{b,-}$, subsequently solving $p(n_{H,-}) = p(n_{b,-})$ for $n_{H,-}$ (both calculations are ϵ independent, see Sec. 4.6.4), and finally solving $tr(J_{ss}(n = n_{H,-})) = 0$ for ϵ (a linear equation in ϵ).

The timescale ratio ϵ has no influence on the bistability region, but severely influences the self-pulsation region (Fig. 4.23 and 4.24). If $\epsilon \to 0$, this region becomes larger. This illustrates how the difference in timescale between thermal and free carrier relaxation is necessary for self-pulsation to occur. However,

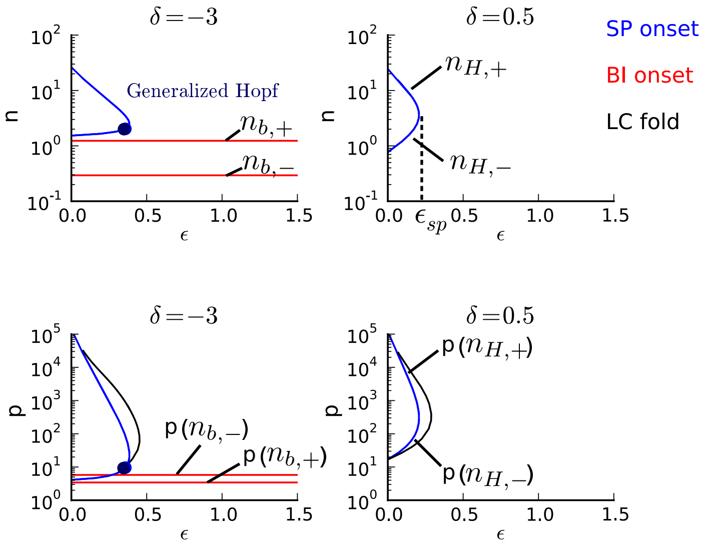

Figure 4.23: While the bistability region is independent of ϵ (with $q = 0.397$ fixed), the self-pulsation region becomes larger for smaller ϵ. For $\delta = -3$ a Generalized Hopf bifurcation is present, while this is not the case for $\delta = 0.5$, as the Hopf bifurcation is then always subcritical. Self-pulsation appears in between $n_{H,-/+}$ (SP onset, blue (or dark gray) lines), while bistability appears in between $n_{b,-/+}$ (BI onset, red (or middle gray) lines). For a given δ, self-pulsation is only possible below a critical value ϵ_{sp}. As before, a limit cycle fold curve (LC Fold, black line) reveals the excitability regions.

the presence of self-pulsation at $\epsilon = 0$ might seem unusual as self-pulsation can only occur in a system which is at least two-dimensional [10]. Indeed, if $\epsilon = 0$, one expects the system to be one-dimensional, as n changes its value instantaneously for a given $\Theta(t)$, such that $\frac{dn}{d\tau} = 0$ is satisfied. Nevertheless, the nullclines ($\frac{dn}{d\tau} = 0, \frac{d\Theta}{d\tau} = 0$) are independent of ϵ and $\frac{dn}{d\tau} = 0$ results in a bistable relationship of n as a function of $\Theta(t)$ (Fig. 4.19), consequently even at $\epsilon = 0$ the system still needs to be considered as two-dimensional. For $\epsilon \to 0$, the transitions between the upper and lower branch of $\frac{dn}{d\tau} = 0$ will go infinitely fast, and Θ will stay fixed during these transitions. The dynamics at this limit thus deviate from the corresponding limit in nanocavities with a non-instantaneous Kerr effect [27].

In this chapter, besides the self-pulsation onset, we are also interested in the excitability threshold (as opposed to [27, 28], where the analysis only focused on the onsets of self-pulsation and bistability of a cavity without thermal heating

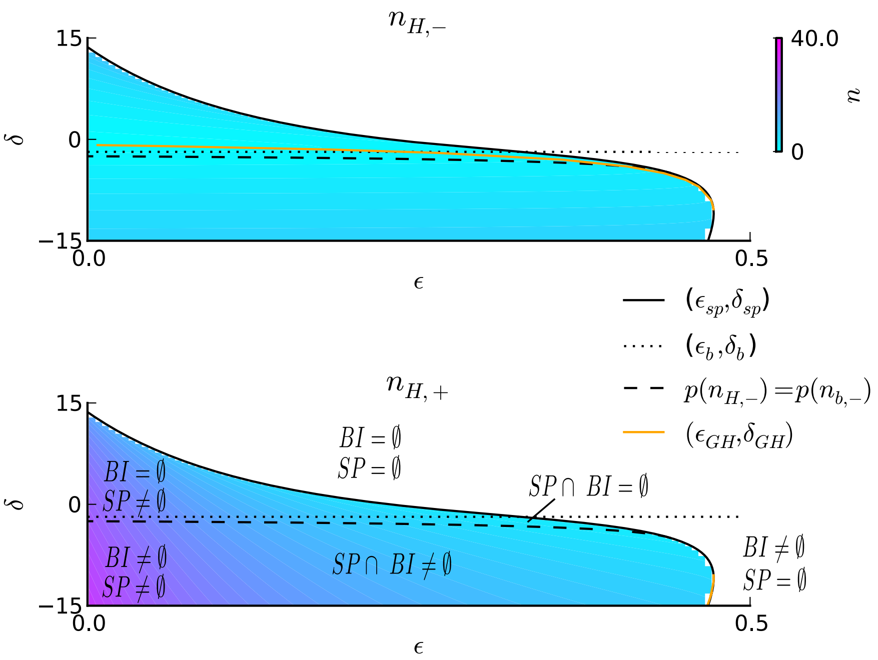

Figure 4.24: Summary of the regions with self-pulsation (SP) and bistability (BI) in the (ϵ,δ)-plane. The color levels represent the 'on' free carrier detuning $n_{H,-}$ and the 'off' free carrier detuning $n_{H,+}$ (with $q = 0.397$ fixed, definitions illustrated in Fig. 4.23). $(\epsilon_{sp},\delta_{sp})$ encloses the region where some input powers result in self-pulsation (solid line), similarly (ϵ_b,δ_b) encloses the region with bistability (dotted line). Furthermore, the curve $p(n_{H,-}) = p(n_{b,-})$ (dashed line) divides the region with bistability into a domain where $BI \cap SP = \emptyset$ where self-pulsation sets in only for powers above the bistable knee for up-switching, and a domain where $BI \cap SP \neq \emptyset$, where self-pulsation is present at the upper branch of the bistability curve. Finally, the Generalized Hopf bifurcation location $(\epsilon_{GH},\delta_{GH})$ on the $n_{H,-/+}$-surfaces is tracked (orange (or light gray) line), indicating excitability is mainly present at the blue side of the resonance.

effects). Therefore, we track the Generalized Hopf bifurcation on the $n_{H,-/+}$-surfaces as this encloses the region where excitability will appear (Fig. 4.24, orange lines). Above $\delta \approx -10.44$ the $(\epsilon_{GH},\delta_{GH})$-curve makes a transition from the $n_{H,+}$-surface to the $n_{H,-}$-surface and the presence of this curve on the $n_{H,-}$-surface encloses the excitability region. If, for a given ϵ, δ is bigger than $\delta_{GH}(\epsilon)$, the (lower) onset of the self-pulsation region is a subcritical Hopf-bifurcation, which implies that for input powers slightly lower than the self-pulsation onset the cavity will be excitable. From Fig. 4.24 it can be inferred that the subcritical Hopf-bifurcation region on the $n_{H,-}$-surface is mainly centered at the blue side (i.e., $\delta > 0$) of the resonance, which confirms that excitability will mainly appear at the blue side of the resonance.

4.6.5.3 Influence of free carrier lifetime τ_{fc}

The most straightforward manner to change $\epsilon = \frac{\tau_{fc}}{\tau_{th}}$ is by tweaking τ_{fc}. In a microring, this can, e.g., be done by reverse biasing a p-i-n diode over the waveguides [31] or by ion implantation [32]. However, as $q \propto \sqrt{\tau_{fc}}$, reducing τ_{fc} also reduces the strength of the free carrier nonlinearities. We analyze this for two typical detuning cases ($\delta = -3$ and $\delta = 0.5$) in Fig. 4.25 and summarize the results in the (ϵ, δ)-plane in Fig. 4.26. In contrast to Fig. 4.23 and Fig. 4.24, due to $q \propto \sqrt{\tau_{fc}}$ and $\epsilon \propto \tau_{fc}$, q is not fixed anymore, but proportional to $\sqrt{\epsilon}$. Moreover, we do not explicitly include $(\epsilon_{sp}, \delta_{sp})$ and $p(n_{H,-}) = p(n_{b,-})$ in Fig. 4.26 as the calculation is severely complicated by the $q(\epsilon \propto \tau_{fc})$-dependence.

As can be expected from Fig. 4.22, if $\tau_{fc} \rightarrow 0$, the self-pulsation region disappears. We remark that in this $\tau_{fc} \rightarrow 0$ limit, as soon as $\tau_{fc} \lesssim \tau_{ph}$, the fast light dynamics can not be neglected anymore, and the model without approximation should be used. Additionally, not only the bistability region corresponding to the one shown in Fig. 4.24 is now dependent on τ_{fc} (and thus on ϵ), but also, due to stronger FCD, an additional bistability region appears for $\epsilon > 1.4$ near $\delta \approx 2.4$. The bistability onset $n_{b,+}$ of the latter region intersects with the self-pulsation onset $n_{H,-}$ in a Bogdanov-Takens bifurcation (BT, red (or middle gray) line in Fig. 4.26). Such a Bogdanov-Takens bifurcation will change the nearby cavity dynamics, as it, e.g., often indicates a transition from 'resonator' (Class 2) excitability to 'integrator' (Class 1) excitability [10]. Finally, similar to Fig. 4.24, above the $(\epsilon_{GH}, \delta_{GH})$-curve on the $n_{H,-}$-surface (orange (or light gray) line in Fig. 4.26) the self-pulsation onset is a subcritical Hopf-bifurcation, which implies the presence of excitability for well-chosen input powers.

Another manner of changing ϵ, one we will not discuss in this chapter, is to drastically change the ambient temperature of the chip, which will change both τ_{fc} and τ_{th}. Indeed, cryogenic experiments of SOI ring resonators show that the timescales of the thermal and free carrier effect change in opposite directions with decreasing temperature [33].

4.6.5.4 Influence of f: FCA versus FCD

Although we already incorporated FCA in the previous calculations ($f \neq 0$ and $e \neq 0$), we did not yet discuss in detail its influence as we used a fixed f value. As can be seen from Eq. (4.16), this value is mainly determined by the choice of

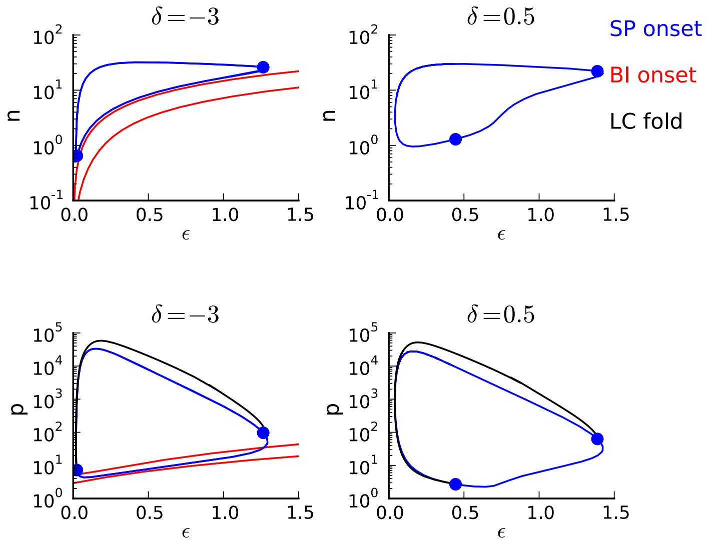

Figure 4.25: If $\epsilon = \frac{\tau_{fc}}{\tau_{th}}$ is changed by tweaking τ_{fc}, $q \propto \sqrt{\epsilon}$ due to $q \propto \sqrt{\tau_{fc}}$. Consequently, the decreasing q for $\epsilon \to 0$ causes the self-pulsation region to disappear (e.g., $\delta = -3$ and $\delta = 0.5$).

material system. In SOI, the high q-value, in combination with a high ef-value makes it impossible to neglect FCA in our microring. If we were to neglect FCA ($f = 0$), or more precisely neglecting the extra heating induced by FCA ($e = 0$), this would drastically change the steady state solutions and the corresponding stability regions. Indeed, it can be calculated that both the self-pulsation region and the bistability region are then mainly centered at the blue side of the resonance (which can be partly understood from an analogue situation in Fig. 4.26, where a high ϵ-value, and thus, by the $\sqrt{\epsilon}$-proportionality, a higher q-value enhances FCD and results indeed in an extra bistability region at the blue side of the resonance). The ring is still excitable, but in different (δ,p)-regions. Moreover, as the self-pulsation region now overlaps with the bistability region, similarly to the high ϵ-region in Fig. 4.26, new bifurcations appear, such as a saddle-node on an invariant circle, which change the nearby dynamics.

Consequently, if $f \neq 0$ and $e \neq 0$, it is mainly the FCA-induced heating that causes the bistability region to be less dependent on the presence of free carriers (Fig. 4.22). Indeed, due to this additional heating the blueshift by FCD is partly compensated by a thermal redshift by the FCA-induced heating. Other theoretical studies confirm the importance of FCA [28, 29] in SOI cavities. Given this significant influence of FCA in SOI, it might be interesting to analyze the nonlinear dynamics in material systems with a different FCA strength.

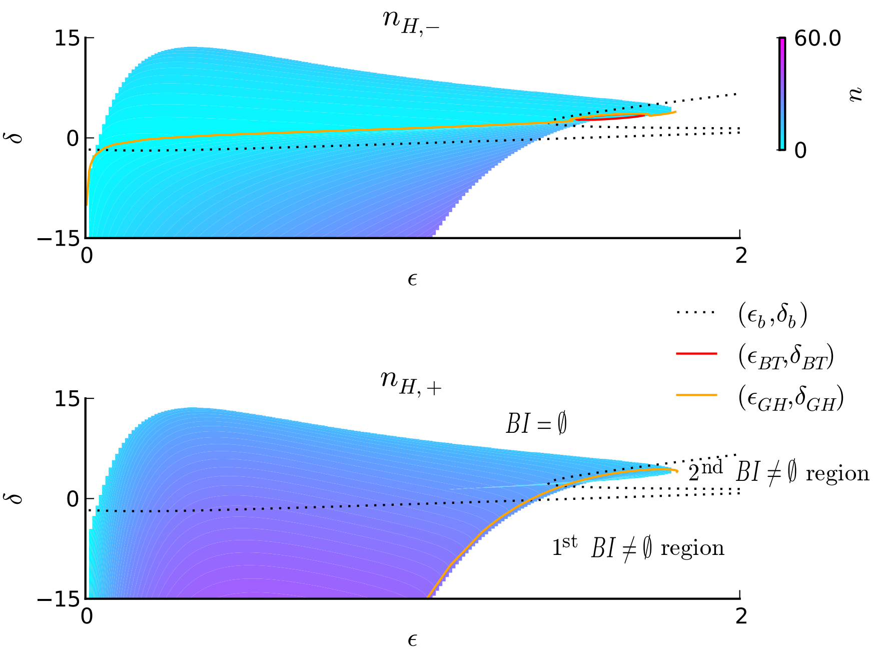

Figure 4.26: If $q = q_0\sqrt{\frac{\epsilon}{\epsilon_0}}$ (q_0, ϵ_0 are the values used in Fig. 4.18), this changes the color levels of the 'on' free carrier detuning $n_{H,-}$ and the 'off' free carrier detuning $n_{H,+}$ with respect to Fig. 4.24, such that the self-pulsation region now disappears for $\epsilon \to 0$. For lower δ the self-pulsation region comes closer towards $\epsilon = 0$, e.g., at $\delta = -15$ the self-pulsation region disappears at $\epsilon \approx 1.5 \times 10^{-3}$. Moreover, δ_b is now slightly ϵ-dependent (dotted line). Additionally, a second bistability region appears for $\epsilon > 1.4$ near $\delta \approx 2.4$, which results in Bogdanov-Takens (BT) bifurcations (red (or middle gray) line) when $n_{b,+}$ intersects with $n_{H,-}$.

4.6.6 Summary of the derivation: towards design guidelines

A microcavity with both thermal and free carrier nonlinearities self-pulsates or is excitable for certain power and wavelength settings of the input light. The required input power of the cavity decreases if the cavity is near critical coupling. If the fast light dynamics (build up time of the cavity light) are neglected, the approximate boundaries of the regions in which this dynamic behaviour is present can be calculated analytically. For instance, in agreement with experiments, excitability is predicted to appear mainly at the blue side of the resonance wavelength.

Improvements in fabrication technology will reduce the linear losses of the waveguides. We predict that free carrier effects become more important if the linear loss of the cavity decreases. Indeed, a decrease in linear losses corresponds to an increase in the intrinsic Q-factor Q_i. A higher Q_i increases the ratio of the characteristic nonlinear powers $q = \frac{P_0^{th}}{P_0^{el}}$, which results in a shift of both the self-pulsation region and the excitability region towards higher detunings (i.e., towards the blue side of the resonance). High-Q_i cavities are therefore needed to obtain this kind of dynamic behaviour for low input powers.

Additionally, in the case of microrings, we predict an optimal cavity-enhancement of the nonlinearities for low loss rings with a small roundtrip length (but still not suffering from additional bend loss). Moreover, the self-pulsation region heavily depends on the timescale ratio $\epsilon = \frac{\tau_{fc}}{\tau_{th}}$, as the size of this region increases if $\epsilon \to 0$. However, in a realistic cavity a decrease in ϵ, e.g, by a decrease in the free carrier lifetime τ_{fc}, implies a corresponding decrease in q. Indeed, $q \propto \sqrt{\tau_{fc}}$. Consequently, if $\tau_{fc} \to 0$, the self-pulsation region disappears. Given this trade-off, to enhance excitability and self-pulsation, τ_{fc} needs to be small compared to the thermal lifetime τ_{th}, but non-zero.

4.7 Future work

The work in the previous sections can be extended in many different directions. In this section, we will discuss three of them.

First, we need to extend the theoretical knowledge of the excitability mechanism. For instance, in Fig. 4.10 we have numerically determined a threshold as a function of the input pulse strength. However, using numerical techniques similar to the ones presented in [34] to calculate the slow manifold for the forced Van der Pol oscillator, in principle, we could calculate the separatrix in the $(\Delta T, N)$-plane that distinguishes excitatory pulses from subthreshold oscillations. Having a geometrical representation of this separatrix would give us more insight on the difference in latency between upward and downward perturbations on the CW pump signal.

Second, whereas our model gives a good indication that we have measured cascadable excitability, the current measurement reads out the output of both rings using the same grating coupler. In future work, we would like to have unambiguous access to the output of each individual ring. One approach is to use AD-rings instead of AP-rings and by reading out the output of the grating couplers of all those rings simultaneously using, e.g., a fiber-array [35]. Another approach is to use excitable rings with slightly different radii and consequently a different Free Spectral Range (FSR). Those radii have to be chosen such that they coincide at one resonance, while the resonances do not overlap at other wavelengths. This allows to trigger a ring on a resonance that does not coincide with a subsequent ring, while pumping it at a coinciding resonance, such that the excitation can be transferred to the subsequent ring. This is also an approach to control the connectivity in a larger network of excitable rings. Indeed, in a large network one can use input signals that have different wavelengths, each wavelength being matched to a different set of microrings. Rings on the same waveguide will only communicate with each other if they have a common resonance wavelength. As one ring is able to react to input signals at different resonance wavelengths, this type of wavelength demultiplexing helps to effectively increase the fan-in/fan-out of the neuron (cfr. Sec. 4.4.4), without the need to use lossy power splitters and combiners (cfr. Sec. 2.2.1).

Third, in the former experiments we did not control the resonance wavelengths of the rings. Although we theoretically know that this can be done using heaters or pn junctions, we still need to prove that the excitability mechanism exists in such tuned rings. Recently, a first demonstration of tunability of the self-pulsation in a SOI-microring using a pn junction has been demonstrated [36]. This is a first indication that the thermo-electrical nonlinear dynamics in passive SOI-rings can indeed cope with the incorporation of such tuning mechanisms.

4.8 Conclusion

A high-Q microring self-pulsates for certain input power and wavelength settings, which can be described with CMT using three variables: the complex mode amplitude a of the light in the cavity, the temperature difference with the surroundings ΔT and the concentration of free carriers N. Neglecting the fast energy and phase dynamics of the light allows a 2D phase-plane analysis. Furthermore, this dimensionality reduction provides a manner to construct two new equations of motion for ΔT and N, which still capture the most important dynamics.

For some wavelengths, when changing the input power, the microring undergoes a subcritical AH bifurcation at the self-pulsation onset. As a consequence the system shows Class 2 excitability. This thorough understanding of the excitability mechanism will allow for a correct characterization of the computational properties of a microring, used as a photonic spiking neuron.

Simulations show that this excitation mechanism is cascadable. Experimental single-ring excitability and self-pulsation behaviour follows the theoretic predictions. Moreover, two identical rings can be excitable or self-pulsate for the same pump power and wavelength, if only their resonance spacing is sufficiently small ($< 100\,\text{pm}$). Ring pair circuits are proposed in which the trigger pulse can address only one ring directly, without perturbing the other one.

Furthermore, we have theoretically determined the influence of the cavity design and the material constants on the excitability region. A ring should preferably be close to critical coupling, and have a free carrier lifetime that is smaller than the thermal lifetime, but non-zero. We have also theoretically confirmed the experimental observation that excitability is mainly observed at the blue side of the resonance.

References

[1] R. H. Clewley, W. E. Sherwood, M. D. LaMar, and J. M. Guckenheimer. *PyDSTool, a software environment for dynamical systems modeling.* 2007.

[2] T Van Vaerenbergh, M Fiers, P Mechet, T Spuesens, R Kumar, G Morthier, B Schrauwen, J Dambre, and P Bienstman. *Cascadable Excitability in microrings.* Opt. Express , 20(18):20292–20308, mar 2012.

[3] T. Van Vaerenbergh, M. Fiers, J. Dambre, and P. Bienstman. *Simplified description of self-pulsation and excitability by thermal and free-carrier effects in semiconductor microcavities.* Physical Review A, 86(6):063808, 2012.

[4] G Priem, P Dumon, W Bogaerts, D Van Thourhout, G Morthier, and R Baets. *Optical bistability and pulsating behaviour in Silicon-On-Insulator ring resonator structures.* Opt. Express , 13(23):9623–8, nov 2005.

[5] Wolfram H. P. Pernice, Mo Li, and Hong X. Tang. *Time-domain measurement of optical transport in silicon micro-ring resonators.* Opt. Express, 18(17):18438–18452, Aug 2010.

[6] Thomas J Johnson, Matthew Borselli, and Oskar Painter. *Self-induced optical modulation of the transmission through a high-Q silicon microdisk resonator.* Opt. Express , 14(2):817–31, jan 2006.

[7] Maia Brunstein, Alejandro M. Yacomotti, Isabel Sagnes, Fabrice Raineri, Laurent Bigot, and Ariel Levenson. *Excitability and self-pulsing in a photonic crystal nanocavity.* Phys. Rev. A, 85:031803, Mar 2012.

[8] A. M. Yacomotti, P. Monnier, F. Raineri, B. Ben Bakir, C. Seassal, R. Raj, and J. A. Levenson. *Fast Thermo-Optical Excitability in a Two-Dimensional Photonic Crystal.* Phys. Rev. Lett., 97:143904, Oct 2006.

[9] Q. Lin, T. J. Johnson, C. P. Michael, and O. Painter. *Adiabatic self-tuning in a silicon microdisk optical resonator.* Opt. Express, 16(19):14801–14811, Sep 2008.

[10] Eugene M. Izhikevich. *Dynamical Systems in Neuroscience: The Geometry of Excitability and Bursting (Computational Neuroscience).* The MIT Press, 1 edition, nov 2006.

[11] Stéphane Barland, Oreste Piro, Massimo Giudici, Jorge Tredicce, and Salvador Balle. *Experimental evidence of van der Pol-Fitzhugh-Nagumo dynamics in semiconductor optical amplifiers.* Physical Review E, 68(3):036209, September 2003.

[12] Francesco Marino, Gustau Catalán, Pedro Sánchez, Salvador Balle, and Oreste Piro. *Thermo-Optical âĂIJCanard OrbitsâĂİ and Excitable Limit Cycles.* Physical Review Letters, 92(7):073901, February 2004.

[13] W. Bogaerts, , P. De Heyn, T. Van Vaerenbergh, K. De Vos, S. Kumar Selvaraja, T. Claes, P. Dumon, P. Bienstman, D. Van Thourhout, and R. Baets. *Silicon microring resonators.* Laser & Photonics Reviews, 6(1):47–73, 2012.

[14] P. Barclay, K. Srinivasan, and O. Painter. *Nonlinear response of silicon photonic crystal microresonators excited via an integrated waveguide and fiber taper.* Optics Express, 13(3):801–820, 2005.

[15] Ardavan F. Oskooi, David Roundy, Mihai Ibanescu, Peter Bermel, J. D. Joannopoulos, and Steven G. Johnson. *MEEP: A flexible free-software package for electromagnetic simulations by the FDTD method.* Computer Physics Communications, 181:687–702, January 2010.

[16] John Guckenheimer and Philip Holmes. *Nonlinear oscillations, dynamical systems, and bifurcations of vector fields.* Applied mathematical sciences. Springer-Verlag, New York, 1983.

[17] Eugene M Izhikevich. *Neural Excitability , Spiking and Bursting.* International Journal of bifurcation and chaos, 10(6):1171–1266, 2000.

[18] Takashi Kohno and Kazuyuki Aihara. *A MOSFET-Based Model of a Class 2.* 16(3):754–773, 2005.

[19] Paul Merolla, John Arthur, Filipp Akopyan, Nabil Imam, Rajit Manohar, and Dharmendra S Modha. *A digital neurosynaptic core using embedded crossbar memory with 45pJ per spike in 45nm.* In Custom Integrated Circuits Conference (CICC), 2011 IEEE, pages 1–4. IEEE, 2011.

[20] Ben Varkey Benjamin, Peiran Gao, Emmett McQuinn, Swadesh Choudhary, Anand R. Chandrasekaran, Jean-Marie Bussat, Rodrigo Alvarez-Icaza, John V. Arthur, Paul a. Merolla, and Kwabena Boahen. *Neurogrid: A Mixed-Analog-Digital Multichip System for Large-Scale Neural Simulations.* Proceedings of the IEEE, 102(5):699–716, May 2014.

[21] Johannes Schemmel and D Bruderle. *A wafer-scale neuromorphic hardware system for large-scale neural modeling.* Circuits and Systems (ISCAS), Proceedings of 2010 IEEE International Symposium on, pages 1947–1950, 2010.

[22] Shankar Kumar Selvaraja, Patrick Jaenen, Wim Bogaerts, Dries Van-Thourhout, Pieter Dumon, and Roel Baets. *Fabrication of Photonic Wire and Crystal Circuits in Silicon-on-Insulator Using 193-nm Optical Lithography.* J. Lightwave Technol., 27(18):4076–4083, Sep 2009.

[23] Peter De Heyn. *Receivers Based on Silicon Ring Resonators for Multi-Wavelength Optical Interconnects.* PhD thesis, UGent-imec, 2014.

[24] B E Little, J P Laine, and S T Chu. *Surface-roughness-induced contradirectional coupling in ring and disk resonators.* Optics letters, 22(1):4–6, January 1997.

[25] P. De Heyn, B. Kuyken, D. Vermeulen, W. Bogaerts, and D. Van Thourhout. *High-performance low-loss silicon-on-insulator microring resonators using TM-polarized light.* Optical Fiber Conference, pages 20–22, 2011.

[26] Dirk Taillaert, Frederik Van Laere, Melanie Ayre, Wim Bogaerts, Dries Van Thourhout, Peter Bienstman, and Roel Baets. *Grating Couplers for Coupling between Optical Fibers and Nanophotonic Waveguides.* Japanese Journal of Applied Physics, 45(8A):6071–6077, August 2006.

[27] Andrea Armaroli, Stefania Malaguti, Gaetano Bellanca, Stefano Trillo, Alfredo de Rossi, and Sylvain Combrié. *Oscillatory dynamics in nanocavities with noninstantaneous Kerr response.* Phys. Rev. A, 84:053816, Nov 2011.

[28] Stefania Malaguti, Gaetano Bellanca, Alfredo de Rossi, Sylvain Combrié, and Stefano Trillo. *Self-pulsing driven by two-photon absorption in semiconductor nanocavities.* Phys. Rev. A, 83:051802, May 2011.

[29] Shaowu Chen, Libin Zhang, Yonghao Fei, and Tongtong Cao. *Bistability and self-pulsation phenomena in silicon microring resonators based on nonlinear optical effects.* Opt. Express , 20(7):7454, mar 2012.

[30] Marin Soljačić, Mihai Ibanescu, Steven G. Johnson, Yoel Fink, and J. D. Joannopoulos. *Optimal bistable switching in nonlinear photonic crystals.* Phys. Rev. E, 66:055601, Nov 2002.

[31] Amy C Turner-Foster, Mark a Foster, Jacob S Levy, Carl B Poitras, Reza Salem, Alexander L Gaeta, and Michal Lipson. *Ultrashort free-carrier lifetime in low-loss silicon nanowaveguides.* Optics express, 18(4):3582–91, feb 2010.

[32] Michael Waldow, Tobias Plötzing, Martin Gottheil, Michael Först, Jens Bolten, Thorsten Wahlbrink, and Heinrich Kurz. *25Ps All-Optical Switching in Oxygen Implanted Silicon-on-Insulator Microring Resonator.* Optics express, 16(11):7693–702, may 2008.

[33] Wolfram H P Pernice, Carsten Schuck, Mo Li, and Hong X Tang. *Carrier and thermal dynamics of silicon photonic resonators at cryogenic temperatures.* Opt. Express , 19(4):3290–6, feb 2011.

[34] Peter Langfield, Bernd Krauskopf, and Hinke M Osinga. *Solving Winfree ' s puzzle : the isochrons in the FitzHugh-Nagumo model.* pages 1–25, tbp.

[35] P Dumon, W Bogaerts, D Van Thourhout, D Taillaert, R Baets, J Wouters, S Beckx, and P Jaenen. *Compact wavelength router based on a Silicon-on-insulator arrayed waveguide grating pigtailed to a fiber array.* Optics express, 14(2):664–9, January 2006.

[36] Libin Zhang, Yonghao Fei, Yanmei Cao, Xun Lei, and Shaowu Chen. *Experimental observations of thermo-optical bistability and self-pulsation in silicon microring resonators.* 31(2):201–206, 2014.

5

Cascadable excitability in microdisk lasers

In chapter 4, cascadable Class 2 excitability was presented in a Silicon-On-Insulator (SOI) microring. However, from an application point-of-view the use of this mechanism is currently still peculiar, as most of the algorithms to train a Spiking Neural Network (SNN) assume Leaky-Integrate and Fire (LIF) neurons as basic units of the network, corresponding to Class 1 excitability instead of Class 2 excitability.

In this chapter, using simulations, we illustrate that it is possible as well to emulate Class 1 excitability on the (hybrid) silicon photonics platform, using optically-injected microdisk lasers. Furthermore, we propose a scalable optical spiking neuron design that results in output pulses that are comparable in strength to the input pulses. This neuron has a clear threshold and an integrating behaviour, leading to an output rate-input rate dependency for subthreshold pulses that is similar to the characteristic of sigmoidal artificial neurons. We also show that the optical phase of the input pulses has influence on the neuron response, and can be used to create inhibitory, as well as excitatory perturbations.

Additionally, we propose a connection scheme that allows the disks to react to excitations from other disks. Phase tuning of the intermediate connections allows to control the disk response. Furthermore, we investigate the sensitivity of the disk circuit to deviations in driving current and locking signal wavelength detuning.

The rest of this chapter is structured as follows. First, we motivate in Sec. 5.1 the need to introduce a new optical excitability mechanism, by analysing the drawbacks of current state-of-the-art solutions. The model used for the microdisk laser is then introduced in Sec. 5.2. Subsequently, the effect of optical injection on the laser dynamics is presented in Sec. 5.3. This optical injection study is interpreted to predict Class 1 excitability. A possible neuron geometry is introduced in Sec. 5.4 and the threshold behaviour, phase dependency and the response to one or more equidistant pulse trains are then investigated.

Next, the step towards cascadability is made. Using the proposed 'neuron' circuit, and by connecting two of these neurons in the topology defined in Sec. 5.5, we will demonstrate in Sec. 5.6 cascadability of the excitation mechanism, as this topology allows one disk to trigger an excitation in another disk. In Sec. 5.7, the sensitivity of this cascade of two disks to variations in laser frequencies and current deviations, respectively, will be discussed. In Sec. 5.8, we give a roadmap for future work. Simulations are done using Caphe, the nonlinear circuit simulator described in chapter 3.

This work has been carried out in the framework of the master thesis of ir. K. Alexander. His dissertation [1] has been used as a starting point for writing this chapter, in which we present the main results published in [2, 3].

5.1 Excitability in integrated semiconductor lasers

The lack of theory dealing with Class 2 excitable neurons in SNN literature, makes it worthwhile to search an optical excitability mechanism in an integrated component that exhibits Class 1 excitability. For this purpose, we will shift to a lasing device in this chapter. In fact, excitability has already been experimentally demonstrated in lasers in 1997 [4, 5], six years before the first demonstration in semiconductor optical amplifiers of the thermo-electronic excitability mechanism that we used in passive microrings in the previous chapters. Indeed, Giudici et al. demonstrated excitability in a semiconductor laser with optical feedback [4], while almost simultaneously Plaza et al. [5] demonstrated excitability in a CO_2 laser with a saturable absorber. Due to the fast time scales and miniaturization capabilities of semiconductors, excitability in semiconductor lasers received a lot of attention during the past decade and, consequently, currently, there is a whole zoo of mechanisms known to cause excitability in semiconductor laser types [6–12]. In this section, we repeat the most important laser-related excitability mechanisms introduced in Sec. 2.2.2 and Sec. 2.4. We will first discuss three types of state-of-the-art solutions to induce excitability in an integrated laser and their limitations (Sec. 5.1.1, 5.1.2

and 5.1.3), before we give a first glimpse of the advantages of our approach (Sec. 5.1.4).

5.1.1 Excitability due to optical injection in single-mode semiconductors

As discussed in Sec. 2.4.1, a suitable excitability mechanism is found in optically-injected single-mode semiconductor lasers [7, 8, 12], as they are, near the bifurcation corresponding to the threshold for injection locking, Class 1 excitable, phenomenologically resembling the well-known Leaky Integrate-and-Fire (LIF) model of a spiking neuron [13]. The locking signal is chosen such that a small perturbation can excite the system across this bifurcation, causing the laser to lose the phase locking for at least a 2π-excursion of the phase of the optical mode, creating pulses in the laser output, relatively invariant of the exact excitation shape. Mathematically, this excitability takes place due to the presence of a nearby Saddle-Node on Invariant Circle (SNIC) bifurcation, a bifurcation mechanism that is also known to cause Class 1 excitability in biological neurons [13]. A possible disadvantage that limits the application of current optical injected lasers, is the fact that the excited output pulse is rather a small ripple compared to the default DC output of the laser in equilibrium [8, 12, 14]. This strong DC output would result in too strong coupling of the lasers in optical SNNs based on this technology, to be practically usable.

5.1.2 Excitability near the onset of passive Q-switching

In the experiment of Plaza et al. excitability is below the threshold for passive Q-switch-like pulsing in lasers with an intra-cavity Saturable Absorber (SA) [5]. In this case, no coherent light injection or holding beam is necessary and excitability arises as a competition between gain and saturable absorption. This phenomenon can also be induced in semiconductor lasers, such as the Vertical Cavity Surface-Emitting Laser (VCSEL) with an intra-cavity SA discussed in [9]. However, as the bifurcation mechanism that causes this excitability is a homoclinic bifurcation instead of the aforementioned SNIC-bifurcation, there are some differences with the excitability observed in biological neurons [15]. As we mentioned in Sec. 2.4, for this type of excitability, the size of the output pulse depends on the energy of the input pulse, whereas for a SNIC bifurcation, the output pulse strength is more-or-less independent on the input pulse strength, as long it is above threshold.

Current research focuses on the use of similar-behaving optical components in an integrated circuit. Recently, Nahmias et al. [14] proposed in simulation a promissing platform based on the aforementioned VCSEL, but with a SA with reduced electron lifetime and a gain section that is pumped rather close to threshold, to increase the similarity with the default LIF behaviour. The current disadvantage of this approach based on a VCSEL with adapted SA is that the interconnection of the different optical neurons probably needs to be done off-chip. An approach more amenable to integration is proposed in [16], in which an RF connection between a photodetector and a hybrid laser allows for both inhibitory and excitatory inputs.

The main advantage of the mechanism based on passive Q-switching is that the device is not lasing in its equilibrium state, resulting in a very high Extinction Ratio (ER) of the output pulses. However, a first experimental demonstration, in which the electron lifetime of the SA is adapted to the settings described in [16], still has to be done. Based on previous results on passive-mode locking with intra-cavity absorbers using hybrid evanescent lasers bonded on the silicon platform [17–19], this design seems feasible with current fabrication technology.

5.1.3 Excitability in asymmetric Semiconductor Ring Lasers

A fully integrated all-optical alternative is demonstrated both numerically and experimentally for Semiconductor Ring Lasers (SRLs) by Gelens, Coomans et al. [6, 11, 20, 21]. SRLs support two counterpropagating modes, which are both linearly and non-linearly coupled to each other by intermodal coupling and cross-gain saturation, respectively. For a restricted phase range of the intermodal coupling coefficient, alternate oscillations will appear, i.e., the optical energy in the laser will oscillate between the two counterpropagating modes. If the laser is operated in the unidirectional regime with two stable states, near the onset of this alternate oscillations regime, theoretically, excitability is expected, but as a drawback of the symmetry of the system, the attraction basins of both stable states are equal in size and, consequently, there will be a competition between mode-hopping events between both stable states and excitable excursions [20]. This drawback can be solved by inducing an asymmetry in the intermodal coupling [6, 11, 21]. This causes the basin of one of these equilibria to shrink drastically, making the state metastable. For very specific phases of the intermodal coupling coefficients, the basin of the remaining state will have a spiralling appearance, allowing for a more reliable type of excitability. However, this mechanism still has a couple of disadvantages. For instance, strong input perturbations can cause a multipulse excitation [11], with the number of pulses increasing with the input perturbation strength, and the device acts as a resonator neuron, which is both not compatible with the more traditional LIF behaviour [13]. Moreover, the fact that the phase of the linear intermodal coupling is of such critical influence, raises questions about the controllability of this method, as this phase is dependent on process variations due to fabrication imperfections.

5.1.4 Excitability due to optical injection in microdisk lasers

Microdisk lasers behave phenomenologically identically to SRLs [11, 22]. As a consequence, inducing a reflection asymmetry also reveals the excitability mechanism found in SRLs. However, in this chapter, to obtain Class 1 excitability in these microdisk lasers we induce asymmetry in the system equations in a different way, i.e., by optical injection in one of the two counterpropagating modes, giving rise to the same excitability mechanism as discussed in Sec. 5.1.1. An advantage of the circular cavity sytem is that we can use the signal of the suppressed mode as output of the system, resulting in a well-behaved input-output behaviour. As is the case for optically-injected single-mode standing-wave semiconductor lasers, the excitability is related to a SNIC bifurcation and the microdisks act as integrating neurons, similar to LIF neurons [13]. Moreover, we show that by using the optical phase, pulse trains can be created that have excitatory or inhibitory effects on the excitability mechanism.

Hence, the microdisk laser forms a promising building block for large photonic SNNs. Indeed, these microdisk lasers are fabricated using hybrid III-V on silicon technology [23, 24], which makes the neurons highly scalable through techniques as wafer bonding [16, 25, 26]. Furthermore, they have a smaller footprint and lower power consumption than many other integrated lasers and operate at higher speed [27]. Being active components in a hybrid platform, these lasers have the advantage of being able to compensate for losses, for example in a hybrid neural network with passive excitable components, such as microring resonators [28], paving the way for integrated ultrafast, all-optical neural networks. This type of network could be useful for a growing number of applications that require lower latencies outside the abilities of the fastest electronic circuits, including processing of the RF spectrum or ultrafast control [16].

5.2 The microdisk laser

The microdisk lasers simulated and discussed in this chapter consist of a disk-shaped InP laser cavity, with an InAsP quantum well gain section, bonded on top of a SOI substrate [23, 24]. The single-mode disk supports two counterpropagating whispering gallery modes, which are evanescently coupled to a silicon waveguide buried in a SiO_2-layer. The inset in Fig. 5.1 phenomenologically depicts the optical coupling between the microdisk laser and the bus waveguide. The lasers are electrically pumped and can be optically injected from both sides through the coupling waveguide.

We will continue this section with a description of the rate equations of this component, followed by a bifurcation analysis in which the influence of the current on the dynamics is explained.

5.2.1 Rate equation model of a single microdisk laser

One can describe the dynamic behaviour of a microdisk laser using a set of coupled rate equations, in the slowly-varying envelope approximation, representing the evolution of the complex mode amplitudes, E^+ and E^- ($|E_\pm|^2$ is the number of photons in the mode, while the optical field oscillates with an additional $e^{-j\omega_{in}t}$-dependency[1]), and the number of free carriers, N, in the cavity [22, 24, 29]:

$$\frac{dE^+}{dt} = \frac{1}{2}\left(1-j\alpha\right)\left(G^+ - \frac{1}{\tau_p}\right)E^+ + j\Delta\omega E^+ + CE^- - j\frac{\kappa\sqrt{\tau}}{\sqrt{\hbar\omega_0}}E_{in,1} \quad (5.1)$$

$$\frac{dE^-}{dt} = \frac{1}{2}\left(1-j\alpha\right)\left(G^- - \frac{1}{\tau_p}\right)E^- + j\Delta\omega E^- + CE^+ - j\frac{\kappa\sqrt{\tau}}{\sqrt{\hbar\omega_0}}E_{in,2} \quad (5.2)$$

$$\frac{dN}{dt} = \frac{\eta I}{q} - \frac{N}{\tau_c} - G^+\left|E^+\right|^2 - G^-\left|E^-\right|^2 \quad (5.3)$$

$$G^\pm = \frac{\Gamma g_N (N-N_0)}{1+\Gamma\epsilon_{NL}\left(|E^\pm|^2 + 2|E^\mp|^2\right)} \quad (5.4)$$

In Eqs. (5.1) and (5.2), α is the line broadening factor, τ_p the photon lifetime in the cavity, τ is the roundtrip time of the cavity, $\Delta\omega = \omega_{in} - \omega_0$ the detuning between the input light ω_{in} and the free-running cavity frequency ω_0, C is the complex intermodal coupling coefficient. This linear coupling can be due to inhomogeneities in absorption and refractive index along the disk, such as surface roughness, or due to external reflections on grating couplers or fiber facets [24, 27]. κ is the coupling with the waveguide. $E_{in,1,2}$ are the complex amplitudes of the optical inputs ($|E_{in,1,2}|^2$ is the power in the waveguide). Equation (5.3) describes the evolution of the number of free carriers. I is the injected current, q the elementary charge of an electron, η a current efficiency factor, and τ_c the carrier lifetime. $G^\pm$ are the gain coefficients of the modes, g_N is the differential gain, N_0 the transparency threshold of free carriers and Γ the confinement factor. The denominator in Eq. (5.3) includes cross- and self-gain modulation, ϵ_{NL} is called the nonlinear gain suppression coefficient. The total output amplitude of the disk depends both on the amplitude of the modes and the input amplitudes. The number of photons that couples from the modes into the output mode per roundtrip time τ can be written as $|\tau\kappa E^{\pm}|^2$. Consequently, the output power from the modes is $\frac{\hbar\omega_0\kappa^2\tau^2}{\tau}|E^{\pm}|^2$ and the total output power becomes:

---

[1] In previous chapters we used a $e^{+j\omega_{in}t}$ phase-convention, we use this new convention in agreement with literature on microdisk lasers, but this choice has no fundamental consequences.

$$E_{out,1} = E_{in,2} - j\kappa\sqrt{\hbar\omega_0\tau}E^- \tag{5.5}$$

$$E_{out,2} = E_{in,1} - j\kappa\sqrt{\hbar\omega_0\tau}E^+ \tag{5.6}$$

5.2.2 Bifurcation diagram for increasing current

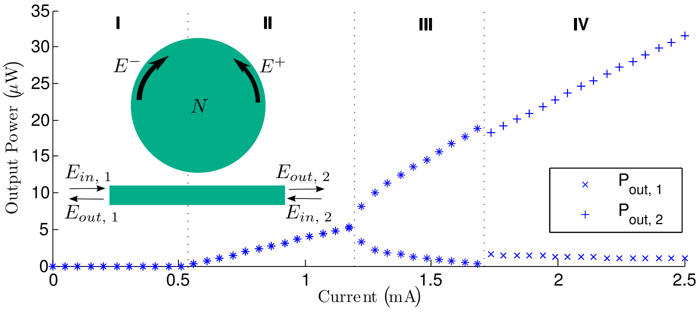

Figure 5.1: The bifurcation diagram of the microdisk laser for increasing current reveals three lasing regimes. Just above the laser threshold the output is bidirectional (II), at high injection currents it is unidirectional (IV), while in between those two regimes an oscillatory regime appears (III). For both output powers $P_{out,\,i} = |E_{out,\,i}|^2$, the extrema are plotted. If the output is constant, maximum and minimum power are equal and the markers overlap. If the output power oscillates, two markers are plotted per current, per mode. Inset: geometry of the microdisk laser.

The bifurcation diagram in Fig. 5.1 shows the different operating regimes of the laser, as a function of the current I. Regime I is below lasing threshold. In the bidirectional regime (II), the energy in both modes is equal, due to the linear intermodal coupling. At very large currents, the cross-gain modulation overrules the linear intermodal coupling and consequently induces a purely unidirectional regime (IV), where one mode carries more power than the other. If the phase ϕ_C of the intermodal coupling is close to $\frac{\pi}{2}$, in between those two regimes, the combination of cross-gain modulation and intermodal coupling results in a current regime with alternate oscillations (III) [20, 29]. In the unidirectional regime, an increase in current improves the contrast between strong and suppressed mode.

Although a detailed inventarisation of C-values and a corresponding experimental characterization of the oscillatory regime still needs to be done, the frequency of the oscillations is known to be in the GHz range [24] and depends on the magnitude of C. The rate equation model was developed and thoroughly validated in the case of SRLs [29, 30]. In this chapter, we use the model parameters for a typical microdisk proposed in [22, 31] (table 5.1), to have qualitative correspondence, on the right order of magnitude, between the numerically obtained diagrams and experimental data obtained in, e.g., [24] or [27].

Parameter	Symbol	Value	Unit	Ref.
Resonance wavelength	$\lambda_0 = \frac{2\pi c}{\omega_0}$	1.55	μm	
Line broadening factor	α	3		[31]
Photon lifetime	τ_p	4.17	ps	[31]
Radius microdisk	R	5	μm	[22]
Cavity roundtrip time	τ	350	fs	[22]
Intermodal coupling	C	$0.449 + 2.82j$	GHz	[22]
Amplitude coupling to the waveguide	κ	171.4	GHz	[22]
Current efficiency	η	0.5		[22]
Group velocity of the mode	v_g	$8.82 \cdot 10^7$	$\frac{\text{m}}{\text{s}}$	[22]
Carrier lifetime	τ_c	600	ps	[31]
'Effective' differential gain	Γg_N	982.3	kHz	[31]
'Effective' nonlinear gain suppression	$\Gamma\epsilon_{NL}$	$1.96 \cdot 10^{-6}$		[31]
Transparency carrier amount	N_0	763500		[31]

Table 5.1: Model parameters used in this chapter are based on the values and definitions proposed in [31] and [22]. Comparable values can be found in [24].

5.3 Optical injection

This chapter treats excitability in microdisk lasers that are locked using external optical injection, i.e., for sufficiently high input power the disk will lase at the same frequency of the input signal. In the unidirectional regime (at $I = 2.3$ mA), we investigated the effect of optical injection in E^+, as a function of the injection amplitude $E_{in} = E_{in,1}$ ($E_{in,2} = 0$), and the detuning $\Delta\omega$. This configuration for optical injection is identical to the one studied for SRLs in [32]. Consequently, as those SRLs are governed by the same physics, the same locking regimes appear. Indeed, the bifurcation diagram in Fig. 5.2 shows three stable locking regimes, in which the power does not oscillate between the two modes: U_1, U_2 and Bi.

U_1 and U_2 stem from the positive and the negative unidirectional regime. Since power is mainly injected in the positive mode, U_1 is most prominent. The locked regime Bi originates from one of the bidirectional solutions, which is not stable in the absence of optical injection at these currents. The size of this regime is controlled by ϕ_c, and increases for values close to $\frac{\pi}{2}$ (in this chapter, $\phi_c = 0.45\pi$).

The regimes lose stability when their surrounding bifurcations are crossed, Hopf-bifurcations are denoted by red lines, saddle-node and other limit points by blue lines. Upon crossing these bifurcations, the laser states can converge to Limit Cycles (LCs), or more complex (chaotic) attractors. In Fig. 5.2, for simplicity, we omitted the bifurcations corresponding to unstable structures or chaotic regions, as they are already thorougly discussed in [32] and not important for the remainder of this chapter.

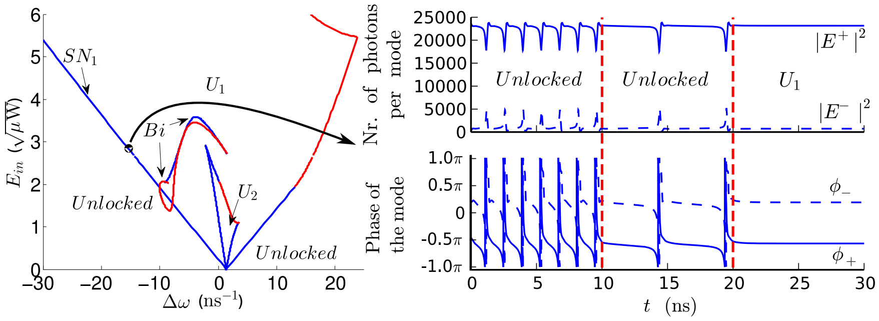

Figure 5.2: (left) The bifurcation lines form the boundaries of the different locking regions. Here, $I = 2.3$ mA, red lines represent Hopf-bifurcations, while blue lines correspond to Saddle-Node on an Invariant Circle (SNIC) bifurcations. We will use the SNIC bifurcation to induce excitability. (right) When crossing the SN_1 bifurcation at $\Delta\omega = -15\ \mathrm{ns}^{-1}$, $|E_{in}| = 2.77\ \sqrt{\mu W}$ the oscillatory unlocked behaviour becomes steady-state. At $t = 10$ ns the locking amplitude is raised from 2.65 to 2.76 $\sqrt{\mu W}$, at $t = 20$ ns, the bifurcation is crossed by again increasing $|E_{in}|$ to 2.78 $\sqrt{\mu W}$.

In this chapter, the laser is used in the positive unidirectional regime U_1, close to the saddle-node bifurcation SN_1. This injection regime behaves identically to the one found in single-mode semiconductor lasers, which has been extensively studied [33]. In the time trace in Fig. 5.2, this bifurcation line is crossed by increasing the optical injection power. There is a transition from a LC (the pulsing state) to an equilibrium (the locked state). This SN_1 transition is a Saddle-Node on Invariant Circle (SNIC) bifurcation. This type of bifurcation is known to induce excitability in biological neurons [13].

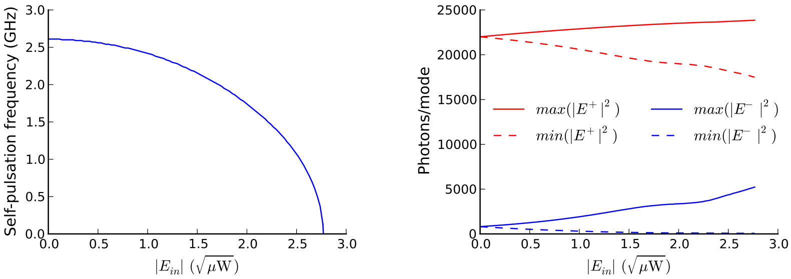

Figure 5.3: (left) When increasing the injection strength $|E_{in}|$ from zero to the locking strength, the self-pulsation frequency decreases to zero. This is a consequence of the SNIC bifurcation. (right) In addition, the amplitude of the of the self-pulsation in the mode energy grows from zero to a finite size for increasing $|E_{in}|$. Both simulations are done at $\Delta\omega = -15\,\text{ns}^{-1}$.

When increasing the optical-injection strength $|E_{in}|$ from zero to the locking threshold, the self-pulsation frequency decreases to zero (Fig. 5.3, left). The convergence to zero at the locking threshold corresponds to the frequency dependence of class 1 neural excitability discussed in Sec. 2.3.2. The self-pulsation frequency for $|E_{in}| \approx 0$, is given by the difference in frequency between the injection wavelength and the lasing wavelength without optical-injection for $I = 2.3$ mA (As can be inferred from Fig. 5.2 this lasing frequency is slightly blue shifted with respect to the original resonance wavelength of the cavity without current injection). Additionally, for increasing $|E_{in}|$, the amplitude of the self-pulsation grows from zero to a finite value (Fig. 5.3, right). Importantly, for $|E_{in}|$-values close to threshold, there is a significant exchange in energy between the two counterpropagating modes.

5.4 Excitability

As explained in chapter 2, *Excitability* is typically defined in the context of a small perturbation at the input of a system in a stable equilibrium. When the perturbation is below a certain threshold, the system responds weakly, and fairly linearly with the perturbation strength. However, when the perturbation is above threshold, the system responds strongly, often with one or more output pulses, and the response above threshold stays nearly constant. As explained in Sec. 2.4.1, at a SNIC-bifurcation, such as SN_1 in Fig. 5.2, one can find Class 1 excitability. This implies that, as a response to a superthreshold

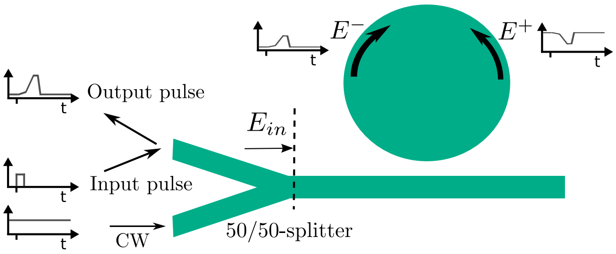

Figure 5.4: In the proposed 'neuron' topology a constant locking signal (CW) locks the microdisk just above the SN_1-bifurcation. Sufficiently strong pulses at the other input of the splitter, perturb the microdisk, and can cause an excitation. The excitation results in a power peak in the E^- mode that can be collected as the actual output of the system.

step input, pulse trains are generated for which the pulse amplitude is close to invariant, whereas the pulse frequency can be made arbitrary low by choosing step heights arbitrary close to the threshold. Due to the similarity with a LIF neuron, this type of neuron behaviour is very interesting from an application's point-of-view [13, 14, 34]. Additionally, whereas the excitation mechanism proposed in [20, 32] is heavily dependent on the precise phase ϕ_c of the intermodal coupling, while ϕ_c is not straightforward to control during fabrication, the currently proposed excitation mechanism is less sensitive to this value, as ϕ_c has less influence on the threshold for optical injection than on the onset of alternate oscillations.

5.4.1 Neuron circuit

Figure 5.4 shows a topology in which the input port of a splitter (used as a combiner) is connected to the bus waveguide of the microdisk laser. We use the splitter to inject the input pulses and the external locking signal at the same side of the disk. This circuit can be used to exploit the aforementioned excitation mechanism. The CW input provides a constant signal that locks the microdisk just above the SN_1-bifurcation. Pulses at the other input of the splitter, cause perturbations on the locking signal. When the disk gets excited, the pulse in the suppressed mode of the laser will be visible as an upward pulse at the same port. The ability to retrieve an output signal proportional to the suppressed mode is a clear advantage with respect to the situation for a single-mode semiconductor laser as in [33], as it can enhance the ER and results in a cleaner pulse shape. To obtain excitability, the amplitude of the locking signal $|E_{CW}| = 4.10\ \sqrt{\mu\text{W}}$ is chosen so that $|E_{in}| = 2.90\ \sqrt{\mu\text{W}}$, while $\Delta\omega$ for both locking signal and input pulse is $-15\,\mathrm{ns}^{-1}$. The saddle-node bifurcation for this detuning lies at $|E_{in}| = 2.77\,\sqrt{\mu\mathrm{W}}$.

Unfortunately, the advantage to be able to collect the output signal of the suppressed mode comes also with some restrictive disadvantages. As the pulses due to the excitations on the suppressed mode are small compared to those of the strong mode, this choice is, in a sense, less power efficient. In addition, the splitter attenuates the power of the pulses by 50%, resulting in a decrease of the output pulse-input pulse power ratio with a factor 4. In theory, this can be avoided by using two bus waveguides for each microdisk instead of one, one for the optical injection signal and one for the optical pulse trains. However, due to the diffulty to control both coupling sections this type of design is not so often used in current fabricated designs. Therefore, we stick to the single bus waveguide design. A final disadvantage is that output and input pulse propagate in opposite directions through the same waveguide. As state-of-the-art integrated isolators are still too lossy to be useful in this type of photonic circuits [35, 36], a disk that excites another disk, will be in turn perturbed by the induced excitation pulse of the other disk. Later on in this chapter, a promising strategy to connect different excitable disks will be proposed, that allows to avoid the back-propagation of excitation. In Sec. 5.4.2, using an example, we will discuss the pros and cons of the neuron topology more in detail.

In this Phd research, we do not investigate how the locking signal can be generated on-chip. However, as this is an important issue for future applications, we will shortly address this topic at the end of this chapter, in Sec. 5.8.

5.4.2 Reaction of the system to a typical trigger pulse

As the external locking power is slightly above the SNIC bifurcation, we have to lower the effective locking power $E_{in}(t)$ during a perturbation, to be able to excite the disk. This can be done by sending input pulses to the disk that are completely out of phase with the external locking signal. Indeed, the resulting signal of the interference of the locking signal with a pulse with a π phase shift compared to this locking signal, results in a signal with the same phase as the locking signal, but diminished amplitude. Consequently, in initial experiments on excitability in a single optically-injected disk, one could as well trigger an excitation by using amplitude modulation of the external locking signal.

We illustrate this for a typical excitation in Fig. 5.5. One can clearly see the effective amplitude modulation of $|E_{in}(t)|$ and the resulting excitation both in the output at the left of the splitter (red line), and the output at the right of the disk (orange line).

Figure 5.5 also shows the advantages of using the circuit proposed in the previous subsection as neuron topology. Indeed, the bias level of the forward

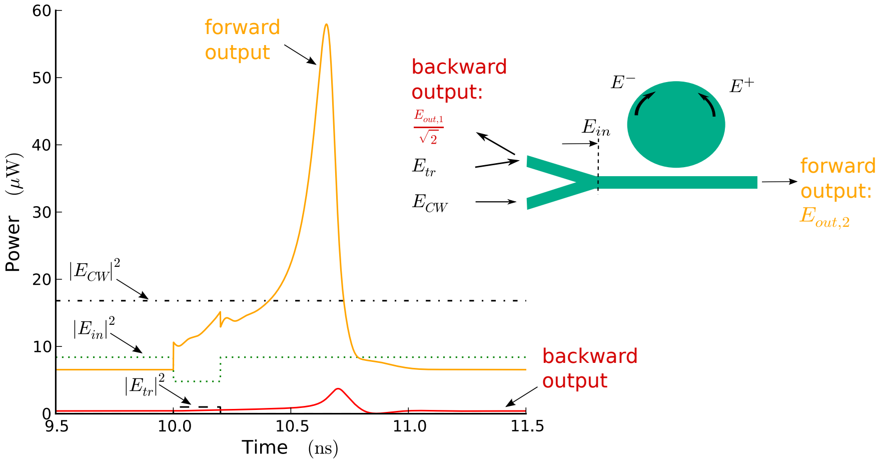

Figure 5.5: The response of the microdisk to a 0.2 ns pulse of 1.0 μW, with a π phase shift with the locking signal, shows that the backward output pulse corresponding to the suppressed mode has the cleanest pulse shape.

output at the right side of the disk is stronger compared to the output that corresponds to the suppressed mode. Consequently, using the forward output of the system would result in increased coupling with other disks in the network. As we will discuss in Sec. 5.6.1, even the relatively low bias output of the suppressed mode can already induce undesired coupling. Hence, the output of the strong mode would cause even more trouble. Furthermore, the output strength of the suppressed mode output is comparable with the output strength of the input pulse, which is good condition to allow cascadability. Of course, the fact that this advantage is not present for the right output could be circumvented by using an attenuator or by dividing the output of this disk over several other receiving disks. But even if one sends only a fraction of the output of the strong mode to another disk, one has to be careful when using this output port. Indeed, for this specific detuning and injection locking scenario the ER of those two outputs is comparable, but for other locking settings the ER of the output at the right of the disk can strongly diminish, while the ER for the output at the left in our system stays relatively fixed. So, using the output of the suppressed mode results in more robustness in ER with respect to the optical and electrical injection settings of the disks.

Additionally, whereas the output at the right side of the disk contains a ripple that corresponds to the input pulse, this is not the case for the output of the suppressed mode. This explains why we choose to inject the trigger pulse in the strong mode, instead of the suppressed mode, even though the latter choice would avoid the need to use a splitter, as the trigger pulse then enters at the opposite site of the disk as the locking signal.

The pulse shape in Fig. 5.5 is very similar to the pulse shape in the LC that can be seen in Fig. 5.2. This is to be expected, as the physical mechanism that generates this pulse is the same. A special feature of the excitation in this particular system, is the interplay between excitability due to optical injection and the coupling between the two modes. As can be seen in Fig. 5.2, during a pulse, the strong mode delivers temporarily a fraction of its photons to the suppressed mode. This coupling can only happen due to the intermodal coupling C and, consequently, the timescale of this excitability mechanism is related to the timescale that corresponds to this intermodal coupling. Further theoretical analysis of the rate equations is necessary to pinpoint the exact influence of C on this excitability mechanism.

Finally, from the width of the excitation in Fig. 5.5, it can be inferred that the excitability mechanism is capable to process ~ GHz spike trains, making it potentially 100× faster than the microring neuron discussed in chapter 4. Additionally, the largest power consumption of the microdisk is the current injection. Indeed, while the optical-injection signals are on the order of a few μW, a typical driving voltage of the disk is on the order of 1 V [37] and, given $I = 2.3\,\text{mA}$, this results in a ~ mW power consumption. If the optical-injection signal would be generated as well by a microdisk laser, the total power consumption of the combination of the driving disk and the neuron disk would still be in the mW-range. Following the same reasoning as in Sec. 4.4.4, this implies that the microdisk neuron will consume ~ 1 pJ energy/spike, being 100× more energy-efficient than the microring neuron. Improvement of the ratio of optical output power and electrical input power can optimize this number even further.

5.4.3 Threshold behaviour as a function of input pulse power

The traces in Fig. 5.6(a) show the responses to square input pulses of duration 0.2 ns, having a π phase shift compared to the locking signal, with input pulse power varying from 0.6 μW to 2.2 μW. The output peak power (Fig. 5.6(b)) shows strong threshold behaviour as function of the input pulse power. Above threshold, the output pulses become in an abrupt way significantly stronger. This is a key-requirement for excitability. The decrease of pulse peak power above threshold deviates from what is usually observed in most biological neurons, where the output pulse power typically increases slightly for further increase of the input power [13]. This decrease in pulse peak power is a reminiscent of the dependence of the amplitude of the self-sustained oscillations of the CCW mode in the unlocked regime on the optical-injection strength. In Fig. 5.3, a decreasing optical-injection strength results in a decreasing extinction ratio of the oscillation amplitude. Similarly, in the excitable regime, a stronger input pulse power results in a (temporarily) lower effective $|E_{in}(t)|$, resulting in less pronounced output pulses.

Furthermore, the output pulse latency (the time between perturbation and excitation) decreases for increasingly stronger input pulses above threshold (Fig. 5.6(c)). This is a known feature for SNIC bifurcations. Indeed, after the perturbation kicked the laser out of its rest state, beyond the threshold manifold, it will quickly relax to the invariant circle corresponding to this bifurcation, and will start a roundtrip on this invariant circle to finally relax back in the rest state (Fig. 5.7 illustrates this using the Adler model). A stronger perturbation will reduce the distance the system has to travel in phase-space, and hence will also reduce the latency of the optical output pulse of the excitation.

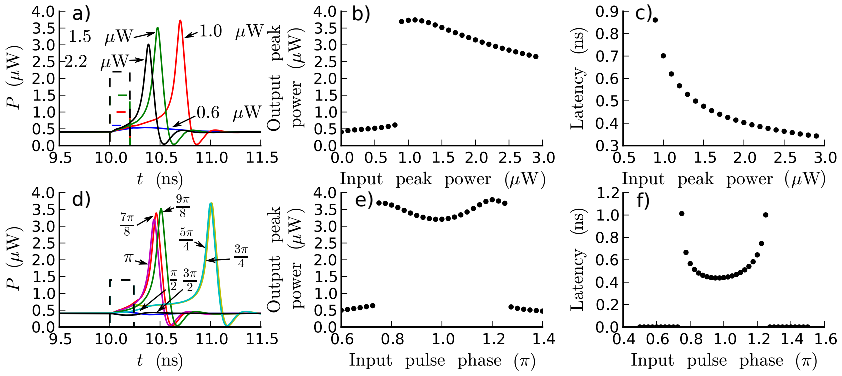

Figure 5.6: The optically-injected microdisk shows clear threshold behaviour as a function of the amplitude and phase of the input pulse. a)-c) Response to pulses of fixed length (0.2 ns), for different pulse powers, out of phase with the locking signal. a: Time traces. b: Output peak power as a function of input peak power. c: Pulse latency as a function of input peak power. d)-f) Response to pulses of fixed peak power and length (1.4 μW, 0.24 ns), but varying phase. d: Time traces. e: Output peak power as a function of phase. f: Pulse latency as a function of input pulse phase.

Based on Fig. 5.6 we could estimate the minimum energy of perturbation of the system to be on the order of ~ 0.2 fJ. However, additional simulations reveal that this value increases by a factor of 2 for a 10× increase of the pulse width, and is as such ill-defined. This can be understood from the rate equations, as the time derivatives of the laser states are linear in the amplitude of the input pulse, and not in its power. Hence, it is the product of the amplitude and the duration of the pulse that stays rougly constant. Consequently, an increase in pulse duration Δt will lower the power threshold, approximately with a $\frac{1}{\Delta t^2}$ dependency.

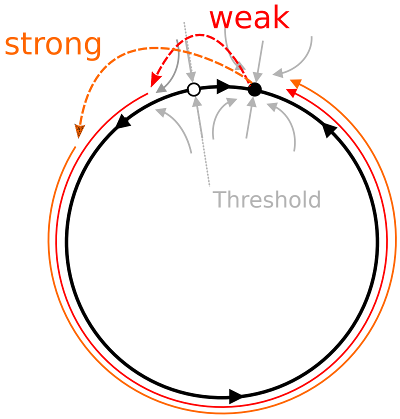

Figure 5.7: The Adler model can help to understand why stronger supertreshold pulses result in less latency of the output pulse: a stronger pulse reduces the roundtrip distance in phase-space the system has to make before it can return to the rest state, and this will in the amplitude domain correspond to a reduced latency of the output pulse of the disk.

5.4.4 Threshold behaviour as a function of input pulse phase

In the simulations of the previous subsections, the input pulses had a π phase shift, relative to the CW input. The traces in Fig. 5.6(d) clarify the influence of the phase. The disk is excitable only for a limited interval around π. At the edges of this interval, clear threshold behaviour is obtained. The sudden increase of output pulse latency, close to these edges, corresponds to the latency increase near threshold for the input pulse power sweep. Clearly, pulses with the same power profile can cause very divergent responses, depending on their phase. Figures 5.6(e) and 5.6(f) show these trends in more detail. For completely randomized phases, only about 25% of all input pulses would result in excitation. Fortunately, the phase difference between the input pulse and the locking signal can be deliberately controlled externally. In contrast, the excitability mechanism in asymmetric SRLs without optical injection is sensitive to the phase difference between the input pulse and the laser state, which is uncontrollable in a practical setup [11].

The dependence of excitability on the phase of the trigger pulse in our simulations can be further clarified by comparing this behaviour with recent

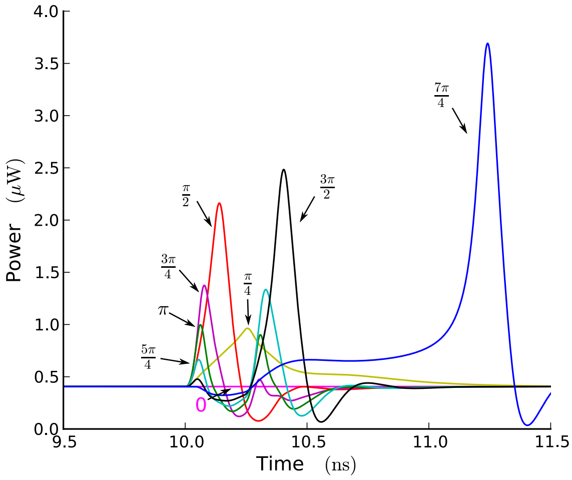

Figure 5.8: The microdisk laser reacts as well to a phase-modulated locking signal, in which the phase of the locking signal experiences a block pulse of fixed length (0.2 ns) and size $n\frac{\pi}{4}$ ($n \in \{0, ..., 7\}$) at 10 ns.

experimental results in a single-mode semiconductor laser under optical injection, in which excitations were triggered using only phase pulses [12]. When phase pulses are added to the locking signal (Fig. 5.8), the microdisk laser reacts with clear excitations for some phases of those pulses (e.g., $\frac{\pi}{2}$), while for other phases it is difficult to identify a clear pulse (e.g., $\frac{\pi}{4}$). This sensitivity to phase jumps in the locking signal implies that the threshold behaviour in Fig. 5.6 is not only a consequence of the changing amplitude of the effective locking signal due to the interference of the CW-input and the phase-shifted pulse, but also a reaction to the kick in phase of this effective locking signal. This 'absolute' phase sensitivity is related to the locking mechanism that we use to induce excitability in a microdisk. In contrast, for the excitation mechanism in a passive microring, similar phase jumps without additional amplitude modulation would not result in an excitation.

The ability of the neuron to react to the phase of the input pulses, makes larger microdisk networks sensitive to phase errors. Consequently, even though an integrated platform intrinsically limits the variable phase noise, one still needs a reliable, power efficient way to compensate for fixed phase offsets in large microdisk network.

5.4.5 Integrating behaviour

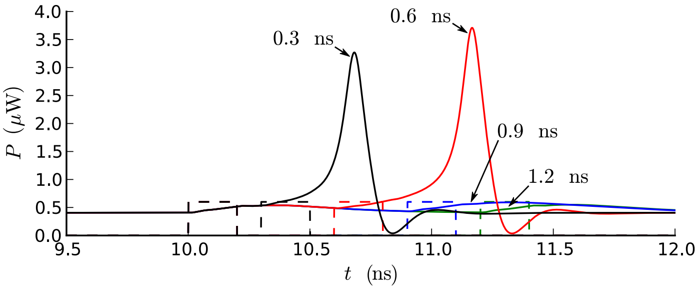

Figure 5.9: If two subthreshold input pulses (in this case, 0.6 μW, 0.2 ns, out of phase with the locking signal) arrive sufficiently close to each other to the microdisk, they can excite the microdisk.

If an input pulse excites the disk it is entitled *superthreshold*, whereas it is entitled *subthreshold*, if otherwise. To be superthreshold, the amplitude, duration and phase of the pulse should be chosen in such a way that the resulting perturbation of the locking signal is sufficiently strong. However, several subthreshold pulses can combine to form a superthreshold excitation, as long as they arrive sufficiently close to each other (Fig. 5.9). This is a characteristic of an *integrating neuron* [13]. Not all excitation mechanisms show this behaviour. When a subthreshold excitation causes oscillations, as is the case for Hopf bifurcations (Class 2 excitability, which appears, e.g., in the passive silicon microrings mentioned in chapter 4) the neuron will act as a resonator: multiple subthreshold excitations can only excite the system if their delay is close to an integer multiple of the natural oscillation period of the oscillations of the system. The excitation mechanism presented by Gelens, Coomans et al. [20, 21, 32] also incorporates resonator instead of integrating behaviour.

Figure 5.10(a) shows the output-versus-input rate, for a series of subthreshold pulses, Figs. 5.10(b) and 5.10(c) show time traces of input and output pulses for two input pulse rates, respectively. The output-versus-input rate curve resembles the typical sigmoidal neuron activity level versus input signal characteristics of classical artificial neurons [34, 38]. As explained in Sec. 2.1.2, this similarity is a general feature of a spiking neuron and intuitively explains why spiking neural networks can have theoretically at least the same computational power as these classical sigmoidal networks. Even more, it has been proven that the computational power of a spiking neural network, due to the more intricate dynamics, can even be higher than that of these sigmoidal networks [34].

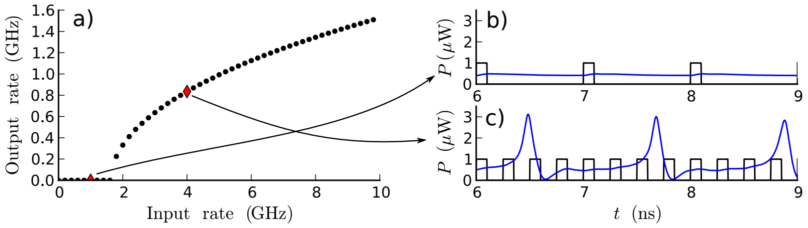

Figure 5.10: The output pulse rate of a microdisk excited with subthreshold pulse-trains is sublinearly dependent on the input-pulse rate and therefore shows similarities with the typical sigmoidal input power versus output power characteristics of classical artificial neurons. a) Input rate-output rate characteristic of the neuron, when the input-pulse train consists of subthreshold pulses ($|E_{in}|^2 = 1\ \mu$W peak power, 1 ns length). b)-c) time-traces, for input rates 1 GHz (a), and 4 GHz (b).

5.4.6 Refractory period

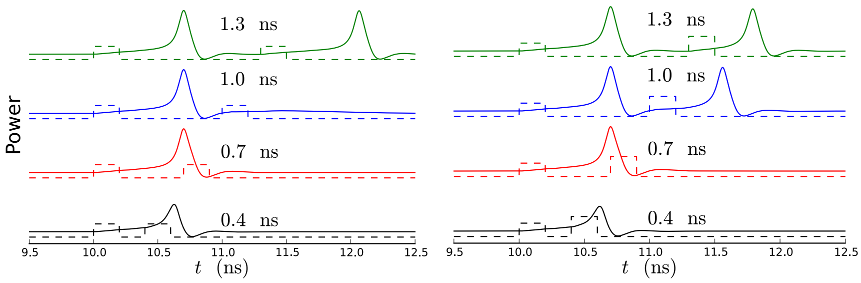

Figure 5.11: The microdisk has a refractory period: after a perturbation, the disk is temporarily less sensitive to new input perturbations. (left) Response to a sequence of two equally high superthreshold pulses (1 μW, 0.2 ns, out of phase with the locking signal). (right) The second pulse has a slightly higher power (1.5 μW).

In the previous subsection we saw how two closely-spaced subthreshold pulses can result in an excitation. When considering the response of the excitable disk on two closely-spaced superthreshold input pulses, interesting behaviour emerges as well. In figure 5.11, the first pulse (which is the same for each pulse sequence) excites the system. The second input pulse will only result in an excitation when the delay is sufficiently large, a clear evidence of the existence of the refractory cycle, a common feature of a neuron [13]. If the second perturbation arrives during the downward stroke of the output pulse, its effect is negligible, whereas a second perturbation during the upward stroke of this pulse decreases the amplitude of the pulse. This is similar to the decrease in output pulse amplitude for stronger single-pulse input perturbations in Fig. 5.6(b). The second graphs shows the reaction of the disk if the second perturbation is a bit stronger. Comparison of both graphs shows the difference between an absolute and relative refractory period (see the discussion in Sec. 4.4.2). If the second pulse has a delay of 1 ns (the blue traces), it falls within this relative period, the system is excitable, but a stronger second input perturbation is required.

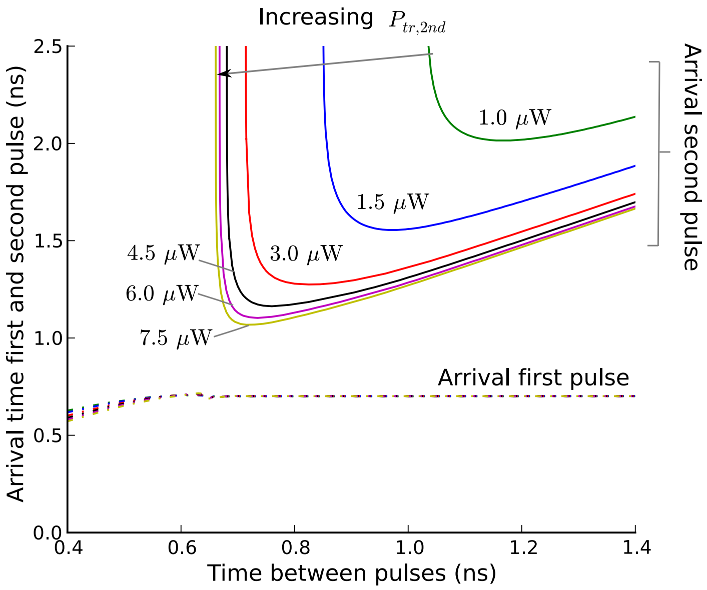

Figure 5.12: The relative refractory period of the microdisk is clearly dependent on the power of the second trigger pulse. For high powers of this second pulse it converges to the absolute refractory time, which corresponds with the moment the disk is having its first excitation. Input pulses are 0.2 ns wide, out of phase with the locking signal and the power of the first input pulse is 1 μW.

To characterize the absolute refractory period more quantitatively, the timing of the maximum of the output pulses as a reaction to two closely-spaced suprathreshold input pulses is tracked as a function of the spacing between those two input pulses (Fig. 5.12). By doing this for increasing strengths of the second input pulse, it can be inferred that the absolute refractory time is ~ 0.66 ns. As the maximum of the first excitation appears at ~ 0.70 ns, the absolute refractory time corresponds to the moment the disk is having its first excitation. Strangely, the disk can be forced to excite for a second time, even before it reached the maximum of its first pulse. As a consequence, in the case the second input pulse is very strong, and the timing between the input pulses is only slightly above the absolute refactory period, the input pulse that triggers the second output pulse can also distort the first output pulse and lower its output amplitude (simulation not shown). This effect is in agreement with the bottom time traces in Fig. 5.12, where the arrival of the input pulse during the upwards stroke of the first excitation indeed decreases the output pulse strength. Finally, if the second input pulse arrives before the absolute refractory time, the latency of the first excitation is slightly lowered.

5.4.7 Complex addition of two input pulse streams

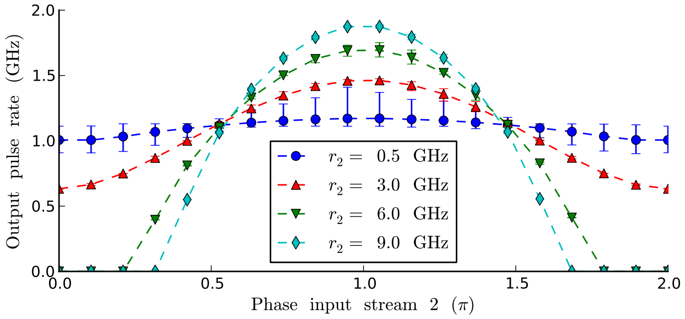

Figure 5.13: The output pulse rate as response to the superposition of two input pulse streams depends on the optical phase difference between the two input pulse trains. One stream is constant (6 GHz, 1 μW peak power and 0.1 ns duration) and purely excitatory (relative phase with respect to the *CW* is π), while the other pulse stream has a varying rate r_2, the horizontal axis represents its phase. Peak power and duration are the same as for the first stream. The error bars give the 80% certainty interval for the inverse interpulse delays.

From Fig. 5.6(d)-(f) can be deduced that pulse trains with a phase difference with the locking signal more-or-less between $\frac{\pi}{2}$ and $\frac{3\pi}{2}$ are *excitatory*, as they tend to excite the system by pushing the system's state towards or even across the bifurcation. In contrast, pulses with an optical phase between $-\frac{\pi}{2}$ and $\frac{\pi}{2}$ are *inhibitory*, as they push the system's state away from the bifurcation. The output pulse rate as a response to a superposition of two input pulse streams, depends on the excitatory or inhibitory character of those pulse streams. This is validated in Fig. 5.13, in which we observe the output pulse rate as a reaction to a combination of a constant, purely excitatory input pulse train and an input pulse train with varying rate and phase with respect to the locking signal. Every curve on the graph corresponds to a specific rate of the second pulse stream r_2, while the phase is shown on the horizontal axis. The constant pulse train by itself would result in an output pulse rate of about 1.12 GHz (see Fig. 5.10(a)). A second input pulse train can clearly influence this output pulse rate. Inhibitory pulses reduce the rate, excitatory pulses increase it. The higher the pulse rate, and the closer the phase of the second pulse train to π (purely excitatory) or 0 (purely inhibitory), the stronger the effect. This phase dependency allows a disk to perform a complex-weighted nonlinear 'addition' of input pulse rates.

This effect provides a potential synaptic tuning mechanism in optical neural networks, since phase delays can play the role of synaptic weights. For photonic hardware implementations of neural networks consisting of analog neurons, such as Semiconductor Optical Amplifiers (SOAs) or photonic cyrstal cavities, it is proven that doing signal processing in the optical domain, in which signals are complex-valued instead of real-valued, increases the performance of the network [38–40]. Consequently, the fact that the optical microdisk neuron allows 'addition' of pulse rates with complex, instead of real-valued weights, indicates that optical SNNs potentially can benefit from similar computational advantages. Phase control of the optical links in a disk network can be achieved using, e.g., heaters [41].

5.5 Towards cascadability

In the previous sections we proposed microdisk lasers as a basic building block for an integrated photonic SNN platform. In the remainder of this chapter we elucidate the pulse transfer mechanism between disks. One clear characteristic of the microdisk excitability is that every downward pulse in the dominant mode is accompanied by an upward pulse in the suppressed mode, of approximately the same absolute strength. It is the upwards pulse we will use to excite another disk. The transfer of an excitation between excitable lasers on an integrated platform is currently only theoretically demonstrated in the case of two coupled SRLs with an asymmetric intermodal coupling [11] and the spiking VCSEL network proposed by Nahmias et al. [14]. In the case of the coupled SRLs, due to the asymmetry of the system, each neuron has a different function, and is not straightforward to scale up the dynamics in this system to larger networks of coupled SRLs. For the approach of Nahmias et al., larger networks were considered, but the details of a practically feasible integrated interconnections are still missing.

In this section, we will propose an easily scalable topology for pulse transfer between two disks and the necessary rate equations to simulate this system. In the next section we will demonstrate how this topology allows excitation transfer between the disks.

5.5.1 Connection of the disk neurons

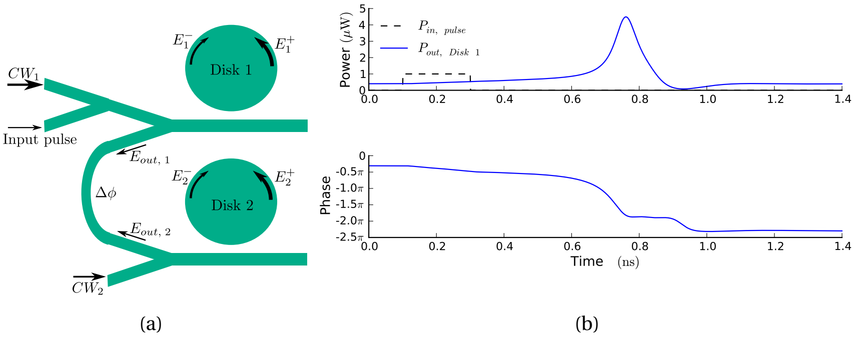

(a) (b)

Figure 5.14: (a) The output of a microdisk neuron can be connected by a waveguide to the input of another microdisk neuron. The connection between both lasers corresponds to a phase difference $\Delta\phi$. (b) Input and output power of the first disk when the second disk is 'turned off' (current as well as locking signal are absent). The bottom graph shows the phase difference between the output pulse and the locking signal. This phase can be used to choose an optimal $\Delta\phi$ to allow the first disk to excite the second one.

Figure 5.14(a) depicts the topology of two connected microdisk lasers that is considered throughout the remainder of this chapter. These microdisk lasers are locked in the unidirectional regime, close to the SNIC bifurcation along which excitability was demonstrated in Sec. 5.4. Both lasers are assumed to be identical, unless mentioned otherwise. All splitters in the circuit have a 50/50 splitting ratio. Consequently, the effective locking signals for the lasers carry a quarter of the CW_1-power (P_{CW_1}) and half of the CW_2-power (P_{CW_2}), for disks 1 and 2, respectively. Similarly, the input pulse power is attenuated by a factor of four, before it arrives at disk 1. If the first disk gets excited, its output pulse will travel through the waveguide connection to the second disk such that this pulse's power will get attenuated as well by a factor of four. Despite this power loss, due to the strong coupling between the disks and their bus waveguide, the coupling between the two different disks is still 1.8× stronger than the intermodal coupling. To increase the possibility that the output from the first disk excites the second one, the detuning of the locking signal is slightly different in the subsequent sections compared to the value mentioned in Sec. 5.4 ($\Delta\omega = \omega_{in} - \omega_{disk\,1,2} = -20\,\text{ns}^{-1}$ instead of $-15\,\text{ns}^{-1}$). The current is still 2.3 mA. For these parameters, the SNIC bifurcation lies at $|E_{in}| = 3.63\,\sqrt{\mu\text{W}}$. Additional details about the simulation model and its parameters are summarized in Sec. 5.5.2.

From the simulations in Sec. 5.4, it is clear that the input pulse is preferably out of phase with the CW locking signal to excite a disk. Therefore, the phase delay $\Delta\phi$, and the relative phase of both locking signals, have a crucial influence on whether or not the first disk will be able to excite the second one. The possibility to use phase tuning to control excitation transfer is a distinctive advantage of an optical implementation of a spiking neuron. This feature is not present in electronic spiking neuron implementations. However, the phase of the output pulse of the first disk is not constant as a function of time. To allow for the first pulse to excite the second one, the phase delay $\Delta\phi$ needs to be chosen such that the pulse is out of phase with the CW_2 input, for a significantly long amount of time. We first assume that the two locking signals, CW_1 and CW_2, arrive at the disks with the same phase. Figure 5.14(b) shows a power and phase trace of the output pulse of first disk (locked with a $3.7\,\sqrt{\mu\text{W}}$ locking signal), while the second disk is turned off. Although the phase of the mode traverses the whole 2π-interval, it stays nearly constant during the whole downward stroke of the pulse (around $-1.9\,\pi$). This pulse should be out of phase with the locking signal at the second disk. This leads to $(2n+1)\pi = -1.9\,\pi + \Delta\phi,\ n \in \mathbb{Z}$, for $n = -1$: $\Delta\phi = 1.9\,\pi - \pi \approx 2.8\,\text{rad}$.

Although the rule of thumb we present here to calculate the optimal $\Delta\phi$ for excitation transfer results in the expected behaviour in the subsequent sections, it should be used carefully. Indeed, in the remainder of this chapter the second disk is turned on. When both disks are lasing, the bias output of the suppressed mode of one disk will couple through the waveguide to the other disk and interfere with the external locking signal, changing the effective power and phase the other disk receives, and consequently also changing the optical output of this laser. So, by finetuning $\Delta\phi$ to obtain an optimal interference of the output pulse with the locking signal of the second disk, one simultaneously also changes the dynamics of the first disk due to the coupling between the two lasers. Even though the bias power of the suppressed mode is rather low, preliminary simulations show that its influence is not negligible.

Additionally, the previous calculation is based on the assumption that both lasers are identical and have, more specifically, an equal intermodal coupling phase ϕ_c. However, as we mentioned in Sec. 5.4, ϕ_c is difficult to control during fabrication, and will most likely vary from disk to disk. As the phase difference between the CW and CCW modes is heavily dependent on ϕ_c, this implies that on an experimental chip these deviations in ϕ_c have to be taken into account. Whereas a shift of the average intermodal coupling phase $\overline{\phi_c} = \frac{\phi_{c1}+\phi_{c2}}{2}$ with respect to the value of Table 5.1, will have no influence on the dynamics of the system if only $\Delta\phi$ is adapted to the new value, the difference in $\Delta\phi_c = \phi_{c2} - \phi_{c1}$ can not be compensated by changing $\Delta\phi$. Indeed, if $\Delta\phi_c \neq 0$, the symmetry of the system is broken and this can only be mitigated by choosing a phase difference between the two locking signals that exactly compensates $\Delta\phi_c$. In Sec. 5.6.2, we will discuss mechanisms to break the symmetry of the coupled laser system intentionally in a controlled way, and show the consequences of this asymmetry on the pulse transfer mechanism. As the dynamics for $\Delta\phi_c \neq 0$ is phenomenologically the same as what happens in these controlled asymmetric systems, we will for the remainder of the chapter assume $\Delta\phi_c = 0$.

In the case of excitation transfer between two SRLs with asymmetric intermodal coupling, not only a different excitation mechanism is used, but also the asymmetry in the intermodal coupling is chosen such that the SRL that is triggered by an external pulse receives the strong mode from the subsequent SRL, while it sends out its suppressed mode to this other SRL. In contrast, in the topology we currently propose the two disks receive each other's suppressed mode. Indeed, from the point-of-view of the interconnecting waveguide the two disks lase in the symmetric outward state S_{out}, as defined in [42] for the case of two SRLs, interconnected by a single bus waveguide, without optical injection.

5.5.2 Rate equation model of two coupled microdisk lasers

In this subsection, the simulation details of the coupled system are summarized. A single microdisk laser can be described in the slowly varying envelope approximation using the coupled rate equations mentioned in Sec. 5.2.1. Caphe, the circuit simulator we use throughout this thesis, converts the equations that describe the coupling of the optical modes to the bus waveguide into the formalism described in chapter 3, which, for the circuit proposed in Fig. 5.14(a), results in the following set of coupled differential equations:

$$\begin{aligned}
\frac{dE_1^+}{dt} &= \frac{1}{2}(1-j\alpha)\left(G_1^+ - \frac{1}{\tau_p}\right)E_1^+ + j\Delta\omega_1 E_1^+ + CE_1^- \\
&\quad - \frac{j\kappa\sqrt{\tau}}{\sqrt{\hbar\omega_0}}\left[-j\kappa\sqrt{\hbar\omega_0\tau}\frac{1}{\sqrt{2}}\left(\frac{e^{j\Delta\phi}E_2^-}{\sqrt{2}}\right) + \frac{1}{\sqrt{2}}\left(\frac{E_{CW,1}}{\sqrt{2}} + \frac{E_{tr}}{\sqrt{2}}\right)\right], \quad (5.7) \\
\frac{dE_1^-}{dt} &= \frac{1}{\sqrt{2}}(1-j\alpha)\left(G_1^- - \frac{1}{\tau_p}\right)E_1^- + j\Delta\omega_1 E_1^- + CE_1^+, \quad (5.8)
\end{aligned}$$

$$\begin{aligned}\frac{dE_2^+}{dt} &= \frac{1}{2}\left(1-j\alpha\right)\left(G_2^+ - \frac{1}{\tau_p}\right)E_2^+ + j\Delta\omega_2 E_2^+ + CE_2^- \\ &\quad -\frac{j\kappa\sqrt{\tau}}{\sqrt{\hbar\omega_0}}\left[-j\kappa\sqrt{\hbar\omega_0\tau}\frac{1}{\sqrt{2}}\left(\frac{e^{j\Delta\phi}E_1^-}{\sqrt{2}}\right)+\frac{E_{CW,2}}{\sqrt{2}}\right], \qquad (5.9)\\ \frac{dE_2^-}{dt} &= \frac{1}{\sqrt{2}}\left(1-j\alpha\right)\left(G_2^- - \frac{1}{\tau_p}\right)E_2^- + j\Delta\omega_2 E_2^- + CE_2^+, \qquad (5.10)\end{aligned}$$

$$\begin{aligned}\frac{dN_i}{dt} &= \frac{\eta I_i}{q} - \frac{N_i}{\tau_c} - G_i^+\left|E_i^+\right|^2 - G_i^-\left|E_i^-\right|^2, \qquad (5.11)\\ G_i^\pm &= \frac{\Gamma g_N\left(N_i - N_0\right)}{1+\Gamma\epsilon_{NL}\left(\left|E_i^\pm\right|^2 + 2\left|E_i^\mp\right|^2\right)}. \qquad (5.12)\end{aligned}$$

In Eqs. (5.7)-(5.10), $\Delta\omega = \omega_{in} - \omega_i$ is the detuning between the input light ω_{in} and the free-running cavity frequency ω_i of disk i ($i \in \{1,2\}$, unless otherwise mentioned $\omega_1 = \omega_2 = \omega_0$); $E_{CW,i}$ are the complex amplitudes of the optical inputs used for the locking of both disks, while E_{tr} is the complex amplitude of the input pulse (in both cases $|E_\alpha|^2$ is the power in the waveguide). $\Delta\phi$ is the phase difference due to the interconnecting waveguide. The factors $\frac{1}{\sqrt{2}}$ are due to the power loss in the splitters. Equation (5.11) describes the evolution of the number of free carriers N_i. I_i is the injected current to each disk, $G_i^\pm$ are the gain coefficients of the modes. The denominator in Eq. (5.11) includes cross- and self-gain modulation. The complex amplitude due to the output of disk i, as felt by the other disk, has propagated through the connecting waveguide and two splitters and can be calculated to be:

$$\frac{1}{\sqrt{2}}e^{j\Delta\phi}\frac{1}{\sqrt{2}}\left(-j\kappa\sqrt{\hbar\omega_0\tau}E_i^-\right). \qquad (5.13)$$

Similar to the intermodal coupling C, this results in an intercavity coupling term $K = -\frac{\kappa^2\tau}{2}e^{j\Delta\phi}$, coupling the suppressed mode of a disk to the strong mode of the other disk. Given $\frac{|K|}{|C|} = 1.80 > 1$, the coupling is clearly stronger than the weak coupling regime as used so far for two coupled excitable SRLs with asymmetric intermodal coupling [11].

5.6 Transfer of the excitation

In this section, we investigate the transfer of excitations in the proposed topology. First, we study the purely symmetric case of two identical disks driven by an equal locking signal, which results in a continuous transfer of the excitation between the two disks. Next, we induce asymmetry in the system to make the excitation transfer unidirectional.

5.6.1 Symmetrical coupling - Oscillations

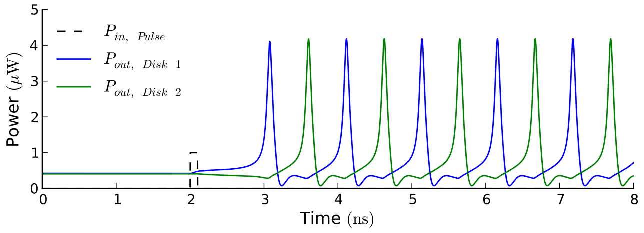

Figure 5.15: If the first disk is excited it will in turn excite the second disk, which will re-excite the first disk, resulting in a continuous excitation transfer between the two disks. Both disks are pumped with a 2.3 mA current and $\Delta\phi = 2.8$ rad. The locking signals for both disks are 3.8 $\sqrt{\mu\text{W}}$. The input pulse is 1 $\sqrt{\mu\text{W}}$ strong and 0.1 ns long.

In Fig. 5.15, both disks are biased identically and a trigger pulse has been sent to the first disk. The time trace demonstrates that an excitation of the first disk can travel through the connecting waveguide and in turn excite the second disk. Apart from the input waveguide for the initial perturbation, the system is purely symmetric. The second disk will therefore in turn excite the first one, forming a repeating cycle. This system is in a sense bistable: in addition to the initial situation, with constant output powers, a LC of alternating excitations exists.

Given the approximate nature of determining $\Delta\phi$, in which we did not even take the coupling between the two lasers into account, it is remarkable that our initial prediction, without any additional corrections, indeed corresponds to this alternating excitation regime. Additional simulations show that the desired behaviour only occurs in a narrow $\Delta\phi$-range. In principle, one would expect that for other $\Delta\phi$-values only the first disk is excited, while the second disk remains silent. Unfortunately, the coupling between the two disks due to the bias output of the suppressed mode partly prevents this desired behaviour. Indeed, due to influence of $\Delta\phi$ on the interference between the external locking power and the output of the suppressed mode of the other disk, there exists a $\Delta\phi$ region, in which the effective locking power is not sufficient to obtain locking, and the lasers start to self-pulsate (sometimes with synchronous pulses, sometimes with interleaved pulses), even without the need for an external trigger pulse to turn on the oscillation, while, in contrast, for other $\Delta\phi$ values the interference effects raise the threshold of the first disk, such that the first disk is not excited by the external input pulse. In principle, by optimizing the external control parameters of the lasers it should be possible to obtain a regime where the system is less sensitive to this coupling. For instance, in the unidirectional regime, for increasing injection current the power of the suppressed mode decreases (Fig. 5.1), so using higher injection currents will diminish the coupling. Similarly, by working with higher external locking signals, the influence of the interference with the suppressed mode output will decrease. Unfortunately, those two solutions intrinsically imply that the lasers need more external power injection to be more robust in parasetric coupling effects. Both the theoretical study of $\Delta\phi$'s influence on the dynamics and the optimization of the control parameters with respect to the robustness-power consumption trade-off can be considered as an important point for future work.

Interestingly, in two SRLs without optical injection (but with symmetrical intermodal coupling), coupled through a single bus waveguide, dependent on the phase and strength of the optical coupling, relaxation oscillations that were not present in the individual SRLs can appear in the outward symmetric state S_{out} [42]. However, although a detailed bifurcation analysis still needs to be done, the similarity in pulse shape and duration between Fig. 5.15 and Fig. 5.14(b), combined with the choice for $\Delta\phi$ needed to obtain this LC, makes it acceptable that the oscillation in the case of coupled optically-injected disks is not just a mere consequence of the optical coupling but is also related to the SNIC bifurcation that appears in the individual optically-injected disks. The success of the proposals to create a unidirectional excitation transfer in the subsequent paragraph strengthen this hypothesis.

5.6.2 Asymmetrical coupling - Unidirectional excitation transfer

Often, a unidirectional pulse transfer is required, i.e., the first neuron excites the second one, but not the other way round. To achieve this, one has to break the symmetry in the system depicted in Fig. 5.14(a). In principle, experimental implementations of this system will never be purely symmetrical. Parameters of the disks (e.g., the deviations of ϕ_c discussed in Sec. 5.5.1), currents, external reflections, the phase difference between the locking signals, etc. will induce unintentional asymmetry. However, a deterministically induced asymmetry is preferable. Based on the simulation in Fig. 5.15, we propose two distinct ways of breaking the symmetry, in a controlled way. A first method is to artificially increase the threshold of the first disk, such that the pulse from the first disk is able to excite the second disk, whereas the (similar) pulse travelling back, is not sufficiently strong to in turn excite the first disk. The threshold of a disk can be externally tuned by either changing its current, or the amplitude of its locking signal. Both decreasing the current or increasing the locking amplitude, will increase the threshold. In Fig. 5.16(a), we demonstrate this approach by induc-

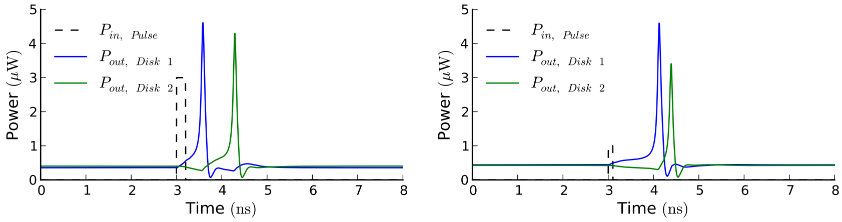

(a)

(b)

Figure 5.16: The excitation transfer between the two disks in Fig. 5.15 can be made unidirectional by breaking the symmetry of the system. (a) Symmetry breaking by difference in locking amplitude. The locking signal for the first disk has an amplitude of 4 $\sqrt{\mu W}$. For the second disk, the locking amplitude is 3.9 $\sqrt{\mu W}$. Both disks are pumped with a 2.3 mA current, $\Delta\phi = 2.8$ rad. The input pulse is 3 μW strong and 0.2 ns long. (b) Symmetry breaking by difference in locking phase. The locking signals for both disks have an amplitude of 3.55 $\sqrt{\mu W}$, while $\phi_{CW_2} = \phi_{CW_1} + \frac{\pi}{2}$. Both disks are pumped with a 2.3 mA current, $\Delta\phi = 4.2$ rad. The input pulse is 1 μW strong and 0.1 ns long.

ing an asymmetry in the locking amplitudes, such that the threshold of disk 1 is larger than the threshold of disk 2. The output pulse of the first disk clearly excites the second one, whereas the first disk is not excited by the returning (green) pulse. Since the threshold of disk 1 is artificially increased, a stronger input pulse is required to excite the first disk. In this particular example, the energy of the external perturbation is 6 times larger than the energy of the pulse used in Fig. 5.15. This energy related disadvantage limits the applicability of this approach to larger circuits of interconnected microdisk lasers.

A second method to deterministically break the symmetry of the system simulated in Fig. 5.15, is to induce a phase difference between the locking signals. For instance, we can set both locking signals in quadrature ($\phi_{CW_2} = \phi_{CW_1} + \frac{\pi}{2}$). As a consequence, the optimal phase delay to transfer the excitation from disk 1 to disk 2 will then increase by $\frac{\pi}{2}$, while the optimal delay for transfer of excitation in the opposite direction decreases by $\frac{\pi}{2}$. This allows to choose the phase delay in such a way that the pulses travelling from disk 1 have an excitatory effect on disk 2, whereas output pulses from disk 2 have an inhibitory effect on disk one.

In Fig. 5.16(b), the phase difference between both CW locking signals is $\frac{\pi}{2}$ and $\Delta\phi = 1.9\pi - \frac{\pi}{2} \approx 4.2$ rad. This brings the lasers in a regime in which a relatively weak pulse can excite the first disk, the first disk in its turn excites the second one, but this excitation does not excite the first disk. To achieve this, due to the change of the phase delay in the connecting waveguide, the locking amplitude has to be changed compared to the case of Fig. 5.16(a). Indeed, the small constant signal from one disk interferes differently with the constant locking signal of the other. An important advantage of this approach is that the threshold of the first disk is not artificially increased.

5.7 Sensitivity to parameter variations

In this section, we investigate the sensitivity of the response of the circuit introduced in Sec. 5.14(a), starting from the parameters used in Fig. 5.16(b), to certain parameter variations. In particular, we analyze the sensitivity to current variations and variations of the frequency detuning. Estimates of the robustness to current variations give an indication of how easily affected the dynamics are to experimental current fluctuations. The sensitivity to the frequency detuning gives not only a rough estimate of the tolerance with respect to variations in the lasing wavelengths between different disks, but also to the locking signal wavelength. The precise lasing wavelength can be seen as a net result of other parameter variations, and can be experimentally easily obtained.

We finalize this section with a demonstration of a possible approach to compensate such parameter variations, illustrated for the case of deviations in detuning.

5.7.1 Influence of current variations

Figure 5.17 relates the dynamics in both disks to the injection currents 2.3 mA + ΔI_1 and 2.3 mA + ΔI_2. Black regions signify that the disk is excited only once. In the white regions, the laser does not get excited, neither does it oscillate. In the light grey regions the laser keeps on oscillating. In the dark grey regions, the laser shows more complex multipulse excitability, in which the first disk excites multiple times before it is able to excite the second disk and the system finally decays back to the initial condition. The region for which excitability in both disks exists is rather small, with a cross-section of about 0.1 mA. Fortunately, a current stability of 0.1 mA can be experimentally obtained. Furthermore, this sensitivity to current variations can be used to make rough estimates of sensitivity to variations in other parameters. Taking into account that the bifurcation locking amplitude at $\Delta\omega = -20\ \mathrm{ns}^{-1}$ changes about 1 $\sqrt{\mu\mathrm{W}}$ per mA , a sensitivity to current variations of 0.1 mA corresponds to a sensitivity to locking amplitude variation on the order of 0.1 $\sqrt{\mu\mathrm{W}}$.

Since, above lasing threshold, the output power of a laser increases linearly with the current, the SNIC bifurcation shifts to higher injection amplitudes

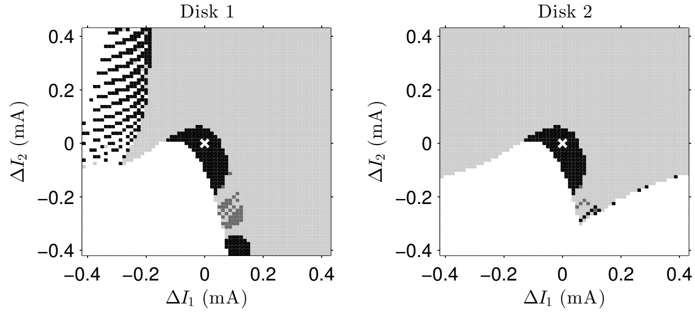

Figure 5.17: Influence of variations of the current through disks 1 and 2, ΔI_1 and ΔI_2, respectively. Unperturbed, both currents are 2.3 mA, $\Delta\phi$ = 4.2 rad. The locking signals for both disks are 3.55 $\sqrt{\mu\text{W}}$ and the input pulse is 1 μW strong and 0.15 ns long. As we are interested in an unidirectional excitation transfer, the optimal current setting appears when both disks only excite once. We represent a single excitation of the respective disk using black pixels, so the cross section of the black regions in both plots defines the domain with a unidirectional excitation transfer. In the light grey regions, the disk output is oscillating, independent of the perturbation. In the white regions, there is neither oscillation, nor excitation. In the dark grey regions, the disk shows more complex multipulse excitability (two pulses or more, after which the system decays again). The white cross represents the unperturbed system ($\Delta I_1 = 0$ and $\Delta I_2 = 0$).

when the current increases, i.e., the input power needed to lock the laser has to increase with increasing driving current. This explains the general behaviour of the two disks in Fig. 5.17. In contrast, for a single disk and at low currents, the bifurcation lies far below the amplitude of the locking signal, and the pulses are too weak to excite the laser. When the current is increased, the locking amplitude at the SNIC bifurcation approaches the current locking amplitude and excitation becomes possible. However, when the current is further increased, the bifurcation locking amplitude ends up above the locking amplitude, and the mode power oscillates. In Fig. 5.17, the same principle is reflected in the behaviour of the coupled disks: for each of the lasers, one can typically find oscillating regimes in higher current regions, unresponsive regions at lower currents and more complex behaviour, such as excitation, in between. In addition, as a result of the coupling between the lasers, more complex dynamic regimes occur that are less easy to interpret. For instance, in the region in the upper left corner, the second disk oscillates, whereas the first disk gets either excited, or not. Indeed, the locking signal of the first disk is produced by interference between the oscillating output of the second disk and a CW locking signal. In this regime, the excitation of the first disk depends on the timing of the pulse within the oscillation period of the second disk.

Another consequence of the current dependence of the bifurcation locking amplitude is that Fig. 5.17 depends on the strength of the input pulses, as the excitation threshold gradually increases when moving away towards lower currents. Consequently, at currents for which weak pulses are not capable of exciting the first disk, excitation can become possible when using stronger pulses, possibly inducing a response of the second disk.

5.7.2 Influence of detuning variations

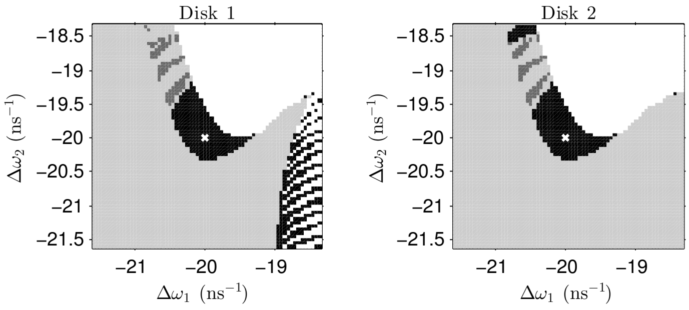

Figure 5.18: Influence of variations of the frequency detunings of both disks, $\Delta\omega_1$ and $\Delta\omega_2$, respectively. Unperturbed, the detuning is -20 ns^{-1}. The locking amplitude for both disks is 3.55 $\sqrt{\mu\mathrm{W}}$. The input pulse is 1 μW strong and 0.15 ns long. The colors represent the same behaviours as in Fig. 5.17.

Fabricated versions of a given disk design, will differ in the exact cavity wavelength. Therefore, if the same wavelength is used for the locking signals of those disks, there will be a certain deviation on the detuning with respect to these locking signals. Figure 5.18 shows how these deviation in detuning influence the dynamic behaviour from Fig. 5.16(b). Clearly, the structure of Fig. 5.18 is similar to Fig. 5.17, but mirrored around the center. The bifurcation diagram in Fig. 5.2 explains this similarity. For a single disk, the locking amplitude of the SNIC bifurcation decreases when the detuning $\Delta\omega$ approaches $\Delta\omega_{CCW} = 1.397\,\mathrm{ns}^{-1}$, i.e., the characteristic detuning offset of the unidirectional CCW solution of the rate equations [32] (this rather small detuning offset represents a change in the free running wavelength of the laser and is due to the influence of the field profile of the unidirectional solution on N, as a change in N changes the refractive index). Hence, bringing $\Delta\omega$ closer to $\Delta\omega_{CCW}$ has an effect similar to decreasing current.

The unidirectional excitability transfer is very sensitive to deviations of the detuning. It can be found in a ~ 1 ns^{-1}-wide region, which corresponds to a width of ~ 1.27 pm in wavelength. Variations larger than a picometer can already drastically change the behaviour. Unfortunately, current fabrication techniques typically result in variations in microdisk laser wavelength on the order of 0.4 nm [43]. Consequently, it is important to know how to deal with those wavelength fabrications. For this reason, we will discuss some compensation techniques in the next subsection.

5.7.3 Compensating for variations in detuning

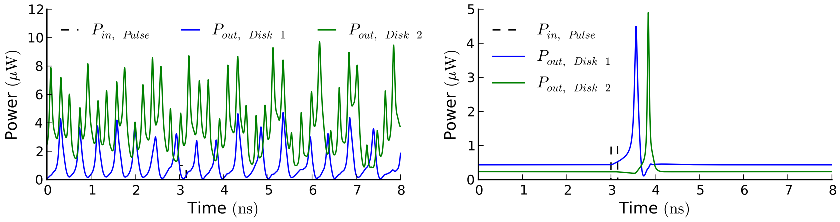

(a) (b)

Figure 5.19: (a) If the detuning of the second laser is -40 ns^{-1} (e.g., due to process variations), the dynamics of Fig. 5.16(b) can not be obtained, even though the other parameters are identical. (b) However, for this -40 ns^{-1} detuning of the second laser the desired unidirectional pulse transfer can be obtained by increasing I_2 to 1.7 mA and using 3.55 $\sqrt{\mu W}$ and $\sqrt{3}\cdot 3.55\ \sqrt{\mu W}$, as locking signal amplitudes for disk 1 and 2, respectively.

In this subsection we will illustrate how one can deal with the detuning variations, being one of the typical examples of process variations discussed in the previous subsections.

The excitable behaviour, and the transfer of excitability between two disks, as presented in section 5.6 and 5.7, is heavily influenced by process variations. However, for the simulations presented in Sec. 5.7.1 and 5.7.2, either currents, or detunings were swept, while all other parameters kept fixed. Nonetheless, a deviation in wavelength can be corrected by changing other parameters. As an example, we illustrate how a -20 ns^{-1} detuning mismatch of the second disk with respect to the first disk (i.e., $\Delta\lambda_2 = 51$ pm instead of $\Delta\lambda_1 = 25.5$ pm) can be compensated. Figure 5.19(a) shows how, without any compensation for this mismatch, both lasers exhibit complex self-pulsating behaviour instead of the desired unidirectional pulse transfer. The reason for this complex behaviour is that, for this wavelength detuning, the threshold value to obtain locking, which is also related to the SNIC bifurcation used for the excitation process, is considerably higher than the current locking amplitude for the second laser. To retrieve the undisturbed dynamic behaviour, either the amplitude of the locking signal can be increased, or the locking threshold can be artificially decreased by lowering the current. In Fig. 5.19(b), the unidirectional excitation transfer is recovered by combining both approaches. The current through the second disk is decreased to 1.7 mA, while its locking power is tripled.

The possibility to retreive the unidirectional excitability transfer in the presence of resonance wavelength imperfections by adapting the current and locking power, allows to relax the fabrication tolerances with one order of magnitude to a few tens of pm. This is still insufficient with respect to state-of-the-art fabrication accuracy. Additional mechanisms, such as deliberately changing the lasing wavelength using thermo-optic effects, should be addressed. Appropriately designed heaters can change the lasing wavelength of microdisk lasers over a range of about 2 nm [44].

5.8 Future work

In future work, the influence of the intermodal coupling C on the excitability mechanism in a single disk needs to be characterized. We need to find out the limitations on $|C|$ to obtain a proper pulse shape of the suppressed mode. As improved fabrication standards for future generation microdisk lasers might result in a lower $|C|$-value, it is important to know whithin what range for C a proper pulse shape can be obtained and how the pulse width of the excitation is affected. While the influence on the pulse shape is not so trivial to predict, we expect the pulse width to increase for decreasing $|C|$, as a lower $|C|$ implies a decrease in switching speed of the energy between the CW and CCW mode. Consequently, to control the value of $|C|$, it might be necessary to add corrugations on the side walls. As preliminary simulations, using the parameters mentioned in [32], show that the Class 1 excitability mechanism proposed in this chapter is also present in a SRL, we believe that this excitability mechanism will be present in other lasers based on whispering gallery mode resonators. Additionally, in the simulations of these SRLs the pulses are broader, which can indeed be linked to the smaller $|C|$-value of these components compared to the $|C|$-value of the microdisk lasers.

Moreover, we will need to find regimes where the interconnected disks are less dynamically coupled by the bias signal of their suppressed modes, making a trade-off between power consumption and robustness. A precise bifurcation study of the alternating excitation mechanism could help to improve the understanding of the excitation transfer mechanism, and hence give indications where optimal optical pumping or electrical injection conditions can be found.

Additionally, we did not yet discuss how we would implement the different locking signals experimentally. Initially, in the experimental demonstration of the excitability mechanism for a single disk, an external, off-chip commercial tunable laser can be used. Such commercial lasers have built-in isolators and will, due to those internal isolators, be insensitive to the dynamics of the on-chip microdisk lasers. On the other hand, in a larger excitable microdisk circuit, the locking sources should be integrated on the same chip, being preferably insensitive to the output of the disks without the need to incorporate isolators on-chip, as integrated versions of isolators are currently still very lossy. To circumvent this problem, we can choose other laser types, with less dynamical behaviour (e.g., based on Fabry-Perot cavities with distributed Bragg reflector gratings as mirrors), to injection-lock the microdisk lasers. Another option is to use a microdisk laser in a regime with high output power as the source of the locking signal. Indeed, in such a high output power regime the microdisk will be less sensitive to external inputs. The output of this laser can be distributed over several 'neuron'-disks by using power splitters, diminishing the possibility for a 'neuron' disk to disturb the 'locking' disk. Additional challenges that still need to be solved are the optimal placement of those external sources, the development of both a scheme that guarantees that all sources are locked, and a low-loss routing design in which the circuit for the locking signals does not interfere with the circuit dealing with the optical spikes.

A final interesting topic to investigate is the possibility to combine the previous excitation transfer mechanism with Wavelength Division Multiplexing (WDM). If a non-lasing side-mode of one of the disks (i.e., one of the other resonance wavelengths of the laser cavity) in the network overlaps with the lasing mode of another disk, even though both lasers have a different lasing wavelength, it could still be sensitive to the excitation of the latter. The design of networks incorporating this type of WDM is non-trivial, because of two reasons:

1. all the disks share the same gain material, and corresponding gain spectrum,

2. to operate in the single-mode regime a large Free Spectral Range (FSR) is needed, making it harder to let resonance wavelengths of the disk cavities overlap.

However, as this excitability mechanism is based on optical injection, it might be possible to reduce the FSR. Indeed, without optical injection a smaller FSR for a given gain spectrum results in multimode lasers and, consequently, the lasing mode can then be selected by the wavelength of the locking signal. In the case that excitations at other resonance wavelengths of the disk do not result in modehopping, this approach potentially paves the way towards multiwavelength optical SNNs. Recently, incoherent optical triggering of excitable pulses has been demonstrated experimentally in injection-locked semiconductor lasers [45].

5.9 Conclusion

In this chapter, we theoretically demonstrated that optically-injected microdisk lasers can exhibit Class 1 excitability. The excitability mechanism shows similar properties to equivalent Class 1 excitability found in biological neurons. Other properties, such as strong influence of optical phase, however, have no equivalent in biological or electrical systems, though they greatly influence the behaviour of this specific excitability mechanisms. In the presented geometry, both output and input are signals with relatively strong power pulses on a small background signal.

Additionally, given the similarity between the input and output pulse of the disk, cascadability of this excitability mechanism was demonstrated. The choice of the phase delay in the waveguide interconnection crucially determines its excitatory (inhibitory) character by forcing destructive (constructive) interference of the output pulse of the sending disk with the locking signal of the receiving disk. The possibility to use phase tuning to control excitation transfer is a feature which is not present in electronic spiking neuron implementations. When simulating a perfectly symmetrical pair of coupled disks, with a phase that corresponds to an excitatory connection, alternate excitations going back and forth between the neurons appear. This oscillating behaviour can be avoided by breaking the symmetry of the system, either by naively increasing the excitation threshold of one of the disks, or by inducing a phase difference between the locking signals of both lasers. Both methods can bring the lasers in a regime where only unidirectional transfer of excitation occurs. The latter behaviour roughly gets lost for current variations of 0.1 mA, and frequency variations on the order of 1 ns^{-1} ($\approx$ 1.27 pm). Fortunately, one can compensate for detuning variations by changing other, more controllable, parameters, such as the locking amplitude or the current, making the transfer of excitation robust to variations in lasing wavelength of several tens of pm. However, using the state-of-the-art production techniques for microdisk lasers, the standard deviation of the lasing wavelength is still about one order of magnitude too large. Additional compensation techniques, e.g., wavelength tuning by heating, will need to be considered.

The most important challenges for future work are a characterization of the influence of the intermodal coupling on the excitation mechanism, a reduction of the coupling of different disks by the bias signal of their suppressed modes and a scalable on-chip incorporation of the locking signal sources.

References

[1] Koen Alexander. *How excitable microdisk lasers can be used as spiking neurons How excitable microdisk lasers can be used as spiking neurons.* Master's thesis, UGent, 2013.

[2] Koen Alexander, Thomas Van Vaerenbergh, Martin Fiers, Pauline Mechet, Joni Dambre, and Peter Bienstman. *Excitability in optically injected microdisk lasers with phase controlled excitatory and inhibitory response.* Opt. Express , 4, submitted.

[3] Thomas Van Vaerenbergh, Koen Alexander, Joni Dambre, and Peter Bienstman. *Excitation transfer between optically injected microdisk lasers.* Opt. Express, 21(23):28922–28932, Nov 2013.

[4] M. Giudici, C. Green, G. Giacomelli, U. Nespolo, and J. R. Tredicce. *Andronov bifurcation and excitability in semiconductor lasers with optical feedback.* Physical Review E, 55(6):6414–6418, June 1997.

[5] F Plaza and MG Velarde. *Excitability following an avalanche-collapse process.* EPL (Europhysics Letters), 85, 1997.

[6] Stefano Beri, Lilia Mashall, Lendert Gelens, Guy Van der Sande, Gabor Mezosi, Marc Sorel, Jan Danckaert, and Guy Verschaffelt. *Excitability in optical systems close to Z2-symmetry.* Physics Letters A, 374(5):739–743, jan 2010.

[7] Sebastian Wieczorek, Bernd Krauskopf, and Daan Lenstra. *Multipulse excitability in a semiconductor laser with optical injection.* Physical review letters, 88(6):063901, 2002.

[8] D. Goulding, S. Hegarty, O. Rasskazov, S. Melnik, M. Hartnett, G. Greene, J. McInerney, D. Rachinskii, and G. Huyet. *Excitability in a Quantum Dot Semiconductor Laser with Optical Injection.* Physical Review Letters, 98(15):153903, April 2007.

[9] Sylvain Barbay, Robert Kuszelewicz, and Alejandro M Yacomotti. *Excitability in a semiconductor laser with saturable absorber.* Optics letters, 36(23):4476–8, dec 2011.

[10] A. Hurtado, K. Schires, I. D. Henning, and M. J. Adams. *Investigation of vertical cavity surface emitting laser dynamics for neuromorphic photonic systems.* Applied Physics Letters, 100(10):103703, 2012.

[11] W. Coomans, L. Gelens, S. Beri, J. Danckaert, and G. Van der Sande. *Solitary and coupled semiconductor ring lasers as optical spiking neurons.* Physical Review E, 84(3):1–8, sep 2011.

[12] M. Turconi, B. Garbin, M. Feyereisen, M. Giudici, and S. Barland. *Control of excitable pulses in an injection-locked semiconductor laser.* Physical Review E, 88(2):022923, aug 2013.

[13] Eugene M. Izhikevich. *Dynamical Systems in Neuroscience: The Geometry of Excitability and Bursting (Computational Neuroscience).* The MIT Press, 1 edition, nov 2006.

[14] Mitchell A Nahmias, Bhavin J Shastri, Alexander N Tait, and Paul R Prucnal. *A Leaky Integrate-and-Fire Laser Neuron for Ultrafast Cognitive Computing.* Selected Topics in Quantum Electronics, IEEE Journal of, 19:1800212, 2013.

[15] J L Dubbeldam, B Krauskopf, and D Lenstra. *Excitability and coherence resonance in lasers with saturable absorber.* Physical review. E, Statistical physics, plasmas, fluids, and related interdisciplinary topics, 60(6 Pt A):6580–8, December 1999.

[16] Mitchell A Nahmias, Alexander N Tait, Bhavin J Shastri, and Paul R Prucnal. *An Evanescent Hybrid Silicon Laser Neuron.* IEEE journal of selected topics in quantum electronics, 4:93–94, 2013.

[17] Brian R Koch, Alexander W Fang, Oded Cohen, and John E Bowers. *Mode-locked silicon evanescent lasers.* Optics express, 15(18):11225–33, September 2007.

[18] Alexander W Fang, Erica Lively, Ying-Hao Kuo, Di Liang, and John E Bowers. *A distributed feedback silicon evanescent laser.* Optics express, 16(7):4413–9, March 2008.

[19] Alexander W Fang, Brian R Koch, Kian-Giap Gan, Hyundai Park, Richard Jones, Oded Cohen, Mario J Paniccia, Daniel J Blumenthal, and John E Bowers. *A racetrack mode-locked silicon evanescent laser.* Optics express, 16(2):1393–8, January 2008.

[20] L Gelens, S Beri, and J Danckaert. *Phase-space approach to directional switching in semiconductor ring lasers.* Applied Physics, (September 2008):1–9, 2009.

[21] L. Gelens, S. Beri, G. Sande, G. Verschaffelt, and J. Danckaert. *Multistable and excitable behavior in semiconductor ring lasers with broken Z2-symmetry.* The European Physical Journal D, 58(2):197–207, March 2010.

[22] Yannick De Koninck, Koen Huybrechts, G Van der Sande, J Danckaert, Roel Baets, and Geert Morthier. *Nonlinear dynamics of asymmetrically coupled microdisk lasers.* In LEOS Annual Meeting Conference Proceedings, 2009. LEOS'09. IEEE, pages 503–504. IEEE, 2009.

[23] J. Van Campenhout, P.R. Romeo, D. Van Thourhout, C. Seassal, P. Regreny, L. Di Cioccio, J.-M. Fedeli, and R. Baets. *Design and Optimization of Electrically Injected InP-Based Microdisk Lasers Integrated on and Coupled to a SOI Waveguide Circuit.* Lightwave Technology, Journal of, 26(1):52–63, 2008.

[24] P Mechet, S Verstuyft, T De Vries, T Spuesens, P Regreny, D Van Thourhout, G Roelkens, and G Morthier. *Unidirectional III-V microdisk lasers heterogeneously integrated on SOI.* Opt. Express , 21(16):1988–1990, 2013.

[25] S. Keyvaninia, M. Muneeb, S. Stanković, P. J. Van Veldhoven, D. Van Thourhout, and G. Roelkens. *Ultra-thin DVS-BCB adhesive bonding of III-V wafers, dies and multiple dies to a patterned silicon-on-insulator substrate.* Optical Materials Express, 3(1):35, December 2012.

[26] S. Stankovicić, R. Jones, J. Heck, M. Sysak, D. Van Thourhout, and G. Roelkens. *Die-to-Die Adhesive Bonding Procedure for Evanescently-Coupled Photonic Devices.* Electrochemical and Solid-State Letters, 14(8):H326, 2011.

[27] Liu Liu, Rajesh Kumar, Koen Huybrechts, Gunther Roelkens, Erik-jan Geluk, Thijs Spuesens, Tjibbe De Vries, Philippe Regreny, Dries Van Thourhout, Roel Baets, and Geert Morthier. *An ultra-small, low-power, all-optical flip-flop memory on a silicon chip Âĺ.* Nature Photonics, 4(January):1–6, 2010.

[28] T Van Vaerenbergh, M Fiers, P Mechet, T Spuesens, R Kumar, G Morthier, B Schrauwen, J Dambre, and P Bienstman. *Cascadable Excitability in microrings.* Opt. Express , 20(18):20292–20308, mar 2012.

[29] Marc Sorel, PJR Laybourn, A Scirè, S Balle, G Giuliani, R Miglierina, and Silvano Donati. *Alternate oscillations in semiconductor ring lasers.* Optics letters, 27(22):1992–1994, 2002.

[30] M. Sorel, G. Giuliani, A. Scire, R. Miglierina, S. Donati, and P.J.R. Laybourn. *Operating regimes of gaas-algaas semiconductor ring lasers: experiment*

and model. IEEE Journal of Quantum Electronics, 39(10):1187–1195, October 2003.

[31] Joris Van Campenhout. *Thin-Film Microlasers for the Integration of Electronic and Photonic Integrated Circuits.* PhD thesis, UGent, 2007-2008.

[32] W Coomans, S Beri, G Van Der Sande, L Gelens, and J Danckaert. *Optical injection in semiconductor ring lasers.* Physical Review A, 81(March):033802, 2010.

[33] Sebastian Wieczorek, Bernd Krauskopf, TB Simpson, and Daan Lenstra. *The dynamical complexity of optically injected semiconductor lasers.* Physics Reports, 416(1):1–128, 2005.

[34] Wolfgang Maass. *Networks of spiking neurons: The third generation of neural network models.* Neural Networks, 10(9):1659 – 1671, 1997.

[35] S. Ghosh, S. Keyvaninia, Y. Shirato, T. Mizumoto, G. Roelkens, and R. Baets. *Optical Isolator for TE Polarized Light Realized by Adhesive Bonding of Ce:YIG on Silicon-on-Insulator Waveguide Circuits.* IEEE Photonics Journal, 5(3):6601108–6601108, June 2013.

[36] Samir Ghosh, Shahram Keyvaninia, Wim Van Roy, Tetsuya Mizumoto, Gunther Roelkens, and Roel Baets. *Adhesively bonded Ce:YIG/SOI integrated optical circulator.* Optics letters, 38(6):965–7, March 2013.

[37] T. Spuesens. *Compact on-chip Optical Interconnects on Silicon by Heterogeneous Integration of III-V Microsources and Detectors.* PhD thesis, Ghent University, 2013-2014.

[38] Kristof Vandoorne, Joni Dambre, David Verstraeten, Benjamin Schrauwen, and Peter Bienstman. *Parallel reservoir computing using optical amplifiers.* IEEE transactions on neural networks, 22(9):1469–1481, 2011.

[39] Kristof Vandoorne, Wouter Dierckx, Benjamin Schrauwen, David Verstraeten, Roel Baets, Peter Bienstman, and Jan Van Campenhout. *Toward optical signal processing using Photonic Reservoir Computing.* Opt. Express , 16(15):11182–11192, JUL 21 2008.

[40] Martin Fiers, Thomas Van Vaerenbergh, Ken Caluwaerts, Dries Vande Ginste, Benjamin Schrauwen, Joni Dambre, and Peter Bienstman. *Time-domain and frequency-domain modeling of nonlinear optical components on circuit-level using a node-based approach.* J. Opt. Soc. Am. B , 29(5):896–900, 2011.

[41] Michael R Watts, Jie Sun, Christopher DeRose, Douglas C Trotter, Ralph W Young, and Gregory N Nielson. *Adiabatic thermo-optic Mach-Zehnder switch.* Optics letters, 38(5):733–5, March 2013.

[42] W. Coomans, G. Van der Sande, and L. Gelens. *Oscillations and multistability in two semiconductor ring lasers coupled by a single waveguide.* Phys. Rev. A, 88:033813, Sep 2013.

[43] P Mechet, F Raineri, A Bazin, Y Halioua, T Spuesens, TJ Karle, P Regreny, P Monnier, D Van Thourhout, I Sagnes, et al. *Uniformity of the lasing wavelength of heterogeneously integrated InP microdisk lasers on SOI.* Optics express, 21(9):10622–10631, 2013.

[44] Liu Liu, Thijs Spuesens, Günther Roelkens, Dries Van Thourhout, Philippe Regreny, and Pedro Rojo-Romeo. *A thermally tunable III–V compound semiconductor microdisk laser integrated on silicon-on-insulator circuits.* Photonics Technology Letters, IEEE, 22(17):1270–1272, 2010.

[45] B. Garbin, D. Goulding, S.P. Hegarty, G. Huyet, B. Kelleher, and S. Barland. *Incoherent optical triggering of excitable pulses in an injection-locked semiconductor laser.* optics letters, (January):(tbp), 2014.

6

Conclusions and perspectives

In this PhD research, we have investigated the potential of two types of nonlinear photonic devices to function as spiking neurons that are integrated on a silicon photonics chip. More specifically, we have characterized the excitability mechanism in Silicon-On-Insulator (SOI) microrings and in optically-injected hybrid III-V on silicon microdisk lasers. Even though both components have an intrinsically different excitability mechanism, we have demonstrated that the optical output pulse due to an excitation in one component is able to trigger an excitation in another component. This corresponds to all-optical cascadability of the excitable components, allowing for pulse-encoded communication between such integrated optical neurons.

Additionally, to simulate the excitable behaviour in circuits containing those integrated devices, we developed a framework that can be used to simulate large circuits of nonlinear components in the time domain, using a phenomenologic lumped-element representation of the components.

In this final chapter, we summarize the main conclusions of this work, and elucidate promising roads for future research.

6.1 High-level simulations of nonlinear photonic integrated circuits

To study the dynamics in circuits of excitable optical components, the time-domain behaviour of those circuits needs to be simulated. Therefore, in chapter 3, we introduced Caphe, an in-house software framework that we have developed to simulate this type of circuits of nonlinear dynamical components. Scalable simulation tools for nonlinear photonic circuits will be crucial during the design of future large-scale optical Spiking Neural Networks (SNNs).

The framework proposed in chapter 3 allows for the modeling of optical circuits both in the time domain and the frequency domain. In the frequency domain, it can be used to calculate the (linear) steady-state characteristics of very large circuits. In the time domain it enables the efficient simulation of highly nonlinear systems by eliminating those components that can be described using only a scatter-matrix. The elimination of this type of components reduces the effective size of the circuit, and consequently speeds up the time-domain simulations. Because of a very flexible definition of the properties of the basic building block of the framework, we believe it can be used for other dynamical systems such as electrical systems and neural networks.

While the software framework was originally developed for time-domain simulations of nonlinear dynamics in nanophotonic integrated circuits, it is already being used frequently for other applications in photonics, such as in optical filter design. The software framework Caphe is therefore a very promising tool, as it is very fast, flexible, and can be combined with other scientific libraries which are readily available in Python.

In future work, this framework will be extended with different features, such as an efficient implementation of noise (e.g., to simulate the influence of amplified spontaneous emission in lasers), multiwavelength simulations (e.g., to simulate four-wave mixing experiments) and the possibility to simulate electronic circuits (e.g., to simulate electro-optic modulation of a Mach Zehnder interferometer).

6.2 Cascadable excitability

The potential to transfer an excitation from one neuron to another is indispensable when building SNNs. Therefore, in this dissertation we have focused on two components that allow for an all-optical excitation transfer: a passive microring and a microdisk laser. In the subsequent subsections we discuss the results for both types of optical spiking neurons and elucidate their individual advantages and challenges. We conclude this section by enlightening how the continuation of this research will result in the demonstration of large-scale optical SNNs.

6.2.1 A microring as a spiking neuron

In chapter 4, we have discussed how the interplay between thermal and free-carrier nonlinearities in a passive high-Q microring resonator can be exploited to obtain excitable pulses. In correspondence with theoretic predictions, this excitability is mainly observed at the blue side of the resonance. Moreover, a ring should preferably be close to critical coupling.

This excitability mechanism is related to the presence of a nearby subcritical Andronov-Hopf (AH) bifurcation at the self-pulsation onset. As a consequence the system shows Class 2 excitability. This thorough understanding of the excitability mechanism is necessary for a correct characterization of the computational properties of a microring, used as a photonic spiking neuron.

Importantly, the output pulses are sufficiently strong to excite other microrings, provided that the rings are both in their excitable regime due to a sufficiently small resonance spacing (< 100 pm). Using such a microring circuit, we have offered the world's first experimental proof of excitable pulse transfer in an integrated optics circuit. However, as we have used two all-pass rings connected by a single bus waveguide, the input perturbation disturbed both rings simultaneously and the output signal of the circuit contained the outputs of both rings. In future work, ring pair circuits should be designed in which the trigger pulse can address only one ring directly, without perturbing the other one, and in which we have access to the output of the individual rings.

6.2.2 A microdisk as a spiking neuron

In chapter 5, using simulations, we have demonstrated Class 1 excitability in optically injected microdisk lasers. From an application point-of-view, this excitability mechanism is easier to deal with than the Class 2 excitability mechanism in a microring, as currently more training algorithms are available for neurons with integrate-and-fire behaviour [1].

Class 1 excitability in optically injected semiconductor lasers is known to show similar properties to equivalent Class 1 excitability found in biological neurons. However, in regular semiconductor lasers with only one lasing mode, the output pulses during an excitation are often only a small ripple on a relatively high bias level of the output [2]. Advantageously, a microdisk laser has two counterpropagating lasing modes, of which one is stronger compared to the other due to the optical injection. Interestingly, due to the coupling between the strong and suppressed lasing mode in the microdisk cavity, the excitation of the disk by a perturbation of the strong mode, results in a pulse of the suppressed mode. This pulse is comparable in strength and size to the input pulse and has only a small background signal due to the low output signal of the suppressed mode in the rest state.

This excitability mechanism shows conceptual similarities with excitability in Semiconductor Ring Lasers (SRLs) with asymmetric intermodal coupling. Indeed, in a microdisk laser without optical injection, and a SRL with symmetric intermodal coupling, external pulses in the unidirectional lasing regime would result in switching between the CW and CCW mode [3]. Inducing asymmetry in this system, using optical injection or an asymmetric intermodal coupling guarantees that after a large amplitude trajectory due to the perturbation, the laser returns to its initial rest state. However, the different underlying physics of the symmetry breaking results in different excitability types: using intermodal coupling asymmetry results in resonator neuron behaviour (Class 2), while optical injection results in integrating neuron behaviour (Class 1). Additionally, we have not only found threshold behaviour as a function of the amplitude of the input pulse, but also as a function of the phase of this input pulse. This corresponds to recent experimental results in regular optical injected semiconductor lasers [2].

Due to the similarity between input pulse and output pulse, the output pulse of the disk is able to excite other disks, again giving rise to cascadable excitability. The choice of the phase delay in the waveguide interconnection crucially determines its excitatory (inhibitory) character by forcing destructive (constructive) interference of the output pulse of the sending disk with the locking signal of the receiving disk. This additional degree of freedom offers a potential advantage compared to traditional SNN implementations. Indeed, in analog hardware implementations of neural networks, interference effects of optical signals due to their phase result in an enhancement of the computational power of such a network [4, 5]. Consequently, we believe that future optical SNNs would encounter similar advantages compared to more traditional electronic implementations due to the sensitivity of the microdisk laser to the phase of the input pulse, and to the phase of the interconnection waveguide between disks.

Apart from the experimental verification of the previous theoretical results, the most important challenges for future work are a characterization of the influence of the intermodal coupling on the excitation mechanism, a reduction of the coupling of different disks by the bias signal of their suppressed modes and a scalable on-chip incorporation of the locking signal sources.

6.2.3 Towards large-scale optical Spiking Neural Networks

The logical continuation of this PhD research is to experimentally demonstrate, for the first time ever, an on-chip trainable all-optical SNN of non-trivial size in silicon photonics. This would push the limits of current research, which mainly focuses on the dynamics in one or two optical neurons, to fully functional networks that can be reconfigured and trained.

To achieve this, dedicated training algorithms should be designed of which the calculations can be efficiently locally implemented on the photonic chip using an additional electronic circuit. This is something which is not seen in current work, but this is a key ingredient, necessary to allow the use of optical SNNs in real-life applications. Additionally, efficient ways to delay the optical spikes between the neurons should be proposed. Indeed, to be able to process time-coded signals, a network needs memory. Intuitively one can understand that a delay in the interconnections of the neurons would allow for such memory. To be usable, this delay needs to be on the order of magnitude of the internal time scale of the neuron. However, due to the small footprints we aim for, the delay induced by the time-of-flight through the waveguides between the neurons is orders of magnitude too small. We believe that cascading several optical excitable components will result in a latency accumulation that might offer a natural mechanism to delay optical spikes.

Building fully-operational SNNs that are trainable would be an important breakthrough in hardware design for computational purposes. Indeed, choosing for integrated photonics implies that the neurons will operate at least a million times faster than their biological counterparts, with an outlook to becoming faster than current state-of-the-art electronic implementations, while the neuromorphic approach guarantees a very efficient processing of many time-varying signals in an energy-efficient way. While initial attempts will probably deal with networks of only 10-20 components, the large-scale integration offered by silicon photonics will allow to scale this up considerably.

The performance of optical SNNs should be validated, both in simulation and in experiment, for standard benchmark tasks, such as the pulse-timing encoded XOR problem or classification of the iris-dataset [6]. However, the final aim should be to go beyond that and identify real-world applications that can benefit from the advantages of this platform. Special emphasis should be placed on applications in which the input data is already in the optical domain, e.g., signal monitoring in optical networks or header recognition. Here, preliminary work has already been undertaken in our group on a non-spiking system [7]. Also, analysis of medical optical imaging (e.g., OCT) or LIDAR data [8] can be considered.

References

[1] Eugene M. Izhikevich. *Dynamical Systems in Neuroscience: The Geometry of Excitability and Bursting (Computational Neuroscience).* The MIT Press, 1 edition, nov 2006.

[2] M. Turconi, B. Garbin, M. Feyereisen, M. Giudici, and S. Barland. *Control of excitable pulses in an injection-locked semiconductor laser.* Physical Review E, 88(2):022923, aug 2013.

[3] Yannick De Koninck, Koen Huybrechts, G Van der Sande, J Danckaert, Roel Baets, and Geert Morthier. *Nonlinear dynamics of asymmetrically coupled microdisk lasers.* In LEOS Annual Meeting Conference Proceedings, 2009. LEOS'09. IEEE, pages 503–504. IEEE, 2009.

[4] Martin Fiers, Thomas Van Vaerenbergh, Francis Wyffels, David Verstraeten, Benjamin Schrauwen, Joni Dambre, and Peter Bienstman. *Nanophotonic reservoir computing with photonic crystal cavities to generate periodic patterns.* IEEE Transactions on Neural Networks and Learning Systems, 25(1):344–355, 2014.

[5] Kristof Vandoorne, Joni Dambre, David Verstraeten, Benjamin Schrauwen, and Peter Bienstman. *Parallel reservoir computing using optical amplifiers.* IEEE transactions on neural networks, 22(9):1469–1481, 2011.

[6] H Paugam-Moisy. *Computing with spiking neuron networks.* .), Handbook of Natural Computing., 2009.

[7] Kristof Vandoorne, Pauline Mechet, Thomas Van Vaerenbergh, Geert Morthier, David Verstraeten, Benjamin Schrauwen, Joni Dambre, and Peter Bienstman. *Experimental demonstration of reservoir computing on a silicon photonics chip.* Nature communications, tbp.

[8] Mitchell A Nahmias, Bhavin J Shastri, Alexander N Tait, and Paul R Prucnal. *A Leaky Integrate-and-Fire Laser Neuron for Ultrafast Cognitive Computing.* Selected Topics in Quantum Electronics, IEEE Journal of, 19:1800212, 2013.